

**The Formation of Craters and the
Remobilisation of Sediment on the Mid
Norway Margin**

Gordon William Mackenzie Lawrence

**Submitted in partial fulfilment of the requirements
for the degree of Ph.D.**

Cardiff University

July 2010

UMI Number: U516991

All rights reserved

INFORMATION TO ALL USERS

The quality of this reproduction is dependent upon the quality of the copy submitted.

In the unlikely event that the author did not send a complete manuscript and there are missing pages, these will be noted. Also, if material had to be removed, a note will indicate the deletion.



UMI U516991

Published by ProQuest LLC 2013. Copyright in the Dissertation held by the Author.
Microform Edition © ProQuest LLC.

All rights reserved. This work is protected against
unauthorized copying under Title 17, United States Code.



ProQuest LLC
789 East Eisenhower Parkway
P.O. Box 1346
Ann Arbor, MI 48106-1346

DECLARATION

This work has not previously been accepted in substance for any degree and is not concurrently submitted in candidature for any degree.

Signed Gordon Lawrence (Candidate) Date 29/11/2010

STATEMENT 1

This thesis is being submitted in partial fulfilment of the requirements for the degree of Ph.D.

Signed Gordon Lawrence (Candidate) Date 29/11/2010

STATEMENT 2

This thesis is the result of my own independent work/investigation, except where otherwise stated. Other sources are acknowledged by explicit references.

Signed Gordon Lawrence (Candidate) Date 29/11/2010

STATEMENT 3

I hereby give consent for my thesis, if accepted, to be available for photocopying and for inter-library loan, and for the title and summary to be made available to outside organisations.

Signed Gordon Lawrence (Candidate) Date 29/11/2010

STATEMENT 4

I hereby give consent for my thesis, if accepted, to be available for photocopying and for inter-library loans after expiry of a bar on access previously approved by the Graduate Development Committee.

Signed Gordon Lawrence (Candidate) Date 29/11/2010

ABSTRACT

Enigmatic craters tens of kilometres in diameter have been mapped previously at the top of Oligo-Miocene ooze on the mid Norway margin. These craters have been linked with sliding and the remobilisation of large volumes of sediment to a palaeo-seabed. In this study seismic reflection data are used to map slides, craters and mounds in the Møre Basin to better understand how the craters form. Many craters are filled by a slide named Slide W, which is by volume similar to the Storegga Slide, but which was translated only a few kilometres. Mounds are mapped in the vicinity of craters filled by Slide W on the top surface of Slide W. These mounds consist of sediment remobilised from the ooze in which the craters are incised. Mounds generally pinch out onto the top surface of Slide W and are emplaced on a palaeo-seabed, suggesting that failure of Slide W, incision of craters filled by Slide W and remobilisation of ooze occurred contemporaneously. A hypothetical model is presented linking these processes to gas hydrate dissociation. Rapid deposition of less permeable sediments burying more permeable ooze leads to shoaling of the base of a gas hydrate stability zone towards the top of the ooze and the base of the rapidly deposited sediments. Dissociation of gas hydrate increases the pore pressure of the ooze. If pore pressure becomes equal to lithostatic pressure, fracturing of the overburden and venting of methane may occur, leading to slope failure. Alternatively, build up of pore pressure primes or triggers the slide. Ooze is liquefied and emplaced on the seabed through vents or faults developing in the slide, forming a crater in the subsurface into which the slide subsides. A new class of structure is defined (Subsurface Gas Expulsion Structures), and the significance of these structures is discussed.

AUTHOR'S NOTE

The text of Chapter 3 of this thesis is modified from the following publication:

Lawrence, G.W.M., Cartwright, J.A., 2009. The initiation of sliding on the mid Norway margin in the Møre Basin. Marine Geology 259, 21-35.

The Geological Setting section was removed, and other consequent changes were made through the remainder of the text of the publication, prior to insertion in this thesis.

The text of Chapter 4 of this thesis is modified from the following publication in press:

Lawrence, G.W.M., Cartwright, J.A., 2010. The stratigraphic and geographic distribution of giant craters and remobilised sediment mounds on the mid Norway margin, and their relation to long term fluid flow. Marine and Petroleum Geology, 27, 733-747.

Part of the Introduction was removed. The Geological Setting was also removed and other consequent changes were made through the remainder of the text, prior to insertion in this thesis.

Chapter 1 consists partly of material removed from the Introduction section of the publication from which Chapter 4 is drawn. Chapter 2 consists partly of a synthesis of material from the Geological Setting and Methodology sections removed from the text of the publications which make up Chapters 3 and 4 above.

These changes were all made to ensure that the thesis presents a continuous narrative, as per the requirements of Cardiff University.

The publications from which parts of Chapters 1, 2, 3 and 4 are drawn are the work of the lead author (GWML), and editorial support was provided by the project supervisor, JAC, in accordance with a normal thesis chapter.

ACKNOWLEDGEMENTS

The project supervisor Joe Cartwright is thanked for his patience, support and guidance. NERC financed the project. The School of Earth and Ocean Sciences and Cardiff University are acknowledged for providing me with all the necessary facilities to conduct this research. Colleagues in the 3D Lab, reviewers of my papers, and countless people met at conferences are acknowledged for stimulating conversations that helped me to refine my ideas. Ian Clark and Suzy Ball are acknowledged for particularly useful discussions, and my office mate Sutieng Ho is thanked for putting up with my end-of-PhD madness. Gwen Pettigrew is acknowledged for technical support, without which this project would not have been possible.

Everyone at the Cardiff University Catholic Chaplaincy is thanked for their support and friendship over the last three and a half years. In particular, the spiritual support of the Catholic Chaplains to Cardiff University during the last three and a half years, Fr. John Owen and, latterly, Fr Gareth Jones, is acknowledged. David Hutchings is thanked for keeping me sane over our many lunches together in the last year or so.

The last year has been particularly stressful on a personal level, and a number of people deserve thanks for their help and support during this time which has enabled me to maintain my focus on this project. In addition to the people listed above, these include John Goode, Becky Barton, Isla Harrison, Crispy McDuck, Helen Godfrey, and Mike Doran.

I would like to acknowledge the loving help and support of my family. During the course of this project I married Alexandra who I met at the beginning of my time in Cardiff. She is thanked for her continuing love and support. My daughter Flora is thanked for giving me a sense of perspective. My parents, Christopher and Nicola Lawrence, and my grandmother, Rachel Cox, are thanked for support with housing. My parents in law, Veronika and Karl-Heinz Kaspari are also thanked for significant support over the last three years. Lastly I would like to acknowledge the support of one of my wife's aunts, Katharina Bresan, who passed away as I was completing this work. She was a remarkable and generous lady. May she rest in peace.

CONTENTS

| | |
|---|------|
| ABSTRACT..... | i |
| AUTHOR'S NOTE..... | ii |
| ACKNOWLEDGEMENTS..... | iii |
| CONTENTS..... | iv |
| LIST OF FIGURES | x |
| LIST OF TABLES | xiii |
| 1 INTRODUCTION | 1-1 |
| 1.1 Background..... | 1-1 |
| 1.2 Previous work | 1-2 |
| 1.2.1 Description of craters in the Norwegian Sea | 1-3 |
| 1.2.1.1 Havsule craters and ooze mounds..... | 1-3 |
| 1.2.1.2 Sklinnadjupet craters and ooze mounds..... | 1-6 |
| 1.2.1.3 Solsikke craters and ooze mounds | 1-6 |
| 1.2.1.4 Vema Dome area..... | 1-6 |
| 1.2.2 Well data | 1-7 |
| 1.2.3 The model presented by Riis et al. (2005) | 1-7 |
| 1.3 Scope of this research | 1-12 |
| 1.3.1 Distribution of craters and mounds..... | 1-12 |
| 1.3.2 Were craters excavated onto the seabed?..... | 1-12 |
| 1.3.3 Well data | 1-12 |
| 1.3.4 Volume of mounds..... | 1-13 |
| 1.3.5 Infill of craters..... | 1-13 |
| 1.3.6 The importance of the opal A/CT transition to crater formation..... | 1-13 |
| 1.4 Aims of thesis | 1-14 |
| 1.5 Structure of thesis | 1-14 |
| 2 METHODOLOGY AND GEOLOGICAL SETTING | 2-1 |
| 2.1 Methodology | 2-1 |
| 2.2 Geological time periods | 2-6 |
| 2.3 Definitions..... | 2-6 |
| 2.3.1 Craters | 2-6 |
| 2.3.2 Mounds | 2-7 |

| | | |
|---------|--|------|
| 2.3.3 | Slides..... | 2-8 |
| 2.4 | Geological Setting..... | 2-9 |
| 2.4.1 | The Møre Basin..... | 2-9 |
| 2.4.2 | Stratigraphy..... | 2-14 |
| 3 | THE INITIATION OF SLIDING IN THE MØRE BASIN ON THE MID NORWAY MARGIN | 3-1 |
| 3.1 | Introduction..... | 3-1 |
| 3.2 | Database and methodology | 3-2 |
| 3.3 | Detailed mapping of slides..... | 3-4 |
| 3.3.1 | Slide Y | 3-8 |
| 3.3.1.1 | Margins and morphology..... | 3-8 |
| 3.3.1.2 | Basal Shear Surface | 3-9 |
| 3.3.1.3 | Internal Geometry | 3-9 |
| 3.3.1.4 | Top Surface..... | 3-13 |
| 3.3.1.5 | Kinematic Indicators..... | 3-13 |
| 3.3.2 | Slide W..... | 3-13 |
| 3.3.2.1 | Gross Morphology | 3-14 |
| 3.3.2.2 | Basal Shear Surface | 3-14 |
| 3.3.2.3 | Internal Geometry | 3-20 |
| 3.3.2.4 | Top Surface..... | 3-20 |
| 3.3.2.5 | Kinematic Indicators..... | 3-21 |
| 3.4 | Discussion..... | 3-21 |
| 3.4.1 | Slide Processes..... | 3-21 |
| 3.4.2 | Basinal Context..... | 3-23 |
| 3.4.3 | Timing..... | 3-24 |
| 3.4.4 | Slope Configuration | 3-26 |
| 3.4.5 | Evaluation of Methods..... | 3-26 |
| 3.5 | Conclusions..... | 3-27 |
| 4 | THE STRATIGRAPHIC AND GEOGRAPHIC DISTRIBUTION OF GIANT CRATERS AND REMOBILISED SEDIMENT MOUNDS ON THE MID NORWAY MARGIN, AND THEIR RELATIONSHIP TO LONG TERM FLUID FLOW..... | 4-1 |
| 4.1 | Introduction..... | 4-1 |
| 4.2 | Database / Methods..... | 4-1 |
| 4.3 | Craters..... | 4-2 |

| | | |
|---------|---|------|
| 4.3.1 | Description of craters | 4-2 |
| 4.3.2 | Relationship of craters to stratigraphy | 4-2 |
| 4.3.3 | Relationship of craters to basin structure | 4-3 |
| 4.4 | Mounds | 4-12 |
| 4.4.1 | Description of mounds | 4-12 |
| 4.4.2 | Morphology of mounds | 4-13 |
| 4.5 | Timing | 4-14 |
| 4.6 | Discussion | 4-15 |
| 4.6.1 | Long term fluid flow | 4-15 |
| 4.6.2 | Observations and previous work | 4-17 |
| 4.6.3 | Formation of craters and emplacement of sediment mounds | 4-18 |
| 4.6.3.1 | Hypothesis A | 4-19 |
| 4.6.3.2 | Hypothesis B | 4-25 |
| 4.7 | Summary and Conclusions | 4-27 |
| 5 | A THREE DIMENSIONAL DESCRIPTION OF CRATERS AND REMOBILISED SEDIMENT MOUNDS ON THE MID NORWAY MARGIN | 5-1 |
| 5.1 | Introduction | 5-1 |
| 5.2 | Database and methodology | 5-3 |
| 5.3 | Results of depth conversions | 5-3 |
| 5.4 | Havsule Survey | 5-4 |
| 5.4.1 | Description of craters A and B | 5-4 |
| 5.4.1.1 | Sidewall of Craters A and B | 5-5 |
| 5.4.1.2 | Basal Surface of Craters A and B | 5-14 |
| 5.4.1.3 | Internal fill of Craters A and B | 5-17 |
| 5.4.1.4 | Top surface of fill of Craters A and B | 5-25 |
| 5.4.2 | Description of mounds | 5-26 |
| 5.4.2.1 | Location | 5-28 |
| 5.4.2.2 | Plan view geometry | 5-28 |
| 5.4.2.3 | External morphology and internal structure | 5-28 |
| 5.5 | Solsikke Survey | 5-38 |
| 5.5.1 | Description of Mound | 5-38 |
| 5.5.1.1 | Well calibration of Mound | 5-38 |
| 5.5.1.2 | External Morphology | 5-44 |
| 5.5.1.3 | Internal Geometry of Mound GJ | 5-45 |

| | | |
|---------|--|------|
| 5.5.2 | Description of Craters | 5-45 |
| 5.5.2.1 | External Morphology and Burial of Craters H and I | 5-45 |
| 5.5.2.2 | Basal Surface and Internal fill of Craters H and I..... | 5-52 |
| 5.6 | Edvarde Survey | 5-57 |
| 5.6.1 | Description of Crater and Crater fill | 5-57 |
| 5.6.1.1 | Plan view geometry..... | 5-57 |
| 5.6.1.2 | Basal surface | 5-57 |
| 5.6.1.3 | Sediments evacuated at Crater D | 5-64 |
| 5.6.1.4 | Burial of Crater D | 5-65 |
| 5.7 | Synthesis | 5-70 |
| 5.8 | Discussion | 5-71 |
| 5.8.1 | Evaluation of Hypotheses A and B | 5-72 |
| 5.8.2 | A new hypothesis..... | 5-74 |
| 5.8.2.1 | Gas Hydrates | 5-74 |
| 5.8.2.2 | Fluidisation or Liquefaction of the Brygge Formation | 5-85 |
| 5.8.2.3 | Remobilisation of the Brygge Formation | 5-88 |
| 5.8.2.4 | Mounds post-emplacement | 5-89 |
| 5.8.2.5 | Crater A..... | 5-90 |
| 5.8.2.6 | Significance of opal A/CT boundary | 5-90 |
| 5.8.3 | Summary of Hypothesis C | 5-91 |
| 6 | DISCUSSION | 6-1 |
| 6.1 | Wider significance of craters on the mid Norway margin..... | 6-1 |
| 6.1.1 | Volume of methane released from craters | 6-1 |
| 6.2 | Comparative study area: The Blake Ridge Depression | 6-4 |
| 6.2.1 | Description..... | 6-4 |
| 6.2.2 | Comparison of craters on the mid Norway Margin with the Blake Ridge Depression | 6-7 |
| 6.3 | Are the craters pockmarks?..... | 6-9 |
| 6.4 | Are the mounds diapirs? | 6-10 |
| 6.5 | Subsurface Gas Expulsion Structures | 6-11 |
| 6.6 | Where else could Subsurface Gas Expulsion Structures form?..... | 6-12 |
| 6.7 | Significance of Subsurface Gas Expulsion Structures..... | 6-14 |
| 6.8 | Further Work..... | 6-15 |
| 7 | SUMMARY AND CONCLUSIONS | 7-1 |

| | | |
|--|--|-----|
| 7.1 | Previous work | 7-1 |
| 7.2 | Conclusions from Chapter 3: Mapping of Slides..... | 7-1 |
| 7.3 | Conclusions from Chapter 4: Regional mapping of craters and mounds .. | 7-2 |
| 7.4 | Conclusions from Chapter 5: Detailed mapping of craters and mounds ... | 7-3 |
| 7.5 | Conclusions from Chapter 6: Subsurface gas expulsion structures | 7-5 |
| 8 | REFERENCES | 8-6 |
| APPENDIX A1: ADDITIONAL EVIDENCE IN SUPPORT OF FINDINGS OF CHAPTER 2 | | 1 |
| APPENDIX A2: ADDITIONAL EVIDENCE IN SUPPORT OF FINDINGS OF CHAPTER 3 | | 8 |
| APPENDIX A3: ADDITIONAL EVIDENCE IN SUPPORT OF FINDINGS OF CHAPTER 4 | | 14 |
| APPENDIX A4: ADDITIONAL EVIDENCE IN SUPPORT OF FINDINGS OF CHAPTER 5 | | 15 |
| Data used for depth conversions | | 15 |
| CDP 4002 Havsule..... | | 15 |
| ILN 2634 Havsule..... | | 17 |
| CDP 4942 Havsule..... | | 19 |
| ILN 2398 Havsule..... | | 21 |
| CDP 2920 Havsule..... | | 23 |
| ILN 2574 Havsule..... | | 24 |
| CDP 4972 Solsikke | | 25 |
| ILN 3174 Solsikke | | 27 |
| Data used to compile dip of thrust faults | | 29 |
| CDP 4942..... | | 29 |
| CDP 4002..... | | 29 |
| Data used to compile dips of crater sidewalls..... | | 30 |
| Crater A – Westward dipping sidewalls | | 30 |
| Crater A – Eastward dipping sidewalls..... | | 30 |
| Crater A – Southward dipping sidewalls | | 31 |
| Crater A – Northward dipping sidewalls | | 31 |
| Crater B – Westward dipping sidewalls..... | | 31 |
| Crater B – Southward dipping sidewalls | | 33 |
| Crater B – Northward dipping sidewalls | | 34 |

| | |
|--|----|
| Crater B – Incision 1 – Westward dipping sidewalls..... | 34 |
| Crater B – Incision 1 – Southward dipping sidewalls..... | 34 |
| Crater B – Incision 1 – Northward dipping sidewalls..... | 34 |
| Crater B – Incision 2 – Westward dipping sidewalls..... | 35 |
| Crater B – Incision 2 – Southward dipping sidewalls..... | 35 |
| Crater B – Incision 2 – Northward dipping sidewalls..... | 35 |
| Crater B – Incision 3 – Southward dipping sidewalls..... | 36 |
| Crater B – Incision 3 – Northward dipping sidewalls..... | 36 |
| Crater B – Incision 4 – Westward dipping sidewalls..... | 36 |
| Crater B – Incision 4 – Southward dipping sidewalls..... | 37 |
| Crater B – Incision 4 – Northward dipping sidewalls..... | 37 |
| Crater B – Incision 5 – Westward dipping sidewalls..... | 37 |
| Crater B – Incision 5 – Southward dipping sidewalls..... | 37 |
| Crater B – Incision 5 – Northward dipping sidewalls..... | 37 |
| Crater B – Mini crater – Westward dipping sidewalls..... | 38 |
| Crater B – Mini crater – Eastward dipping sidewalls | 38 |
| Crater B – Mini crater – Southward dipping sidewalls..... | 39 |
| Crater B – Mini crater – Northward dipping sidewalls..... | 39 |
| Data used to compile dip of top surface of ooze mounds | 40 |
| CDP 4002 – Westward dipping slopes | 40 |
| CDP 4002 – Eastward dipping slopes..... | 40 |
| ILN 2634 – Northward dipping slopes | 41 |
| ILN 2634 – Southward dipping slopes | 42 |
| CDP 4942 – Westward dipping slopes | 42 |
| CDP 4942 – Eastward dipping slopes..... | 43 |
| ILN 2398 – Northward dipping slopes | 43 |
| ILN 2398 – Southward dipping slopes | 44 |

LIST OF FIGURES

| | |
|---|------|
| Fig. 1-1: A map of the mid Norway margin, indicating the areas studied by Riis et al. 2005 | 1-4 |
| Fig. 1-2: Seismic profile across the Havsule Structure after Riis et al. 2005..... | 1-5 |
| Fig. 1-3: Craters and Mounds in the Skilinadjupet Slide area after Riis et al 2005 | 1-8 |
| Fig. 1-4: Craters and Mounds in the in Storegga and North Sea Fan areas after Riis et al 2005..... | 1-9 |
| Fig. 1-5: Craters and Mounds in the Vema Dome area after Riis et al 2005.. | 1-10 |
| Fig. 1-6: A model which may explain the formation of craters and mounds after Riis et al. (2005).... | 1-11 |
| Fig. 2-1: Seismic wavelets, adapted from Hart (1999). | 2-3 |
| Fig. 2-2: Schematic illustration of a well penetrating an anticline. | 2-4 |
| Fig. 2-3: Pre- and post- migration Fresnel Zone diameters, Adapted from Brown (2004)..... | 2-4 |
| Fig. 2-4: Map of dataset referred to in this thesis. | 2-10 |
| Fig. 2-5: Maps of the mid Norway margin, showing the location of figures, and wells..... | 2-11 |
| Fig. 2-6: Seismic lines across the Møre Basin and a chronstratigraphic column..... | 2-12 |
| Fig. 2-7: Seismic line demonstrating inter-relationship of 3 units that comprise Brygge Formation. | 2-21 |
| Fig. 2-8: A section showing the normal fault tier that deforms the Neogene stratigraphy. | 2-22 |
| Fig. 3-1: A bathymetry map of the mid Norway margin showing the location of the Møre Basin | 3-3 |
| Fig. 3-2: A section through the Neogene stratigraphy of the Møre Basin (see Fig. 3-1 for location) ... | 3-5 |
| Fig. 3-3: Sections showing the dating of Slide Y and Slide W..... | 3-7 |
| Fig. 3-4: A contoured isopach map of Slide Y in the Møre Basin..... | 3-10 |
| Fig. 3-5: A section through the northern portion of Slide Y | 3-11 |
| Fig. 3-6: A coherency map of and profile through the headwall region of Slide Y..... | 3-12 |
| Fig. 3-7: A contoured Isopach map of Slide W in the Møre Basin..... | 3-15 |
| Fig. 3-8: Sections through the headwall of Slide W | 3-17 |
| Fig. 3-9: An amplitude map of the basal shear surface of Slide W at a sidewall..... | 3-17 |
| Fig. 3-10: An amplitude map of the basal shear surface of Slide W near the headwall | 3-19 |
| Fig. 3-11: A section showing the normal fault tier that deforms the Neogene stratigraphy | 3-25 |
| Fig. 3-12: A time section showing the location of slides with respect to the continental shelf. | 3-28 |
| Fig. 4-1: Maps of the mid Norway margin, showing the location of the Møre Basin and Craters | 4-4 |
| Fig. 4-2: Craters A, B, C and D. | 4-8 |
| Fig. 4-3: Craters B,C, E, F, G, H, I, J and K..... | 4-8 |
| Fig. 4-4: Seismic lines across the Møre Basin..... | 4-10 |
| Fig. 4-5: Subcrop map of the regional surface that acts as a basal shear plane to Slide W. | 4-11 |
| Fig. 4-6: Hypothesis A. | 4-21 |
| Fig. 4-7: Hypothesis B..... | 4-23 |
| Fig. 5-1: Map showing location of surveys and subsequent figures..... | 5-2 |
| Fig. 5-2: A map of Crater A, Crater B, Mound A Mound BCF..... | 5-6 |
| Fig. 5-3: A crossline in time through Crater B and Mound BCF..... | 5-7 |
| Fig. 5-4: A crossline in time through Crater B and Mound BCF..... | 5-8 |

| | |
|--|------|
| Fig. 5-5: A crossline in time through Crater A and Mound A | 5-9 |
| Fig. 5-6: An inline in time through Crater B and Mound BCF | 5-10 |
| Fig. 5-7: An inline in time through Crater B and Mound BCF | 5-11 |
| Fig. 5-8: An inline in time through Crater A and Mound A. | 5-12 |
| Fig. 5-9: A dip map of a portion of the basal surface of Crater B. | 5-19 |
| Fig. 5-10: An irregularity on the basal surface of Crater B. | 5-19 |
| Fig. 5-11: A coherency slice, highlighting the internal geometry of Crater B | 5-23 |
| Fig. 5-12: Thrust faulting within the internal fill of Crater B. | 5-24 |
| Fig. 5-13: A map of Craters A and B, Mound A Mound BCF. | 5-27 |
| Fig. 5-14: A time map of the top surface of Slide W and Mound BCF. | 5-30 |
| Fig. 5-15: A rose diagram showing the orientation of the long axes of ridges | 5-31 |
| Fig. 5-16: Distribution of slope dips | 5-33 |
| Fig. 5-17: Distribution of slope dips | 5-34 |
| Fig. 5-18: A close up of the mound in Fig. 5-3. | 5-36 |
| Fig. 5-19: Gas escape conduit inside mound. | 5-37 |
| Fig. 5-20: Detailed map and sections through a portion of Mound BCF | 5-40 |
| Fig. 5-21: A map of a portion of Mound GJ in the vicinity of Crater J | 5-41 |
| Fig. 5-22: A crossline in time through Mound GJ | 5-42 |
| Fig. 5-23: A crossline in time through Mound GJ | 5-43 |
| Fig. 5-24: A time map of the top surface of Mound GJ | 5-47 |
| Fig. 5-25: A map of a Craters H and I. | 5-48 |
| Fig. 5-26: A crossline in time through Crater I | 5-49 |
| Fig. 5-27: A crossline in time through Crater H | 5-50 |
| Fig. 5-28: A crossline in time through Mound GJ and Crater H. | 5-51 |
| Fig. 5-29: A dip map of a portion of the basal surface of Crater I | 5-54 |
| Fig. 5-30: A coherency slice, highlighting the internal geometry of Crater H. | 5-55 |
| Fig. 5-31: A coherency slice, highlighting the internal geometry of Crater I | 5-56 |
| Fig. 5-32: A map of a Crater D and Mound D | 5-58 |
| Fig. 5-33: A crossline in time through Crater D and Mound D | 5-59 |
| Fig. 5-34: A crossline in time through Crater D | 5-60 |
| Fig. 5-35: A traverse in time through Crater D | 5-61 |
| Fig. 5-36: An inline in time through Crater D | 5-62 |
| Fig. 5-37: A dip map of a portion of the basal surface of Crater D | 5-63 |
| Fig. 5-38: A time map of the top surface of Package 1 in the area of Crater D | 5-67 |
| Fig. 5-39: A dip map of the basal surface of Package 3 (The Storegga Slide) above Crater D | 5-68 |
| Fig. 5-40: Compaction profiles from Praeger (2009) | 5-76 |
| Fig. 5-41: Graphs of seafloor depth vs. depth of base of the gas hydrate stability zone | 5-80 |
| Fig. 5-42: $\delta^{18}\text{O}$ records for the North Atlantic after Sosdian and Rosenthal (2009) | 5-81 |
| Fig. 5-43: Record of Northern Water Component flux after Wright and Miller (1996) | 5-82 |
| Fig. 5-44: Mg/Ca record from the North Atlantic after Sosdian and Rosenthal (2009) | 5-82 |

| | |
|--|-----|
| Fig. 5-45: Schematic hypothesis explaining formation of craters and mounds on mid Norway margin .5-93 | |
| Fig. 6-1: A map of the Blake Ridge Depression (BRD) after Holbrook et al. (2002) | 6-5 |
| Fig. 6-2: Seismic reflection data illustrating Blake Ridge Depression after Holbrook et al. (2002). | 6-6 |

LIST OF TABLES

| | |
|---|------|
| Table 2-1: Characteristics of the data used in this study. | 2-10 |
| Table 2-2: Data on the Brygge Formation, Kai Formation and the base of the Naust Formation, obtained from selected wells inside and outside the mapping area. | 2-17 |
| Table 3-1: Characteristics of Slide Y and Slide W. | 3-6 |
| Table 4-1 Characteristics of craters mapped in the study area. | 4-5 |
| Table 4-2 Characteristics of mounds mapped in the study area. | 4-6 |
| Table 5-1: Internal velocity values. Values utilised for depth conversions in this chapter are highlighted in bold. | 5-13 |
| Table 5-2: Measurements of the dip of the sidewalls of Craters A and B. The western sidewall of Crater B is complex is considered separately below. See Table A4- 19 to Table A4- 25 in Appendix A4 for data used to compile these average dips. | 5-15 |
| Table 6-1: Estimates of the percentage of pore space in the gas hydrate stability zone occupied by gas hydrate at the Blake Ridge. | 6-3 |

1 INTRODUCTION

1.1 Background

Large enigmatic craters with a circular–elliptical planform up to 20 km in diameter and 300 m deep have recently been discovered in the Møre Basin offshore Norway (Riis et al., 2005). Similar craters have also been found further north on the mid Norwegian margin (Riis et al., 2005, Rise et al., 2006). These craters do not resemble the craters formed by the impact of projectiles on the earth's surface (e.g. Chicaxalub, Hildebrand et al., 1991), the collapse of volcanic calderas (e.g. Santorini, Druitt and Francaviglia, 1992), erosional processes (e.g. Makhtesh Ramon, Ben-David et al., 2002) or surface pockmarks (Hovland and Judd, 1988, Judd and Hovland, 2007). They are therefore of geological interest because they may reveal another mechanism by which craters can form on the surface of this planet, and by extension, on the surface of other planets.

Large lens shaped mounds of remobilised sediment have also been mapped on the mid Norway margin (Chapter 4, Hjelstuen et al., 1997, Hovland et al., 1998, Riis et al., 2005, Rise et al., 2006), and these may represent the largest sediment remobilisation features involving transposition of strata yet recognised on earth. Previously interpreted as diapirs (Chapter 4, Hjelstuen et al., 1997, Hovland et al., 1998), some of these mounds have been more recently linked with the formation of the giant craters in the subsurface (Riis et al., 2005).

The remobilised sediment bodies mapped by Riis et al. (2005) are emplaced on the top surfaces of mass flow deposits which fill the craters (Riis et al., 2005). Thus there is a potential link between slope failure on the mid Norway margin, the formation of giant craters and the large scale remobilisation of sediments upwards transposing strata. The craters mapped by Riis et al. (2005) are mapped at the top of an Oligo-Miocene ooze formation (Riis et al., 2005), and the mass transports deposits which fill these craters are therefore the first of a series of mass transport deposits which have occurred on the mid Norway margin between the Miocene and the present day (e.g. Evans et al., 1996, 2005). This would suggest a link between the initiation of sliding on the mid Norway margin after the Miocene which remains relatively poorly

understood, and the formation of craters and the large scale remobilisation of sediment upwards towards the seabed.

The mid Norway margin is also of interest because there is evidence of movement of hydrocarbons from the subsurface towards the seabed since emplacement of dykes and sills in the late Palaeocene and early Eocene (Planke et al., 2005, Svensen et al., 2003, Svensen et al., 2004, Jamtveit et al., 2004) for at least 50 Ma (Svensen et al., 2003). It has previously been noted that the movement of fluids in the subsurface can be linked to the liquefaction, deformation and remobilisation of sediment (Maltman, 1994), therefore a detailed understanding of the craters and mounds mapped on the mid Norway margin will enable a better understanding of how fluid movements, mass transport deposits and sediment deformation can interact.

The location of these craters and mounds on the mid Norway margin, which is an area of significant hydrocarbon exploration (Möller et al., 2004), adds a further economic imperative to better understanding the processes involved in the formation of craters and large scale remobilisation of sediment. The craters and mounds may represent a hazard to drilling operations, and furthermore represent a poorly understood process which may affect fluid movements and reservoir geometry in the subsurface.

In this chapter previous mapping of craters and mounds on the mid Norway margin is reviewed and unanswered questions regarding the formation of the craters and remobilisation of sediment are identified. A research plan is then presented to enable the craters and mounds to be better understood in the context of the history of the mid Norway margin.

1.2 Previous work

Buried craters up to two orders of magnitude larger than pockmarks and mound structures have been described in the Norwegian Sea (Riis et al., 2005). The craters are termed “evacuation structures” (Riis et al., 2005). The term “crater” is preferred here, because “crater” does not favour any one interpretation as to how these features formed. Almost all of the craters described by Riis et al. (2005) incise Oligocene-Miocene siliceous ooze formations in the Norwegian Sea, and are filled in by mass transport deposits belonging to the Plio-Pleistocene Naust formation.

1.2.1 Description of craters in the Norwegian Sea

Craters have been described from four areas in the Norwegian Sea on the mid Norway margin, near wells known informally as Havsule and Solsikke, underneath the Sklinnadjupet slide and in the area of the Vema Dome (Riis et al., 2005, Fig. 1-1).

1.2.1.1 Havsule craters and ooze mounds

Two craters between 10 and 20 km wide located along the crest of an anticline on the mid Norway margin in the Norwegian Sea defined at the top of upper Oligocene ooze sediments are described by Riis et al. (2005) in a 3D seismic survey area informally known as Havsule (see Chapter 2 below for more information on this survey). The smaller crater described in this area is located southwards of the larger crater. The southern crater has a depth of 150 – 200 m (Riis et al., 2005). The northern Havsule crater has a depth of 100 – 150 m (Fig. 1-2). These craters are labelled Craters A and B in Chapters 4 and 5 below.

The craters are filled by Pleistocene glacigenic deposits which are divided into two intervals (Riis et al., 2005). The thicker lower interval is characterised by imbricated and tilted reflectors (Riis et al., 2005). The intervals that bury the craters are interpreted as mass transport deposits (Riis et al., 2005).

Each crater is overlain by a mound that is located stratigraphically above the craters on top of the two sequences that fill the craters described above and some 20 km west north-westwards of the craters (Riis et al., 2005). The mound associated with the northern crater is around 150 m thick (Fig. 1-2), and the mound associated with the southern crater is around 200 m thick (Riis et al., 2005). Thus there is a good first order match between the volume of the mound, and the volume of sediments removed from the crater (Riis et al., 2005).

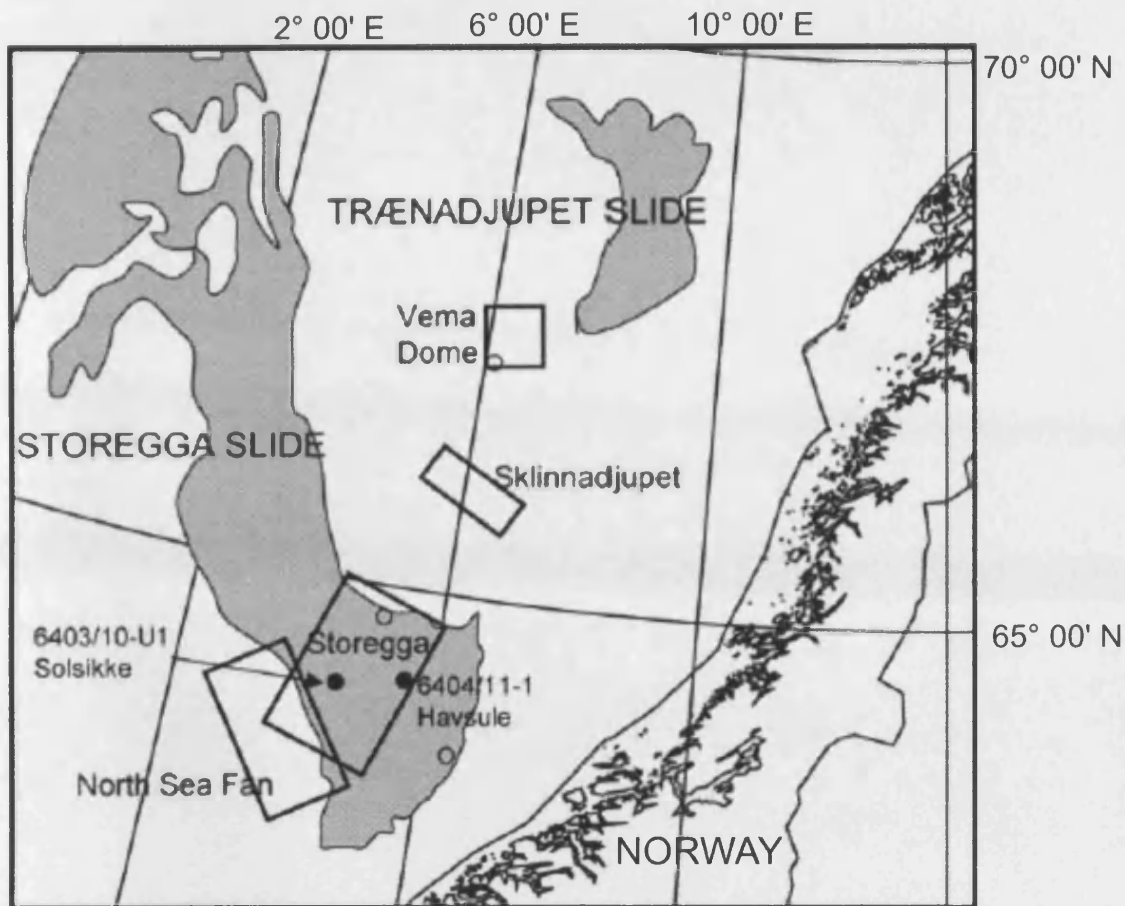


Fig. 1-1: Adapted from Riis et al 2005. A map of the mid Norway margin, indicating the areas studied by Riis et al. 2005, which are enclosed in boxes.

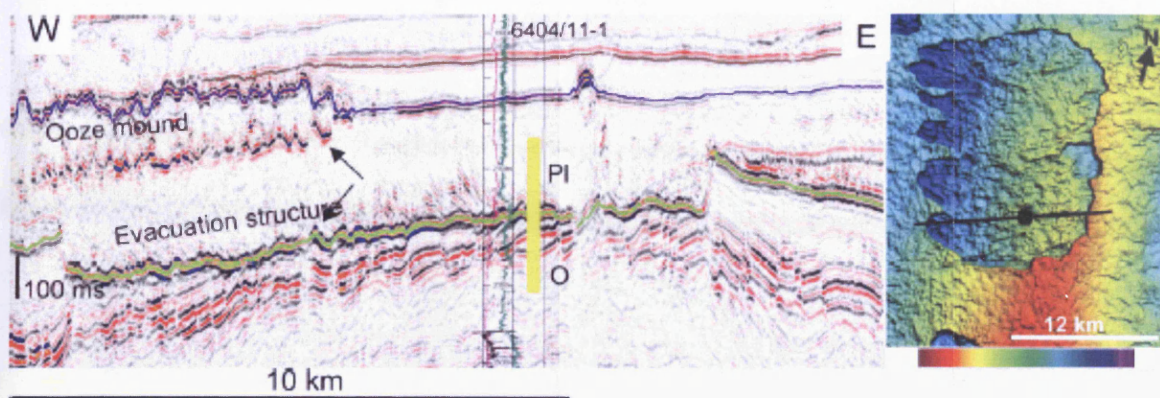


Fig. 1-2: Seismic profile across the Havsule Crater adapted from Riis et al. (2005). The top of the ooze underlying the crater is shown by a green line in the seismic section, while the top of the overlying slide is shown in blue. Note the crater in the top of the ooze, and the ooze mound overlying the slide. On the time depth map to the right, blue represents the greatest depth, with green, yellow and red respectively representing progressively shallower depths.

1.2.1.2 Sklinnadjupet craters and ooze mounds

There are six craters in the Sklinnadjupet area (Riis et al., 2005, Fig. 1-3). All of the craters are filled by the Sklinnadjupet Slide, which is a late Pleistocene, pre Weichselian event (Riis et al., 2005, Rise et al., 2006). Unlike the structures described in the Havsule area, one of the structures filled by the Sklinnadjupet Slide does not penetrate the top of upper Oligocene ooze sediments, and there is no mound located stratigraphically above this feature (Riis et al., 2005). The other structures filled by the Sklinnadjupet Slide are overlain by mounds which are emplaced on the top surface of the Sklinnadjupet Slide, and also penetrate the top of an ooze formation (Riis et al., 2005). The craters range from being approximately circular with diameters between 1 and 3 km in diameter to being elongate in an east to west direction with a width of 10 km and a length of 20 km (Riis et al., 2005). The craters buried by the Sklinnadjupet Slide range from being 100 – 200 m deep (Riis et al., 2005).

1.2.1.3 Solsikke craters and ooze mounds

Structures are described in the area of the Solsikke and Gloria Valley troughs and of the Faeroe-Shetland Escarpment that are over 20 km wide (Fig. 1-4), with one structure over 140 km long (which will be termed formally as Crater K in Chapter 4) being elongate parallel to the Faeroe-Shetland Escarpment (Riis et al., 2005). This structure is associated with mounds which are located above Pliocene sediments, and which are located downslope (Fig. 1-4) from the structure (Riis et al., 2005). Craters labelled as Craters E, H, I, J and K in Chapters 4 and 5 below are located in this area.

1.2.1.4 Vema Dome area

The Vema Dome (Fig. 1-5) is a dome that formed in the Miocene (Riis et al., 2005). The geometry of evacuation structures on this dome is complex because of many evacuation events and because mounds are stacked on top of each other (Riis et al., 2005).

1.2.2 Well data

A well was drilled through the Havsule Crater shown in Fig. 1-2. The well is sampled every 10 m, and samples 50 m of the overlying slide, and the underlying ooze (Riis et al., 2005). The overlying slide deposits contain no microfossil assemblages that can be uniquely ascribed to the underlying ooze (Riis et al., 2005).

A well penetrates a mound in the area of Fig. 1-4. It is found that the mound contains similar microfossil assemblages to the ooze formations beneath, and that neutron porosity, density and gamma ray readings from the mounds and the ooze formations are similar (Riis et al., 2005). It is therefore concluded that the mounds consists of ooze sourced from the underlying ooze formation (Riis et al., 2005). This conclusion is supported by the seismic characteristics of the mounds (Riis et al., 2005), which are discussed further in Chapters 4 and 5.

1.2.3 The model presented by Riis et al. (2005)

The conceptual model developed by Riis et al. (2005) is displayed (Fig. 1-6). A mass flow erodes to the base of a glacial sequence of sediment unloading overpressured ooze (Riis et al., 2005). Evidence from drilling shows that ooze in this area is currently overpressured (Riis et al., 2005). Ooze is evacuated, and due to its low density rises up to the surface of the slide, where it is carried downslope from the crater. High pore fluid pressure and gas saturation would have facilitated mobilisation of the ooze through liquefaction, fluidisation and gas expansion (Nichols, 1995), however it is believed by Riis et al. (2005) that the ooze is not liquefied but rises to the top of the fill of the crater as ooze blocks, because well data shows no apparent mixing of ooze sediments within one mound in the area. As the mass flow continues the crater becomes more elongate mobilising more of the ooze (Riis et al., 2005). Eventually the bottom side of the structure is breached, and the fill drained, with the ooze being carried further downslope on top of the slide (Riis et al., 2005).

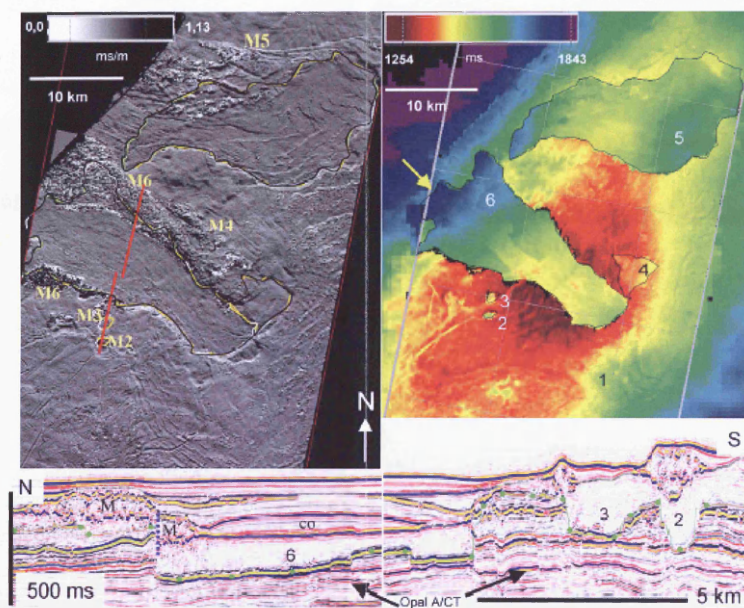


Fig. 1-3: From Riis et al. (2005). Upper left: Azimuth map of the top of the Skinnadjuet slide showing the geographical spread of dip direction illuminated from the north. M: Ooze mounds, these are numbered to show which structure they are associated with, and show a rough surface. Upper right: Two way travel time map of top of the ooze (and the base of the Naust formation in the top right hand corner) in the Skinnadjuet area. Note the anticlinal structure. The craters (numbered 1-6) are found on the crest of this anticline. The west wall of structure 6 has been breached (yellow arrow). Bottom: A seismic section through the structures. The location of the seismic section is indicated by red lines on the azimuth map above. Contouritic deposits (CO) and the mounds associated with structure 6 appear to be faulted (blue dotted line). A seismically interpreted opal A/CT transition which seems to coincide with the lowest level of structure 6 is indicated. Green dots indicate the base of the Skinnadjuet slide.

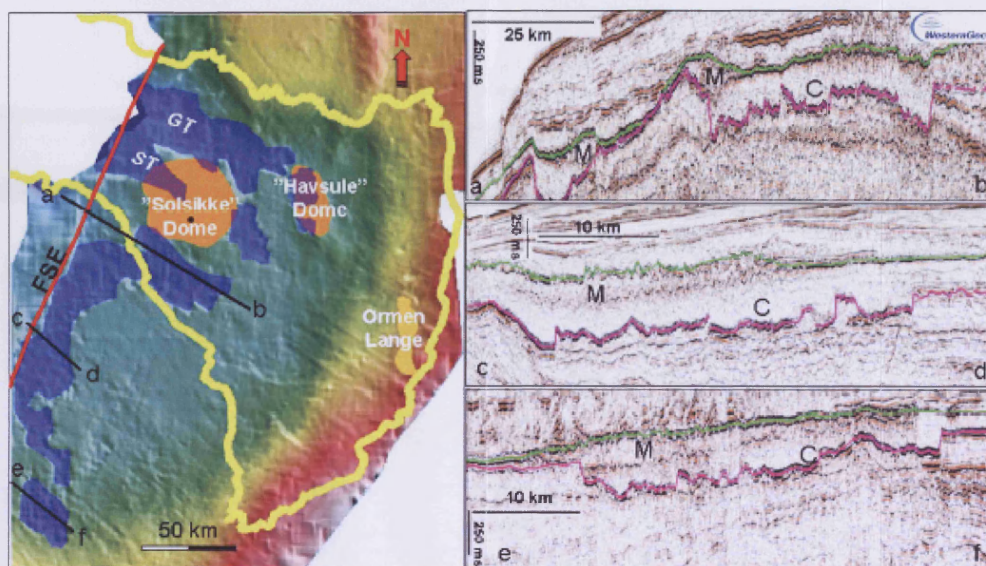


Fig. 1-4: From Riis et al. (2005). Left: Location map of crater like structures in Storegga and North Sea Fan areas. FSE: Faeroe-Shetland Escarpment. ST: Solsikke Trough. GT: Gloria Valley Trough. Yellow line: Storegga slide area. Blue represents the greatest depth, with green, yellow and red respectively representing progressively shallower depths. Right: Seismic profiles displaying characteristics of the structures and ooze mounds. The base of the ooze is interpreted in pink. The top of the slide is interpreted in green. M: Mounds. C: Craters.

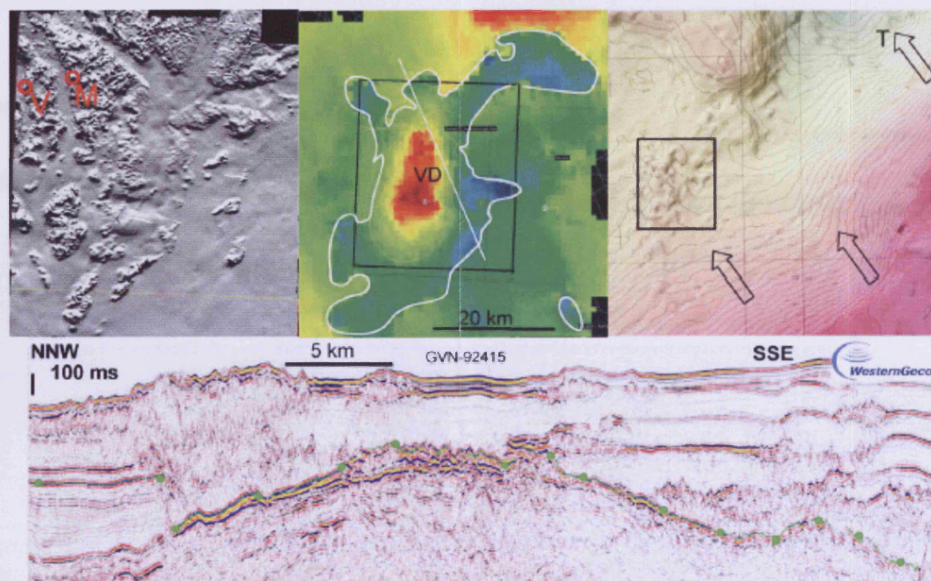


Fig. 1-5: Adapted from Riis et al. (2005). Upper right: Seabed topography in the Vema Dome area. Upper middle: Two way time map of top of ooze formation. VD: Vema Dome. Ooze is mobilized and evacuation structures form in area outlined in white. Blue represents the greatest depth, with green, yellow and red respectively representing progressively shallower depths. Upper left: Sea floor topography within the rectangle (upper middle, upper right), interpreted from 3D seismic reflection data. Rough topography represents ooze mounds which have been draped by recent sediments. Pink represents the shallowest depths, with yellow and green respectively indicating greater depths. Bottom: Seismic profile through Vema Dome. See upper middle for location. The top of the ooze is interpreted in green.

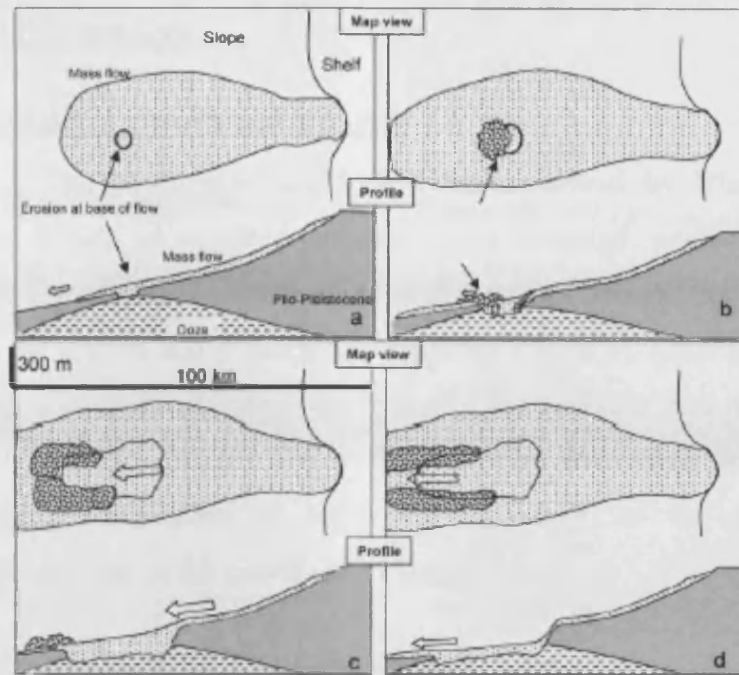


Fig. 1-6: A model which may explain the formation of craters and ooze mounds, from Riis et al. (2005). See the text for a fuller explanation of this model. (a) A slide uncovers and erodes into the top of ooze sediments. (b) Evacuation starts, with ooze sediments rising upwards to the seabed through the slide due to having a low density. (c) Slide continues to flow into the crater, mobilising further ooze. The crater continues to grow. Ooze mounds are transported downslope. (d) The lower wall of the evacuation structure is breached, draining the fill to a lower level.

1.3 Scope of this research

1.3.1 Distribution of craters and mounds

Many craters in the Norwegian Sea have been described by Riis et al. (2005). However more work is required to achieve a detailed understanding of the geographical and stratigraphic distribution of the craters. For example, it is not clear whether all of the craters and mounds described by Riis et al. (2005) incise the same ooze formation, and whether craters described in the Havsule area and the Solsikke area are filled by the same mass transport deposit or by other mass transport deposits. Regional mapping will allow a better understanding of the geographic and stratigraphic distribution of the craters and mounds.

1.3.2 Were craters excavated onto the seabed?

From the evidence presented by Riis et al. (2005) it is possible that craters are pre-existing features on the seabed that are modified by slides. Indeed, Riis et al. (2005) suggest when discussing the Havsule structures that,

“The dating and the seismic character of the infill show that the evacuation structure was developed and existed as a negative feature on the sea floor, and that it was filled by local slides in the Pleistocene.”

Further research into the geometry of the craters and mounds will enable a better understanding of whether the craters were excavated on the seabed or not.

1.3.3 Well data

The exact dating of slide sediments on the mid Norway margin and the sedimentological properties of the sediments in which the craters form and which bury the craters remain poorly understood. The relative sonic velocities of the late Oligocene ooze formation, the slides, and the mounds described above are also poorly understood. Paleontological data from additional wells in the study area will yield information which will allow slide sediments to be dated more accurately. Geophysical wireline logs from publicly available wells on the mid Norway margin will allow a better understanding of the relative densities of sediment formation the late Oligocene ooze formation, the slides, and the mounds to be better understood, as well as yield useful velocity information, which in turn will enable a better

understanding of the detailed geometry of the mounds and craters, which are currently confused by uncertainties introduced by pull up and push down effects in the data.

1.3.4 Volume of mounds

It is stated by Riis et al. (2005) that the time thickness of the mounds associated with the southern crater in the Havsule area shows a good first-order match to the time thickness of missing material from the underlying evacuation structure, suggesting that all of the ooze evacuated from the craters is emplaced in mounds. The same is true for one of the structures in the Sklinnadjupet Slide area. There is, however, a need to better understand how the volume of other mounds compares to the volume of other craters. This will enable more to be learnt about the emplacement process of the mounds.

1.3.5 Infill of craters

A more detailed examination of the internal fill of craters on the mid Norway margin will yield further information which may allow the formation of the craters to be better understood. For example, a more detailed examination of the internal fill of the slides which fill the craters may allow a better understanding of the dynamics of these mass transport deposits, which may in turn yield further information about the formation of craters and emplacement of mounds, because of the close relationship described between mass transport deposits, craters and mounds (Riis et al., 2005). A closer examination of the internal geometry of the fill of the craters will also enable a better understanding of the process by which ooze ascends from the base of the craters to the top of the mass transport deposits which bury the craters.

1.3.6 The importance of the opal A/CT transition to crater formation

It has been highlighted by Riis et al. (2005) that the depth of the base of some of the craters in the Norwegian Sea is controlled by an Opal A/CT transition; however the importance of this transition in the formation of the craters is not considered. There is a need to understand the characteristics of the regional opal A/CT transition on the mid Norway margin, the relationship of craters to the opal A/CT transition on the mid Norway margin, and the importance of this transition as a fluid source in the area in which the craters are found.

1.4 Aims of thesis

This study is motivated by the realisation that there is still much that is not understood about craters and mounds in the Norwegian Sea. The aim of this thesis is to use an extensive suite of 2D and 3D seismic reflection data to map in greater detail some of the craters and mounds described by Riis et al. (2005) to better understand the significance of these features in the history of the mid Norway margin. These findings will be combined with data from publically available well reports and industry well reports. Specifically, the geometries of the craters and mounds and the internal fill of the craters will be described in greater detail by mapping of seismic reflection data, and the mass transport deposits which fill craters in the Havsule and Solsikke areas will be more accurately dated using well data. The sonic velocity of the Oligocene-Miocene ooze formations, the mass transport deposits and the mounds will be obtained from well data and iteration. The seismic reflection data on which this thesis is based are of superior quality to those available to previous workers who have worked on these craters, and thus the data available represents an opportunity to build on previous work.

The following questions, some of which were posed by Riis et al. (2005), and some of which arise from the work of Riis et al. (2005), will be discussed in this thesis:

- (a) Are the mounds the result of remobilisation and excavation of craters (Chapters 4 and 5)?
- (b) Did the mounds form at the surface or after burial of the ooze, and if the ooze was buried, at what depth (Chapter 5)?
- (c) What are the mechanisms of formation of the craters, and can they be active today (Chapters 5 and 6)?
- (d) How important was the Opal A/CT boundary in the formation of the craters and emplacement of mounds (Chapters 2 - 5)?
- (e) If the mounds consist of ooze sourced from the craters, how is the ooze remobilised into the mounds (Chapter 5)?

1.5 Structure of thesis

Before investigating the formation of craters and the emplacement of ooze mounds, it is important to have a good appreciation of the limitations of the data available, and the characteristics of key geological formations and the geological setting of the mid

Norway margin. Chapter 2 therefore focuses on these topics, with well data being used to better understand geological formations on the mid Norway margin.

Inspection of previous work performed on the craters and mounds on the mid Norway margin by Riis et al. (2005) shows a close relationship between crater formation, mound emplacement and mass transport deposits on the mid Norway margin, however the dynamics of early mass transport deposits on the mid Norway margin remain poorly understood. Chapter 3 therefore focuses on mass transport deposits which fill the craters described by Riis et al. (2005) in the Havsule area. Well data are used to more accurately date the sediments which make up these mass transport deposits, and 2D and 3D seismic reflection data are used to map these mass transport deposits, and to describe the dynamics of these mass transport deposits.

In Chapter 4 2D seismic reflection data are used to perform regional mapping of the mid Norway margin so that the geographic and stratigraphic distribution of the craters can be better understood. These findings are combined with information on subsurface fluid flow obtained from geological literature, and two opposing hypotheses which might explain the formation of craters and emplacement of mounds are presented and discussed.

Detailed 3D seismic reflection data are then combined with velocity information obtained from geophysical well logs and iteration based on pull-up and push-down effects in Chapter 5 to accurately describe the detailed geometries of craters and mounds in selected areas of the mid Norway margin. On the basis of this description, the hypotheses presented in Chapter 4 are critically evaluated, and a new hypothesis presented which would explain the formation of craters and the emplacement of mounds on the mid Norway margin.

In Chapter 6, some of the consequences of this new hypothesis are discussed, and the craters are compared to the Blake Ridge Depression on the Blake ridge offshore the eastern USA, which may have formed by a similar process to the craters on the mid Norway margin described here.

2 METHODOLOGY AND GEOLOGICAL SETTING

2.1 Methodology

In this thesis seismic reflection data are used to describe the first mass transport deposits to occur on the mid Norway margin (Chapter 3), subsurface craters, and mounds of remobilised sediment (Chapters 4 and 5). Seismic reflection data interpretation is performed on UNIX Sun workstations running Schlumberger's Geoframe IESX and GeoViz software.

Seismic reflection data consists of the arrival times of P-waves at a surface receiver which have been reflected at a low angle of incidence from surfaces in the subsurface showing an impedance contrast (Fowler, 2005). The acoustic impedance of a rock mass is proportional to the seismic velocity and density of that rock mass (Gardner et al., 1974). The seismic velocity of a rock will in turn depend on the composition, texture, porosity, fluid content, elastic modulus and density of the rock (Keary et al., 2002)

The data available to the interpreter consists of a series of wavelets (e.g. Fig. 2-1). Seismic reflection data can be displayed in zero phase SEG (Society of Exploration Geophysicists) normal polarity (e.g. James Brown et al., 2000). Where data are displayed in zero phase SEG normal polarity, P-waves which are reflected from an interface showing positive downwards impedance contrast will be correlated with a peak on the wavelet whereas P-waves reflected from a surface showing negative downwards impedance contrast will be correlated with a trough on the wavelet (Fig. 2-1, James Brown et al., 2000). The amplitude or height of any given peak or trough increases with an increasing magnitude of impedance contrast (Fig. 2-1, Hart, 1999). Some data are displayed in zero phase SEG reversed polarity, which means that p-waves which are reflected from a surface showing a positive impedance contrast downwards will correlate with a trough on the wavelet (Fig. 2-1, James Brown et al., 2000). Reflections from surfaces showing positive downwards impedance contrast are referred to in this thesis as "acoustically hard reflections", and reflections from

surfaces showing negative downwards impedance contrast are referred to in this thesis as “acoustically soft reflections” (Fig. 2-1).

Geological boundaries in the subsurface could be defined as a discontinuous change in rock property above and below that boundary (e.g. Beaudoin and Head, 2004). Where there is an impedance contrast across that geological boundary, the geological boundary will be correlatable with a P-wave reflection on seismic reflection data (Brown, 2004).

Not all P-wave reflections will be correlatable with a geological boundary in the subsurface. For example, P-wave reflections imaged beneath the seabed which are similar in geometry to P-wave reflections from the seabed may represent P-waves that are reflected from the seabed more than once (seabed multiples, Stagg 1984). Geometries in the subsurface with a shorter wavelength than the seismic wavelength may cause diffraction effects in the data (Fowler, 2005). Data can be processed to minimise reflections due to P-waves that have undergone reflections more than once, and to remove diffraction effects (Brown, 2004).

To definitively correlate a reflection with a geological boundary requires well data. If the seismic velocity field at a well is known, reflections can be then tied to geological boundaries observed in well data (Badley, 1985; Yilmaz, 2001). There are uncertainties inherent in estimating a seismic velocity field within a well, therefore the process of tying observed geological boundaries in the well to reflections observed on seismic reflection data may be imprecise (e.g. Martin et al., 2010). This may lead to large uncertainties at a distance from wells, if the uncertainty of a tie to a geological surface at the well lies between two reflections which diverge at a distance from the well (e.g. Fig. 2-2). Well ties here are based on confidential industry well reports and published literature.

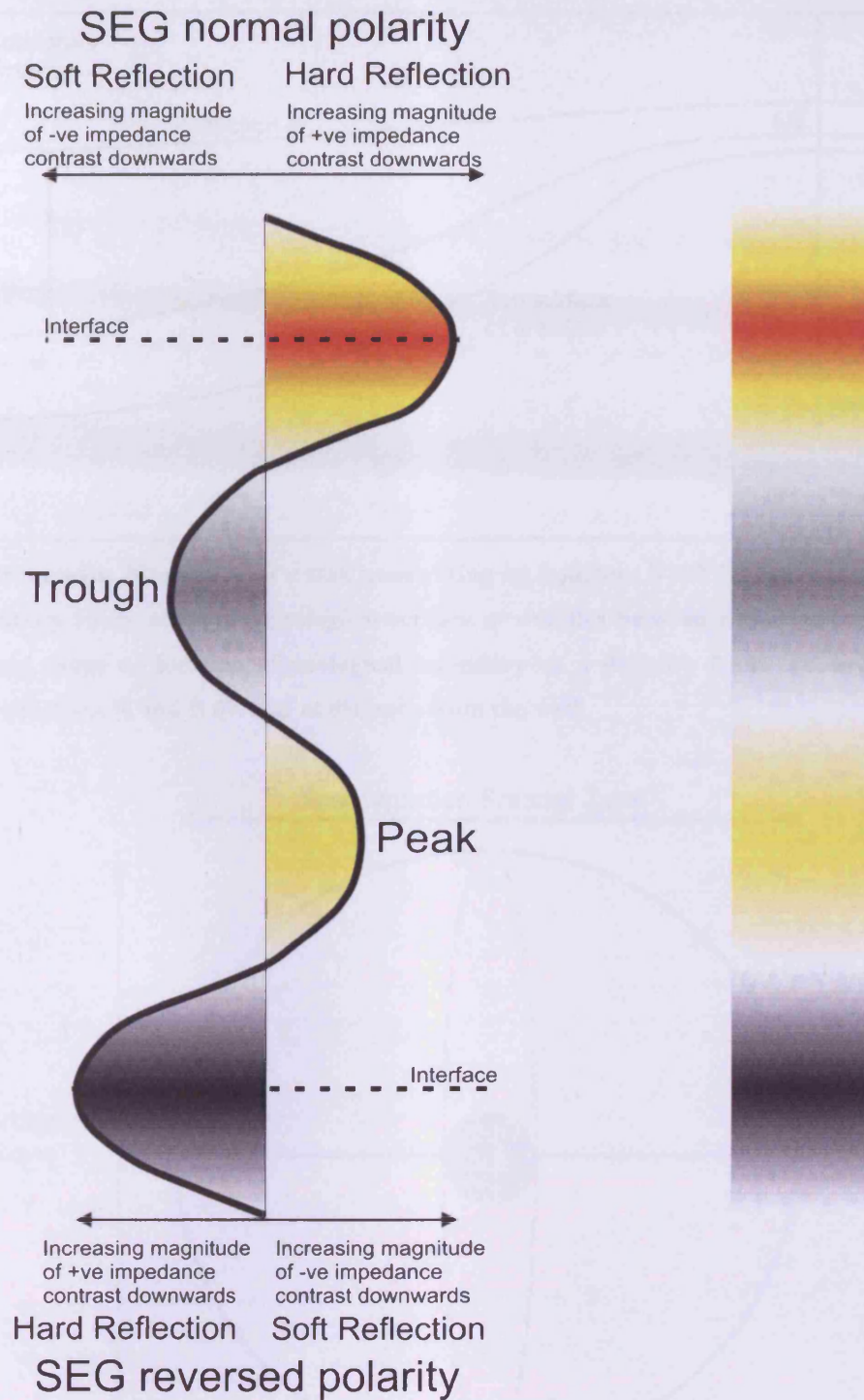


Fig. 2-1: Adapted from Hart (1999). Left: Seismic wavelets, illustrating the concepts of SEG normal polarity and SEG reversed polarity. Zero phase is assumed. Right: Appearance of seismic wavelets to left on seismic display.

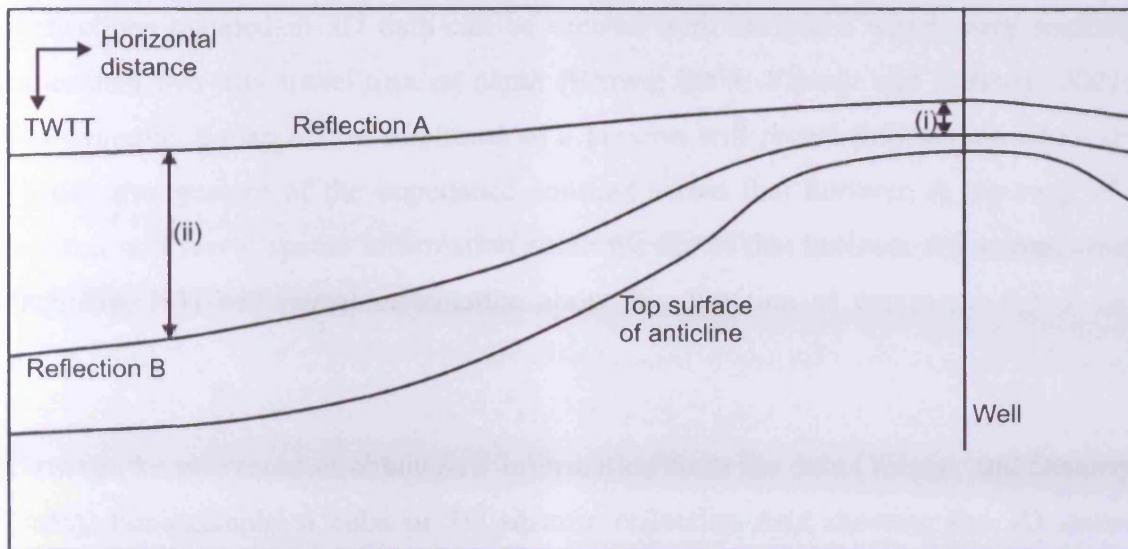


Fig. 2-2: Schematic illustration of a well penetrating an anticline. TWTT: Two way travel time. (i) Uncertainty range of tie of a geological surface at well lies between reflections A and B. (ii) Uncertainty range of location of geological boundary at a distance from the well is larger, because reflections A and B diverge at distance from the well.

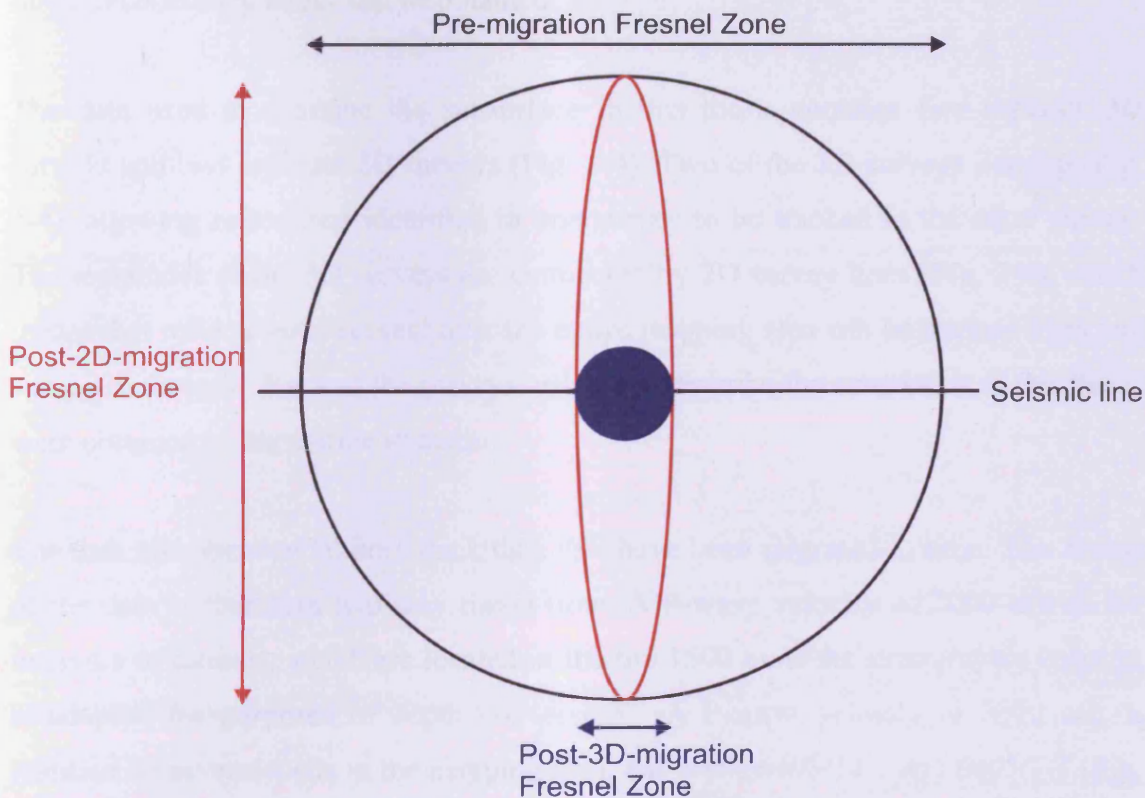


Fig. 2-3: Adapted from Brown (2004). Pre- and post- migration Fresnel Zone diameters.

Reflections mapped in 3D data can be viewed with attributes which vary spatially other than two way travel time or depth (Brown, 2004; Yilmaz and Doherty, 2001). For example, a map of the amplitude of a horizon will reveal information about the spatial arrangement of the impedance contrast across that horizon. A dip map of a horizon will reveal spatial information about the dip of that horizon. An azimuth map (e.g. Fig. 1-3) will reveal information about the direction of maximum dip of any given point.

Data can be processed to obtain new information from the data (Yilmaz and Doherty, 2001). For example, a cube of 3D seismic reflection data showing the 3D spatial arrangement of amplitude may be processed into a coherence cube, which highlights the degree of discontinuity of reflections imaged in the data (Brown, 2004; Yilmaz and Doherty, 2001). This technique is particularly useful for imaging subsurface faults which may displace horizons. Like seismic reflection amplitude data, horizontal slices through coherency cubes can be obtained.

The data used to describe the subsurface in this thesis contains five separate 3D surveys and two separate 2D surveys (Fig. 2-4). Two of the 3D surveys overlap (Fig. 2-4), allowing reflections identified in one survey to be tracked in the other survey. The remainder of the 3D surveys are connected by 2D survey lines (Fig. 2-4), which means that reflections if present over the entire mapping area can be tracked from one survey to the next. Each of the surveys utilised to describe the subsurface in this thesis were obtained in the marine domain.

The data are commercial post-stack data that have been migrated in time. The Z-axis of the data is therefore two way travel time. A P-wave velocity of 2000 m/s in the intervals of interest, which are located in the top 1500 m of the stratigraphic column, is adapted for purposes of depth conversion. A P-wave velocity of 2000 m/s is justified by several wells in the mapping area, e.g. wells 6403/10-1 and 6405/7-1 (Fig. 2-5, Chapter 5), where the seismic velocity of P-waves has been found to be between 1694 m/s and 2345 m/s in the intervals of interest. Therefore, 1 ms on the data is assumed to be equivalent to a depth of 1 m, unless otherwise noted (for example in Chapter 5, where selected lines are depth converted using more accurate velocity information from nearby wells).

The characteristics of the surveys are summarised in Table 2-1. Horizontal resolution is dependent on line spacing and the width of the Fresnel zone. For a flat lying reflection, the horizontal sampling will be equivalent to half of the detector spacing (Keary et al., 2002), which is equivalent to line spacing (or bin size). The Fresnel zone is the area over which reflections from a surface constructively interfere. After migration of the data, this will be one quarter of a wavelength for perfect migration (Brown, 2004). In practice, the width of the Fresnel Zone after migration will be half a wavelength (Brown, 2004), and a value of half a wavelength is assumed in Table 2-1. Vertical stratigraphic resolution is calculated to be one quarter of a wavelength (after Brown, 2004, Sheriff and Geldart, 1995). Line spacing varies between 12.5 and 40 m, the width of the Fresnel zone varies between 16 and 25 m with an uncertainty of ± 3 m, and the vertical resolution varies between 8 and 13 m with an uncertainty of ± 2 m. All of the data are 8 bit data, and are sampled every 4 ms (Table 2-1). The dominant or source frequency of the data varies between 40 Hz and 63 Hz, with an uncertainty of ± 5 Hz (Table 2-1). Chapters 3, 4 and 5 contain further information on methodologies specific to these chapters.

2.2 Geological time periods

During this study the Pliocene and Pleistocene were redefined, with the Gelasian period (2.6 – 1.8 Ma) being moved from the Pliocene to the Pleistocene by the International Commission on Stratigraphy. In this study, the Gelasian period is defined to be part of the Pliocene, to facilitate easier comparison with previous work.

2.3 Definitions

2.3.1 Craters

Riis et al. (2005) described craters which were identified by mapping the top of the Oligo-Miocene Brygge and Kai Formations (Riis et al., 2005). The craters are fully or nearly completely enclosed features with steeply dipping sidewalls incising Oligo-Miocene ooze formations, and are up to 20 km wide and 300 m deep (Riis et al., 2005).

In this study a crater is defined on seismic reflection data as being mostly or fully enclosed by sidewalls, which are defined as being a surface where reflections of the Oligo-Miocene Brygge and Kai Formations are truncated against reflections of

younger sediment which fill the crater. Sidewalls of craters will have a dip which is steep with respect to the local bedding of the Oligo-Miocene Brygge and Kai Formations. The base of a crater is defined on seismic reflection data as a reflection which acts as a boundary between the older sediments which are incised by the crater and the newer sediments which fill the crater. The base of a crater will be sub-parallel to regional bedding of the Oligo-Miocene Brygge and Kai Formations. On well data the basal surface of a crater will be defined by a time gap which is at least equivalent to the time gap incised at the sidewalls. This time gap may be larger, if there was a period of non deposition between the top-most sediment layer to be truncated at the crater wall and later sediment deposition.

2.3.2 Mounds

Riis et al. (2005) described mounds which are located further up the stratigraphic succession and geographically downslope relative to the crater from which they are sourced, generally being emplaced on the top surface of the infilling slide. Because evidence from a well shows that the mounds consist of sediment evacuated from Oligo-Miocene ooze beneath (Riis et al., 2005), they are informally referred to as “ooze mounds” (Riis et al., 2005).

A mound in this study is defined on seismic reflection data as a feature located stratigraphically above a crater, and is defined on the basis of a top surface and a basal surface. The top surface of a mound is defined on seismic reflection data as the reflection which separates reflections of sediments which are deposited above the mounds from the internal reflections of the mound. The basal surface of a mound is defined on seismic reflection data as the reflection which separates the internal reflections of the mound above from the reflections of sediments located beneath the mound. Reflections from sedimentary formations beneath and above the mound may be truncated against the basal surface and top surface of the mound respectively. Alternatively, the reflections of sedimentary formations above and below the mound may be sub-parallel to the top surface and basal surface of the mound respectively. Riis et al. (2005) present well data penetrating a mound (see Chapter 1 above). The definition of a mound on well data follows the findings of Riis et al. (2005). On well data, a mound is defined as an interval consisting of sediments which are similar in

characteristics to those of the Oligo-Miocene Brygge and Kai Formations, bounded below and above by more recent sediments

In this study, the edges of a mound on seismic reflection data are defined by pinch out of the internal reflections of the mound, such that the reflection of the top surface of the mound downlaps onto the reflection of the basal surface of the mound, or the reflection of the basal surface of the mound is truncated by the reflection of the top surface of the mound.

2.3.3 Slides

Inspection of previous work reveals a close relationship between the formation of craters, the remobilisation of sediment and slides on the mid Norway margin. There is considerable variation in the literature regarding the classification of slumps and slides (Frey Martinez et al., 2005). In this thesis large features resulting from slope failure are referred to collectively as slides in that they generally exhibit coherent internal structure and have boundaries that are relatively well defined with distinct sides and a distinct failure surface (Mulder and Cochonat, 1996). Slides are recognised on seismic reflection data as discrete bodies which exhibit a highly disrupted to chaotic internal structure (Frey Martinez et al., 2005). They are bounded up-dip by a headwall (Bull et al., 2009a, Frey Martinez et al., 2005, Mulder and Cochonat, 1996, Varnes, 1978), which in seismic reflection data is recognised by the termination of reflections against a surface bounding the slide body in an upslope direction (Frey Martinez et al., 2005). The lateral edge of the slide body is delineated by lateral margins (Bull et al., 2009a, Frey Martinez et al., 2005). These are recognised in seismic reflection data as being the region where the distorted internal structure of the slide mass terminates. Sidewalls may be vertical or dip steeply towards the slide body. A zone of depletion forms a topographic depression between the headwall, sidewalls and slide body, and this depression may be infilled by post-slide units (Frey Martinez et al., 2005) or form a topographic depression if the slide is not buried (Varnes, 1978). The downslope limit of the slide body is the toe region (Bull et al., 2009a, Frey Martinez et al., 2005), and may be recognised on seismic reflection data from evidence of shortening of the slide mass, e.g. in the form of thrusts ramping up from the basal shear plane, or where the slide body thickens in the accumulation zone (Varnes, 1978). Later sediments may then onlap the resulting topographic high. Where frontal thrusts define the downslope

limit of the slide body the slide can be classified as frontally confined, but where the slide body ramps up and over the original slope surface, the slide may be classified as frontally emergent (Frey-Martinez et al., 2006).

Slides are delineated below and above by a basal shear surface and a top surface. The basal shear surface separates highly stratified in situ slope sediments below from the less stratified, deformed or disrupted reflections comprising the slide body. It may ramp up and down stratigraphy, but will be a smooth surface that may show kinematic indicators (Frey Martinez et al., 2005, Gee et al., 2005, Moscardelli and Wood, 2008). The top surface is defined as a surface separating the chaotic facies below and the highly stratified facies or slide above.

2.4 Geological Setting

2.4.1 The Møre Basin

This study is centred on the Møre Basin, offshore Norway (Fig. 2-5). The Møre Basin is a large depocentre around 200 km in diameter, bounded to the north by the Jan Mayen Fracture Zone and the Vøring Plateau (Fig. 1A, Skogseid et al., 1992, 2000, Planke et al., 1991), bounded to the west by the Faeroe-Shetland Escarpment and the Møre Marginal High (Fig. 1A, Brekke, 2000, Planke et al., 1991, Smythe et al., 1983), and bounded to the east by the Norwegian Continental Shelf (Fig. 2-5A). The Møre Basin is bounded to the south by the North Sea Fan, which is a wedge of glacial sediments prograding from the Norwegian Channel and the Møre Shelf to the south. This depocentre was closed in Eocene times by the extrusion of the Møre Marginal High (Planke et al., 1991).

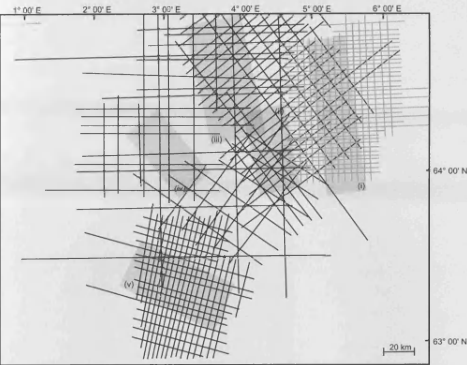


Fig. 2-4: Map of dataset referred to in this thesis. Grey lines: g2d; Black lines: e2d. (i) Grip 3D; (ii) Havsule 3D; (iii) Edvarde 3D; (iv) Solsikke 3D; (v) Tulipan 3D.

| | Grip 3D | Havsule 3D | Edvarde 3D | Solsikke 3D | Tulipan 3D | e2d | G2d |
|--|-----------------------|---------------------|---------------------|-----------------------|---------------------|---------------------|---------------------|
| Display | SEG reversed polarity | SEG normal polarity | SEG normal polarity | SEG reversed polarity | SEG normal polarity | SEG normal polarity | SEG normal polarity |
| Data Quality | 8 bit | 8 bit | 8 bit | 8 bit | 8 bit | 8 bit | 8 bit |
| Line Spacing | 25 m | 25 m | 25 m | 25 m | 12.5 m | 40 m | 40 m |
| Width of Fresnel Zone | 21 m | 24 m | 20 m | 16 m | 23 m | 22 m | 25 m |
| Dominant Frequency | 48 Hz | 42 Hz | 50 Hz | 63 Hz | 44 Hz | 45 Hz | 40 Hz |
| (time interval used for measurement) | (2 s – 3 s) | (2 s – 3 s) | (2.75 s – 3.25 s) | (2.5 s – 3.5 s) | (2 s – 3 s) | (2 s – 3 s) | (2 s – 3 s) |
| Vertical Resolution | 10 m | 12 m | 10 m | 8 m | 11 m | 11 m | 13 m |
| Vertical Sampling of reflection data in time | 4 ms | 4 ms | 4 ms | 4 ms | 4 ms | 4 ms | 4 ms |

Table 2-1: Characteristics of the data used in this study.

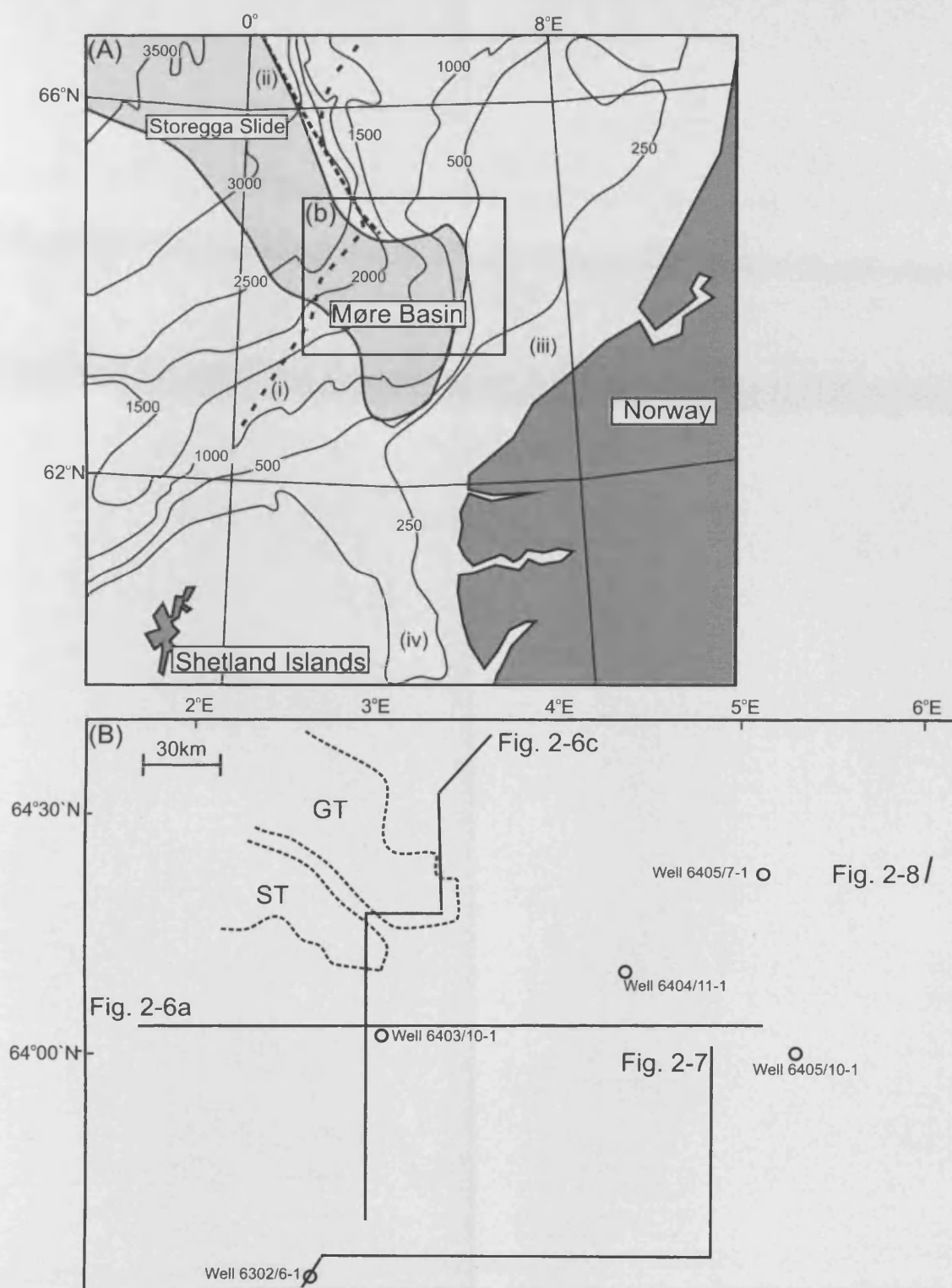


Fig. 2-5: (A) A map of the mid Norway margin, showing the location of the Møre Basin. Contours are in meters. (i) Faeroe-Shetland Escarpment. (ii) Jan Mayen Fracture Zone. (iii) Continental Shelf. (iv) Norwegian Channel. (B) A map demonstrating the location of figures in this chapter and wells. ST: Solsikke Trough. GT: Gloria Valley Trough.

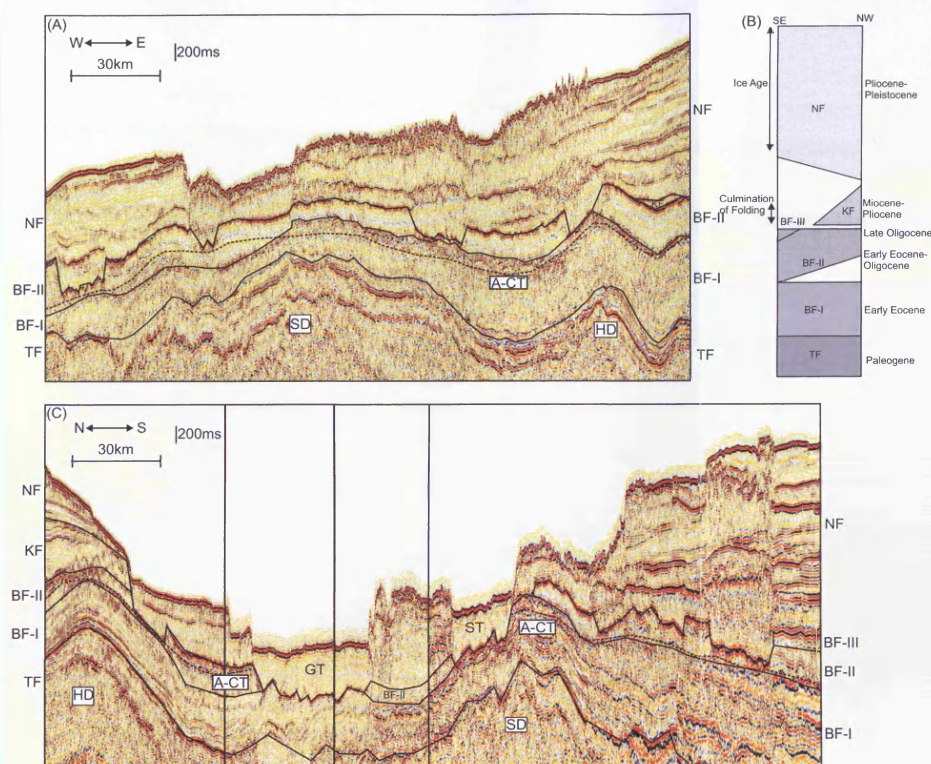


Fig. 2-6: (A) A seismic line across the Møre Basin. See Fig. 2-5B for location. A-CT: Opal A/CT boundary (indicated by a dashed line). HD: Havsule Dome. SD: Solsikke Dome. TF: Tare Formation. BF-I: Brygge Formation Unit I. BF-II: Brygge Formation Unit II. KF: Kai Formation. NF: Naust Formation. (B) A chronostratigraphic column demonstrating the inter-relationship between sedimentary units and formations in the Møre Basin. BF-III: Brygge Formation Unit III. (C) A seismic line across the Møre Basin. See Fig. 2-5B for location. See Appendix A1 for time structure maps compiled from 2D seismic reflection data of the base of the Brygge Formation (Fig. A1- 1), the top of Brygge Formation Unit I (Fig. A1- 2), the top of Brygge Formation Unit II (Fig. A1- 3) and the top of Brygge Formation Unit III (Fig. A1- 4); and for isochron maps compiled from 2D seismic reflection data of Brygge Formation Unit I (Fig. A1- 5), Brygge Formation Unit II (Fig. A1- 6) and Brygge Formation Unit III (Fig. A1- 7).

The onset of the Miocene saw the culmination of doming in the Møre Basin (Løseth and Henriksen, 2005), forming several large north-south trending domes (Fig. 2-6A & C). The reasons for this doming event are not well understood (Doré et al., 2008), but potential explanations include gravity loading, spreading and sliding; flank enhancement by sedimentary loading (Kjeldstad et al., 2003, Stuevold et al., 1992); a transfer of orogenic stress from the Alpine Orogeny (Brekke, 2000, Våagnes et al., 1998); reactivation of basement lineaments such as the Jan Mayen Fracture Zone (Doré and Lundin, 1996); plate driving forces (Bodreel and Andersen, 1998); and body forces, possibly generated by the Iceland Insular Margin (Lundin and Doré, 2002). In the study area there are three significant domes. The eastern dome is known as the Helland Hansen Arch (Skogseid and Eldholm, 1989, Stuevold et al., 1992). Well 6405/7-1 (Fig. 2-5B) on this dome contained oil, while well 6405/10-1 (Fig. 2-5B) which is yet to be evaluated contains gas. The central dome is known informally as the Havsule Dome, and has a width of 30 km. Well 6404/11-1 was drilled on the crest of the Havsule Dome (Fig. 2-5B), was described by Riis et al. (2005), and did not contain hydrocarbons. The western dome, known informally as the Solsikke Dome, has a larger width of 100 km. Well 6403/10-1 (Fig. 2-5B) was drilled in the middle of the Solsikke Trough on the Solsikke Dome, was also described by Riis et al. (2005), and was also found not to contain hydrocarbons. In the south of the study area there was an accumulation of sediment against the Solsikke Dome, marking the beginning of deposition of the North Sea Fan (King et al., 1996).

During the Pliocene, the uplift of Norway coupled to increased erosion due to cooling climatic conditions ensured that increasingly large amounts of sediment were shed from the Norwegian Margin to the east and Norwegian Channel to the south and emplaced in the Møre Basin and elsewhere on the Norwegian Margin unconformably as large prograding sediment wedges (STRATAGEM, 2003). The onset of extensive northern hemisphere glaciation, often cited as being between 2.6 and 2.7 Ma on the basis of ice-rafted debris (Hjelstuen et al., 2005, Jansen et al., 2000), ensured that large volumes of sediment continued to be shed into the Møre Basin from the Norwegian Margin to the east and from the Norwegian Channel to the south (King et al., 1996). During interglacial periods contourites were deposited on the continental slope (Berg et al., 2005). Progradation of glacial sediments and contourite sequences created the conditions for continued slope instability in this area of the mid

Norwegian margin resulting in mass transport deposits sourced from the North Sea Fan to the south and the continental slope to the east occurring to the present day (Berg et al., 2005, Evans et al., 1996, 2005, King et al., 1996, Solheim et al., 2005).

The most recent large scale slide to occur on this margin is the Holocene Storegga Slide (Bryn et al., 2005a, Gauer et al., 2005, Kvalstad et al., 2005, Bünz et al., 2005, Haflidason et al., 2004, 2005). This slide may have eroded significant escarpments (Haflidason et al., 2004), correlated to the Gloria Valley and Solsikke Trough in the study area of this thesis in the western Møre Basin.

2.4.2 Stratigraphy

A column summarising the sediments that filled the Møre Basin is presented in Fig. 2-6B. In the early Eocene a series of claystones and tuffs were deposited, known as the Tare Formation (Dalland et al., 1988). This is correlated with Unit IV sampled at ODP sites on leg 104 (Hempel et al., 1989), which consists of volcanic ash and other volcanic rocks and is dated as being Eocene in age.

This was followed by deposition of the Brygge Formation from the Eocene to the early Miocene, which consists of claystone with stringers of sandstone, siltstone, limestone and marl, with pyrite, glauconite and shells being observed within the sandstone (Dalland et al., 1988). More recently these sediments have been described on the basis of short borehole sections in the vicinity of the Ormen Lange Dome (south of our study area) as consisting of kaolinite-rich oozes (Forsberg and Locat, 2005). These sediments were described as biogenic ooze by Riis et al. (2005). In well 6407/1-3 east of the study area the average bulk density of the Brygge Formation is 1.85 g/cm^3 (Dalland et al., 1988). The Brygge Formation is correlated with Unit III which is sampled at ODP sites on leg 104 (Hempel et al., 1989), spans the early to middle Miocene, and is rich in biogenic silica and smectite. Thyberg et al (2000) attempt to link the stratigraphy they found in several wells south of the crater field (24/6-1, 30/3-3, 34/7-1, 34/7-2 and 34/7-6, Table 2-2) with sequence stratigraphy developed by Jordt et al. (1995). They find that Eocene-Oligocene smectite mudstones have high porosity and low seismic velocity compared with the underlying Palaeocene sediments and the overlying Miocene-Pliocene sequences. These Eocene-Oligocene smectite mudstones are also correlated with the Brygge Formation. The characteristics

of the Brygge Formation as found in different wells on the mid Norway margin are summarised in Table 2-2.

In this study the Brygge Formation is subdivided informally into three seismic stratigraphic packages, defined by the amplitude of the internal reflections and the seismic characteristics of the boundaries between these packages (Fig. 2-6, Fig. 2-7). The bottom-most package, Unit I, is well stratified and shows internal reflections of medium amplitude (Fig. 2-6A & C, Fig. 2-7). Unit I varies in thickness from 200 m thick in the west to over 400 m thick in the east (Fig. 2-6A). This thickness is as much as 1100 m in the south east of the study area (Fig. A1- 5, Appendix A1). Unit I is bounded above by a hard reflection (Fig. 2-7), and is dated palynologically as being early Eocene in age on the basis of information obtained from wells 6405/10-1 and 6302/6-1 (Fig. 2-5). The middle package, Unit II, is more seismically transparent than Unit I beneath in the region of the craters (Fig. 2-A & C). Unit II is up to 300 m thick (Fig. 2-A & C, see also Fig. A1- 6, Appendix A1). This package is bounded above by a soft reflection (Fig. 2-7) and is dated palynologically as being early Eocene to Oligocene in age. Unit III is similar to Unit I in its seismic characteristics, but is bounded above by a soft reflection (Fig. 2-7). This is not laterally continuous and is only present in the south of the study area. Unit III displays an onlap relationship to Unit II beneath (Fig. 2-7), and is up to 300 m thick (Fig. A1- 7, Appendix A1). This unit is dated palynologically as being of late Oligocene age.

Deposition of the Brygge Formation was followed in the Miocene by deposition of the Kai Formation (Dalland et al., 1988). These sediments are abundant in calcareous and siliceous fossils (STRATAGEM, 2003), and are rich in smectite (Forsberg and Locat, 2005). The Kai Formation is correlated with Unit II at ODP sites 642, 643 and 644 (Hempel et al., 1989), which spans the middle Miocene to late Pliocene interval. Unit II has variable carbonate content, some biogenic silica, and large amounts of smectite. The Kai Formation is also correlated with Miocene-Pliocene sediments described by Thyberg et al (Thyberg et al., 2000). In well 6407/1-2 and 6407/1-3 (east of our study area) the bulk density of the Kai Formation rises from 1.9 g/cm³ at the base to 2.25 g/cm³ at the top (Dalland et al., 1988). The characteristics of the Kai formation in various wells on the mid Norway margin are summarised in Table 2-2.

The Kai Formation was deposited in synclinal lows between domes (Løseth and Henriksen, 2005) such as the Solsikke Dome and the Havsule Dome (Fig. 2-6). This unit is not laterally continuous, but where it accumulates in synclinal lows or as contourite mounds it can be over 400 m thick (Fig. 2-6C). The Kai Formation is topped by a regional early-Pliocene unconformity (STRATAGEM, 2003). Large contourite drifts of the Kai Formation were deposited against the Vøring Plateau to the north of the basin (Bryn et al., 2005b).

In the Møre Basin, the Brygge and Kai formations are deformed by an extensive tier of normal faults that are mapped elsewhere as polygonal faults (e.g. Berndt et al., 2003, Cartwright and Dewhurst, 1998, Hustoft et al., 2007). This normal faulting spans an interval from the base of the Brygge Formation to a datum in the Kai Formation. The fault spacing within the faulted tier is typically of the order of around 200 m (Fig. 2-8). Maximum heave across the faults is 25 m, while the maximum throw at the centre of the tier is typically around 25 m (Fig. 2-8). This faulting deforms a fossilized opal A/CT boundary that underlies the study area (Chapters 3, 4 and 5). The maximum observed throw of the opal A/CT boundary across individual normal faults is 10 m (Fig. 2-8), which is smaller than the typical maximum vertical displacement across individual normal faults, showing that the boundary arrested shortly before the cessation of normal faulting, in agreement with the conclusions of Brekke (2000). These observations are in agreement with what is observed elsewhere on this margin (e.g. Neagu et al., 2010). The opal A/CT transition is frequently adjacent to the boundary between Brygge Formation Unit I and Brygge Formation Unit II in the study area (Fig. 2-6), although in the south of the study area this diagenetic transition is positioned adjacent to the boundary between Brygge Formation Unit II and III (Fig. 2-7).

| <u>References</u> <u>Formation</u> <u>Location with</u> <u>respect to</u> <u>mapping area</u> <u>Composition</u> | <u>ODP 642/643/644</u> (Hempel et al., 1989, Pittenger et al., 1989) | | | <u>24/6-1, 30/3-3, 34/7</u> (Thyberg | |
|---|--|---|---|--|---------------------------------|
| | <u>Brygge</u> | <u>Kai</u> | <u>Base Naust</u> | <u>Brygge</u> | <u>I</u> |
| | 300 km north of mapping area | | | 500 km south | |
| | 50 – 60 % biogenic silica, 15 - 20 % smectite, 10 – 15 % non-smectite clay minerals. | 0 – 50 % carbonate, 0 – 50 % biogenic silica, 5 - 40 % smectite, 10 – 30 % non-smectite clay minerals. | 0 – 40 % carbonate, 15 – 20 % smectite, 25 – 40 % non-smectite clay minerals. | n/a | n/a |
| <u>Density</u> | 1.2 – 1.3 g/cm ³ (Core data) | 1.1 – 1.4 g/cm ³ (Core data) | 1.2 – 1.9 g/cm ³ (Core data) | n/a | n/a |
| <u>Porosity</u> | 60 % (Geophysical), 70 – 80 % (Core data) | 60 % (Geophysical), 40 – 70 % (Core data) | 55 % (Geophysical), 50 – 70 % (Core data) | Higher than overlying and underlying sequences | Lower than underlying sequences |
| <u>Sonic Velocity</u> | 1600 – 1800 m/s | 1600 m/s | 1500 m/s | 2000 – 2100 m/s | 1900 – 2100 m/s |
| <u>Permeability</u> | 1 X 10 ⁻⁷ – | 1 X 10 ⁻⁸ – | 1 X 10 ⁻⁹ – | n/a | n/a |
| <u>Coefficient</u> | 1 X 10 ⁻⁵ cm/s | 1 X 10 ⁻⁵ cm/s | 1 X 10 ⁻⁶ cm/s | | |
| <u>Compression</u> | 0 – 3 | 2 – 6 | 0 – 4 | n/a | n/a |
| <u>Index</u> | | | | | |
| <u>Shear Strength</u> | 20 – 120 kPa | 48 – 92 kPa | 7 – 27 kPa | n/a | n/a |

Table 2-2: Data on the Brygge Formation, Kai Formation and the base of the Naust Formation, obtained from selected wells inside

| 4-1 and 28 (Forsberg and Locat, 2005) | | | | | |
|---|---|---|--|--|----------|
| References | Brygge | Kai | Base Naust (W) | Brygge | 6 |
| Formation | 50 km south of | In mapping area | In mapping area | In mapping area | Comm |
| Location with | mapping area | (Well 28) | (Well 28) | | |
| respect to | (Well 4-1) | | | | |
| mapping area | | | | | |
| Composition | Kaolinite-rich ooze. 25 – 35 % Quartz, 20 – 30 % Illite, 20 – 25 % Kaolinite, 5 – 15% Plagioclase 3 % Smectite. | Smectite-rich fossiliferous clays or clayey oozes 20 % Quartz, 15 – 20 % Illite, 15 % Kaolinite, 20 - 25 % Smectite, 0 – 5 % Chlorite, 5 – 10 % Feldspar, 0 – 15 % Plagioclase, 2 % Calcite. | Illite dominated hemipelagic and glacial sediments 20 – 25 % Quartz, 15 – 30 % Illite, 5 – 15 % Kaolinite, 15 – 30 % Smectite, 0 – 7 % Chlorite, 7 – 10 % Feldspar, 10 – 30 % Plagioclase, 0 - 7 % Calcite. | Mudstone with rare limestone stringers, 80 – 90 % of some mudstones are low density ooze sediments. | n/a |
| Density | n/a | n/a | n/a | 1.8 (Geophysical) | n/a |
| Porosity | n/a | n/a | n/a | 60 % (Geophysical) | n/a |
| Sonic Velocity | n/a | n/a | n/a | 1692 ms | n/a |
| Permeability | n/a | n/a | n/a | n/a | n/a |
| Coefficient | | | | | |
| Compression | n/a | n/a | n/a | n/a | n/a |
| Index | | | | | |
| Shear Strength | n/a | n/a | n/a | n/a | n/a |

Table 1-1 (continued)

6403/6-1

Commercial reports

References**Formation****Brygge****Kai****Base Naust****Location**

In mapping area, little eastwards of Crater D

with respect**to mapping****area****Composition**Claystones and
siliceous oozes.Claystones and
siliceous oozes.Partly remoulded
glacial marine clays.**Density**2.25 – 2.45
(Geophysical)2.35 – 2.55
(Geophysical)2.45 – 3.05
(Geophysical)**Porosity**

> 45 % (Geophysical)

> 45 %

0 – 50 %

Sonic

1580 (calculated from

1481 (calculated

1667 (calculated from

Velocity

seismic line)

from seismic line)

seismic line)

1522 – 1692

1522 – 1692

1522 – 1692

(calculated from
wireline log)(calculated from
wireline log)(calculated from
wireline log)**Permeability**

n/a

n/a

n/a

Coefficient**Compression**

n/a

n/a

n/a

Index**Shear**

n/a

n/a.

n/a

Strength

Table 1-1 (continued)

The Naust Formation was deposited between the late Pliocene and the present (Dalland et al., 1988). The Naust Formation consists of interbedded contourite and mass wasting deposits (Solheim et al., 2005), with its lithology consisting of interbedded claystone, siltstone and sand, with very coarse clastics in its upper part (Dalland et al., 1988). The earliest slides mapped in the Naust Formation are Slides Y and W (Chapter 3). The Naust Formation is correlated with Unit I at ODP sites 642, 643 and 644 (Hempel et al., 1989), which spans the Pliocene to Holocene interval. Unit I has variable carbonate content, no biogenic content, and moderate quantities of smectite. The Naust Formation has been subdivided into five sequences, from bottom to top W, U, S, R, O (Evans et al., 2005). More recently a new notation has been suggested (Rise et al., 2006), however the older notation is preferred here to facilitate easier comparison with previous work. A borehole in the north of our study area in the Ormen Lange Dome shows that the Naust Formation consists of illite dominated hemipelagic and glacial sediments. The bulk density of the base of the Naust Formation in well 6407/1-2 east of our study area is 2.3 g/cm^3 (Dalland et al., 1988). The characteristics of the Naust Formation are summarised in Table 2-2.

The craters described in this thesis are incised in the Brygge and Kai Formations (Chapters 4 and 5), and are buried by Slide W (Chapter 3) and other sediments of the Naust Formation (Chapters 4 and 5), therefore this thesis focuses on the interval encompassing the Brygge, Kai and the Naust Formations.

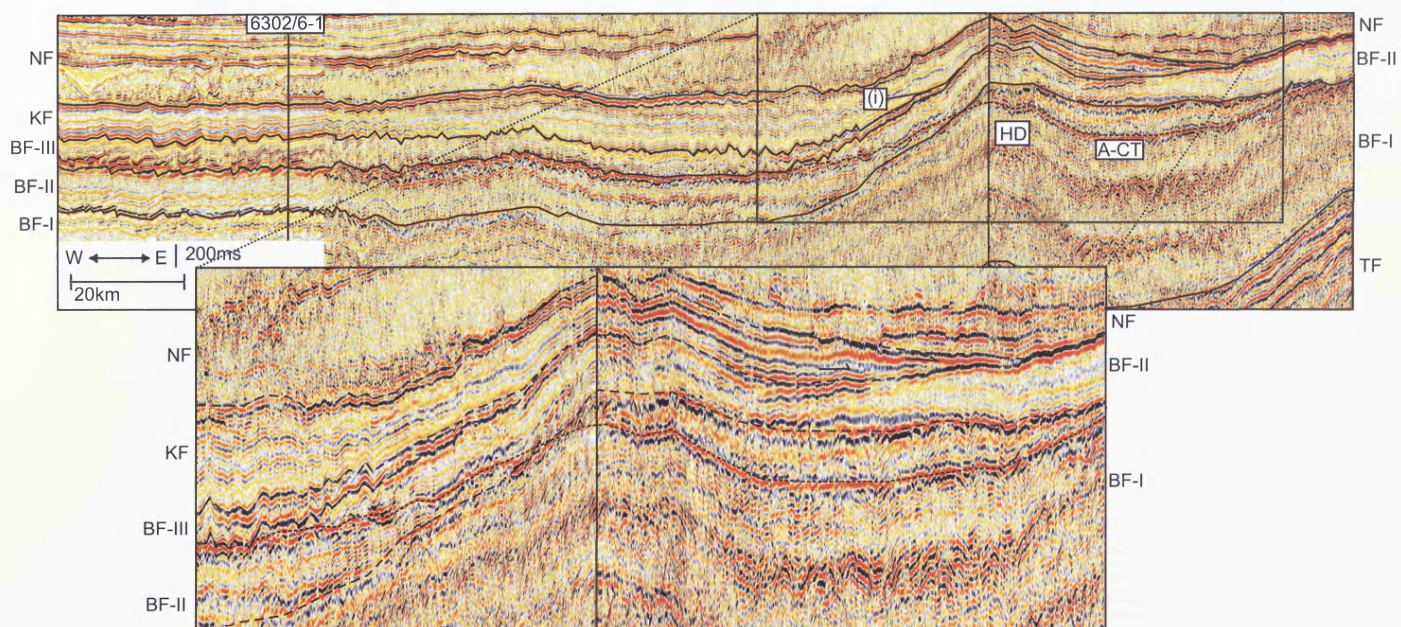


Fig. 2-7: A seismic line demonstrating the inter-relationship of the three units that comprise the Brygge Formation. See Fig. 2-5B for location. TF: Tare Formation. BF-I: Brygge Formation Unit I. BF-II: Brygge Formation Unit II. BF-III: Brygge Formation Unit III. NF: Naust Formation. KF: Kai Formation. NF: Naust Formation. (i) Brygge Formation Unit III onlaps Brygge Formation Unit II.

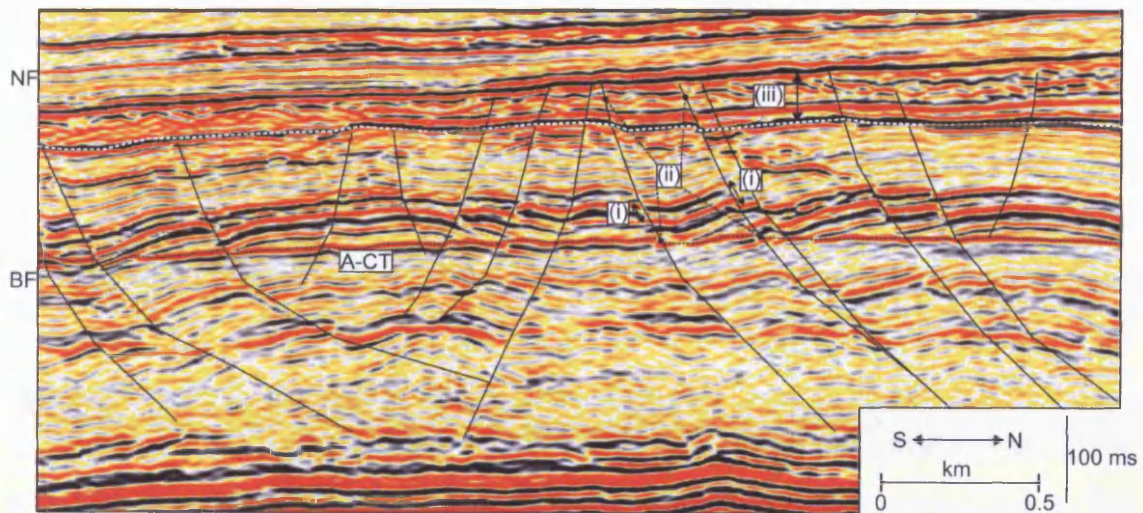


Fig. 2-8: A section showing the normal fault system that deforms the Neogene stratigraphy in this area. (i) Displacement of beds across fault. (ii) Displacement of opal A/CT boundary is less than that of the beds around it, and similar to the displacement of beds near the top of the tier of faulting. (iii) Normal Faulting tips out. There is some uncertainty as to the exact tip out point, this is shown by arrows.

3 THE INITIATION OF SLIDING IN THE MØRE BASIN ON THE MID NORWAY MARGIN

3.1 Introduction

The continental margin off Mid Norway is one of the most unstable margins in the world (cf. Bryn et al., 2005a). It has been a locus for large-scale slides of the slope depositional system from the late Pliocene until the present day (Evans et al., 1996, 2005). Some of the largest individual slides in the world have been mapped in this area, including the important Storegga Slide (Bryn et al., 2005a, Gauer et al., 2005, Kvalstad et al., 2005, Bünz et al., 2005, Haflidason et al., 2004, 2005). This is the largest of the numerous slide events to have occurred on this margin in the last 3 Ma, and because it occurred in the Holocene, understandably it has received the most intensive research effort to date. The economically important Ormen Lange Field is Europe's third largest gas accumulation (Möller et al., 2004), and lies beneath the headscarp region of the Storegga Slide, thus adding an economic imperative to a full understanding of what triggered the slide (Bryn et al., 2005a, Rise et al., 2005, Solheim et al., 2005).

In contrast little is known of the earliest slides on this margin, yet their role is important in developing a coherent understanding of the origins of the instability of the margin as a whole. Early sliding in this area has been linked to the formation of several giant craters buried in the Møre Basin. Riis et al. (2005) showed a spatial and temporal correlation between craters that are over 10 km in diameter excising siliceous ooze of the Brygge Formation and early sliding; and from this suggested that the action of submarine sliding loaded the underlying ooze (see Chapter 1 above). Ooze was remobilised by this rapid loading mechanism, evacuated from the craters onto the top of the slide, and transported basin wards (Riis et al., 2005). An accurate description of this early sliding is therefore important to learn more about the formation of these craters, which are potential geohazards, in addition to the wider objective of unravelling the causes of earliest slope instability.

This chapter aims to describe the geometrical, internal and external characteristics of the two earliest slides to occur in the Møre Basin (Fig. 3-1) using regional 2D seismic

reflection lines for context, and five separate 3D seismic reflection surveys that allow the detailed configuration of the slides to be mapped to high spatial resolution. A subsidiary aim of this chapter is to discuss the timing of the earliest slides in the Møre Basin with respect to the development of the slope, and also to other basin-wide phenomena such as silica diagenesis (e.g. Berndt et al., 2004, Cartwright, 2007, Chaika and Dvorkin, 2000, Davies and Cartwright, 2002, Davies and Clark, 2006, Davies et al., 2008, Volpi et al., 2003, Hein et al., 1978), contourite deposition (Bryn et al., 2005b, Solheim et al., 2005, Berg et al., 2005) and normal faulting (Berndt et al., 2003, Cartwright and Dewhurst, 1998, Hustoft et al., 2007), in an attempt to shed some light on the triggering mechanisms and the causes of slope instability. This knowledge will allow us to better understand the wider significance of these early slides in the evolution of this petroliferous passive continental margin.

3.2 Database and methodology

In this study the two 2D seismic reflection surveys described in Chapter 2 are used to map the bottom and top surface of the two bottom-most slides in the Naust Formation (Fig. 3-2) in order to describe their large scale morphology. The five dispersed 3D surveys described in Chapter 2 are then used for detailed mapping of selected areas of the slides. Time structure maps, dip maps, coherency maps and amplitude maps (Brown, 2004) can be used to provide much information on the basal shear surface, internal geometry and palaeoflow directions of submarine slides (Frey Martinez et al., 2005, Bull et al., 2009a, Bull et al., 2009b, Frey-Martinez et al., 2006, Huvenne et al., 2002, Moscardelli and Wood, 2008).

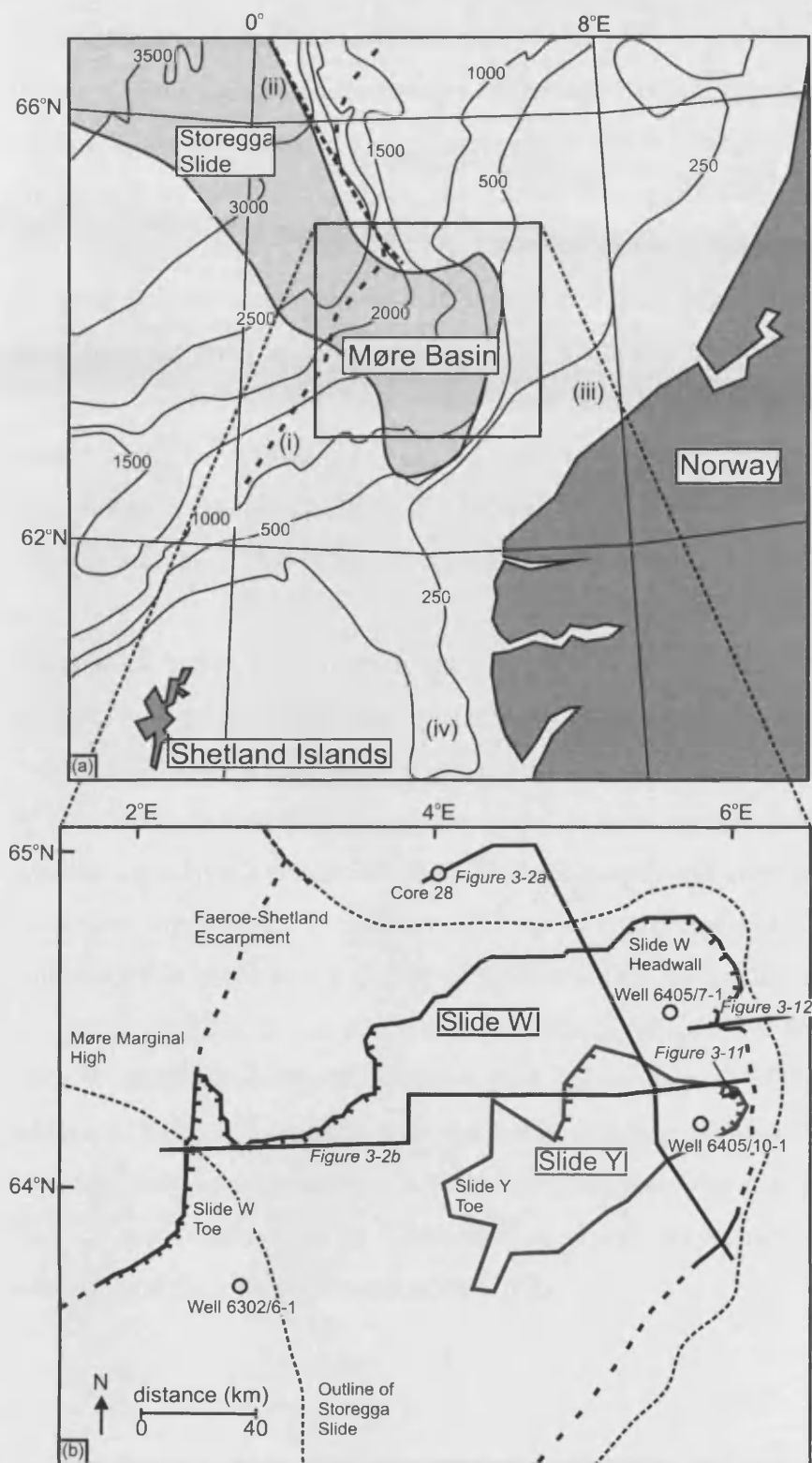


Fig. 3-1: (a) A bathymetry map of the Northern North Sea and the South-east Norwegian Sea showing the location of the Møre Basin. Contours are in metres. (i) Faeroe–Shetland Escarpment. (ii) Jan Mayen Fracture Zone. (iii) Continental Shelf. (iv) Norwegian Channel. (b) A map of the two slides in this area demonstrating the spatial relationship between the two slides and the Møre Marginal High to the west. The ticked lines indicated the mapped headwall and toe of the slide.

3.3 Detailed mapping of slides

In this chapter the two earliest slides of the mid Norway margin are considered. The first of these slides has not been recognised before. The second of these has been recognised by previous workers and named Storegga Palaeoslide W (Evans et al., 2005, Solheim et al., 2005). Storegga Palaeoslide W is here referred to as Slide W. Mapping presented here shows that Slide W covers a larger area than the slide of the same name mapped by Solheim et al. (2005), and that the slide mapped as NFS-1 by King et al. (1996) in the south of the study area is part of Slide W. The older and smaller slide is termed Slide Y because it is below Slide W (Fig. 3-2). This terminology is consistent with the pre-existing nomenclature of slides on the Mid Norway margin (Evans et al., 2005, Solheim et al., 2005).

Both slides cover large portions of the palaeoslope of this part of the Norwegian margin, with head regions located in mid- to upper slope positions. Slide Y covers an area of 3800 km², whilst Slide W covers an area of > 21,600 km². Slide Y and Slide W are clearly discrete slide events separated in time because in the east of the area, a laterally extensive layer greater than 20 km in length and composed of several stratal reflections separates the two slides. This unit is interpreted as being an in situ deposit, indicating that there was a period of well-stratified hemipelagic deposition between the events of Slide Y and the events of Slide W (Fig. 3-2). The bottom surface of Slide W ramps down through this stratified unit in the west of the area so that the top surface of Slide Y coincides with the bottom surface of Slide W (Fig. 3-2b). This boundary between the slides is not always clear, therefore it is possible that parts of Slide Y are cannibalised by Slide W (Fig. 3-2b). Key characteristics of the slide intervals and the slides are summarised in Table 2-1.

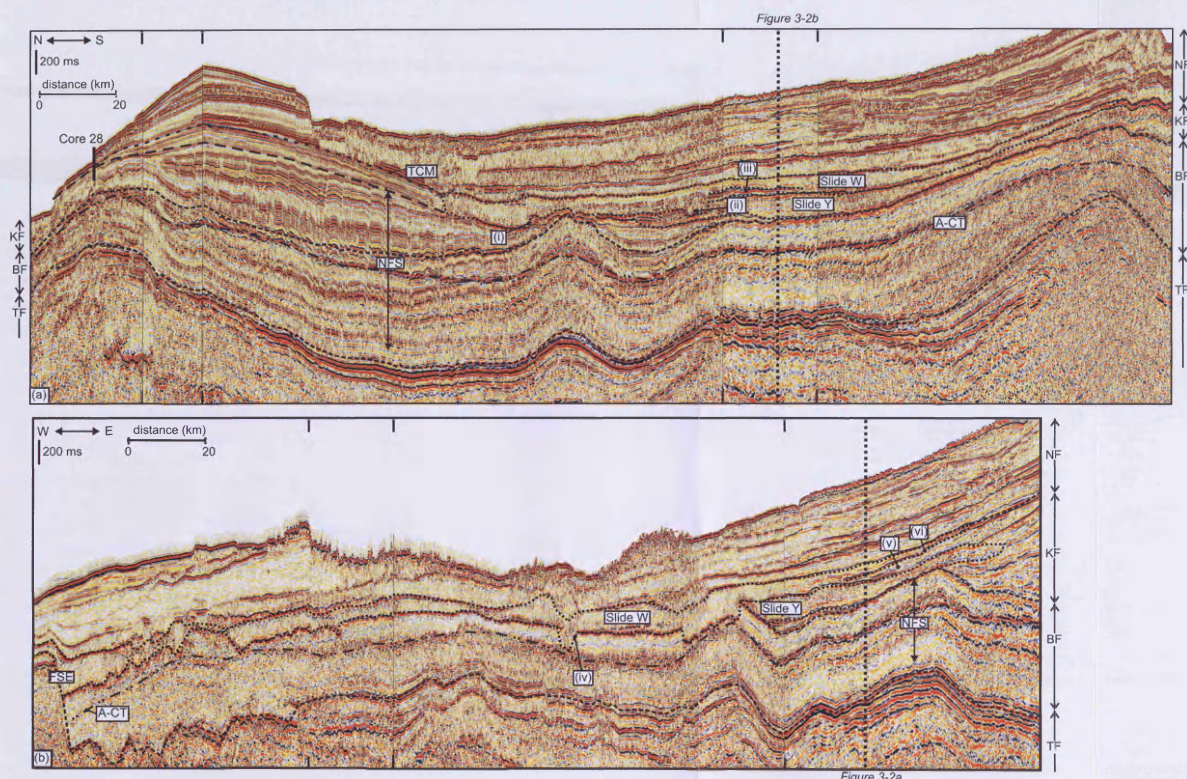


Fig. 3-2: (a) A section through the Neogene stratigraphy of the Møre Basin (see Fig. 3-1 for location). Core 28 is tied to seismic reflection data after Bryn et al. (2005b). TCM (top contourite mound) is the uppermost reflection incised by Slide W; therefore Slide W occurred when this reflection was at the sea bed. (i) Erosive basal shear surface of Slide W. (ii) Slide W cannibalises Slide Y. (iii) Layer of stratified material between Slide Y and Slide W. Abbreviations: NFS = Normal Fault System, A-CT = opal A/CT boundary, BF = Brygge Formation, KF = Kai Formation, NF = Naust Formation. (b) A section through the Neogene stratigraphy of the Møre Basin (see Fig. 3-1 for location). (iv) Erosive basal shear surface of Slide W. (v) Layer of stratified material between Slide Y and Slide W. (vi) Slide W ramps down to top of Slide Y. Abbreviations: FSE = Faeroe-Shetland Escarpment.

| Slide Name | Ma p | Palynological Dating | Flow Direction | Length | Width | Depth | Area | Volume sediment |
|---------------|---------|--|-------------------|--------|-------------|------------|----------------------------|--------------------------|
| | Fig. | | | | | | | |
| Slide Y | 3-4 | Piacenzian to Gelasian (3.6- 1.8 Ma) | East- West | 100 km | 20-40 km | 0-100 m | 3800 km ² | 380 km ³ |
| Slide W | 3-7 | Late Zanclean to Gelasian (4.0-1.8 Ma) | East- West | 180 km | >100 km | 0-300 m | >21,600 km ² | >4320 km ³ |

Table 3-1: Characteristics of Slide Y and Slide W.

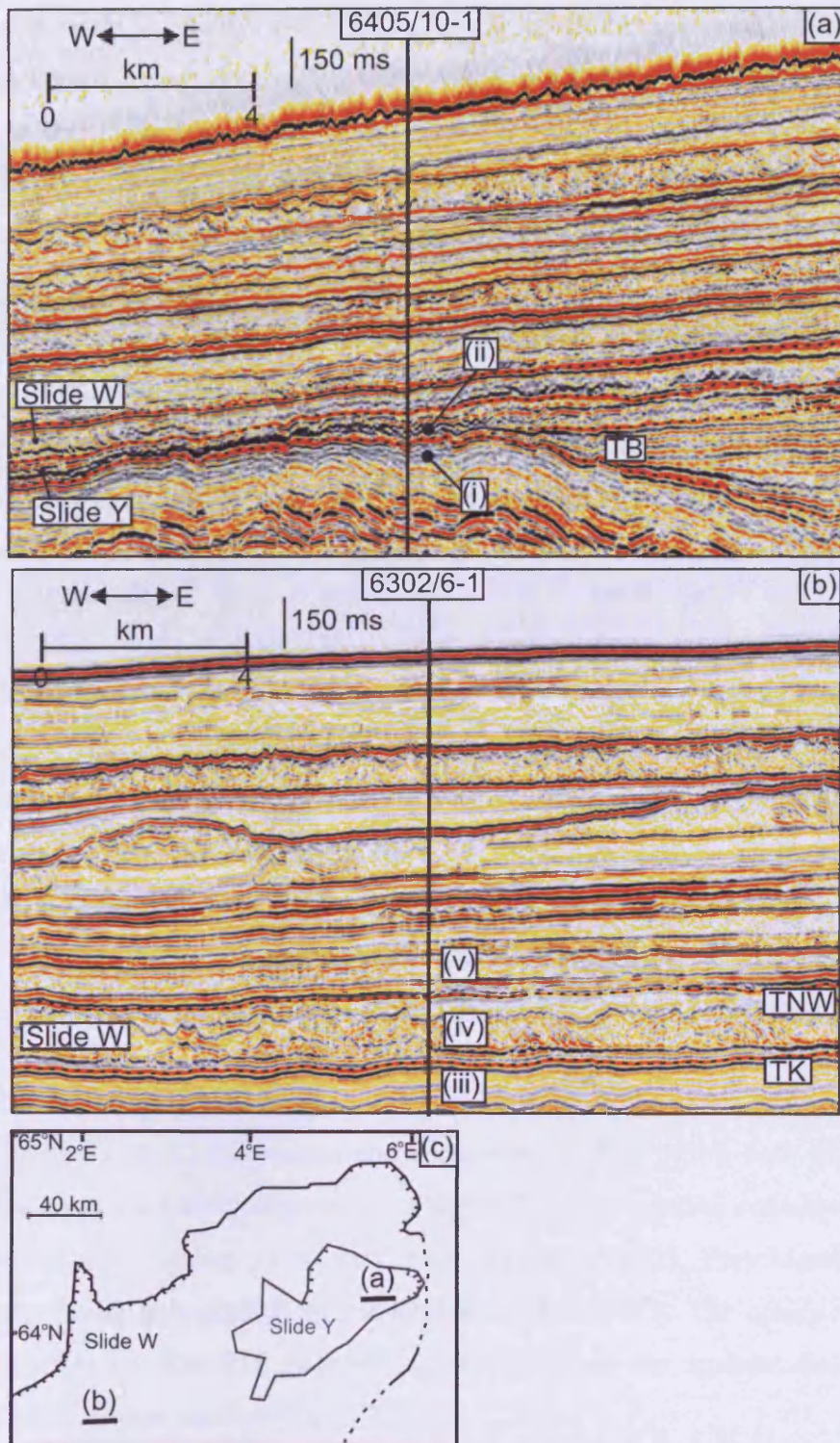


Fig. 3-3: (a) A section showing the dating of Slide Y. (i) Late Oligocene sediments. (ii) Late Pliocene (Piacenzian to Gelasian) sediments. The Top Brygge (TB) boundary is the top boundary dated in this well. (b) A section showing the dating of Slide W. (iii) Middle–Late Miocene sediments. (iv) Pliocene Sediments. (v) Late Pliocene (Gelasian) and Pleistocene Sediments. Abbreviations: TNW = Top Naust W.

Slide Y is penetrated by well 6405/10-1 (Fig. 3-3a). Sediments within Slide Y have been dated approximately in confidential industry well reports from palynology in the range from the Piacenzian to Gelasian (3.6–1.8 Ma). No dating of the overlying stratigraphy was possible. Slide W is penetrated by well 6302/6-1 (Fig. 3-3b) and sediments within the slide are dated in confidential well reports from their palynology as being within the range of the late Zanclean to Gelasian (4.0–1.8 Ma). This information is summarised on Table 1, and a further discussion about the use of palynological data for dating slides is found in the discussion section of this chapter. This biostratigraphic interpretation is consistent with previous dating results for Slide W sediments (Berg et al., 2005; Solheim et al., 2005) and implies that Slide Y could have occurred at any time between the Piacenzian and the time of deposition of the sediments incorporated into Slide W.

3.3.1 Slide Y

Slide Y (Fig. 3-4, Fig. 3-5 and Fig. 3-6) is the earliest major slide to occur on this part of the Norwegian margin. The headwall is located midway up the continental slope at the eastern edge of the Møre Basin and the toe is located downslope of the basin axis of the Møre Basin (Fig. 3-2). The northern portion of Slide Y is confined against a middle-Miocene inversion dome (Chapter 2) while the southern portion is not confined (Fig. 3-5). An isopach map of Slide Y showing its basinal disposition is presented in Fig. 3-4.

3.3.1.1 Margins and morphology

Slide Y exhibits a zone of depletion and accumulation (Fig. 3-5b), both of which are key diagnostics in the slide interpretation (Chapter 2). The depletion zone is remarkably small however (cf. Varnes, 1978, Frey Martinez et al., 2005, Frey-Martinez et al., 2006), representing only c. 10% of the total area of the slide. The upslope region of Slide Y exhibits a wedge-like geometry, pinching out in the upslope direction with downlap onto the upper surface (Fig. 3-5a).

The headwall is not typical of slides of comparable volume reported elsewhere (e.g. Frey-Martinez et al., 2006) in that it varies markedly in geometry laterally. At the north east corner of the slide the headwall dips steeply (Fig. 3-5a) whilst further south the headwall dips more gently (Fig. 3-5b). The northern and southern edges of Slide Y are

clear scarp features, interpreted as side-scarps. Towards the western limit the slide overflows these side-scarps. The northern portion of the western edge of the slide is a pinch out against the eastern flank of a prominent middle Miocene dome (Fig. 3-5).

The thickness of Slide Y varies from east to west, being below seismic resolution near the upslope limit of the slide and 150 m thick downslope east of the middle Miocene dome (Fig. 3-4). The southern portion of the slide is not confined by the middle Miocene dome (Fig. 3-5b).

3.3.1.2 Basal Shear Surface

The basal shear surface is a generally high amplitude reflection with an acoustically soft impedance contrast (Chapter 2). It has a steep average slope in the east of the area, but to the east and south of the middle Miocene dome there is a break of slope in the basal shear surface, before resuming its westward dip to the west of the dome (Fig. 3-5b). The basal shear surface is planar to highly irregular, and locally steps up and down through the underlying stratigraphy by up to 10 or 20 m of relief (Fig. 3-5a, c.f. Bull et al., 2009a). In the upslope region of the slide the morphology of the basal shear surface has been influenced by normal faulting (Chapter 2) that is interpreted to have propagated upwards from the Brygge and Kai Formations (Chapter 2) after the slide formed (Fig. 3-6). There are also elongate blocks of intact material welded to the basal shear surface (Fig. 3-6), these blocks are aligned east–west.

3.3.1.3 Internal Geometry

The average thickness of the slide is 100 m, with a maximum depth to detachment of 150 m. Internally, Slide Y is generally weakly stratified with weak to moderate amplitude reflections exhibiting often considerable lateral continuity over distances of up to 5 km (Fig. 3-5). Locally higher amplitude reflections are considered to result from later gas charging of the slide sediments (c.f. gas charging of sediments surrounding a gas chimney, Løseth et al., 2009).

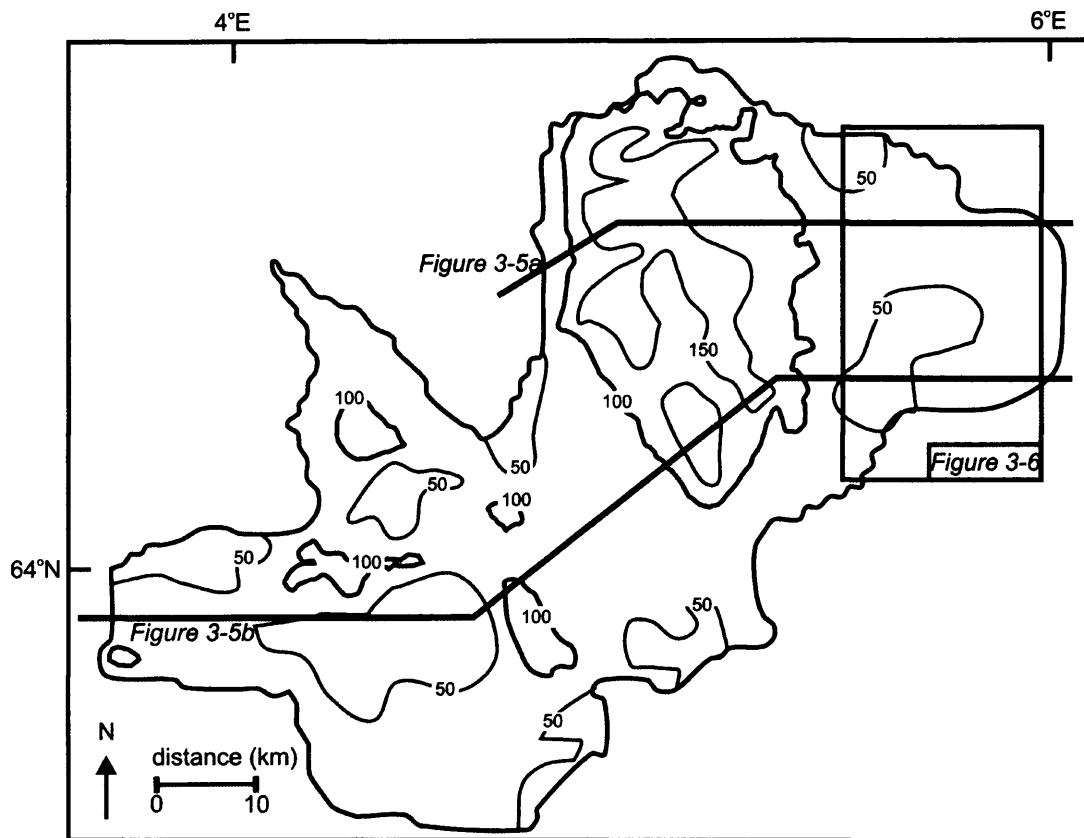


Fig. 3-4: A contoured isopach map of Slide Y in the Møre Basin, constructed from regional 2D surveys. Contours are in metres. See Appendix A2 for time structure maps compiled from 2D seismic reflection data of the basal shear surface of Slide Y (Fig. A2- 1) and top surface of Slide Y (Fig. A2- 2); and for an isochron map compiled from 2D seismic reflection data of Slide Y (Fig. A2- 3).

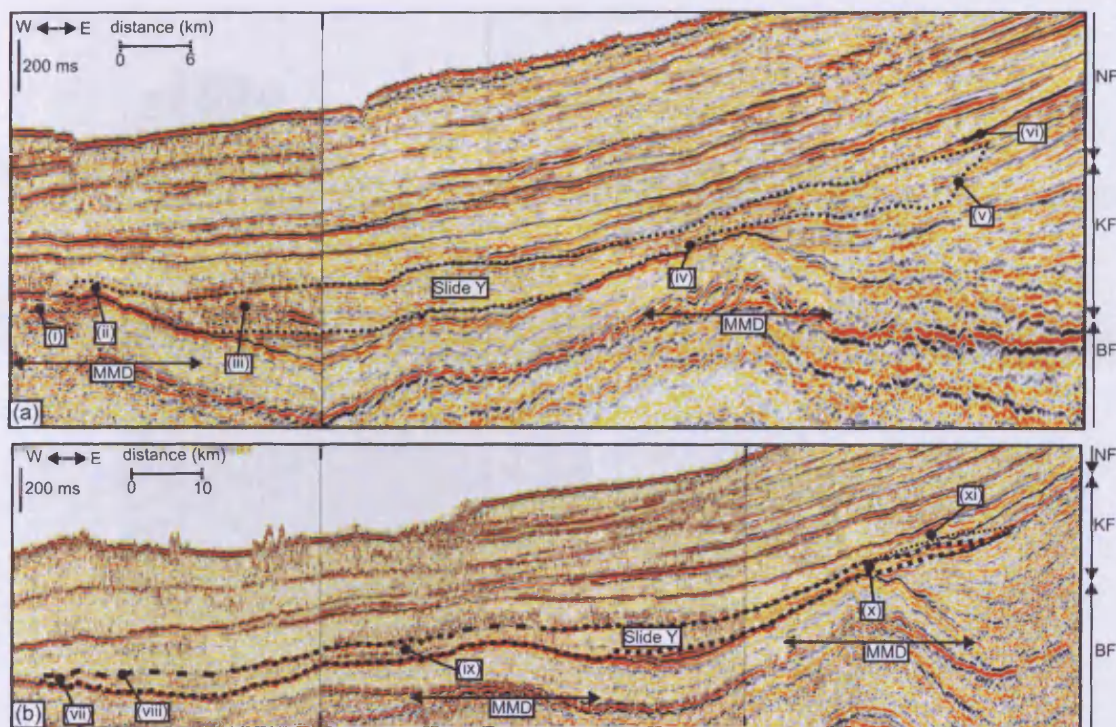


Fig. 3-5: (a) A length section through the northern portion of Slide Y (see Fig. 3-4 for location). (i) Crest of middle Miocene dome. (ii) Slide Y pinches out against middle Miocene dome. (iii) Localised high amplitude reflections within Slide Y. (iv) Step in basal shear plane of Slide Y. (v) Steep headwall of Slide Y. (vi) Top lap onto Slide Y. Abbreviations: MMD = middle Miocene dome. (b) A length section through the southern portion of Slide Y (see Fig. 3-4 for location). (vii) Run out of Slide Y. (viii) Slide W cannibalises Slide Y. (ix) Localised high amplitude reflections within Slide Y. (x) Slide Y pinches out upslope. (xi) Projection of pre-slide geometry.

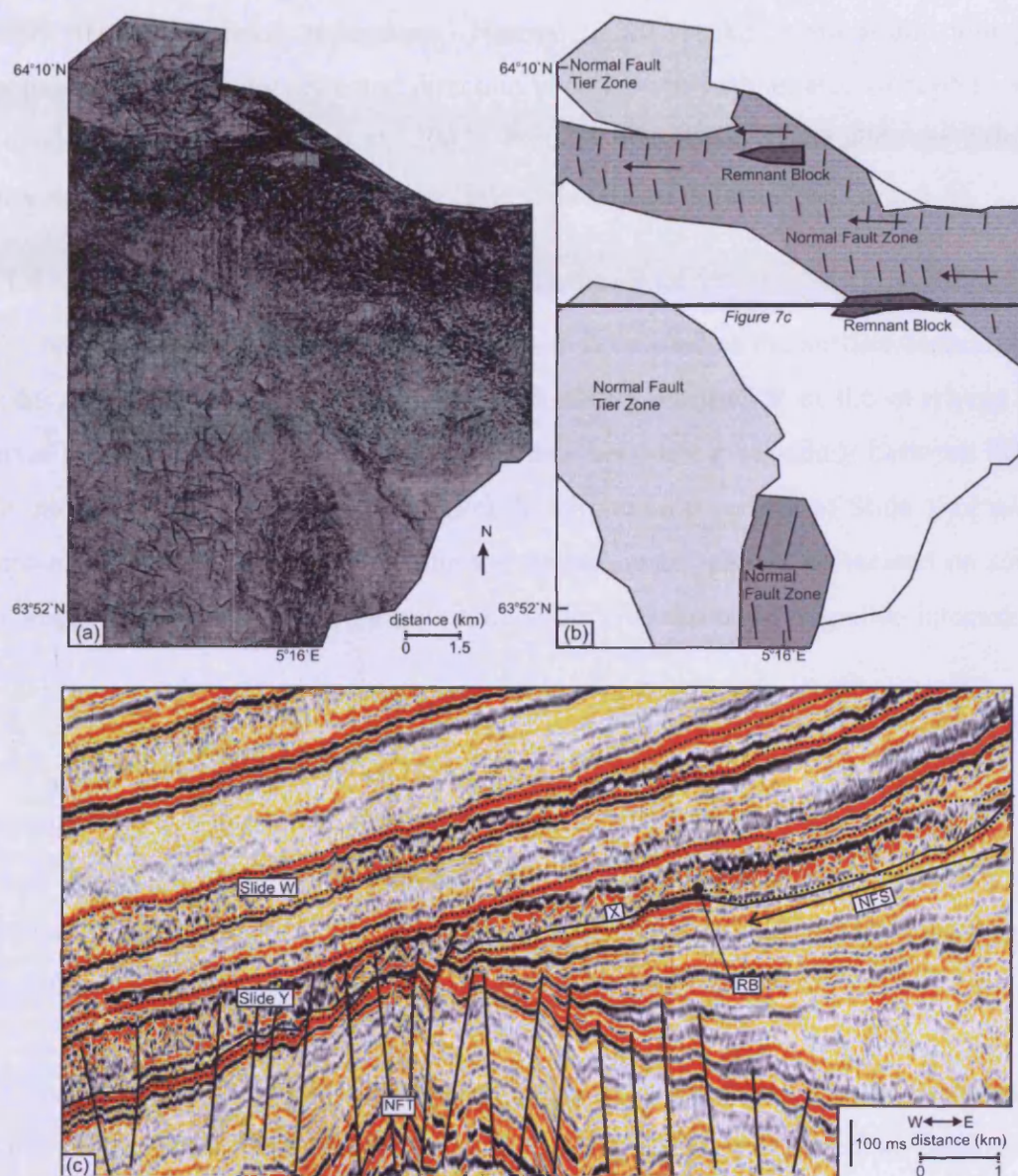


Fig. 3-6: (a) A coherency map of the headwall region of Slide Y (see Fig. 3-4 for location). This map is a slice obtained 10 ms above the basal shear surface of Slide Y or 10 ms above the reflection that is correlated with the basal shear surface of Slide Y were the basal shear surface ramps up or down. Highly discontinuous areas (zones of low coherency), are shown in darker tones. Areas of higher coherence, that is more continuous areas, are shown in lighter tones. (b) An interpretation of the coherency map in (a). (c) A cross section through the headwall region of Slide Y (see (b) for location). x: Cross sectional level of coherency map displayed in (a) is shown as a black solid line. Up slope the slide is intensely deformed by normal faulting (NFS), further downslope the slide is deformed by a normal fault tier (NFT). Abbreviations: RB = Remnant block.

The upslope region of Slide Y has a complex internal geometry (Fig. 3-6) dominated by densely faulted internal reflections. Normal faults strike north–south along the palaeoslope. The faulting style and direction is consistent with an area of depletion near the headwall (Frey Martinez et al., 2005). Parts of this region of the slide are deformed by normal faults (Chapter 2) and show little slide related deformation (Fig. 3-6).

3.3.1.4 Top Surface

In the upslope region of Slide Y the top surface is defined as the surface separating the chaotic facies below and the stratified facies above. Further west the overlying slide interval ramps down such that the same surface becomes a boundary between the two slide intervals. This surface may represent the original top surface of Slide Y or may be an erosional surface. In some areas the top surface is not clearly delineated on seismic data, suggesting possible cannibalisation of Slide Y by the overlying slide interval (Fig. 3-5b).

3.3.1.5 Kinematic Indicators

The morphology of the slide, with a headwall to the north-east and a toe region to the west (Fig. 3-5) suggests that material was translated from east to west. This is corroborated by remnant blocks of material that are elongate in an east–west direction (Fig. 3-6).

This flow direction is further corroborated by the faulting pattern imaged in the eastern portion of the slide described above (Fig. 3-6). Flow is interpreted as having been perpendicular to the normal faulting (c.f. Frey Martinez et al., 2005, Frey-Martinez et al., 2006).

3.3.2 Slide W

Slide W (Fig. 3-7, Fig. 3-8, Fig. 3-9 and Fig. 3-10) is the second slide to have occurred in this area of the Norwegian margin. The headwall is located close to the upper limit of the continental slope, and the slide covers a large portion of the basin floor, confined by the Faeroe–Shetland escarpment at its distal limit (Fig. 3-2b). King et al. (1996) suggested that a component of this slide is sourced from the North Sea Fan and Møre Shelf to the south, but the data does not extend over these areas, so this cannot be

confirmed. An isopach map showing the basinal disposition of Slide W is presented in Fig. 3-7, and the main quantitative features are summarised in Table 3-1.

3.3.2.1 Gross Morphology

Zones of depletion and accumulation (Chapter 2) are evident for Slide W (Fig. 3-8a). Slide W shows a wedge-like geometry pinching out towards the eastern margin. However unlike Slide Y there is no downlap onto the top surface. The thickness increases from east to west, ranging from less than 10–20 m in the east close to the headwall in the region of maximum depletion (e.g. on Fig. 3-8a) to upwards of 200 m in the west in the accumulation zone abutting the Faeroe–Shetland Escarpment (Fig. 3-8c and d).

In the north-east of the study area it is found that the headwall is unusual in that it has two steps in it (Fig. 3-8a). Local mapping shows that the headwall strikes south-east–north-west in this area (Fig. 3-7). The eastern portion of the northern sidewall dips steeply southwards (Fig. 9b), with overthrusting of Slide W (Fig. 3-8b). The coverage of the data allows the northern toe region of Slide W to be mapped. In this area Slide W is confined against the Faeroe–Shetland escarpment (Chapter 2, Fig. 3-2 and Fig. 3-8d), although in places there is limited overspill of Slide W over the top of the Faeroe–Shetland Escarpment.

3.3.2.2 Basal Shear Surface

The basal shear surface dips westwards, becoming more gently dipping further west (Fig. 3-2). The geometry is planar to highly irregular, and locally steps up and down through the underlying stratigraphy by 20–30 m of relief (Fig. 3-8). The base of Slide W can be correlated over large areas of the western part of the Møre Basin with large craters with local relief of over 200 m (e.g. shown as (ix) on Fig. 3-8d, see Chapters 4 and 5 for further details). We follow Riis et al. (2005) in correlating the surface defining these craters with the basal surface of Slide W. The enclosed depressions formed by these craters are thus closely related to Slide W (see the discussion section of this chapter below, and Chapters 4 and 5). In addition to negative relief on the basal surface, we have also mapped several large elongate, undeformed east–west aligned remnant blocks of positive relief on the basal shear surface of Slide W (Fig. 3-8c).

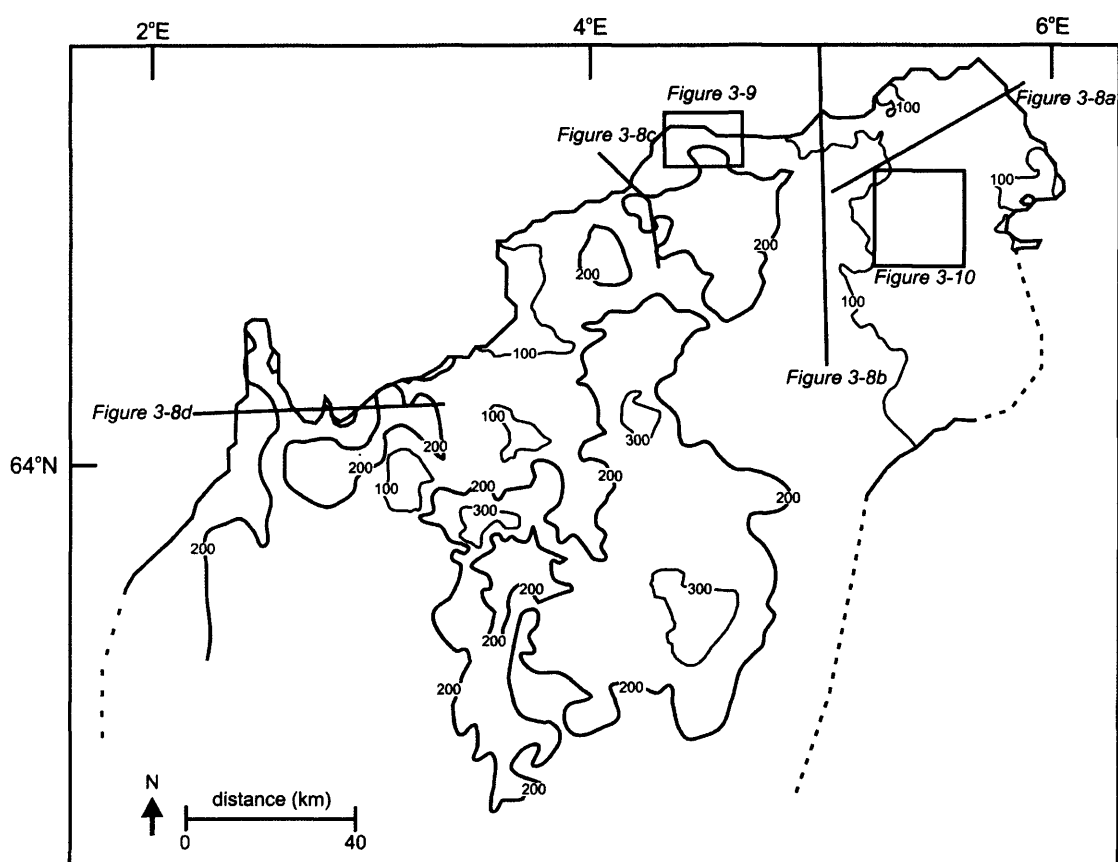


Fig. 3-7: A contoured Isopach map of Slide W in the Møre Basin, constructed from regional 2D surveys. Contours are in metres. See Appendix A2 for time structure maps compiled from 2D seismic reflection data of the basal shear surface of Slide W (Fig. A2- 4) and top surface of Slide W (Fig. A2- 5); and for an isochron map compiled from 2D seismic reflection data of Slide W (Fig. A2- 6).

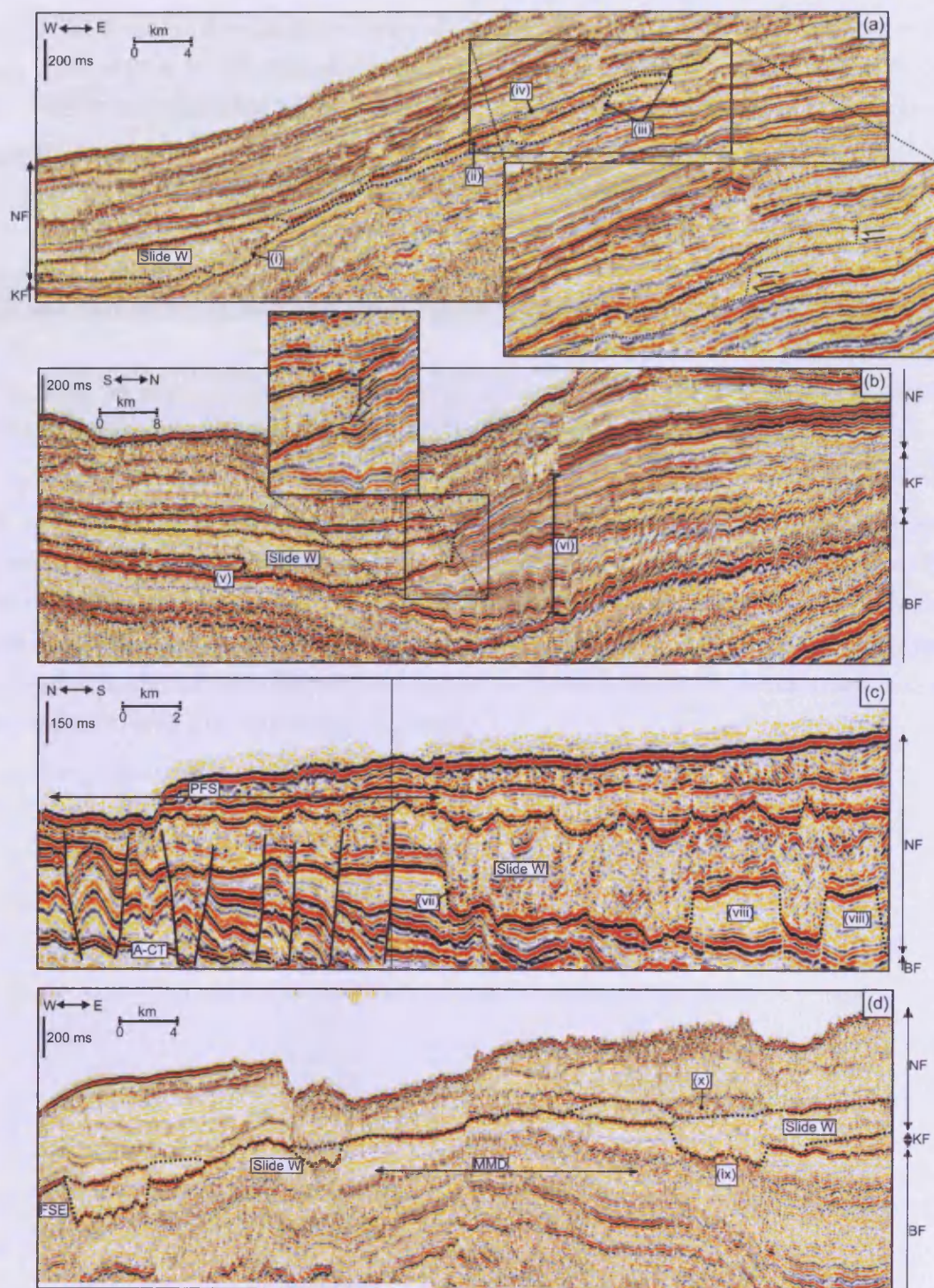
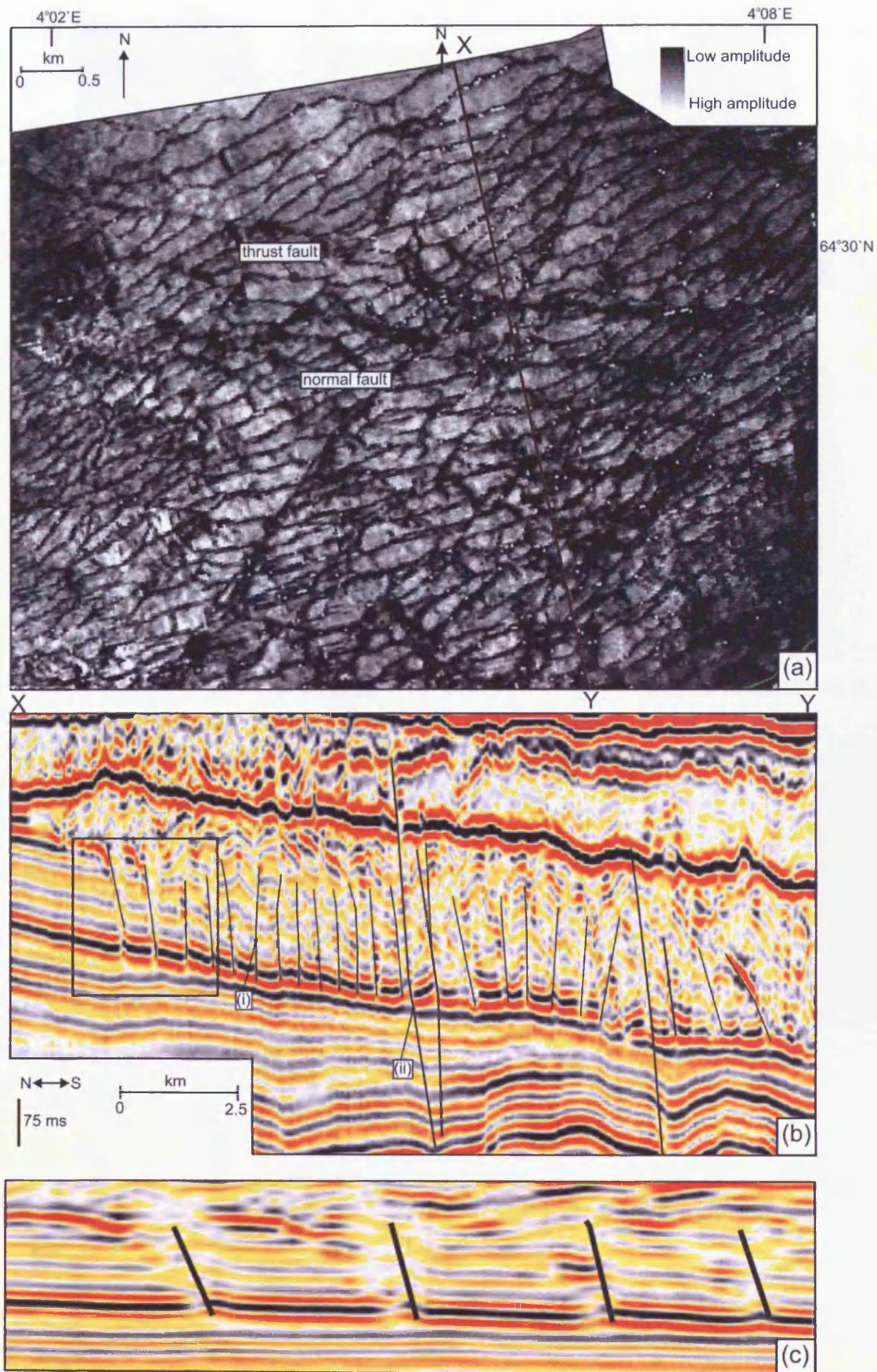


Fig. 3-8: (a) A section through the headwall of Slide W (see Fig. 3-7 for location). (i) Step in basal shear plane of Slide W. (ii) High amplitude reflections within Slide W. (iii) Headwall of Slide W. The headwall is distinguished by the truncation of reflections and has two steps in it. (iv) Projection of pre-slide geometry. (b) A section through the northern flank of Slide W (see Fig. 3-7 for location). The sidewall is distinguished by the truncation of continuous reflections. (v) Step in basal shear plane of Slide W. (vi) Contourite mound. (c) A section through the northern flank of Slide W (see Fig. 3-7 for location). Slide W is deformed in areas by a tier of normal faulting, and there are steps and remnant blocks on the basal shear plane. (vii) Step in basal shear plane of Slide W. (viii) Remnant blocks. The long axes of these blocks is aligned east-west out of the page. (d) A section through the toe region of Slide W. Slide W is confined against the Faeroe Shetland Escarpment (FSE). (ix) Crater on basal shear plane of slide W. (x) Ooze mound on top of Slide W.

Fig. 3-9: (a) A map of the basal shear surface of Slide W showing the magnitude of the reflection amplitude of this surface, which shows up some internal geometry (see Fig. 3-7 for location.) (b) A section showing thrusting within Slide W (see (a) for location). A series of east–west trending thrust faults (i) are disrupted by normal faults in a variety of orientations (ii). (c) A close up of the box in (b), with 4 X vertical exaggeration, highlighting the reverse geometry of the faults (c.f. Frey Martinez et al., 2005, Frey-Martinez et al., 2006)



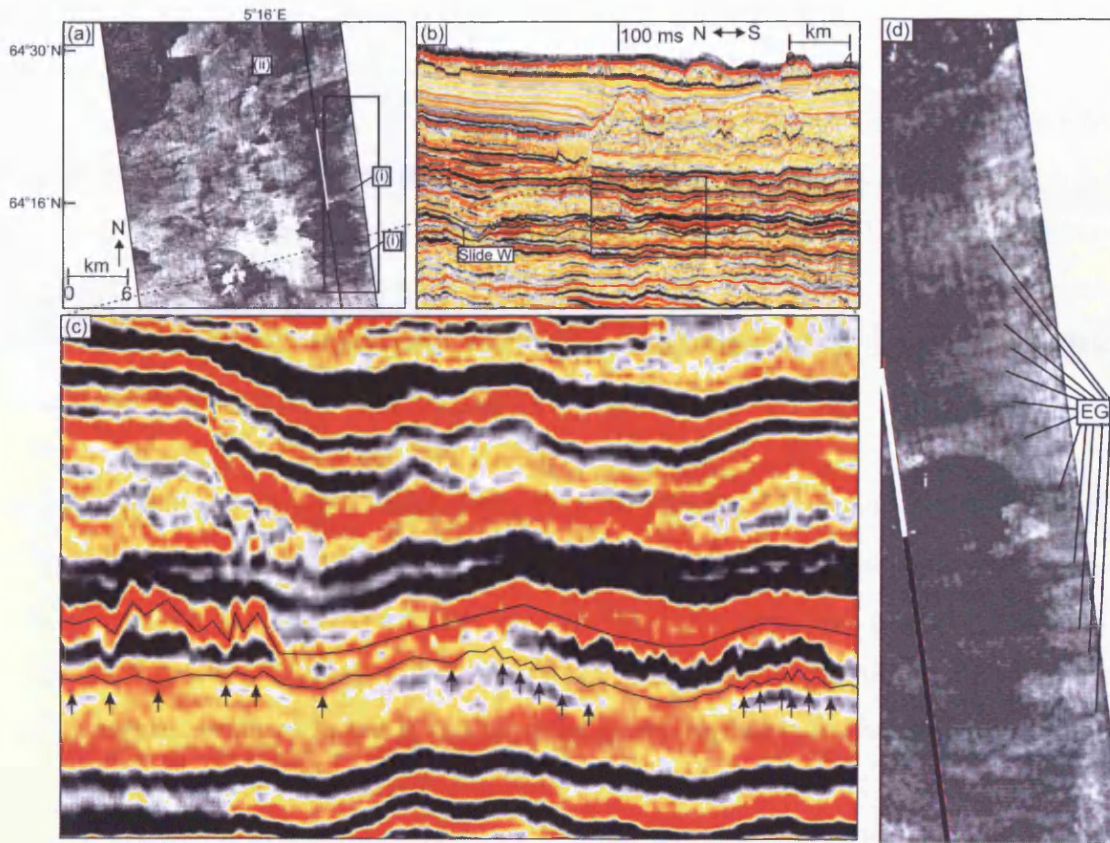


Fig. 3-10: (a) An amplitude map of the basal shear surface of Slide W near the headwall (see Fig. 3-7 for location.) (i) Erosive grooves. (ii) Step in basal shear plane. (b) A section showing the basal shear plane of Slide W mapped. (c) A zoomed in section. Erosive grooves are indicated with arrows. (d) A close up of the area boxed in (a). EG: Erosive Grooves.

3.3.2.3 Internal Geometry

The mapped extent of Slide W has a volume of at least 4320 km³, although it should be noted that it has not been possible to map the continuation of the slide beyond the limits of seismic data coverage in the south of our study area (Fig. 3-7). The average thickness of the slide is 200 m, with a maximum value of 350 m. It is characterised by weak to moderate amplitude intra-slide reflections exhibiting often considerable lateral continuity over distances of up to 3 km (Fig. 3-8).

Reverse faulting is imaged within Slide W in the region of its north-east sidewall (Fig. 3-9). A series of north-verging thrusts are interpreted across an area some 6 km by 5 km on one of the 3D seismic surveys on the basis of the offset geometry of internal reflections of Slide W (Fig. 3-9b&c). This thrust fault array generally strikes east–west, and is parallel to the sidewall in this area. Some individual faults have displacements of less than the vertical stratigraphic resolution of the seismic data (< 10 m). The faults are therefore difficult to map using conventional horizon correlation, but an amplitude map of the basal shear plane of the slide reveals their planform geometry (Fig. 3-9). The thrust faults are cross-cut by a set of normal faults that are longer in planform extent, and strike north-east–south-west, north-west–south-east and east–west (Fig. 3-9). These normal faults are rooted at depth (below Slide W) in normal faults deforming the Kai and Brygge Formations (Chapter 2, Fig. 3-9). Nearby regions of the slide have been deformed by the same normal faulting (Fig. 3-8c).

3.3.2.4 Top Surface

The top surface shows low relief over large regions of Slide W (Fig. 3-8a, b & d), although in some areas relief is greater (e.g. Fig. 3-8c). Slide W is mainly overlain by younger slides, although it is overlain locally by well stratified sediments (e.g. Fig. 3-8c). The top surface of Slide W is not erosive where it is overlain by later slides, because there is no significant depression in relief with respect to where it is overlain by well stratified sediments (Fig. 3-8c).

3.3.2.5 Kinematic Indicators

The morphology of the slide, with a headwall to the north-east and a toe region to the west (Fig. 3-8) suggests that material was translated from east to west. This is corroborated by the elongate remnant blocks of material mapped on the basal shear surface (Fig. 3-8c). A number of east–west lineations 1–2 km long are mapped on a large ramp in the basal shear surface in the upslope region of Slide W (Fig. 3-10a). By analogy with similar features described elsewhere (Bull et al., 2009a, Gee et al., 2005, Moscardelli and Wood, 2008), these are interpreted as small scour marks created by material being translated across the basal shear surface. These are consistent with an east-to-west transport direction. In this context the north verging thrusts on the northern sidewall are somewhat enigmatic, since they imply a localised northward shortening (Fig. 3-9). This shortening is localised to this margin, and could represent an outwards spreading of flow trajectories (cf. Moscardelli and Wood, 2008, Woodcock, 1979).

3.4 Discussion

3.4.1 Slide Processes

The Storegga Slide and the slides described in this paper are part of a series of slides in the Møre Basin known as the Storegga Slide Complex (Solheim et al., 2005). Slide Y is partially confined by a middle Miocene dome and Slide W is frontally confined (cf. Frey-Martinez et al., 2006) by the Faeroe–Shetland Escarpment (Chapter 2, Brekke, 2000, Planke et al., 1991, Smythe et al., 1983). In particular Slide W has a volume that is larger than the Holocene Storegga Slide although it covers a vastly smaller area. This confinement has consequences for the interpretation of translation distances of the slides described here.

The stratal continuity of the internal units of Slide Y suggests that they have not been translated far from their original depositional positions, and in this respect this slide is reminiscent of the frontally-confined slides described by Frey-Martinez et al. (2006), where much of the deformation is by an almost in situ remobilisation with limited downslope translation and disaggregation. In support of this interpretation, several blocks that are welded to the basal shear plane, surrounding which there is only minor deformational intensity (Fig. 3-6). There are also regions that do not seem to be

deformed by any slide-related faulting (Fig. 3-6), also suggesting that movement in these areas was minimal. Projections of the pre-slide geometry in the headwall region suggest a maximum translation distance of c. 2–3 km (Fig. 3-5b), but we note that the lateral variation in headwall geometry complicates such a simple estimate. Over much of the slide, movement is considered to have been less than this maximum value, simply because > 60% of the volume is represented by laterally continuous and stratified seismic facies. The area covered by the zone of depletion is small with respect to the total area covered by the slide, whilst the zone of accumulation is larger (Fig. 3-5). Translation distance would then likely decrease away from this zone towards those regions where Slide Y is confined, and where downslope translation is effectively buttressed.

The internal sediments of Slide W, like Slide Y, did not move far from their original depositional positions. In support of this it has been shown that Slide W exhibits good internal stratification with reflections that can be traced for c. 3 km. Projections of pre-slide geometry (Fig. 3-8a) suggest that translation was minimal, and is likely to be c. 2 or 3 km at most. Translation distance would then likely decrease away from this zone towards those regions where Slide W is confined by the Faeroe–Shetland Escarpment.

Slide W has two steps in parts of its headwall (Fig. 3-8a), and this strongly suggests that Slide W was a poly-phase slide with several episodes of slide movement, similar to the Holocene Storegga Slide (Bryn et al., 2005a, Gauer et al., 2005, , 2005, Kvalstad et al., 2005, Bünz et al., 2005, Haflidason et al., 2004). Further evidence for this comes from ramps imaged in the basal shear surface of Slide W (Fig. 3-8). These ramps could represent the toe and sidewalls of an earlier slide event.

Solheim et al. (2005) suggest that later slides in the Storegga Slide Complex are cyclic occurrences that are closely linked with glacial cycles. The onset of northern hemisphere glaciation is often cited as occurring between 2.6 and 2.7 Ma (Jansen et al., 2000, Hjelstuen et al., 2005). There are considerable uncertainties in estimating the extent of ice during these early glacial times. There is however consensus that glacial

processes are not implicated in the triggering of the slide mapped as Slide W (Solheim et al., 2005, Haflidason et al., 1991, Sejrup et al., 2000, STRATAGEM, 2003).

3.4.2 Basinal Context

In the Early Pliocene when Slide Y and Slide W occurred the basin floor of the Møre Basin would have exhibited significant topography, with the crests of middle Miocene Domes and the western edge of the Møre Marginal High (Chapter 2) acting as local topographic highs. Slide Y in particular interacted with this topography (Fig. 3-5). The confinement of Slide Y against a middle Miocene dome demonstrates that Slide Y post-dated the initiation of folding in this area. The minor folding in the basal shear plane of Slide Y where the basal shear plane dips eastwards (Fig. 3-5) suggests that inversion may either have continued after sliding or that the morphology of the basal shear plane was influenced by pre-existing local structure.

The deformation of Slide Y by normal faulting allows some inferences to be drawn about the timing of Slide Y relative to the normal fault forming process in this area. In the area of Slide Y normal faulting tips out at a datum in the package of sediments that fails as Slide Y (Fig. 3-11). Normal faulting is dated as having ended at the uppermost reflection displaced by the faulting, because it has been shown that active tiers of closely spaced normal faults extend to the sea bed (e.g. Gay et al., 2004). This means that the normal faulting in this area became inactive during or shortly after the deposition of sediments that failed as Slide Y. Parts of the internal geometry of Slide Y are deformed by normal faulting (Fig. 3-6). Given that Slide Y has not moved far, it is likely that these deformed regions represent areas where there was limited downslope translation and instead sediments were deformed locally. This would imply that normal fault deformation has been overprinted elsewhere by Slide Y, and this adds further support for the argument that the main phase of normal fault activity ended at around the time of failure of Slide Y.

The relative timing of cessation of normal faulting and the occurrence of Slide Y have further significance when their relationship to the timing of arrest of the opal A/CT boundary that underlies our study area is considered, because it has already shown that this boundary arrested shortly before the cessation of normal fault activity (Chapter 2).

Thus there is a temporal link between the cessation of migration of the opal A/CT boundary and the triggering of Slide Y.

Some of the normal faulting described in the study area deforms the internal layering within Slide W (Fig. 3-8c). The deformation of the Slide W fabric by normal faulting rooted in a normal fault system below (Fig. 3-9) suggests that the normal faulting deforming the internal geometry of Slide W is reactivated normal faulting that occurred after the main phase of normal faulting (cf. Gay and Berndt, 2007).

3.4.3 Timing

Seismic reflection data tied to Core 28 by Bryn et al. (2005b) allows Slide W to be dated relative to the deposition of contourite mounds in the northern Møre Basin (Fig. 3-2a). Core 28 penetrates a regional unconformity (Bryn et al., 2005b) which is traced to the topmost reflection of the northern sidewall of Slide W. Bryn et al. (2005b) suggest that this unconformity marks the cessation of contourite deposition at 4 Ma when the pattern of sedimentation changed, possibly due to the closure of the Central American Seaway (Bryn et al., 2005b, Stoker et al., 2005). Other workers date this same unconformity as late Pliocene (e.g. Hustoft et al., 2007), which is in better agreement with the dating of Slide W above.

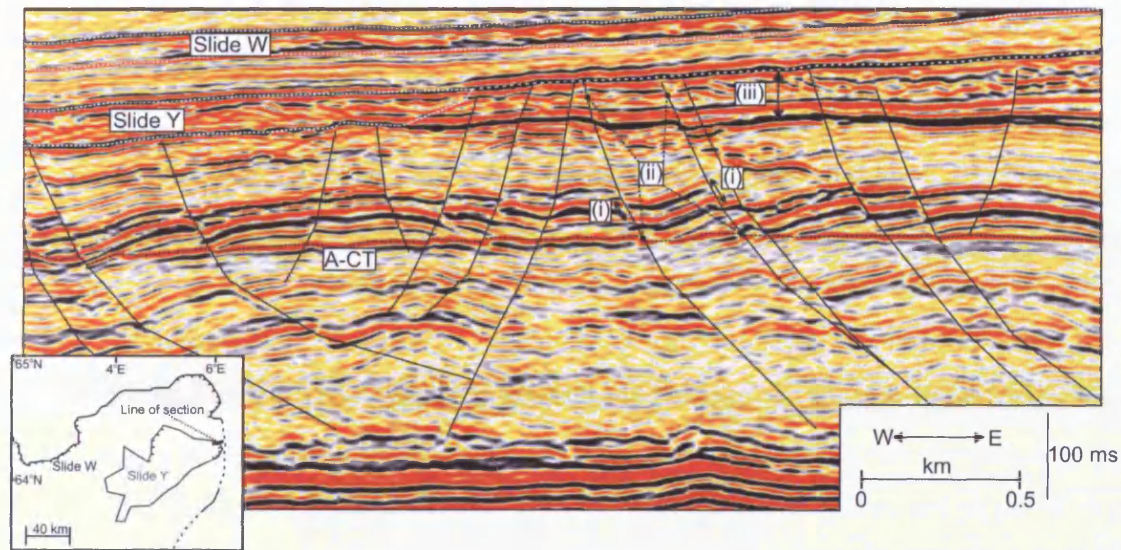


Fig. 3-11: A section showing the normal fault system that deforms the Neogene stratigraphy in this area. A-CT: Opal A/CT boundary. (i) Displacement of reflections across faults. (ii) Displacement of opal A/CT boundary is less than that of the beds around it, and similar to the displacement of beds near the top of the tier of faulting. (iii) Normal Faulting tips out in the package of sediments that fails as Slide Y. There is some uncertainty as to the exact tip out point, this is shown by arrows.

3.4.4 Slope Configuration

The gradient of the slope in this area of the Norwegian margin has slowly increased through the Plio-Pleistocene due to the aggradation of sediment from the Norwegian margin to the east and south from the earliest Pliocene to the present day due to climatic deterioration and continental uplift (STRATAGEM, 2003). To investigate whether these changes may have played a role in preconditioning the margin for failure, a transect in our study interval is used to study the variation of slope angle with depth (Fig. 3-12). The transect is split into six segments spaced at c. 1.5 km intervals bounded by pins labelled A, B, C, D, E, F and G, and then the average depth converted slope of every reflection in these six segments from Miocene times to the present day is measured. Fig. 3-12 demonstrates that over half of the segments (B–C, C–D, E–F and F–G, Fig. 3-12) show a gradual increase in average slope angle with time. The slope of the basal shear planes of slides at their uppermost point is normally in excess of 2° (i.e. (i), (ii), (iii), (iv) and (v), Fig. 3-12). It is noted that there has been basin subsidence since 2.6 Ma, particularly in the last 1 Ma (Ceramicola et al., 2005, Dahlgren et al., 2002, Hjelstuen et al., 2005) and that the slope therefore would have had a shallower gradient at the time of failure. It is also noted that similar slope gradients to here are found on the south Vøring Plateau north of our mapping area (Haflidason et al., 2003). Despite this it is clear from our analysis that steepening is an important process that preconditions this margin for failure, because slides initiate where the slope is steepest. It is considered that there may be trigger processes acting on this part of the margin that do not act further north, and that the slope stability angle is thus shallower in this study area.

3.4.5 Evaluation of Methods

The mapping of Slide Y and Slide W using 2D and 3D seismic reflection data has highlighted some of the strengths and limitations of using such data to map large buried submarine slides, as well as in challenging aspects of conventional slide recognition criteria. Regional mapping was greatly enhanced by the detailed mapping in the 3D seismic data volumes, which gave wealth of information not obtainable from 2D datasets. When a large slide such as Slide W is mapped with incomplete 3D data coverage however, a good 2D data set is important because local kinematic information

obtained from a 3D dataset can be misleading as local flow can be different from large scale flow (Fig. 3-9a, Moscardelli and Wood, 2008, Strachan, 2002, Woodcock, 1979).

Mapping of Slide W was hampered by having a 2D regional survey that covered too small an area and did not cover the entirety of the slide. This meant that the positive identification of small sections of headwall and sidewalls had to be relied upon to formally identify Slide W as a slide as opposed to an area of essentially in situ remobilisation, and this emphasises the importance of having clear slide identification criteria. Dating of Slide W was hampered at well 6302/6-1 by the reworking associated with sliding, which meant that we were only able to assign an age range based on the basal shear plane and top surface of Slide W. Well 6405/10-1 was used to date Slide Y, however the stratigraphy dated here was the topmost stratigraphy sampled at this locality. This meant that only the basal shear plane of Slide Y could be dated. Future work on Slide Y and Slide W should focus on dating these slides more accurately.

3.5 Conclusions

A proper understanding of the initiation of sliding is vital in developing a coherent understanding of slope instability on this margin. By using 2D and 3D seismic data to map the first slides to occur on this margin in detail it has been possible to evaluate why sliding initiated on this margin.

1) Sliding was initiated on the mid Norway margin before significant glaciation when there was a large depocentre at the foot of the continental slope, with some topography related to earlier regional inversion events.

2) Slide Y is a small slide that fails above a package of underlying biogenic ooze, and on the basis of confidential palynological reports occurred sometime between the beginning of the Piacenzian (3.6 Ma) and the deposition of sediments that fail as Slide W. Kinematic indicators such as morphology, remnant blocks and internal geometry suggest that Slide Y flowed from east to west. Slide Y was translated by a maximum of 2–3 km. The northern portion of the slide is confined by a middle Miocene inversion dome while the southern portion of the slide is not confined.

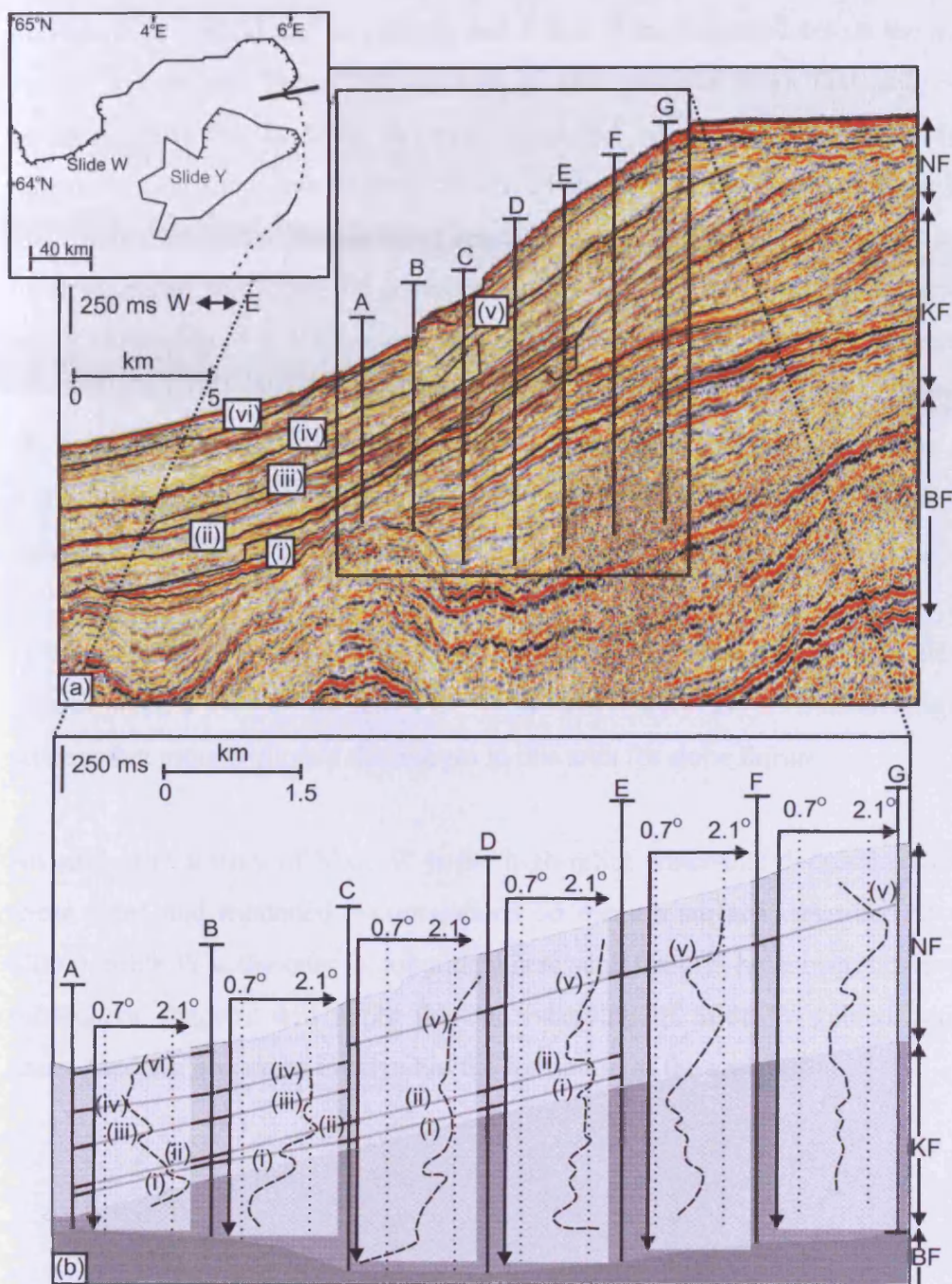


Fig. 3-12: (a) A time section in the east of the mapping area showing the location of slides with respect to the continental shelf. Pins defining ends of segments are labelled A–G. Reflections interpreted by a black line are basal shear planes and are labelled (i) to (vi). (b) A schematic time section showing the average slope of reflections at intervals across the section. Pins defining ends of segments are labelled A–G. A graph of segment-averaged slope angle vs. time is superimposed over each segment. The basal shear planes of slides are indicated in bold and are labelled (i) to (vi). Angles quoted are true angles, with an uncertainty of 0.3°. When calculating angles it is assumed that 1 ms is equivalent to 1 m.

3) Slide W is $> 4320 \text{ km}^3$ in volume, and is one of the largest slides on the mid Norway margin by volume. These findings concur with previous work that suggests that the sediments that fail as Slide W were deposited between 2.6 and 1.8 Ma. Various kinematic indicators such as morphology, remnant blocks and scours in the basal shear plane constrain palaeoflow as being approximately east to west, although there are large local variations in this on the northern margin. Slide W has probably experienced only minor translation of c. 2-3 km, and is confined by the Faeroe Shetland Escarpment.

4) There is a tier of normal faulting in the Møre Basin that mainly tips out at a datum within the package of sediments that fails as Slide Y. An opal A/CT boundary arrested shortly before normal faulting ceased.

5) Since the early Pliocene there has been a gradual increase in slope angle due to the deposition of a prograding sediment wedge. It is likely that oversteepening was a key process that preconditioned the margin in this area for slope failure.

An enigmatic feature of Slide W is the high relief crater-like depressions on the basal shear plane and mounded accumulations on the top surface described by Riis et al. (2005). Slide W is the only major slide where such features have been observed, and the subsequent chapters will apply the understanding of Slide W gained here to better understand the processes involved in the formation of the craters.

4 THE STRATIGRAPHIC AND GEOGRAPHIC DISTRIBUTION OF GIANT CRATERS AND REMOBILISED SEDIMENT MOUNDS ON THE MID NORWAY MARGIN, AND THEIR RELATIONSHIP TO LONG TERM FLUID FLOW

4.1 Introduction

A key test of the model developed by Riis et al. (2005) and described in Chapter 1 is to map the relation of craters and mounds (defined in Chapter 2) to the stratigraphy and structure of the study area, and to investigate how craters and mounds interact with long term fluid flow on the mid Norway margin. Therefore this chapter aims to use extensive 2D seismic data covering the Møre Basin to describe the spatial distribution of craters and mounds with respect to underlying geological structure, stratigraphy and slide events on the mid Norwegian margin, integrating the findings with what is known about long term fluid flow on the Norwegian margin. This will allow a better understanding of the factors which control the genesis of these structures, which in turn will enable a better understanding of the history of the Møre Basin.

4.2 Database / Methods

This study utilises an extensive commercial seismic 2D reflection dataset of over 10,000 line kilometres, covering the Møre Basin and the Vøring Plateau to the north consisting of over a hundred 2D seismic profiles in a variety of orientations, to map the distribution of craters within the crater field and mounds with respect to the regional geology. Some craters and mounds will be mapped with 3D seismic reflection data in Chapter 5.

4.3 Craters

4.3.1 Description of craters

Eleven craters spaced at intervals of 10 to 40 km are mapped in the study area (see Chapter 2 for definition of a crater). A time structure map showing the geometry of the craters is displayed (Fig. 4-1B). Each crater is assigned a label for ease of description. None of the craters outcrop on the current seabed. The craters are large, having diameters spanning the range of 5–50 km and volumes spanning the range from 10 to 400 km³ (Table 1). They vary in shape from being perfectly elliptical to irregular (Table 4-1). The sidewalls of the craters are all smooth and shallowly dipping with dips ranging between 20° and 45° (Fig. 4-2 and Fig. 4-3), with the exception of the north-east corner of Crater G which has a dip of 5° (Table 4-1), Fig. 4-3E). The western sidewall of Crater C and the eastern sidewall of Crater F are linked by a trough (Table 4-1), which is interpreted to be eroded by Slide W because this slide fills the trough (Fig. 4-2A & B, Fig. 4-3A & B). The basal surface of all of the craters is an acoustically soft reflection which exhibits low relief, with the exception of the basal surface of Crater J which is crudely domed (Fig. 4-3D). The craters are all located in the western part of the Møre Basin, and in the region where they occur, they cover at least 35% of the total surface area (Fig. 4-1B).

The craters are all filled by Slide W (Fig. 4-2 and Fig. 4-3) with the exception of Crater D which is filled by a deposit that may have undergone in situ remobilisation (Fig. 4-2D), and Craters H and I which are filled by a deposit which is interpreted to be a younger slide on the basis of the chaotic internal geometry of the deposit and the truncation of Slide W reflections against the base of the deposit (Chapter 5).

4.3.2 Relationship of craters to stratigraphy

All of the craters mapped here are interpreted to have formed as a result of the removal of sediments that are mapped as Unit II, early Eocene to Oligocene biogenic ooze (Chapter 2), with a fossilised Opal A/CT boundary (Chapter 2 & 3) being the bottom-most limit of the evacuation (Fig. 4-2 and Fig. 4-3). Sediments mapped as Brygge

Formation Unit III are also removed from Crater G (Fig. 4-3E). The base of these craters (Fig. 4-2 and Fig. 4-3) is an acoustically soft reflection (Chapter 2), suggesting that sediments evacuated from the crater are acoustically softer than the sediments that fill the craters.

The uppermost surface evacuated by each of the craters is a regionally correlative, acoustically soft reflection that is coincident with the basal shear plane of Slide W (Fig. 4-4, Fig. 4-2, Fig. 4-3 and Fig. 4-5). The sediments that fail as Slide W were deposited on this surface some time between the late Zanclean and Gelasian (4 and 1.8 Ma) (Chapter 3). The stratigraphy beneath this surface is condensed in the regions of the Solsikke and Havsule Domes in the west of the Møre Basin, such that Eocene to Oligocene sediments subcrop on this surface (Fig. 4-5). Northwards, eastwards and southwards of this western region later sediment such as Brygge Formation Unit III, the Kai Formation, and Naust Y (Chapter 2) subcrops, while north-westwards of the central region the earlier Brygge Formation Unit I subcrops in the region of the Solsikke Trough and the Gloria Valley Trough (Fig. 4-5, Haflidason et al., 2004, Riis et al., 2005). Craters are located in the western region of the Møre Basin where Brygge Formation Unit II subcrops.

4.3.3 Relationship of craters to basin structure

All of the craters are located near the present day base of the continental slope in the west of the Møre Basin (Fig. 4-4). The subcrop map of the uppermost surface evacuated by the craters shows that during deposition of Naust W sediments the locations where the craters developed were at the base of the continental slope (Fig. 4-5).

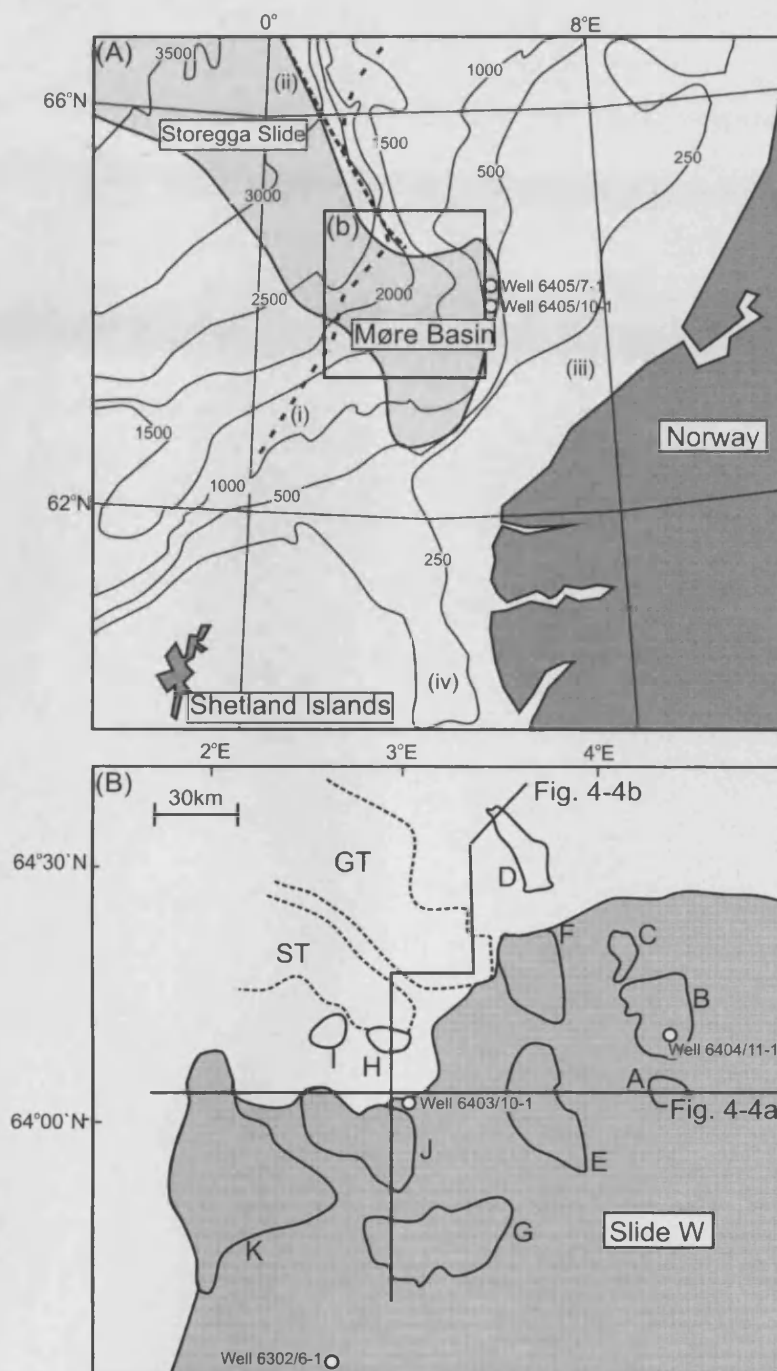


Fig. 4-1: (A) A map of the mid Norway margin, showing location of the Møre Basin. Contours are in meters. (i) Faeroe-Shetland Escarpment. (ii) Jan Mayen Fracture Zone. (iii) Continental Shelf. (iv) Norwegian Channel. (B) A map demonstrating the location of the craters with respect to Slide W (Chapter 3). The craters are labelled A-K. ST: Solsikke Trough. GT: Gloria Valley Trough.

CHAPTER 4

| Crater | Location | Coverage by 2D data | Average Dimensions | Estimated volume |
|-----------------|--|--|--|---------------------|
| A (Fig. 4-2) | Slightly westwards of crest of Helland Hansen Arch | Seven lines in five different orientations | 10 km (length), 7 km (width), 200 m (depth) | 14 km ³ |
| B (Fig. 4-2) | Slightly westwards of crest of Helland Hansen Arch | Seven lines in four different orientations | 30 km (length), 15 km (width), 150 m (depth) | 68 km ³ |
| C (Fig. 4-2) | Slightly westwards of crest of Helland Hansen Arch | Four lines in two different orientations | 10 km (length), 5 km (width), 150 m (depth) | 8 km ³ |
| D (Fig. 4-2) | Westwards of crest of Helland Hansen Arch | Nine lines in three different orientations | 30 km (length), 10 km (width), 150-300 m (depth) | 70 km ³ |
| E (Fig. 4-3) | Eastern flank of Solsikke Dome | Nine lines in five different orientations | 40 km (length), 15 km (width), 200 m (depth) | 120 km ³ |
| F (Fig. 4-3) | Eastern flank of Solsikke Dome | Nine lines in four different orientations | 30 km (length), 20 km (width), 150 m (depth) | 90 km ³ |
| G (Fig. 4-3) | Western flank of Solsikke Dome | Seventeen lines in five different orientations | 40 km (length), 20 km (width), 200 m (depth) | 160 km ³ |
| H (Fig. 4-3) | Crest of Solsikke Dome | Three lines in two different orientations | 10 km (length), 5 km (width), 100 m (depth) | 5 km ³ |
| I (Fig. 4-3) | Crest of Solsikke Dome | Two lines in one orientation | 10 km (length), 10 km (width), 100 m (depth) | 10 km ³ |
| J (Fig. 4-3) | Western flank of Solsikke Dome | Six lines in three different orientations | 40 km (length), 20 km (width), 150 m (depth) | 120 km ³ |
| K (Fig. 4-3) | Adjacent to Faeroe-Shetland Escarpment | Seven lines in three different orientations | 50 km (length), 40 km (width), 200 m (depth) | 400 km ³ |

Table 4-1 Characteristics of craters mapped in the study area. The volumes of the craters were calculated assuming the craters to

CHAPTER 4

| Mound | Location with respect to associated crater and Slide W | Coverage by 2D data | Average Dimensions | |
|-----------------------------|--|---|--|----|
| A (Fig. 4-2) | Slightly westwards (geographically downslope) from Crater A. | Ten lines in five different orientations. | 15 km (length), 15 km (wide), 150 m (depth) | 2 |
| BCF (Fig. 4-2, Fig. 4-3) | Between Crater B, Crater C and Crater F. North western corner coincides with northern flank of Slide W. | Twenty-one lines in six different orientations. | 80 km (length), 20 km (width) 175 m (depth) | 2 |
| E-1 (Fig. 4-3) | Above northern portion of Crater E. | Seven lines in four different orientations. | 20 km (length), 15 km (width), 100 m (depth) | 30 |
| E-2 (Fig. 4-3) | Above southern bay in eastern sidewall of Crater E. | Three lines in three different orientations. | 10 km (length), 5 km (width), 100 m (depth) | 5 |
| GJ (Fig. 4-3) | Located above and eastwards of Crater J, and above and northwards of Crater G. Northern edge coincides with northern flank of Slide W. | Twenty-six lines in six different orientations. | 80 km (length), 30 km (width), 200 m (depth) | 50 |
| K (Fig. 4-3) | Located above northern edge of Crater K | Six lines in two different orientations. | 50 km (length), 10 km (width), 150 m (depth) | 70 |

Table 4-2 Characteristics of mounds mapped in the study area.

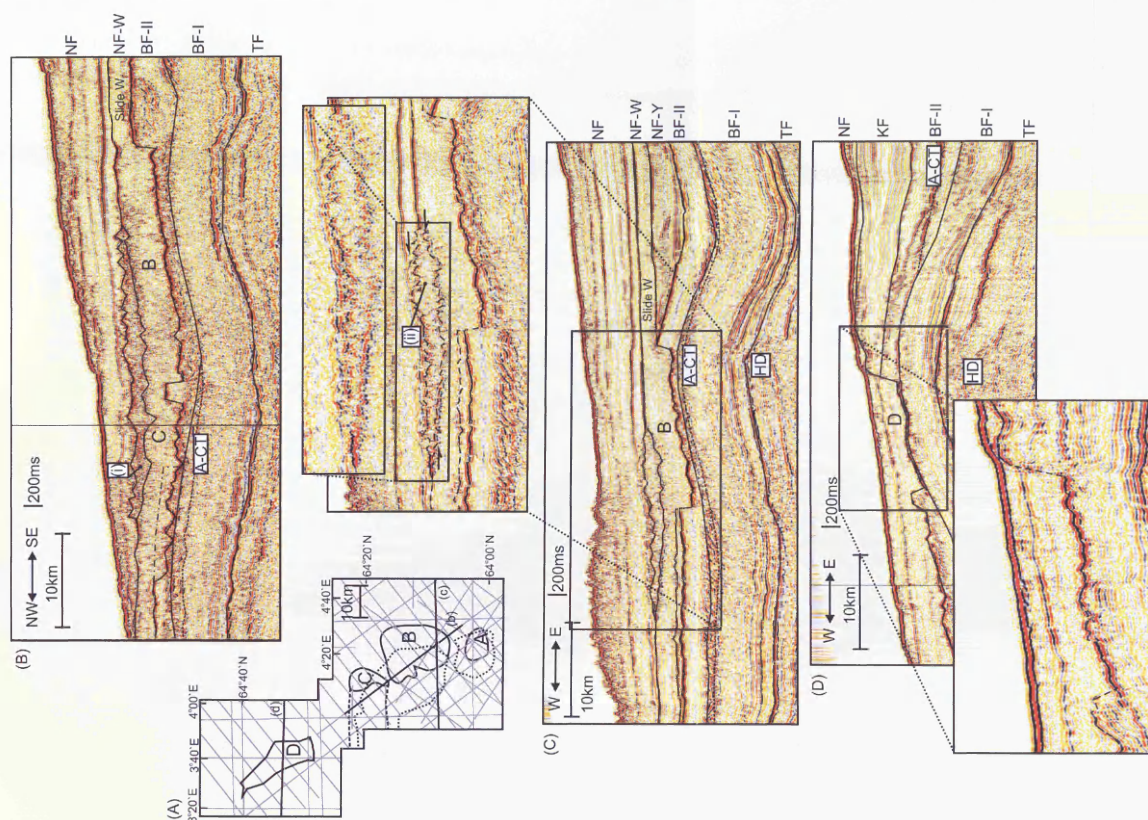
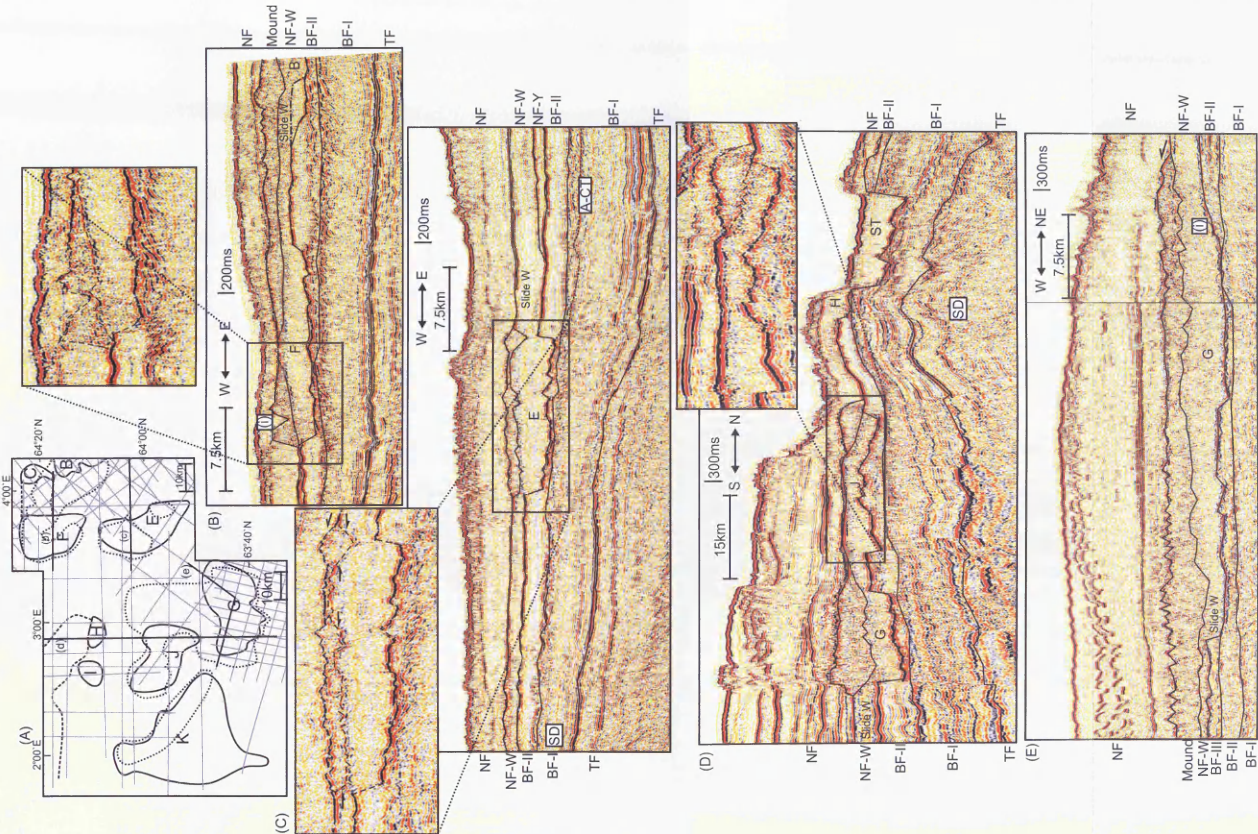


Fig. 4-2: Craters A, B, C and D. (A) A map showing the 2D seismic data coverage over Craters A, B, C and D. Craters A, B, C and D are delineated by a solid line, while the associated mounds are delineated by dotted lines. Note that Crater C is linked to Crater F (Fig. 4-3) by a trough, indicated by a dashed line. (B) A seismic line through Craters B and C. See (A) for location. (i) Vertical correlation between peak on top surface of mound and trough on basal surface of mound is not perfect, suggesting that the morphology on the basal surface of the mound is real and not wholly a velocity artefact. (C) A seismic line through Crater B. Stratal relationships to the overlying mound are indicated. See (A) for location. (ii) Localised vertical correlation between peaks on the top surface of the mounds and troughs on the basal surfaces of the mounds. Craters A, B and C are filled by Slide W. (D) A seismic line through Crater D. See (A) for location. Crater D is not filled by a Slide W, but is filled by sediments that may have undergone in situ remobilisation or sliding.

Fig. 4-3: Craters B, C, E, F, G, H, I, J and K. (A) A map showing the 2D seismic data coverage over Craters B, C, E, F, G, H, I, J and K. Craters B, C, E, F, G, H, I, J and K are delineated by a solid line, while the associated mounds are delineated by dotted lines. Note that Crater F is linked to Crater C (Fig. 4-2) by a trough, indicated by a dashed line. (B) A seismic line through Crater F. See (A) for location. (i) Peaks and troughs on the top surface of mounds have dips of up to 30°. (C) A seismic line through Crater E. See (A) for location. Stratal relationships to the overlying mound are indicated. (D) A seismic line through Crater G, H and J. See (A) for location. Crater H is not filled by Slide W, but is filled by a later slide. The basal surface of Crater J is crudely domed. (E) A seismic line through Crater G. See (A) for location. Note that Crater G incises Brygge Formation Unit III. (i) North-eastern sidewall of Crater G has shallow dip of 5°. Note that Craters E, F, G, J and K are filled by Slide W.



THE STRATIGRAPHIC AND GEOGRAPHIC
DISTRIBUTION OF GIANT CRATERS AND
REMOBILISED SEDIMENT MOUNDS ON THE MID
NORWAY MARGIN, AND THEIR RELATIONSHIP TO
LONG TERM FLUID FLOW

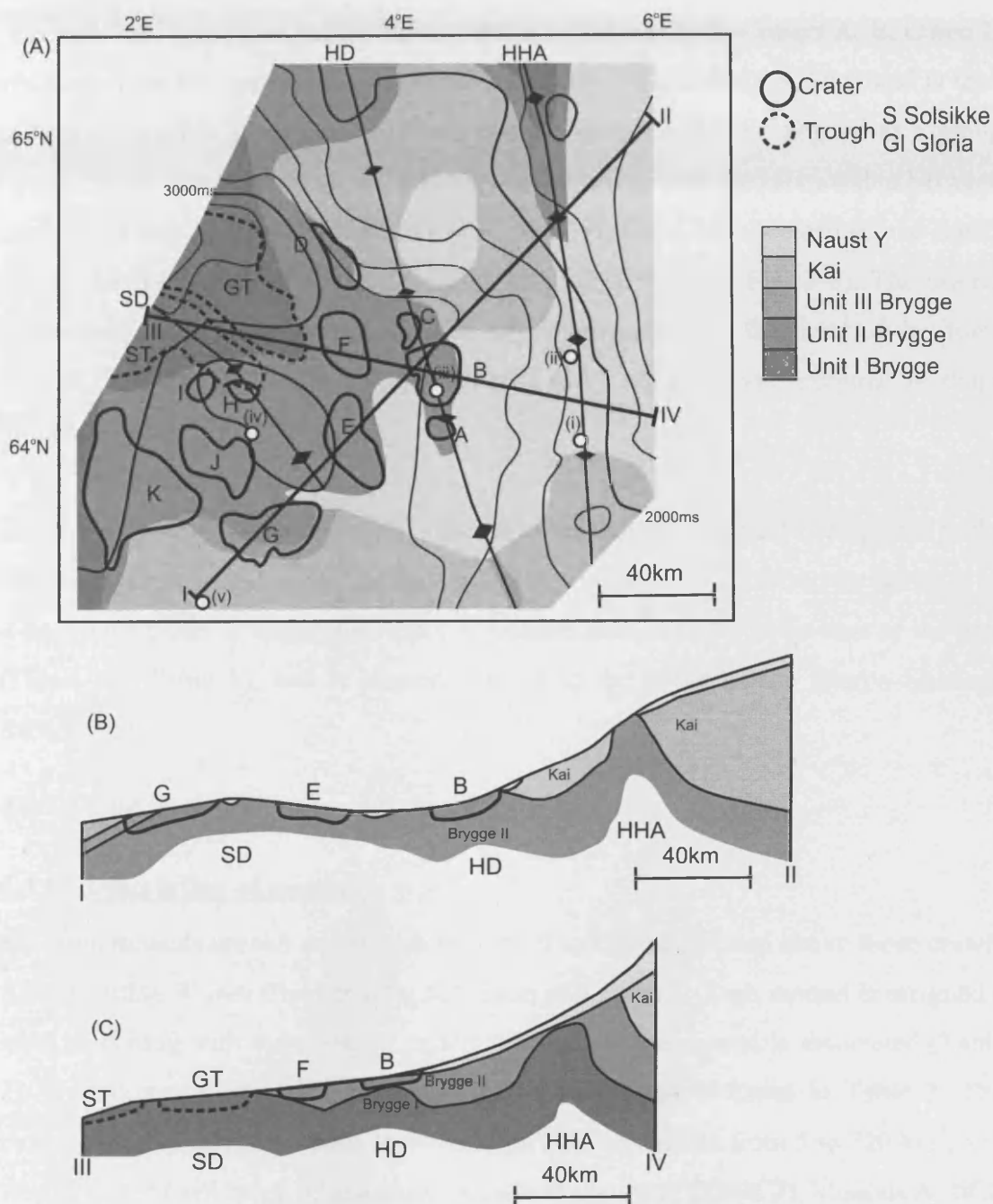


Fig. 4-5: (A) Subcrop map of the regional surface that acts as a basal shear plane to Slide W, showing the location of Craters A–K and underlying structure. HHA: Helland Hansen Arch. (i) Well 6405/10-1. (ii) Well 6405/7-1. (iii) Well 6404/11-1. (iv) Well 6403/10-1. (v) Well 6302/6-1. **(B)** A south west–north east cross-section through the study area with the subcrop surface mapped in (A) at the seabed. See (A) for location. **(C)** A west north west–east south east cross-section through the study area with the subcrop surface mapped in (A) at the seabed. See (A) for location.

No craters are positioned on the eastern Helland Hansen Arch. Craters A, B, C and D are located on the Havsule Dome (Fig. 4-2 and Fig. 4-5). Craters A, B, C and D tend to be a little offset from the dome axis, but are elongate and are aligned as a group parallel to the dome axis (Fig. 4-2 and Fig. 4-5). Further west the relationship between craters and doming is less clear. Craters E, F, G, H, I and J are located on the flanks and in the crestal region of the Solsikke Dome (Fig. 4-3 and Fig. 4-5). The craters positioned on this dome do not show an alignment parallel to the trend of the dome (Fig. 4-3 and Fig. 4-5). Craters E, F, G, H, I and J are also more irregular in shape (Table 1, Fig. 4-3 and Fig. 4-5).

Crater K is positioned immediately adjacent to the Faeroe–Shetland Escarpment to the west of the basin, and is not located on the crestal region of a Miocene dome (Fig. 4-4A). This crater is larger than those associated with doming in the east of the area (Fig. 4-3A, Table 1), and is aligned parallel to the strike of the Faeroe–Shetland Escarpment.

4.4 Mounds

4.4.1 Description of mounds

Six large mounds spaced at intervals of 5 to 10 km are positioned above those craters filled by Slide W (see Chapter 2 for definition of a mound). Each mound is assigned a label, matching with the crater or craters with which the mound is associated (Table 2). A summary of the mounds found in the study area is found in Table 2. The mounds vary in thickness from 100 to 300 m, vary in volume from 5 to 720 km³, and vary in shape from being elliptical to irregular in planform (Table 2). Mounds A, BCF and GJ are up to twice the volume than the craters they overlie, while Mounds E-1, E-2 and K are considerably smaller in volume than the craters they overlie. Mounds associated with the Solsikke Dome craters are positioned directly above the craters (Table 2, Fig. 4-3D & E). Some mounds such as Mound GJ extend eastwards and northwards from the craters whilst others such as E-2 are located over the eastern portion of craters (Table 2). The tops of the mounds are an acoustically soft reflection, while the bottoms of the mounds are an acoustically hard reflection. These observations of reflection polarity are consistent with the mounds containing

acoustically soft material with respect to the surrounding sediment. This is consistent with the mounds consisting of ooze evacuated from the craters (Riis et al., 2005).

4.4.2 Morphology of mounds

The mounds are crudely lens shaped in cross-section, although in detail the basal and top surfaces of the mounds exhibit significant relief consisting of peaks and troughs up to 50 m in height (see (ii) on Fig. 4-2C). The slopes of these peaks and troughs are steep, reaching 30° locally (see (i) on Fig. 4-3B). Generally troughs of any given depth on the basal surface of a mound are associated with peaks of a similar magnitude of relief on the top surface of a mound and vice versa (e.g. (ii) on Fig. 4-2C). Troughs on the basal surface of a mound were labelled as velocity artefacts by Riis et al. (2005, their Figure 2).

Analysis of the shape of the mounds shows that there is only localised vertical correlation between peaks on the top and troughs on the base of the mounds (see (i) on Fig. 4-2B). This demonstrates that the irregular relief of the bases of the mounds is partly real, and is not entirely a velocity artefact associated with the data.

The mounds pinch out onto the reflection that defines the top of the filling slide (Riis et al., 2005). This slide is Slide W (Fig. 4-2B & C, Fig. 4-3, Table 2). There are some exceptions to this, with the edges of Mounds BCF, GJ and K being positioned on the northern flank of Slide W. These mounds partly pinch out onto the uppermost surface evacuated by the craters.

Overlying sediments onlap all of the mounds in our study area (e.g. Fig. 4-2B C, Fig. 4-3C & E), suggesting that the mounds were emplaced on the seabed (Riis et al., 2005). Had these mounds been emplaced as intrusions, substantial deformation of stratigraphy above the mounds would be expected similar to that predicted above diapirs (Davison et al., 1993). This is not observed. The relationship of the mounds to underlying strata is not clear, because the underlying strata have been disturbed by Slide W. However, indications are that the basal surface of the mounds is incisional,

cutting into underlying strata (e.g. Fig. 4-2C and Fig. 4-3C). This topic is addressed in Chapter 5.

4.5 Timing

If the ooze mounds consist of biogenic ooze evacuated from the craters, as suggested by Riis et al. (2005) and supported from observations presented here, then the date of formation of the craters associated with the mounds can be found by finding the date of emplacement of the mounds. The crater and mound forming process is assumed to be instantaneous with respect to background sedimentation, because the pinch out of most of the ooze mounds is a single correlative reflection around the perimeter of the mound. Importantly, it is observed that the datum for the timing of all the ooze mounds occurs at a single, regionally correlative seismic horizon which corresponds with the top surface of Slide W, and that they were emplaced at the seabed. Therefore they would be emplaced at the time of sliding of Slide W. It has been demonstrated on the basis of palynological data that the sediments that comprise Slide W were deposited at sometime within a period that can only be dated approximately in the interval between the late Zanclean and the Gelasian (4 to 1.8 Ma) (Chapter 3). Hence the timing of formation of those craters associated with ooze mounds falls within the same period.

This method fails to date Craters D, H and I because these craters are not filled by Slide W and are not associated with ooze mounds. While the uppermost surface evacuated by these craters is correlated to the basal shear plane of Slide W and the uppermost surface evacuated by the other craters, it does not follow that these craters necessarily formed at the same time as the other craters, because the uppermost surface evacuated by these craters in the region of Craters D, H and I remained at the seabed during deposition of Naust W sediments and their subsequent failure as Slide W, and was not buried till a later date.

4.6 Discussion

4.6.1 Long term fluid flow

The Møre Basin is part of a volcanic rifted margin, and the emplacement of magmatic sills in the subsurface in late Palaeocene and early Eocene times (Planke et al., 2005, Svensen et al., 2003, Svensen et al., 2004, Jamtveit et al., 2004) may have had a marked influence on the development of fluid flow pathways to the present day. During emplacement of the sills and dykes, large hydrothermal vent complexes developed, allowing fluid in the sediments adjacent to sills and dykes to escape to the seabed rapidly (Planke et al., 2005, Svensen et al., 2003, Svensen et al., 2004, Jamtveit et al., 2004). It is estimated that there may be 2000–3000 vent complexes in the Møre Basin and the Vøring Basin to the north (Planke et al., 2005), and during the emplacement of the dykes and sills significant quantities of methane may have been released into the atmosphere, possibly contributing to a period of global warming (Svensen et al., 2004).

Post emplacement, these vent complexes were buried, however geochemical analysis of Eocene to Pliocene sediment above a vent complex in the Vøring Basin has shown that the vent complex may have continued to be a conduit for fluid flow for around 50 Ma after the emplacement of the dykes and sills (Svensen et al., 2003). This fluid may have been sourced from the generation of hydrocarbons at lower levels in the basin (Svensen et al., 2003). An analysis of Pliocene to Pleistocene sediment above the vent complex mapped by Svensen et al. (2003) was not possible due to incomplete well data, however the continued deposition of the Naust Formation would suggest that lower levels of the Møre Basin would continue to become hotter and increase in pressure as they undergo greater burial, thereby potentially permitting the continued generation of hydrocarbon fluids at depth to the present day. Riis et al. (2005) describe seismic amplitude anomalies interpreted to be gas effects adjacent to craters on the Havsule Dome which post dates the formation of craters, and this is evidence of continued hydrocarbon migration after the formation of the craters and the emplacement of Slide W.

Another potential long term source of fluid flow is serpentinisation of the mantle and of the intrusions emplaced in late Palaeocene and early Eocene times, which can give rise to fluids such as H₂, CO, CO₂, and CH₄ (Hovland, 2008). This has been recognised as a potentially important process in the Porcupine Basin (Hovland, 2008). It is envisaged that these could exploit the Jan Mayen Fracture Zone and the hydrothermal fracture vents described above, although this hypothesis would require further testing.

The Brygge, Kai, and bottom Naust Formations that bury the vent complexes have undergone extensive polygonal faulting (Chapter 2, Berndt et al., 2003, Cartwright and Dewhurst, 1998, Hustoft et al., 2007), and these may represent a conduit for fluids leaking from the hydrothermal vents and the Jan Mayen Fracture Zone beneath.

In addition to deeply buried sediment and serpentinisation of the intrusions and mantle being potential sources of long term fluid flow, there are also shallower sources of upward migrating fluid. A process in this region giving rise to pore fluid expulsion is the diagenesis of opal A sediments to opal CT sediments (e.g. Berndt et al., 2004, Cartwright, 2007, Chaika and Dvorkin, 2000, Davies and Cartwright, 2002, Davies and Clark, 2006, Davies et al., 2008, Volpi et al., 2003, Hein et al., 1978), as evidenced by the opal A/CT boundary exhibited in this region (Chapter 3, Berndt et al., 2004, Brekke, 2000). It has been estimated that the porosity of sediments beneath similar boundaries could be 20% less than that of the sediments above the boundaries (Chaika and Dvorkin, 2000), therefore this could be a significant source of fluid (Davies and Clark, 2006, Davies et al., 2008). Another potential shallow source of fluid is the polygonal faulting (Berndt et al., 2003). However, both of these processes became inactive before the deposition of sediments that fail as Slide W, although there was some reactivation of normal faults after emplacement of Slide W (Chapter 3).

4.6.2 Observations and previous work

Earlier workers who mapped remobilised sediment mounds in the Vøring Basin to the north also noted that the remobilised ooze was sourced from Eocene to Miocene biosiliceous sediments (Hjelstuen et al., 1997, Hovland et al., 1998, and references therein). Deep Sea Drilling Project (DSDP) sites 339 and 340 were drilled into mounds in the Vøring Basin, sampling late Eocene ooze and middle Oligocene diatom ooze respectively (Talwani et al., 1976). ODP leg 104 (site 643) sampled in situ Miocene ooze with a porosity of between 80 and 90% (Eldholm et al., 1987). The mounds were interpreted as diapirs (Hjelstuen et al., 1997, Hovland et al., 1998). Hjelstuen et al. (1997) suggested that the emplacement of diapirs was induced by differential loading by more dense and less porous prograding Pliocene and Pleistocene sediments with small offset late Oligocene to Pliocene faults and zones of weakness acting as migration pathways for the ooze. Hovland et al. (1998) built on this by arguing that there are four factors that may explain the emplacement of diapirs: (a) a buried low density, high porosity layer of deformable material (the ooze), (b) a doming substratum which causes extension and faulting, (c) migration of light hydrocarbons through some of the faults and fault zones, and (d) possible tectonic activity. The geological setting of the Møre Basin described above is similar to that of the Vøring Basin (Brekke, 2000, Gay and Berndt, 2007, Hempel et al., 1989, Hovland et al., 1998, Pittenger et al., 1989, Riis et al., 2005, Skogseid and Eldholm, 1989, Skogseid et al., 1992, Stuevold et al., 1992, Svensen et al., 2003), with a wedge of prograding denser sediments burying domes of lower density biosiliceous ooze.

Riis et al. (2005) linked some of the remobilised sediment mounds with the craters in the subsurface, and noted on the basis of well data that the mechanism of removal of ooze from the craters was efficient, and that the removal of ooze could have pre-dated the emplacement of the slide deposit. Riis et al. (2005) attempted to solve this problem by thinking of the slides and the crater formation as two parts of a simultaneous process. As the slide is emplaced, it loads the low density biosiliceous ooze, which is overpressured (Riis et al., 2005). The ooze is then remobilised and ascends up onto the top surface of the slide due to its low density, where it is transported downslope (Riis et al., 2005). In the model it is the slide that causes the

craters to form. Riis et al. (2005) noted that seismic amplitude anomalies that are interpreted as gas effects are positioned adjacent to two of the craters they describe, and suggest that fluid flow from beneath could facilitate mobilisation of the ooze through liquefaction, fluidization and gas expansion (c.f. Nichols, 1995). Thus the model presented by Riis et al. (2005) builds on the models suggested by Hjelstuen et al. (1997) and Hovland et al. (1998).

Mapping of the early slides within this area presented in Chapter 3 has improved understanding of Slide W, which fills the craters. Slide W is a large slide with a generally low displacement in a downslope direction (Chapter 3). This would mean that the craters would have formed in the subsurface, as crater locations would have been buried by ~ 200 m of Naust W sediments when ooze was first mobilised from the craters (see isopach map of Slide W presented in Fig. 3-7, Chapter 3). These locations would not be thinly buried as envisaged by Riis et al. (2005), who imply in their model (see their Figure 9) that the filling slide was translated over tens of km into the area in which the craters were to form.

Results presented in this chapter show that there are eleven large craters, from all of which sediments mapped as Unit II of the Brygge Formation (Chapter 2) are evacuated and most of which are filled by Slide W. The top most surface evacuated by all of the craters is a regional surface that is correlated to the basal shear plane of Slide W. Most of the craters are located on the crests and flanks of the Havsule Dome and the Solsikke Dome. Where the craters are filled by Slide W large mounds of sediment, interpreted to be ooze sourced from the craters (Riis et al., 2005), are found further up the stratigraphic succession. These mounds pinch out onto the top surface of Slide W and, on the flanks of Slide W, onto the top most surface evacuated by the craters.

4.6.3 Formation of craters and emplacement of sediment mounds

The results of earlier work and findings presented in this chapter prompt two important questions, both of which are relevant to understanding how the craters were formed and the sediment mounds were emplaced. Was the fluid flow from below

intermittent or continuous? Did fluid flow from below cause crater formation and initiate slide development, or did the slide develop first? It can be appreciated that a variety of models could be presented to show how the fluid flow, sliding and crater formation interact. Here two hypotheses are presented covering the different end member answers to illustrate some of the processes that might be involved. In the first hypothesis (Hypothesis A, Fig. 4-6) fluid flow from beneath is highly intermittent. In this hypothesis an eruption of fluid flow from below is responsible for the initiation of crater formation, which in turn is responsible for the initiation of sliding. In the second hypothesis (Hypothesis B, Fig. 4-7) continuous fluid flow from below is trapped beneath the prograding Naust Formation, with sliding loading the low density Brygge Formation, causing it to undergo liquefaction, a process which may have been facilitated by the trapped fluid, initiating crater formation and sediment remobilisation. These hypotheses and their application to this area are discussed further below.

4.6.3.1 Hypothesis A

Fluids at depth are considered beneath the sills emplaced in late Palaeocene and early Eocene times. The fluids become overpressured (e.g. Berndt, 2005). The abundance of filled gas reservoirs near the Møre Basin (e.g. Ormen Lange, Möller et al., 2004), suggests that in our study area gas may be dissolved in this fluid. If the fluid were to become overpressured and breach its reservoir seal, pore fluid pressure would be released and degassing would occur as the fluid would become super-saturated due to the loss in pressure. As the gas moves upwards with the pore fluids, potentially exploiting hydrothermal vents and the polygonal fault system, it would encounter more porous and less cohesive sediment above the opal A/CT boundary (c.f. Chaika and Dvorkin, 2000). Both fluid and gas might mobilise the less cohesive ooze above. This system is perhaps similar to a champagne bottle, where thermodynamic equilibrium between gas dissolved in the fluid and gas in the headspace is lost on uncorking leading to degassing of carbon dioxide (Liger-Belair, 2005). The carbon dioxide lifts or entrains fluid and passes rapidly through a narrow neck into the open air.

In the mapping area considered here, the low porosity sediment beneath could represent the neck of the champagne bottle. Less cohesive sediment above the opal A/CT boundary could be mobilised by both fluid and escaping gas and ascend through Naust W sediments. Naust W sediment would be displaced to allow ooze to ascend through it. This could destabilise Naust W sediments, located at the base of the then continental slope, giving rise to retrogressive slope failure (c.f. Gauer et al., 2005) and Slide W.

Hypothesis A would explain why there are no observed deformation structures related to the emplacement of ooze mounds within the infill where Slide W fills the craters (Riis et al., 2005), and would also explain why well 6404/11-1 (Fig. 4-1 and Fig. 4-5) shows no remobilised ooze within Slide W (Riis et al., 2005). If ooze mound emplacement occurred before failure, then any deformation would be overprinted by slope failure. Because Slide W has a low displacement (Chapter 3) this deformation would not be displaced far downslope.

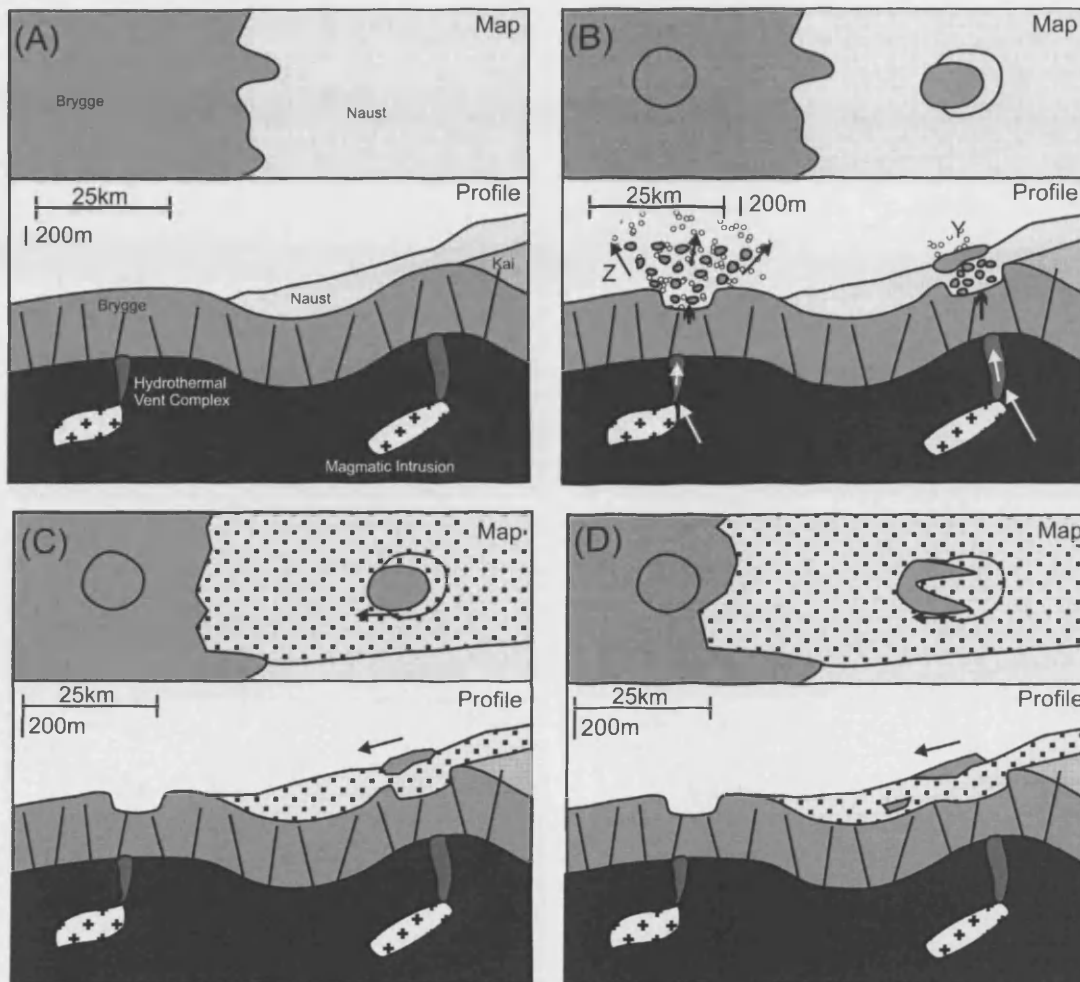


Fig. 4-6: Hypothesis A. (A) Sediment is deposited on domed normally faulted biosiliceous ooze which buries hydrothermal vent complexes associated with magmatic intrusions in lower levels of the basin. (B) Biosiliceous ooze in the regions of Crater Y and Crater Z is remobilised by an eruption of fluid from beneath (indicated by c. vertical white arrows). In the region of Crater Y ooze ascends through the sediment drape, possibly entrained in the ascending fluid, accumulating in ooze mounds at the seabed. In the region of Crater Z ooze is lost to the water column. (C) In the region of Crater Y the ooze ascending to the seabed destabilises the sediment drape at the foot of the continental slope, bringing about a retrogressive slide. (D) The slide moves the ooze mound downslope, modifying the morphology of Crater Y.

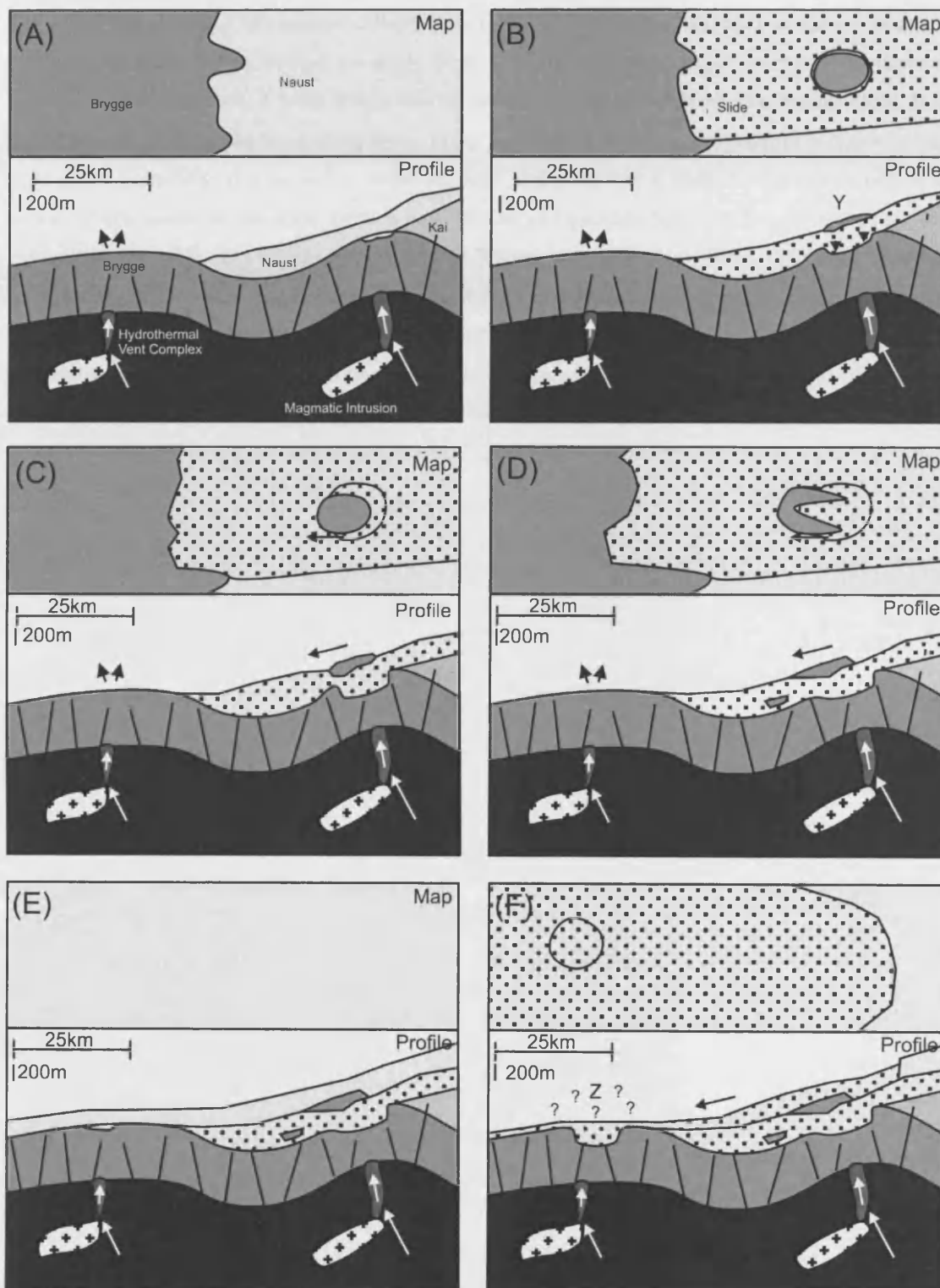


Fig. 4-7: Hypothesis B. Continuous fluid flow is represented by c. vertical white arrows. (A) Sediment is deposited on domed normally faulted biosiliceous ooze which buries hydrothermal vent complexes associated with magmatic intrusions in lower levels of the basin. Fluid flow continuously exploits the vent complexes. Fluid is trapped between prograding sediments and opal A/CT boundary. (B) Deposited sediment fails and moves as a slide. Sediments in region of Crater Y are loaded by the slide. Ooze is remobilised and ascends due to its low density to the top surface of the slide. (C) Ooze mound is transported downslope by Slide. (D) Slide modifies morphology of Crater Y. (E) Further sediments are deposited above the system described in (A)-(D). (F) These new sediments fail, loading biosiliceous ooze in the region of Crater Z. Ooze is remobilised and ascends due to its low density to the top of the new slide, and is either lost to the water column or transported far downslope out of the study area.

Hypothesis A would explain why mounds associated with the Solsikke craters extend eastwards and northwards of the craters they are sourced from (e.g. Mound GJ, Table 2, Fig. 4-3A), in spite of a general westwards flow direction of Slide W (Chapter 3). If the ooze was emplaced on the seabed shortly before Slide W became active, the ooze could flow in the direction of the local slope away from the crater, and would not be constrained in moving in the same direction as the slide initially. For example, one of the mounds associated with Crater E (mound E-2) is positioned over the eastern portion of Crater E (Table 2, Fig. 4-3A), which is the local downslope direction. This mound may have been emplaced and flowed eastwards, before being transported westwards towards its original emplacement position by Slide W.

The observation that all of the craters associated with Slide W were evacuated synchronously would suggest that the fluid flow event that resulted in the formation of these craters was a basin wide and potentially catastrophic event. A basin wide fluid flow event as envisaged by Hypothesis A would be expected to yield a greater geographic spread of craters than that which is observed in our study area. Hypothesis A might require Unit III of the Brygge Formation and the Kai Formation (Chapter 2) to form a seal which would prevent remobilisation of Unit II where domes containing Unit II would be buried by later sediments. In contrast to this, Naust W sediments prior to failure would present a very poor seal to allow upwards remobilisation of ooze. This is considered unlikely, as the Kai Formation exhibits polygonal faulting which is associated with fluid flow (e.g. Chapter 2, Berndt et al., 2003, Gay and Berndt, 2007, Hustoft et al., 2007). Alternatively it may be that the craters could only form up to a maximum burial depth in the subsurface, and that the cover of Naust W sediments over the uppermost surface incised by the craters was only thin enough where Unit II subcrops on or near this surface. Our results would support this latter suggestion, as we have shown that Crater G evacuates later sediments.

Hypothesis A would require further testing to ascertain how fluids would be trapped at depth, which formations could act as a seal, and how the ooze would move through the sediments above the Brygge Formation to the seabed. Vents could not be imaged

with the 2D seismic data used in this study, the presence of hydrothermal vents underneath craters could be tested with 3D prestack depth migrated seismic data.

4.6.3.2 Hypothesis B

Hypothesis B envisages that fluid migrating upwards from the lower levels of the basin becomes trapped between the prograding Naust Formation and the opal A/CT boundary, and that this trapping of fluid might generate overpressure and facilitate liquefaction of the Brygge Formation. Such a hypothesis would require further testing to understand whether the Naust Formation could act as a seal, whether fluid would move up dip and at what velocity it would do so in the Brygge Formation above the opal A/CT boundary, and whether sufficient overpressure could come about in the time between the emplacement of the Naust Formation and the failure of the Naust Formation as a slide. These questions are not considered further here, but could be the focus for further work. Answering these questions would most likely require advanced basin modelling to be performed to understand the history and rates of fluid migration from depth, as well as an advanced understanding of lateral and vertical permeability in the Brygge Formation and a better understanding of the sealing properties and relative vertical permeability of the Naust Formation.

A hypothesis such as Hypothesis B whereby craters are eroded in the basal shear surface of a slide would be expected to yield craters over the entirety of the basal shear plane of Slide W, with there being no necessary relationship to doming. Because the formation of the craters is restricted to where Unit II of the Brygge Formation subcrops on the basal shear surface of Slide W, it must be surmised that Unit II sediments are more prone to erosion by sliding than later sediments such as Unit III of the Brygge Formation and the Kai Formation. In particular, the close relationship observed between Craters A, B, C and D with the Havsule Dome would indicate that fluid sourced from beneath had a role in predisposing the craters to erosion by subsequent slides. This would be in agreement with Riis et al. (2005), who describe seismic amplitude anomalies interpreted to be gas effects adjacent to craters on the Havsule Dome which post dates the formation of craters, and would be consistent with the long term fluid flow described above further continuing into the late Pliocene

or early Pleistocene. Hypothesis B would require there to be at least two phases of crater formation, because our findings show that some craters are filled by Slide W and some by later slides.

Given the long term nature of fluid flow from depth in the region, it is easier with a hypothesis such as Hypothesis B to envisage two or more phases of crater formation. Fluid would continuously be lost to the seabed through the top of the Brygge Formation domes. As and when the domes are buried by clay sourced from the continental margin, fluid would be trapped between the opal A/CT boundary beneath and the Naust Formation above. When the Naust Formation fails in a slide the Brygge Formation is loaded, undergoes liquefaction, a process that might be facilitated by trapped fluid, and rises upwards due to its low density, before being transported downslope by the slide, in a manner similar to that envisaged by Riis et al. (2005). This process would have to occur over a long enough timescale for the ooze to be evacuated to the top of the slide efficiently to be then transported downslope.

A hypothesis such as Hypothesis B is supported by the observed erosive behaviour of later slides in the study area and elsewhere. Later slides such as the Storegga Slide carved out the giant Gloria Valley Trough and Solsikke Trough in the study area (Haflidason et al., 2004). Elsewhere it has been observed that large submarine slides can carve giant grooves 9 km long, and under 15 m deep (Gee et al., 2005) in their basal shear planes. Within our study area giant enclosed linear slots 30 km long, 4 km wide and 80 m deep have been observed on the basal shear planes of the Storegga Slide (Bull et al., 2009a). If slides are capable of carving out giant grooves and slots that are smaller than the craters described here and giant troughs that are considerably larger, it seems plausible that a slide could carve out the craters described here as well.

If Hypothesis B explains the formation of these craters, then these craters would be the only example we are aware of whereby material incised at the basal shear surface ascends upwards through the slide to the seabed.

4.7 Summary and Conclusions

(1) All of the craters described in this study were formed because of the removal of early Eocene to Oligocene biosiliceous ooze down to the depth of a fossilised Opal A/CT boundary, which is present in this unit in the Møre Basin. It is found that most of the craters are associated with doming that culminated in the Miocene. It is found that all of the craters are located on a regionally correlative seismic surface that is coincident with the basal shear plane of Slide W (Chapter 3), a slide located at the base of the Naust Formation which progrades into the basin burying the Brygge and Kai Formations beneath. Not all of the craters are filled by Slide W.

(2) All of the ooze mounds in the Møre Basin pinch out on the same regionally correlative surface, which is the top of Slide W. It is assumed that ooze mounds are emplaced at the time of crater formation, because the emplacement of mounds at any other time would require the ooze to be removed from the crater forming system. Thus all of the craters associated with ooze mounds formed at the same time.

(3) Geochemical evidence presented in the literature suggests that long term fluid flow from lower levels in the basin towards the seabed has been an active process from the early Eocene, exploiting hydrothermal vent complexes that are associated with the emplacement of sills in the late Palaeocene and early Eocene. The association of craters with subsurface doming where fluid sourced from lower levels in the basin may be lost to the seabed or be trapped under prograding sediments from the Norwegian margin would suggest a link with long term fluid flow.

(4) Two end member hypotheses are presented which might explain the formation of these craters. In one hypothesis an eruption of fluid flow from beneath mobilises ooze to the seabed at the foot of the continental slope where the ooze is emplaced as ooze mounds, causing slope failure because of undermining of the foot of the continental slope. In the other hypothesis the slide loads biosiliceous ooze causing it undergo liquefaction, a process that might be facilitated by continuous fluid flow sourced from the lower levels of the basin, causing the ooze to ascend through the slide due to its low density and be emplaced on top of the slide.

5 A THREE DIMENSIONAL DESCRIPTION OF CRATERS AND REMOBILISED SEDIMENT MOUNDS ON THE MID NORWAY MARGIN

5.1 Introduction

At the end of Chapter 4 two end member hypotheses were presented that might explain the formation of craters and remobilisation of the Brygge Formation from the craters. In one hypothesis, the flow of fluid from beneath remobilises the Brygge Formation upwards, potentially triggering Slide W (Hypothesis A, Fig. 4-6). In the other hypothesis, loading of the Brygge Formation by Slide W results in liquefaction of part of the Brygge Formation, which is emplaced on the top surface of Slide W (Hypothesis B, Fig. 4-7). Hypothesis B may be facilitated by fluid flow from beneath.

It still remains to be established whether Hypothesis A or Hypothesis B reflects the formation of Craters and remobilisation of Brygge Formation sediment. An improved understanding of the geometry of the craters should enable a better distinction to be made between these two hypotheses. In this chapter therefore use is made of 3D seismic reflection data and well data to describe the 3D geometry of Craters A, B, D, H and I; and Mounds A, BCF, D (not previously described), and GJ. The dimensions of these craters and mounds is summarised in Table 4-1 and Table 4-2 respectively in Chapter 4. The use of 3D seismic reflection data allows generation of time maps of key horizons, such as the basal surface of the craters, the base of the mounds and the top surface of the mounds. In addition, the use of horizontal slicing allows the mapping of the interior geometry of units of interest. Attribute maps are used here to gain an improved understanding of the slides that bury the craters in the subsurface and of the geometries and processes associated with the mounds and craters.

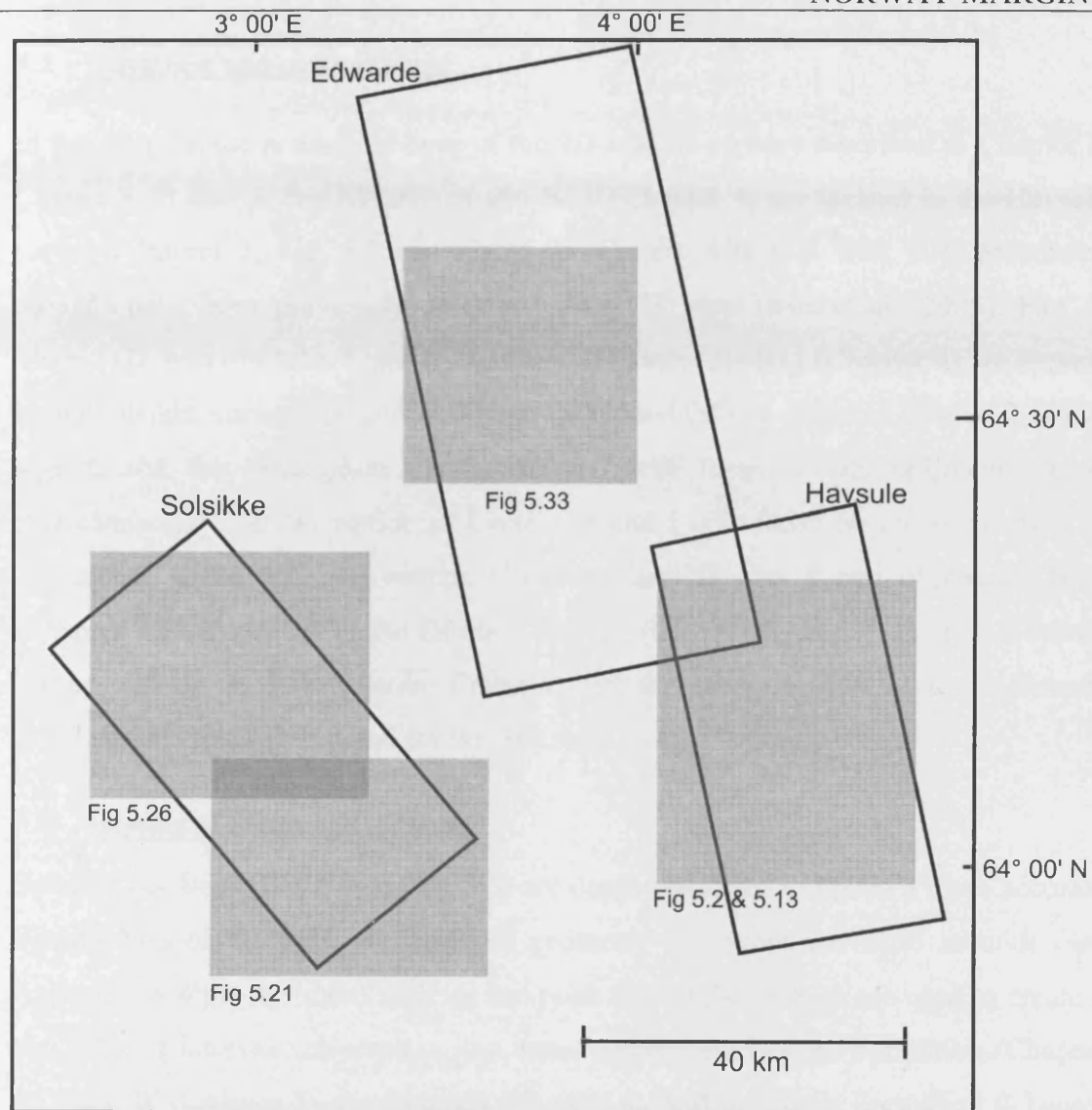


Fig. 5-1: Map showing location of surveys and subsequent figures.

5.2 Database and methodology

In this chapter, use is made of three of the 3D seismic surveys described in Chapter 2. Craters A, B and C, and Mounds A and BCF (Chapter 4) are located in the Havsule survey (Chapter 2, Fig. 5-1 and Fig. 5-2). Craters A and B with their associated mounds have been previously described using 3D data (Riis et al., 2005). Part of Mound GJ, part of Crater J, and the entirety of Craters H and I (Chapter 4) are located in the Solsikke survey (Chapter 2, Fig. 5-1). Mound GJ is penetrated by a well in this region, and the description of this mound will focus on its sedimentological characteristics. The description of Craters H and I will focus on the interaction of subsequent slides with the craters. Craters C and D, and a part of mound BCF (Chapter 4) are located in the Edvarde Survey (Chapter 2, Fig. 5-1). The Edvarde survey will be used to describe Crater D and the characteristics of the sediments evacuated at Crater D in detail for the first time.

5.3 Results of depth conversions

Selected key lines (Fig. 5-3 to Fig. 5-8) are depth converted to obtain a more accurate visualisation of the cross dimensional geometry of craters and ooze mounds (see Appendix A-4 for raw data). Pull up and push down relationships are used to create a hierarchy of interval velocities in key units, namely the Brygge Formation (Chapter 2), Slide W (Chapter 3), the Mounds (Chapter 4), and the Naust Formation (Chapter 2) that overlies Slide W. Because there is pull up in the Brygge Formation associated with the craters filled by Slide W (e.g. Fig. 5-3), it is deduced that the internal velocity of Slide W is greater than that of the Brygge Formation. Because there is push down in the Brygge Formation associated with the mounds above the craters (e.g. Fig. 5-3), it is deduced that the internal velocity of the mounds is less than that of Slide W and the overlying sediments that bury the mounds. Because density normally increases with depth, and because velocity is proportional to density (Gardner et al., 1974), the overlying Naust Formation above Slide W is considered to have a slower velocity than Slide W. From this it is deduced that the unit with the fastest velocity is Slide W, with the other units having slower velocities. A value for the interval velocity of the overburden is obtained by a simple calculation performed on well 6403/10-U1 (Fig. 5-21) drilled in the Solsikke survey, using the time picks and the depth of those picks

to compute a velocity. Iteration is then performed across all of the selected lines, to minimise pull down and push up effects as far as possible, and the resulting values are checked against known internal velocities obtained by coring, against velocities calculated from well 6403/10-U1. The results are summarised in Table 5-1.

5.4 Havsule Survey

5.4.1 Description of craters A and B

In the Havsule Survey are found the Craters named as Crater A and Crater B in Chapter 4 (Fig. 5-2). Craters A and B are located c. 5 km west of the crest of the Helland Hansen Arch (Chapter 4, Fig. 5.6 - Fig. 5.8, Riis et al., 2005). They are enclosed features, forming a contact between the Brygge Formation at the base of the crater and Slide W within the Naust Formation which fills the craters (Chapter 4, Fig. 5-3 to Fig. 5-8). The edges of the craters are characterised by internal reflections of the Brygge Formation being truncated against the internal reflections of Slide W within the Naust formation (Fig. 5-3 to Fig. 5-8). Craters A and B are features mapped on the basal shear surface of Slide W (Fig. 5-3 to Fig. 5-8), described in Chapter 3.

Crater B was previously mapped using seven 2D lines in four different orientations which revealed two incisions in its western sidewall (Chapter 4). Here mapping with 3D seismic reflection data that offers a higher resolution demonstrates that there are five incisions (Fig. 5-2), details that could not be mapped with 2D seismic reflection data because of the spacing of the lines. The geometry of these incisions is discussed further below.

3D seismic reflection data are used to accurately calculate the volume of sediments removed from Crater A. The crater is split into cells 500 m by 500 m, and an average depth of the crater is calculated in each cell. The obtained values are depth converted, using a velocity of 1793 m/s (the velocity of the Brygge Formation, see Table 5-1 above), and a total volume for Crater A of $6.5 \pm 1.4 \text{ km}^3$ is obtained. This is significantly lower than the volume obtained for this crater in Chapter 4 of 14 km^3 (Table 4-1 in Chapter 4). In Chapter 4 Crater A was modelled as a rectangular crater.

In Chapter 4 the average time depth of the crater was overestimated by 50 ms, and a velocity of 2000 m/s was assumed for depth conversion.

5.4.1.1 Sidewall of Craters A and B

The sidewalls of Craters A and B are defined by the truncation of Brygge Formation sediments against Slide W within the Naust Formation (e.g. (i) on Fig. 5-3). The dips of the sidewalls are measured at 500 m intervals in the orientation of maximum dip, and the results are summarised on Table 5-2. The table shows that the average dip of the eastern and western sidewalls of Crater A, and the eastern sidewall of Crater B range between 28.4° and 29.7°. The western sidewall of Crater A is more complex and considered separately below. The average dips of the northern and southern sidewalls of Craters A and B range between 29.7° and 41.2°. While there is some overlap in uncertainty (see Table 5-2) these results indicate that on average the northern and southern sidewalls of Craters A and B are steeper than the eastern and western sidewalls of Crater A and the eastern sidewall of Crater B. The direction of movement of Slide W is from east to west in this area (Chapter 3). This means that sidewalls of Craters A and B which dip towards or away from the headwall of Slide W have steeper dips than the sidewalls of Craters A and B which dip towards the lateral margins of Slide W, demonstrating a relationship between the flow direction of Slide W and crater morphology.

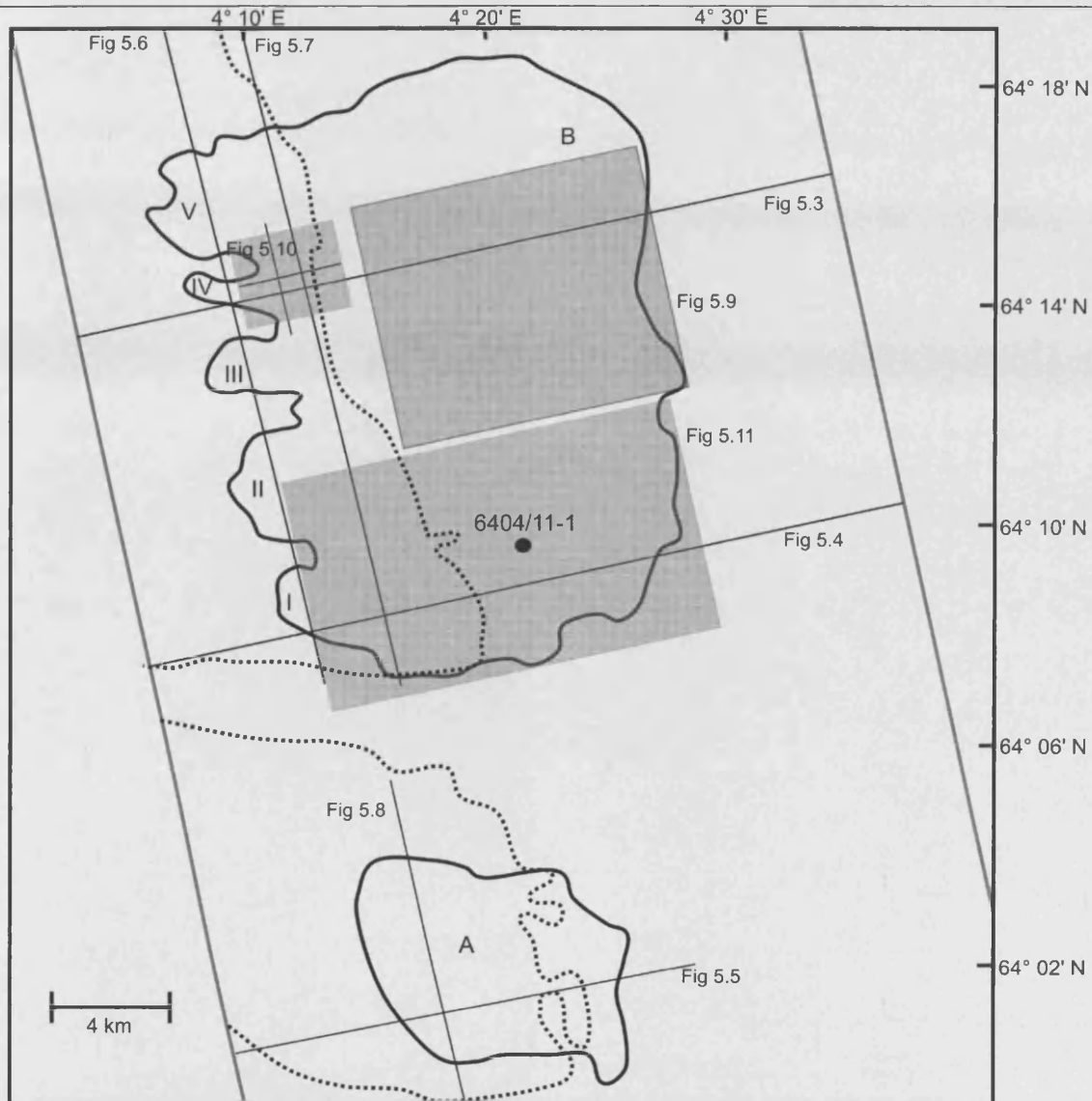


Fig. 5-2: A map of Crater A, Crater B, Mound A and the portion of Mound BCF associated with Crater B in the Havsule survey highlighting the planforms of these features and the locations of figures pertaining to Craters A and B. The location of the sidewalls of Craters A and B are delineated by a solid line, and the location of the edges of Mound A and the portion of Mound BCF associated with Crater B are delineated by a dotted line.

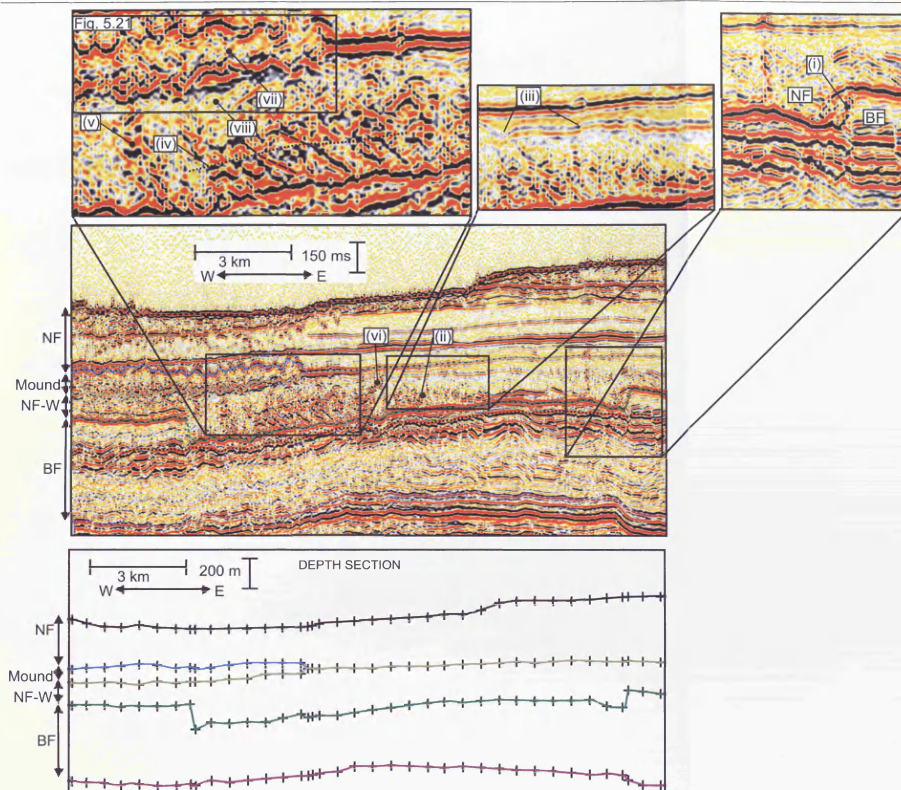


Fig. 5-3: A crossline in time through Crater B and the portion of Mound BCF associated with Crater B. A smoothed depth section is also displayed, with data points indicated. See Fig. 5-2 or Fig. 5-13 for location and a planform map. NF: Naust Formation, NF-W: Naust Formation W, BF: Brygge Formation. The opal A/CT boundary is indicated by a dotted line. (i) Crater sidewalls are defined by truncation of the Brygge Formation against the Naust Formation. (ii) Eastward dipping reflections within the fill of Crater B. (iii) Thrust offset of continuous reflection above eastward dipping planes. (iv) Interpreted line, showing the level of a polarity change on eastward dipping planes in the fill of Crater D. Selected planes are highlighted. (v) Possible vertical amplitude anomaly trail. (vi) Westward dipping anomaly trail. (vii) Westward dipping plane in internal architecture of ooze mound. (viii) Possible extension of planes within ooze mound into Slide W.

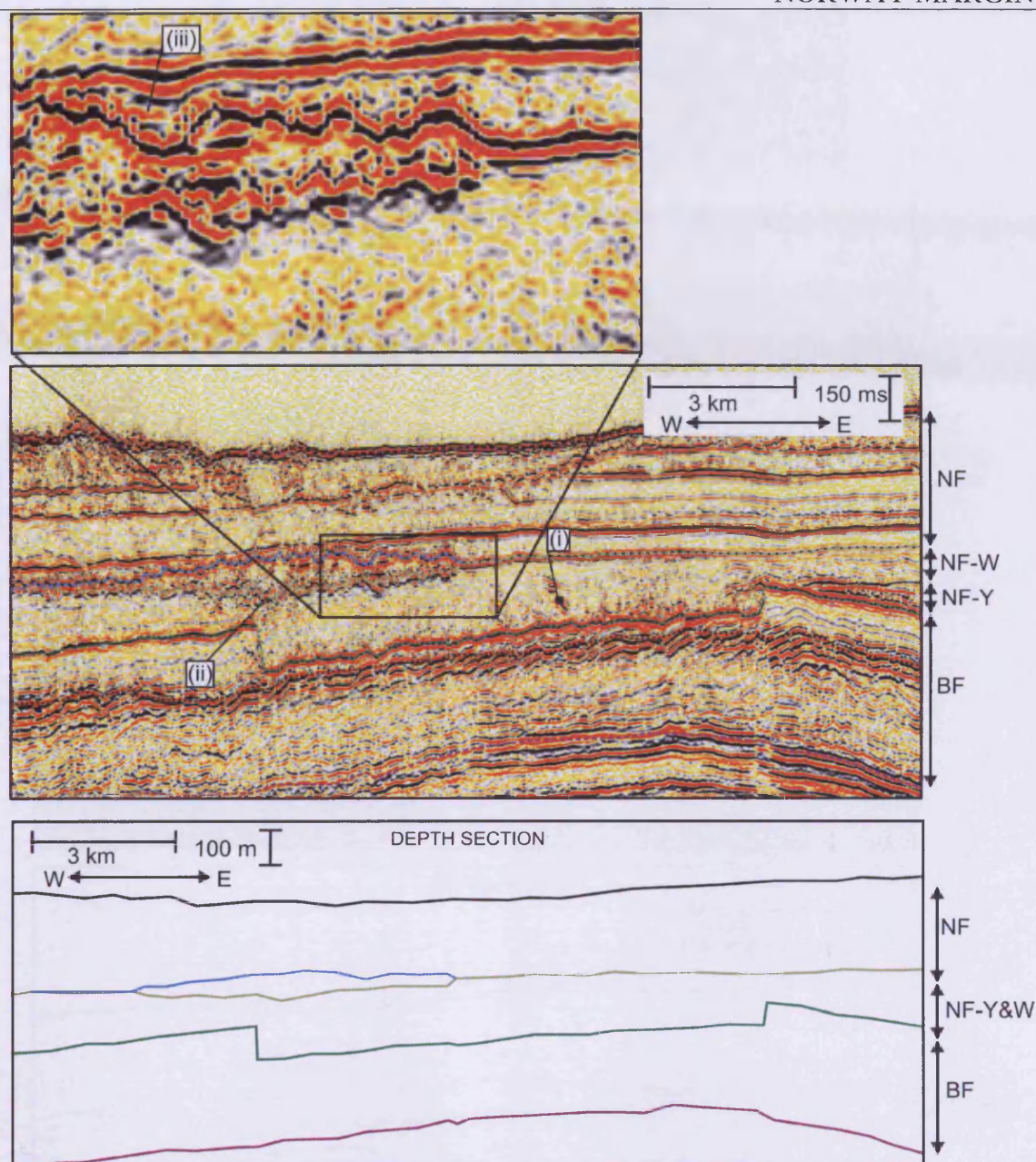


Fig. 5-4: A crossline in time through Crater B and the portion of Mound BCF associated with Crater B. A smoothed depth section is also displayed. See Fig. 5-2 or Fig. 5-13 for location and planform maps. NF: Naust Formation, NF-Y: Naust Formation Y, NF-W: Naust Formation W, BF: Brygge Formation. The opal A/CT boundary is indicated by a dotted line. (i) A stacked amplitude anomaly following an eastward dipping plane. (ii) Depression in the top surface of Slide W to the west of the crater. The smoothed depth section shows this to be real, and not a velocity artefact. (iii) Later sediments onlap the top of the mound.

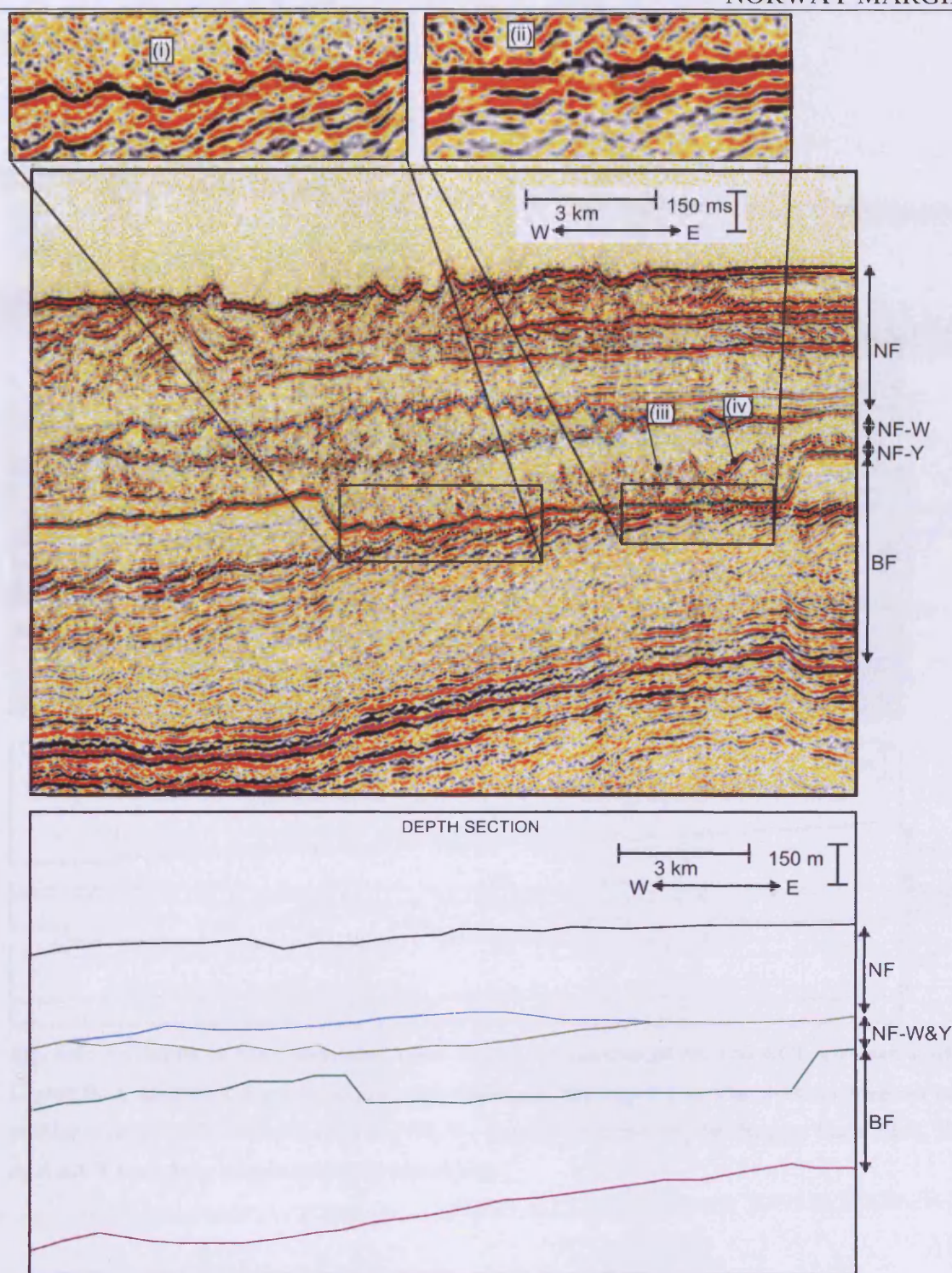


Fig. 5-5: A crossline in time through Crater A and Mound A. A smoothed depth section is also displayed. See Fig. 5-2 or Fig. 5-13 for location and planform maps. NF: Naust Formation, NF-Y: Naust Formation Y, NF-W: Naust Formation W, BF: Brygge Formation. The opal A/CT boundary is indicated by a dotted line. (i) Base of the crater is concordant with stratigraphy underneath the crater. (ii) Base of the crater is smoother than the stratigraphy underneath the crater. (iii) Eastward dipping planes in the fill of Crater A. (iv) The top surface of Slide y, dipping inwards into Crater A.

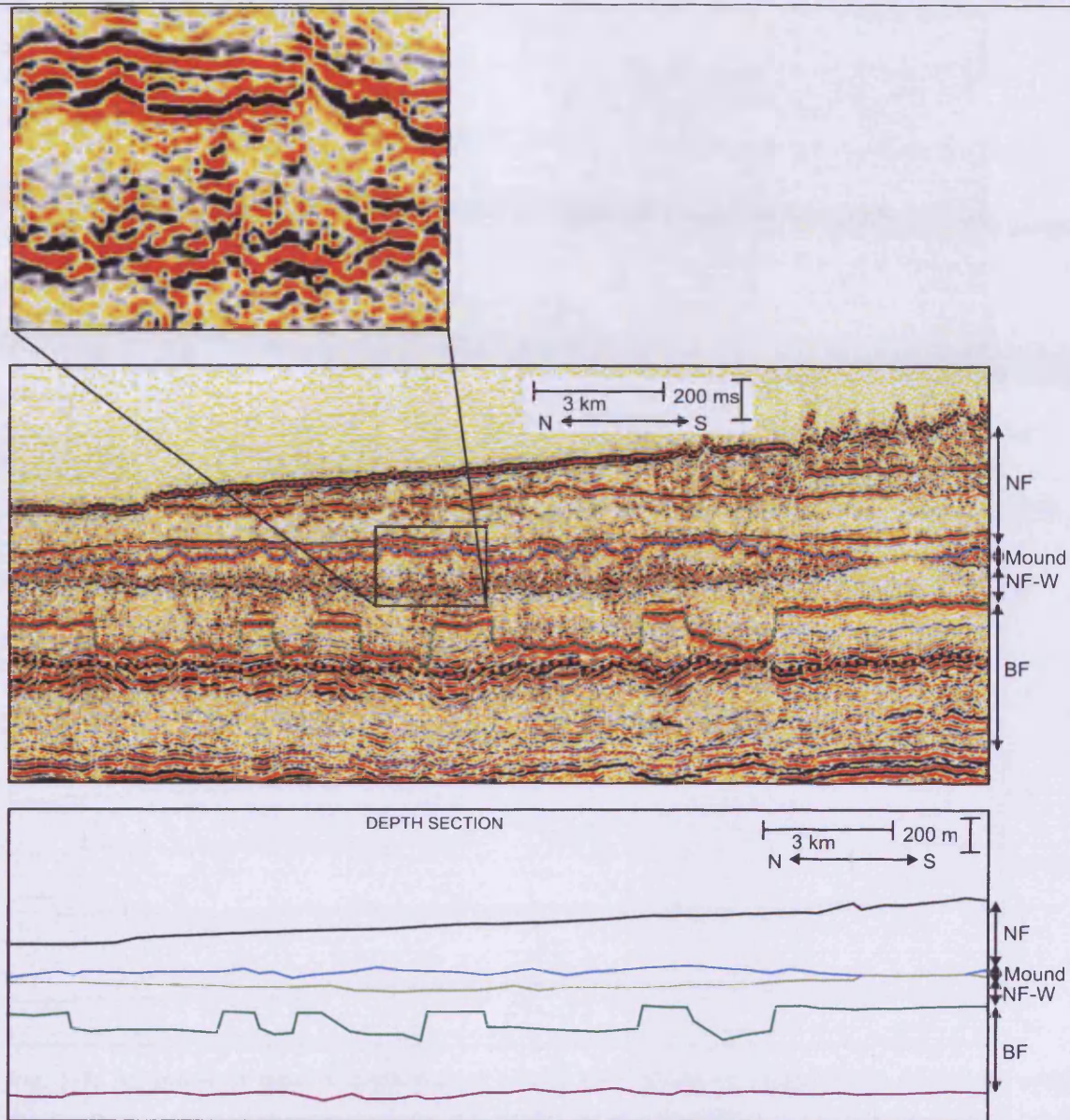


Fig. 5-6: An inline in time through Crater B and the portion of Mound BCF associated with Crater B. A smoothed depth section is also displayed. See Fig. 5-2 or Fig. 5-13 for location and planform maps. NF: Naust Formation, NF-W: Naust Formation W, BF: Brygge Formation. The opal A/CT boundary is indicated by a dotted line.

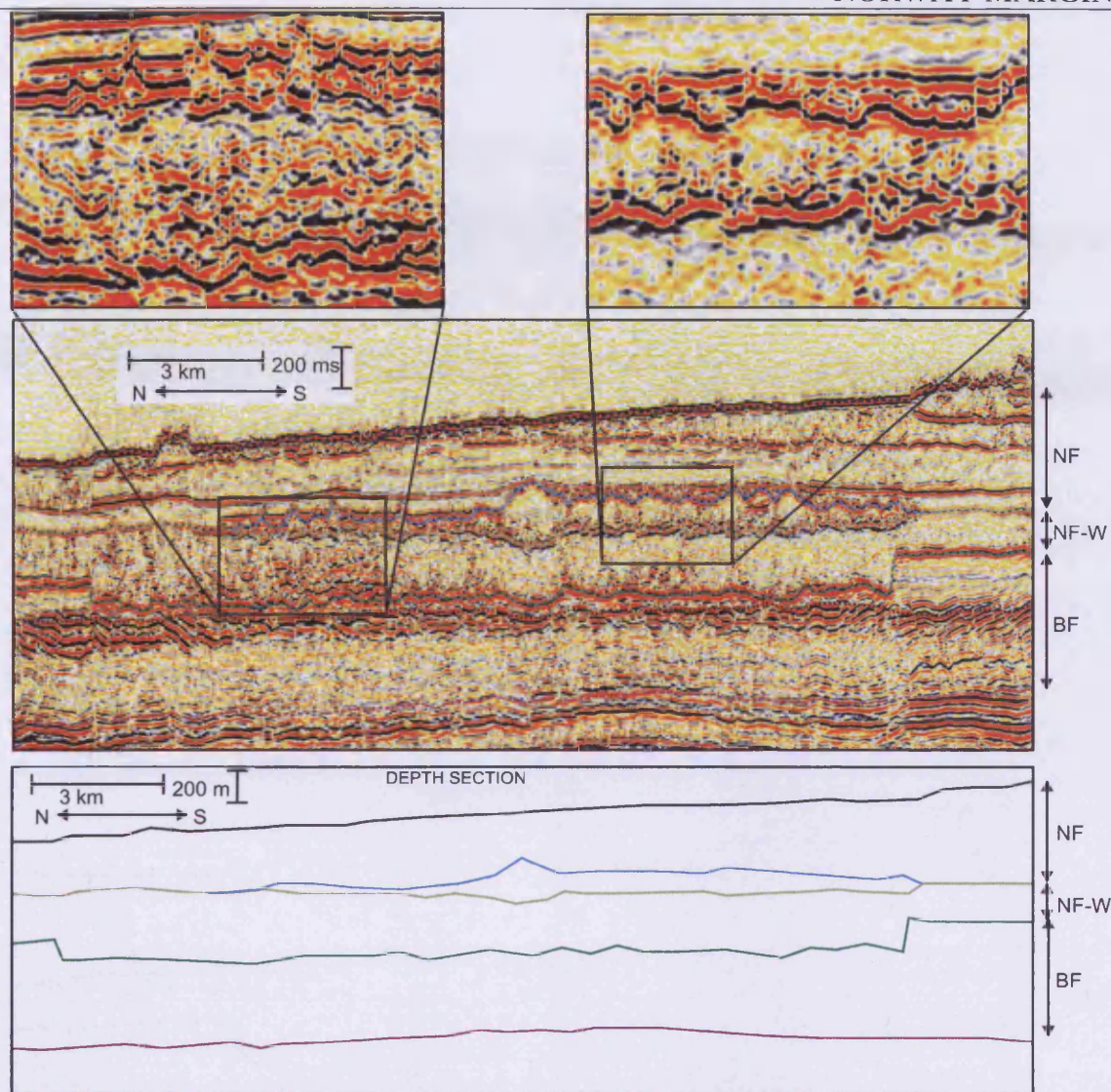


Fig. 5-7: An inline in time through Crater B and the portion of Mound BCF associated with Crater B. A smoothed depth section is also displayed. See Fig. 5-2 or Fig. 5-13 for location and planform maps. NF: Naust Formation, NF-W: Naust Formation W, BF: Brygge Formation. The opal A/CT boundary is indicated by a dotted line.

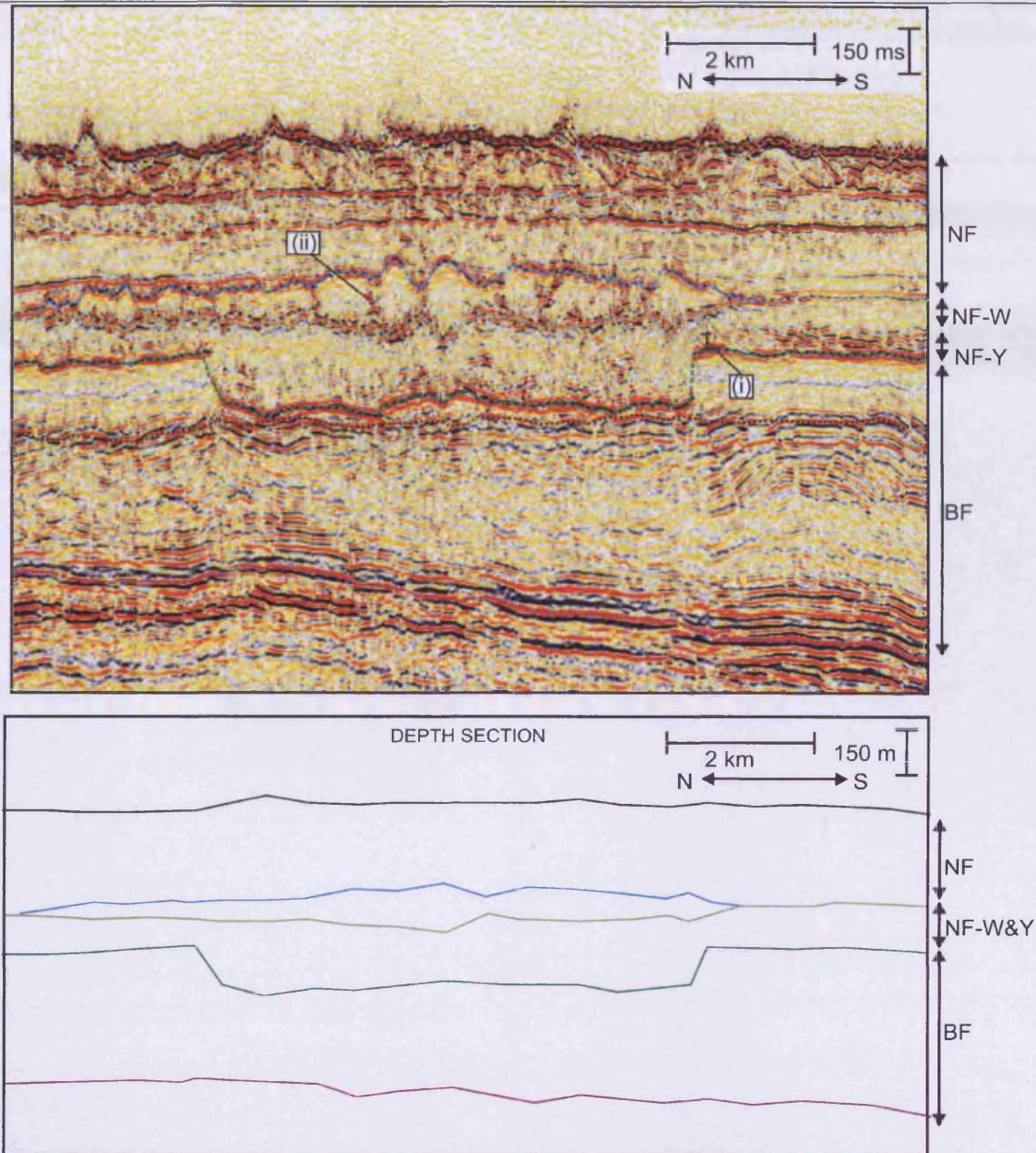


Fig. 5-8: An inline in time through Crater A and Mound A. A smoothed depth section is also displayed. See Fig. 5-2 or Fig. 5-13 for location and planform maps. NF: Naust Formation, NF-Y: Naust Formation Y, NF-W: Naust Formation W, BF: Brygge Formation. The opal A/CT boundary is indicated by a dotted line. (i) c. 25 m of Slide Y truncated at the southern sidewall of Crater A. (ii) Vertical amplitude anomaly trails in mound.

| <u>Unit</u> | <u>Velocity (well</u> <u>6403/10-U1)</u> | <u>Velocity (Iteration,</u> <u>±100 m/s)</u> |
|-------------------------------|---|---|
| Naust Formation (above Mound) | 1723 m/s | N/A |
| Mound | 1708 m/s | 1614 m/s |
| Slide W | | 2116 m/s |
| Brygge Formation | 1715 m/s | 1793 m/s |

Table 5-1: Internal velocity values. Values utilised for depth conversions in this chapter are highlighted in bold.

As indicated above, the western sidewall of Crater B is not as smooth as the other sidewalls of Craters A and B, but consists of five U-shaped incisions which are incised into the Brygge Formation bounded by four tongues of Brygge Formation sediment which protrude into Crater B and the eastern and western sidewalls of Crater B (Fig. 5-2). These incisions are labelled I, II, III, IV, and V from south to north (Fig. 5-2). The average dip of the northern and southern sidewalls of these incisions is 33.3° , with a standard deviation from the mean of 13.2° (53 measurements were performed, see Table A4- 27, Table A4- 28, Table A4- 30, Table A4- 31, Table A4- 33, Table A4- 34, Table A4- 36, Table A4- 37, Table A4- 39 and Table A4- 40 in Appendix A4 for data), whereas the average dip of the western sidewalls of the incisions is 25.4° , with a standard deviation from the mean of 7.1° (20 measurements were performed, see Table A4- 26, Table A4- 29, Table A4- 32, Table A4- 35 and Table A4- 42 in Appendix A4 for data). Thus the morphology of these incisions is also related to the flow direction of Slide W.

5.4.1.2 Basal Surface of Craters A and B

The basal surfaces of Craters A and B are acoustically soft reflections with high reflection amplitude, and an irregular topography (Fig. 5-3 to Fig. 5-8). The basal shear surface of Slide W (Chapter 3) coincides with the basal surface of the crater (Fig. 5-3 to Fig. 5-8). The trace of polygonal faulting in the underlying Brygge Formation (Chapter 2, Berndt et al., 2003, Gay and Berndt, 2007, Hustoft et al., 2007, Stuevold et al., 2003) is partially outlined on a dip map of the basal surface of Crater B (Fig. 5-9). The cross sections through Craters A and B show that the basal surface can be concordant with the stratigraphy beneath (e.g. (i) on Fig. 5-5), although there are areas where the basal shear surface is smoother than the stratigraphy beneath (e.g. (ii) on Fig. 5-5). The basal surface of Craters A and B is subparallel to a regional opal A/CT boundary, but is only coincident with this boundary over 0 - 10 % of the basal surface of the craters.

| <u>Sidewall</u> | <u>Number of</u> <u>measurements</u> | <u>Mean dip</u> | <u>Standard</u> <u>deviation from</u> <u>mean</u> |
|--------------------|---|-----------------|---|
| Crater A, eastern | 21 | 28.5° | 6.5° |
| Crater A, western | 21 | 29.7° | 6.2° |
| Crater A, northern | 17 | 39.0° | 9.6° |
| Crater A, southern | 16 | 33.8° | 15.7° |
| Crater B, eastern | 52 | 28.4° | 6.6° |
| Crater B, northern | 29 | 29.7° | 12.0° |
| Crater B, southern | 25 | 41.2° | 14.4° |

Table 5-2: Measurements of the dip of the sidewalls of Craters A and B. The western sidewall of Crater B is complex is considered separately below. See Table A4- 19 to Table A4- 25 in Appendix A4 for data used to compile these average dips.

Other features of interest on the basal surface of Crater B are small rises on the basal surface of Crater B with a relief of 30 m, which are elongate in an east to west orientation, and which have a shallowly dipping eastern edge of 1° and a steeply dipping western edge of 45° (Fig. 5-10). These features display a geometry with Slide W which is reminiscent of the geometry of Roche Moutonnées underneath glaciers, with a shallowly dipping slope dipping towards the headwall of the glacier being abraded, and a steeper slope dipping towards the toe of the glacier being plucked (Sugden and John, 1976). Here the features mapped have a shallowly dipping slope which dips towards the headwall of Slide W, and a steeply dipping slope dipping towards the toe of Slide W. It is considered that the shallowly dipping slope of this feature facing the headwall of Slide W is formed in the subsurface by abrasion, a similar mechanism to that which forms Roche Moutonnées (Sugden et al., 1992, Sugden and John, 1976). The process which forms the downslope of this feature may be different, because it is unlikely that the conditions for freezing of fluids in cracks would exist during incision of the craters (c.f. Sugden and John, 1976)

A small crater like depression is imaged on the basal surface of the crater, located midway along the eastern sidewall of Crater B (Fig. 5-9). This mini-crater is approximately square, with two embayments in its western sidewall, and is 2 km in diameter and 50 m in depth. The eastern sidewall of this mini crater has a mean dip of 29.2° (5 measurements made, standard deviation from mean 6.6° , see Table A4- 41 in Appendix A-4 for data), the western sidewall has a mean dip of 14.4° (5 measurements made, standard deviation from mean 7.1° , see Table A4- 42 in Appendix A-4 for data), the northern sidewall has a mean dip of 24.6° (4 measurements made, standard deviation from mean 2.9° , see Table A4- 43 in Appendix A-4 for data), and the southern sidewall has a mean dip of 23.9° (5 measurements made, standard deviation from mean 9.6° , see Table A4- 44 in Appendix A-4 for data). Thus, on average and as above, the eastern and western sidewalls have a lower mean dip than the northern and southern sidewalls, indicating that like Crater A and Crater B there is a relationship between the morphology of the mini-crater and the flow direction of Slide W.

Lineations around 1 km in length striking east to west are imaged on the basal surface of Crater B (Fig. 5-9), and which are similar to those described on the basal shear plane of Slide W in Chapter 3. The lineations on the basal surface of Craters A and B could be interpreted as the trace of polygonal faulting in the Brygge Formation beneath the craters. However it is not considered likely that the lineations on the basal surfaces of Craters A and B are the trace of polygonal faulting, because the lineations are considerably shorter than the traces of faulting described above (Fig. 5-9). Instead, the lineations on the basal surface of Crater B are interpreted to be related to translation of Slide W across the basal surface of the craters, being similar to scour marks that have been imaged on the basal shear planes of Slide W (Chapter 3). The scour marks described here are considerably shorter than those observed elsewhere in the literature (Gee et al., 2005), however this might reflect the minimal translation distance of Slide W (Chapter 3).

5.4.1.3 Internal fill of Craters A and B

Craters A and B are filled by the Slide W deposits. Well 6404/11-1 drilled in the centre of Crater B (Fig. 5-2 and Fig. 5-13) shows that Slide W in this region is composed of a grey mudstone sequence with occasional traces of sandstone and lithic gravel fragments.

The internal fill of Craters A and B is characterised for the most part by highly disrupted discontinuous reflections with low reflection amplitude being cross cut over c. 60 % of the area of the crater by a series of eastward dipping planar reflections of variable reflection amplitude within the slide body (Fig. 5-3 - Fig. 5-5). The eastward dipping planar features exhibit higher reflection amplitude close to the basal surface of Craters A and B and lower reflection amplitude close to the top surface of Slide W (Fig. 5-3 - Fig. 5-5).

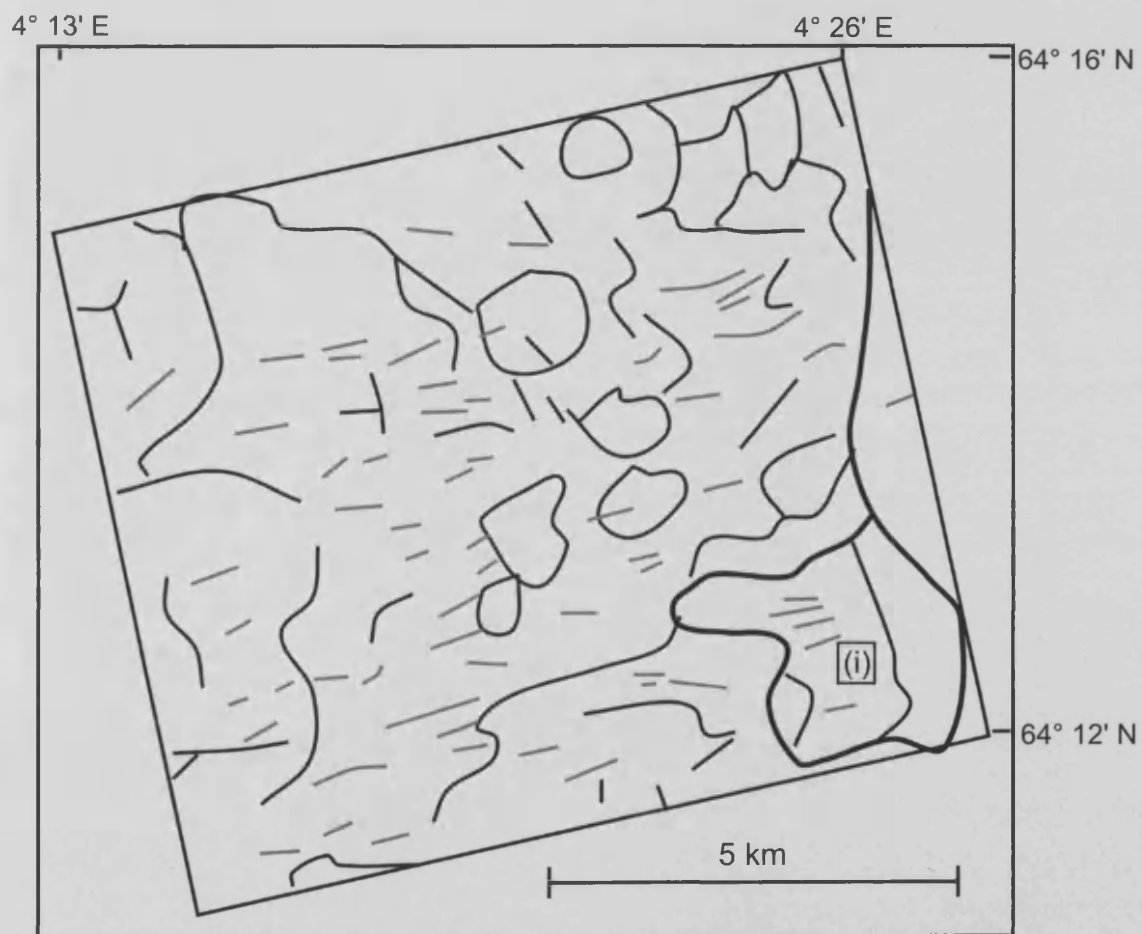
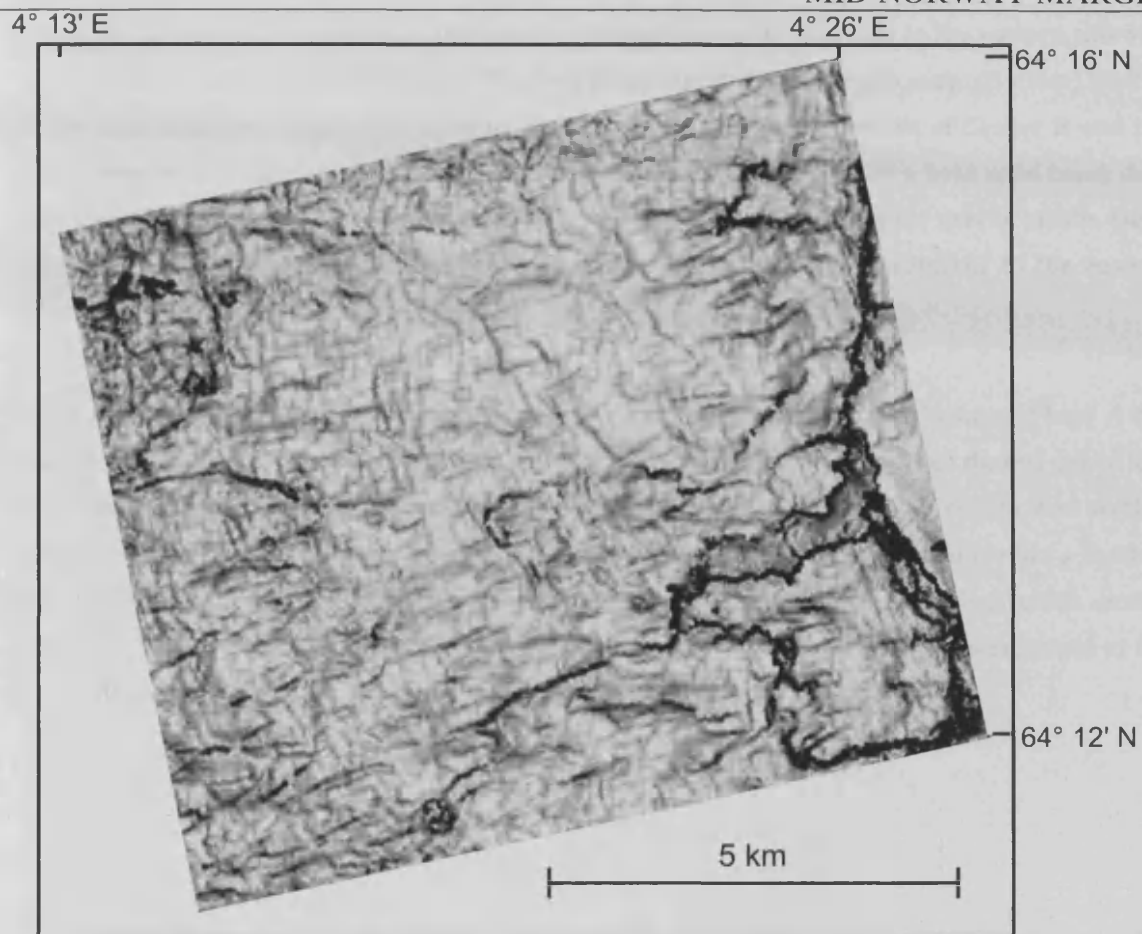
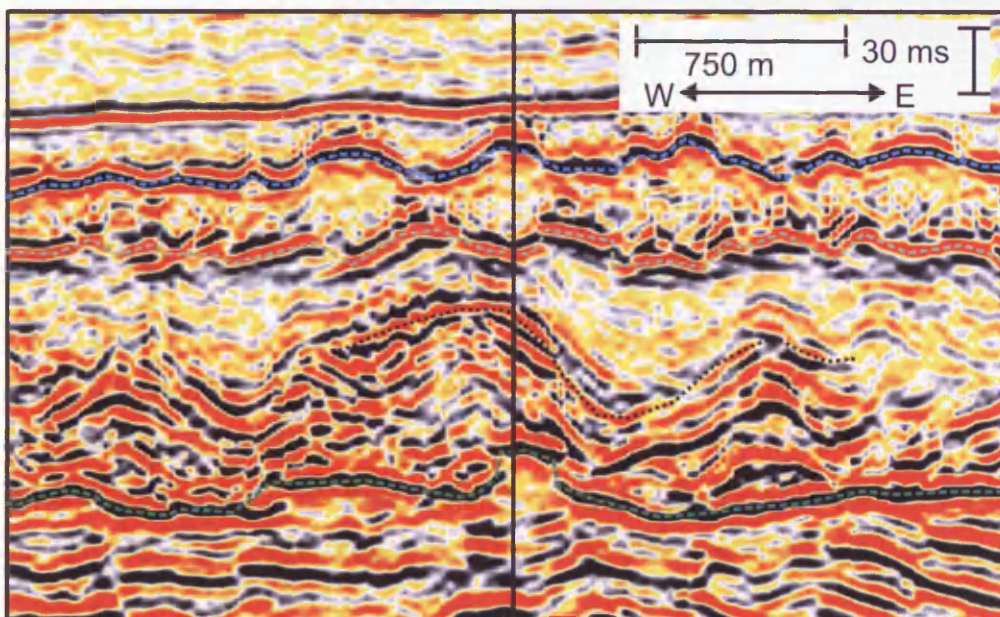
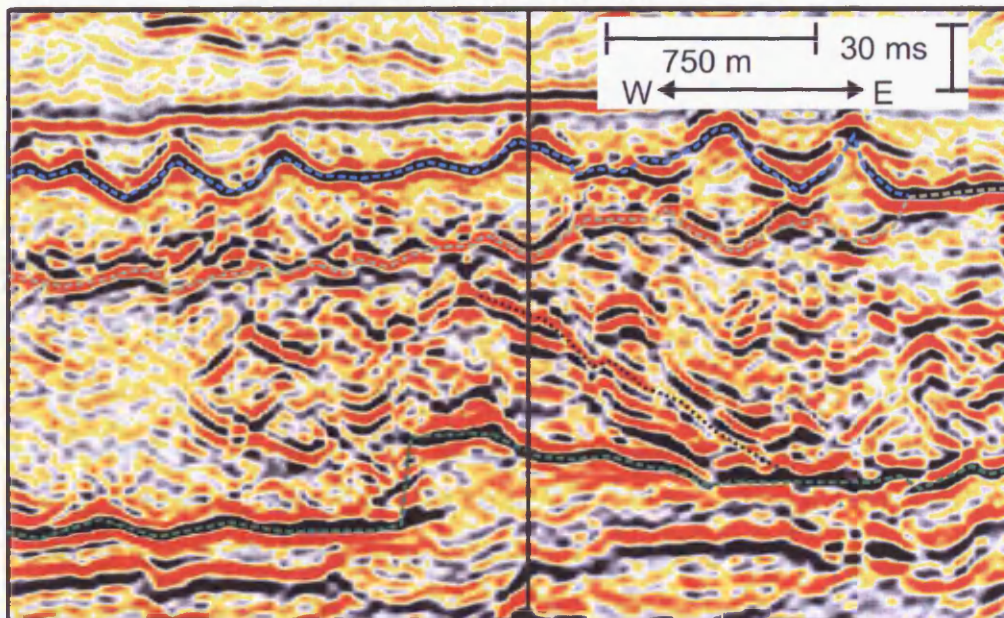
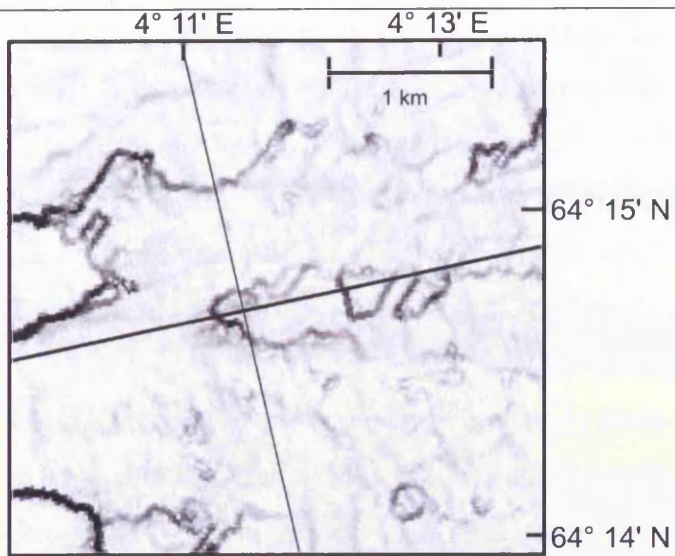


Fig. 5-9: A dip map of a portion of the basal surface of Crater B, adjacent to the eastern sidewall of the crater. For an exact location, see Fig. 5-2. (Top) Non-interpreted dip map. (Bottom) Sketch of dip map displayed above, highlighting important features. The sidewalls of Crater B and the mini crater located adjacent to the sidewall of Crater B are highlighted by a bold solid black line. The trace of polygonal faulting is delineated by a fine black line, and scour marks on the basal surface of crater B are highlighted by fine grey lines. (i) Mini crater adjacent to the eastern sidewall of Crater B.

Fig. 5-10: An irregularity on the basal surface of Crater B. See Fig. 5-2 for location. (Top) A dip map of a portion of the basal surface of Crater B highlighting the feature. The dashed green line represents the base of the crater and the top of the irregularity. (Middle) An east to west section across the feature. See (Top) for location. Note that the eastern slope of the feature has a shallow dip and that the western slope of the feature has a steep dip. (Bottom) A north to south section across the feature. See (Top) for location. Note that both the northern and southern slopes of the feature have a steep dip.



Horizontal coherency slices (Brown, 2004) (Chapters 2 and 3) through Slide W within Crater B demonstrate that the internal architecture of the slide consists of a series of curving lineations spaced at intervals of 200 m which vary in strike between North to South and North East to South West (Fig. 5-11). These are very clearly exhibited in the northern area of Crater B, but are much less so in the southern area of Crater B. These lineations are correlated with the eastward dipping planes described above.

Given that these planes strike predominantly from north to south, east to west profiles displayed in Fig. 5-3 and Fig. 5-4 are used to measure the average dip of these planes. A total of 32 measurements are made, and it is found that the average dip of these planes is 11.2° , with a standard deviation from the mean of 2.1°

These eastward dipping planes in Craters A and B offset reflections in a manner that would be consistent with thrust faulting (e.g. (iii) on Fig. 5-3), and are reminiscent of the closely spaced thrust faulting at the northern edge of Slide W described in Chapter 3 above (Fig. 5-12). The geometry of faults is also in some ways reminiscent of thrust faulting found at the toes of frontally confined slides (e.g. Frey-Martinez et al., 2006). The thrust faults exhibited at the northern edge of Slide W were spaced at intervals of approximately 250 m and exhibited a curving geometry, comparing with a spacing of 200 m observed within Slide W in the fill of Crater B (Fig. 5-11), whereas Frey-Martinez et al. (2006) demonstrates thrust faulting with a spacing of c. 1000 m at the toe of a slide deposit. The eastward dipping planes within Slide W in the internal fill of Craters A and B are therefore interpreted as closely spaced thrust faults, which would indicate that Craters A and B are located in the zone of accumulation of Slide W (c.f. Frey-Martinez et al., 2006). This interpretation is further supported by the thickening of Slide W within Craters A and B (Fig. 5-3 - Fig. 5-5). The displacement of the thrust faults is of the order of 10 m (e.g. (iii) on Fig. 5-3). The dip of these thrust faults is unusually low.

The variable reflection amplitude exhibited by the eastward dipping thrust faults could be because of gas exploiting the fault planes as a path for fluid flow (see Løseth et al. (2009) for amplitude anomalies associated with gas escape pipes), or alternatively may be because of remnant Brygge Formation ooze within Slide W. Polarity changes

are observed within the fault planes imaged within Slide W (e.g. (iv) on Fig. 5-3). These are often associated with accumulations of hydrocarbon gas (e.g. Brown, 2004), therefore fault planes exhibiting high reflection amplitude may contain hydrocarbon gas.

The internal fill of Craters A and B is also cross cut by steeply dipping or vertical amplitude anomaly trails, which link the basal surfaces of Craters A and B with sediment remobilisation mounds which overlie the craters (e.g. (v) on Fig. 5-3, Chapter 4, see below for a further discussion of sediment remobilisation mounds). These features are reminiscent of gas charging adjacent to gas escape conduits described by Løseth et al. (2009), and are therefore interpreted as such. It is however acknowledged that the evidence for these is weak.

Some of these potential gas escape conduits cross cut the trend of eastward dipping thrust faults and dip westwards (e.g. (vi) on Fig. 5-3). Others partially exploit thrust faulting that has developed within the craters (e.g. (v) on Fig. 5-3). One potential gas escape conduit is conically shaped (e.g. Fig. 5-3) and developed within one of the incisions in the western sidewall of Crater A described above. These possible gas escape conduits therefore developed subsequent to the development of thrust faults within the crater and formed subsequent to the development of incisions on the western sidewall of Crater A, and probably formed as a result of continuing fluid flow from depth to the present after crater formation (e.g. Chapter 4 and references within).



Fig. 5-11: (Top) A coherency slice, highlighting the internal geometry of the southern portion of Crater B. See Fig. 5-2 for location. (Bottom) A sketch, highlighting important features of the coherency slice in (Top). The sidewalls of Crater B are highlighted by a bold solid black line, lineations within the fill of Crater B are highlighted by fine black lines and the edge of Mound A is highlighted by a bold dotted line.

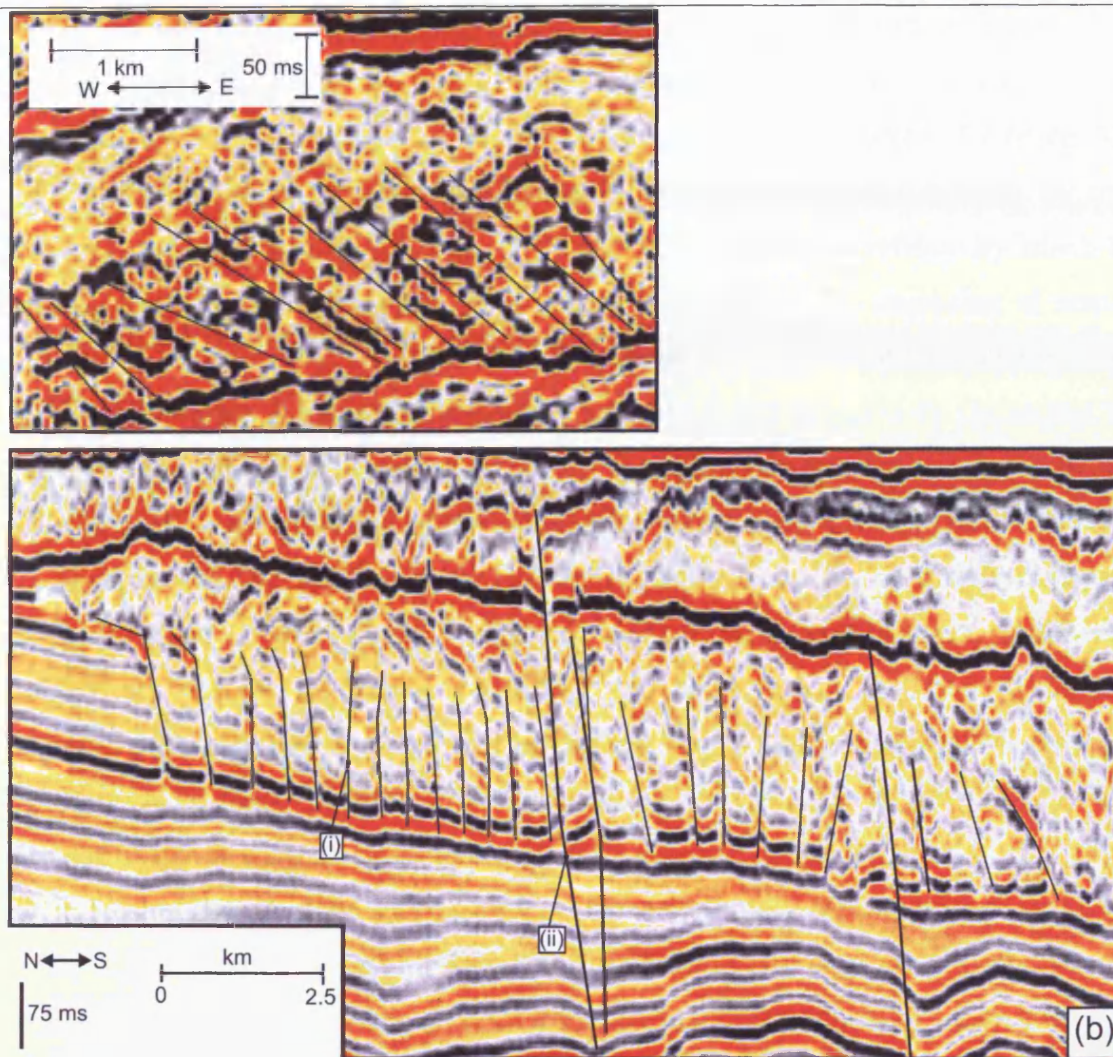


Fig. 5-12: (Top) Thrust faulting within the internal fill of Crater B. (Bottom) Thrust faulting within Slide W at the northern sidewall of Slide W (see Fig. 3-9b for more details).

Within Crater A a high amplitude hard reflection is observed dipping westwards into the fill of the Crater (e.g. (iv) on Fig. 5-5). This reflection is the top surface of Slide Y, which has been remobilised by Slide W in the region of this crater (c.f. Chapter 3). The sediments which are bounded above by this boundary, and beneath by the sidewall and basal surface of Crater A (Fig. 5-5), show internal reflectivity which is similar to that exhibited by the other sediments in the crater, consisting of semi-continuous low amplitude reflections. 25 m depth of Slide Y are truncated against Slide W sediments at the southern sidewall of Crater A ((i) on Fig. 5-8). On an east to west cross section across Crater A (Fig. 5-5), it is estimated that the area in the crater fill bounded by the reflection of the top of Slide Y, the sidewalls of Crater A and the basal surface of Crater A is $150\,000\text{ m}^2$. The reflection of the top of Slide Y in Crater A shows good continuity (Fig. 5-5), and therefore the possibility that sediments located between the top surface of Slide Y, the basal surface of Crater A and the sidewall of Crater A were mixed into the sediments of Slide Y from Slide W above is not considered likely. If prior to crater formation, the thickness of Slide Y over the area of Crater A were 25 m, as indicated at the southern edge of Crater A (Fig. 5-8), then if a similar area of the section were occupied by Slide Y prior to crater formation, Slide Y would bury a length of 6 km from the eastern edge of Crater A, and would almost entirely bury the crater, save for a small area above the west of where Crater A is now located.

5.4.1.4 Top surface of fill of Craters A and B

The top surface of Slide W in the region of Craters A and B is flat in the eastern portion of the craters, however westwards of the craters a topographic depression is mapped (e.g. (ii) on Fig. 5-4). This depression is imaged on seismic cross sections (Fig. 5-3 to Fig. 5-8). Depth conversions demonstrate that this depression is real, and that it is not solely a velocity artefact associated with the mound that fills the depression (Fig. 5-3 to Fig. 5-8). Depth conversions show that westwards of Crater B the thickness of Slide W is 100 - 150 m, whereas northwards, southwards and eastwards of Crater B, the thickness of Slide W is 150 - 200 m (Fig. 5-3 to Fig. 5-8).

The topographic depression mapped on the top surface of Slide W westwards of Craters A and B might come about because the kinetic energy of Slide W is

insufficient to translate material upwards over the lip of the crater. Kinetic energy within the slide must be converted to potential energy to move the slide upwards over the lip of the crater. If the kinetic energy of the slide is smaller than the potential energy the slide must attain to be translated upwards over the lip of the crater, the slide will stop within the crater, and material will accumulate inside the crater and deplete westwards of the crater.

5.4.2 Description of mounds

Craters A and B are associated with mounds, which are located on the top surface of Slide W (Chapter 4), a little westwards and downslope of the craters (Chapter 4, Riis et al. (2005), Fig. 5-13). The Mound associated with Crater A is named Mound A (Chapter 4). The mound associated with Crater B is part of a larger mound sourced from Craters B, C and F, and is therefore named Mound BCF (Chapter 4). Here Mound A and the portion of mound BCF located adjacent to and above Crater B are described.

3D seismic reflection data are used to accurately calculate the volume of Mound A. The mound is split into cells 500 m by 500 m and an average time depth is obtained in each cell. These are depth converted, using a velocity of 1614 m/s (the velocity for ooze mounds, see Table 5-1 above). A total volume of $9.0 \pm 2.8 \text{ km}^3$ is obtained. Part of Mound A is not covered by the 3D seismic reflection data, it is estimated that the portion of the mound not imaged by the data has a volume of $1 \pm 0.3 \text{ km}^3$. This yields a total volume of $10 \pm 3.1 \text{ km}^3$, which is significantly lower than the estimated volume of this mound of 28 km^3 presented in Chapter 4 above. However in Chapter 4 the average time thickness of the mound was over estimated by 50 ms, a velocity of 2000 m/s was assumed, and it was assumed that the mound was rectangular.

The volume of Mound A calculated here is larger than the volume of Crater A calculated above ($6.5 \pm 1.4 \text{ km}^3$, see section 5.4.1 above), although there is some overlap in uncertainty.

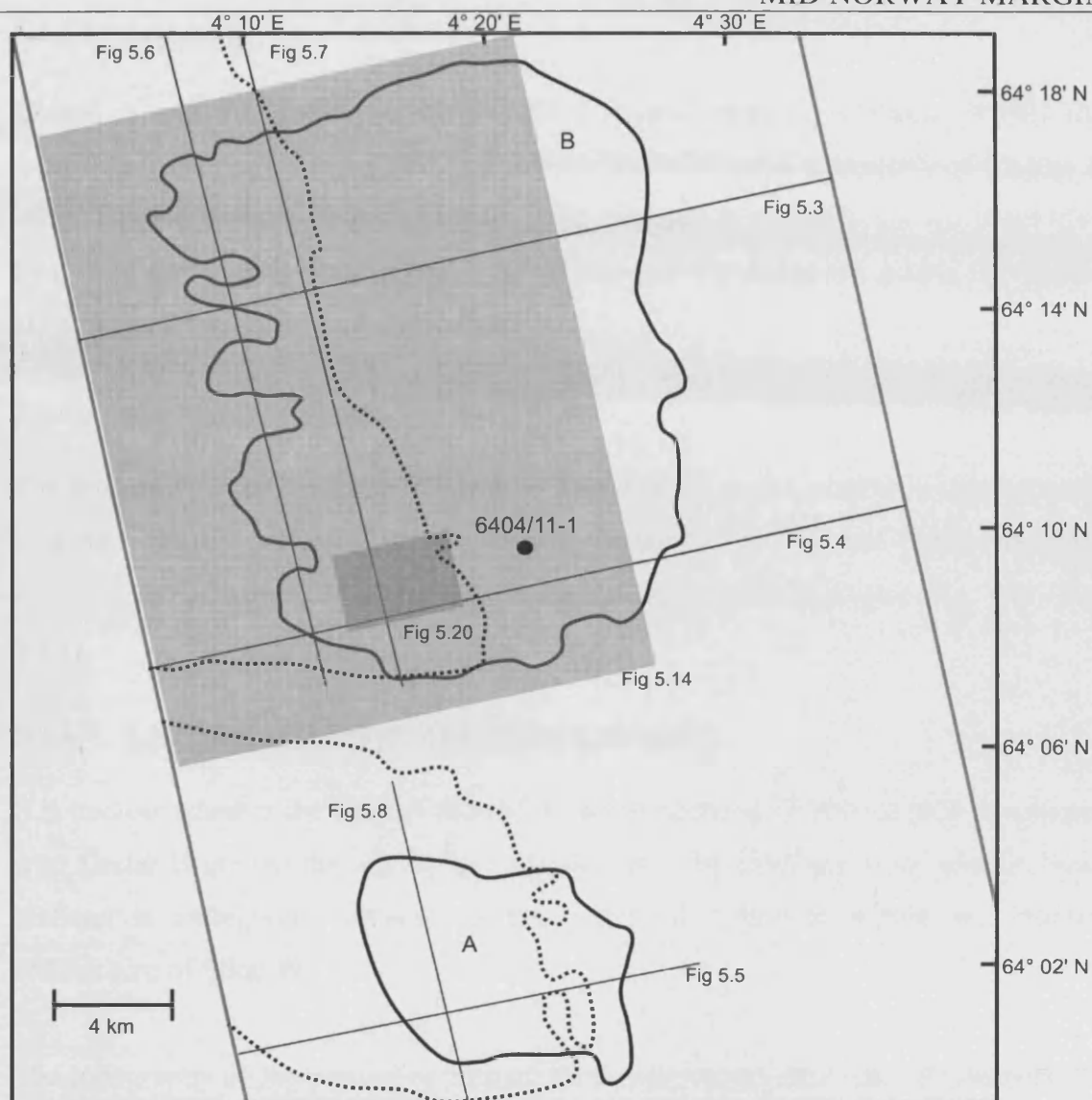


Fig. 5-13: A map of Crater A, Crater B, Mound A and the portion of mound BCF associated with Crater B in the Havsule survey highlighting the locations of figures pertaining to Mound A and the portion of Mound BCF associated with Crater B. The location of the sidewalls of Craters A and B are delineated by a solid line, and the location of the edges of Mound A and the portion of Mound BCF associated with Crater B are delineated by a dotted line.

5.4.2.1 Location

Mound A and the portion of Mound BCF located adjacent to Crater B fills the topographic depression mapped on the top surface of Slide W westwards of Craters A and B described above (Fig. 5-3 to Fig. 5-8). Mounds A and BCF are not penetrated by a well, therefore it is not possible to confirm that the sediments within the mound are sourced from the Brygge Formation.

5.4.2.2 Plan view geometry

The long axis of the portion of Mound BCF associated with Crater B is aligned north to south, with this portion of the mound being at least 6 km wide and 20 km long (Fig. 5-2 - Fig. 5-13). Mound A is crudely circular, being 15 km in diameter (Fig. 5-2 - Fig. 5-13).

5.4.2.3 External morphology and internal structure

It is unclear whether the base of Mound A and the portion of Mound BCF associated with Crater B incises the top surface of Slide W. The evidence from seismic cross sections is ambiguous, because of the disruption observed within the internal architecture of Slide W.

The topography of the portion of Mound BCF associated with Crater B consists of a series of ridges which trend between north - south and northwest to southeast, surrounded by troughs (Fig. 5-14). This topography is particularly clear in the south eastern part of the mound, and is highlighted by a time map (Fig. 5-14). The strike of every ridge on the top surface of the portion of Mound BCF associated with Crater B is measured, and the results are summarised on a Rose diagram, which confirms that the ridges on average are elongate in a south south east – north north west direction (Fig. 5-15).

The ridges on the top surface of Mound A and the portion of Mound BCF associated with Crater B are correlated vertically with troughs on the bottom surface of Mound BCF (Fig. 5-3 to Fig. 5-8). Depth conversions demonstrate that the troughs on the bottom surface of Mound A and the portion of Mound BCF associated with Crater B are real and not velocity artefacts (Fig. 5-3 to Fig. 5-8).

The cross sectional geometry of the mounds described is in some ways reminiscent of the geometry of sandstone bodies which undergo layer parallel stretching in a mudstone matrix (Cowan, 1986). This gives rise to a cross sectional geometry, where ridges on the top surface of the unit are correlated with troughs on the basal surface of the unit, with necking and shear geometries similar to what is observed within Mound A and the portion of Mound BCF associated with Crater B (Fig. 5-3 to Fig. 5-8).

The depth converted angle of slope of the ridges and troughs on the top surface of mound BCF are measured. Two lines are used in a west south west – east north east orientation at right angles to the strike of the structures (Fig. 5-3 and Fig. 5-4), and two lines are used in a south south east – north north west orientation parallel to the strike of the structures (Fig. 5-6 and Fig. 5-7), to ensure that dip angles measured are real dips. For the lines in a west south west – east north east orientation, it is found that the westward dipping slopes are on average steeper than the eastward dipping slopes, with the westward dipping slopes having an average dip of 6.3° (standard deviation from mean is 3.1° , 47 measurements) and the eastward dipping slopes having an average dip of 4.8° (standard deviation from mean is 2.5° , 47 measurements) (Fig. 5-16). On the lines with a south south east – north north west orientation it is found that the average dips of northward and southward dipping slopes are more similar, being 4.5° and 4.4° respectively (standard deviation from mean is 2.3° and 3.7° respectively, 68 measurements in each orientation) (Fig. 5-17). Noting a considerable overlap in standard deviations from the mean, it seems that the ridges may be nonetheless asymmetric in cross section, but symmetric in length section.

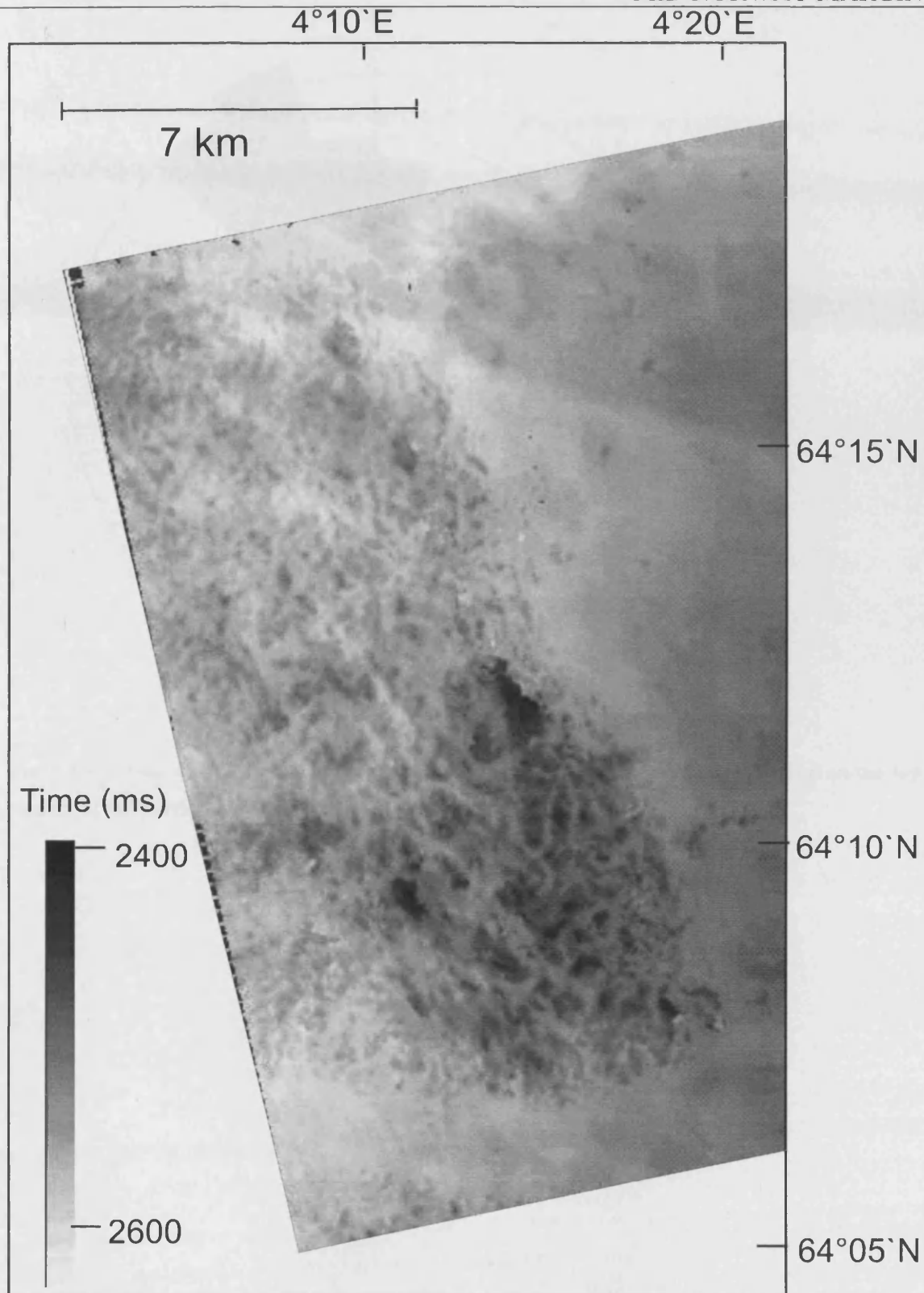


Fig. 5-14: A time map of the top surface of Slide W and Mound BCF.

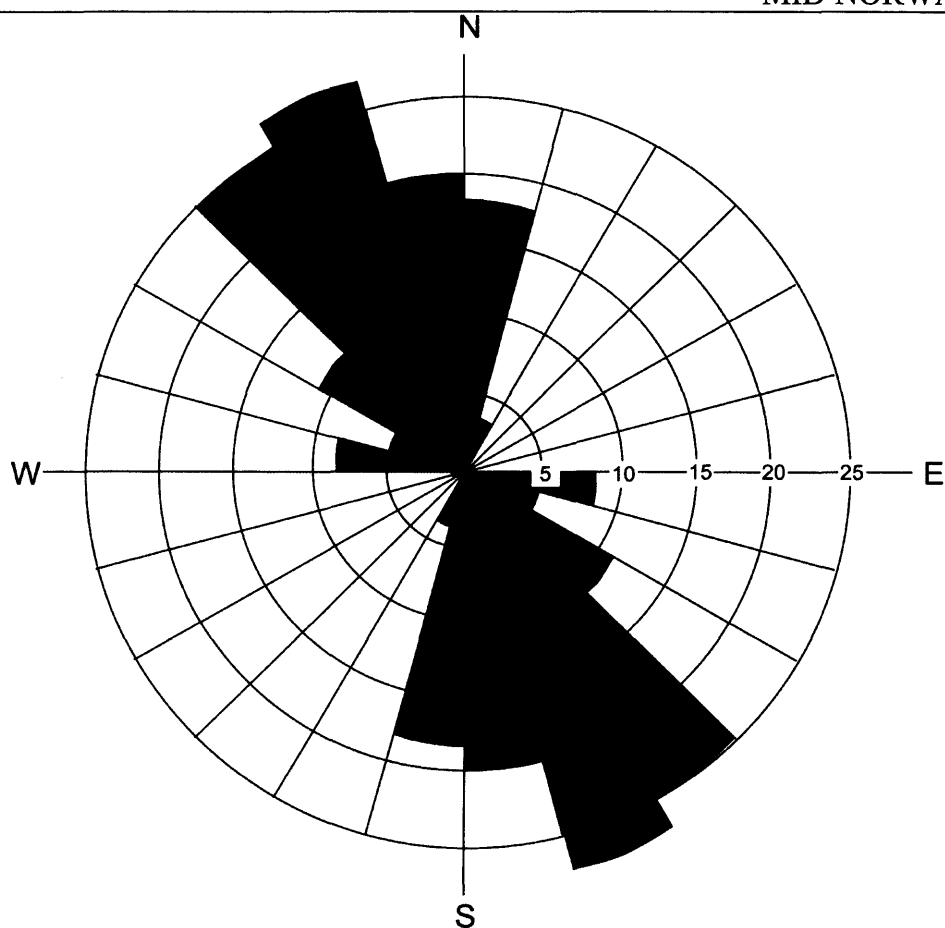


Fig. 5-15: A rose diagram, showing the orientation of the long axes of ridges observed on the top surface of the portion of Mound BCF associated with Crater B.

Features of Mound A and the portion of the mound associated with Crater B visible on the 3D seismic reflection data are a series of planar features with low reflection amplitude that cross cut the mound on lines with an east to west orientation (e.g. (vii) on Fig. 5-3). The planes which dissect the mounds mainly dip westwards, but a few dip eastwards (Fig. 5-3 - Fig. 5-5). The planes that cross cut mound BCF are spaced at intervals of approximately 500 m and dip predominantly westwards, such that the western slope of a ridge on the top surface of a mound is linked to the eastern slope of the trough associated vertically with a ridge on the top surface further westwards (e.g. (vii) on Fig. 5-3). The dip of the westward dipping planes dissecting Mound BCF is similar to the average dip of westward dipping slopes on the top surface of Mound BCF (e.g. (vii) on Fig. 5-3).

The planar features that cross cut the ooze mounds on lines with an east to west orientation are reminiscent of normal faulting or shear zones striking north to south. The similarity with normal faulting is suggested by the geometry of the planar features linking a slope of a ridge on the top surface of the mound with the opposite slope of a trough located beneath the adjacent ridge. In Mound BCF the faults intersect with the troughs on the top surface of the mound and the ridges on the bottom surface of the mound (Fig. 5-18). This resembles a half graben arrangement, with ridges on the top surface of the mound acting as a hanging wall and the troughs on the basal surface of the mound acting as a footwall, displaced downwards from the hanging wall (Fig. 5-18). On Mound BCF the shallowly dipping eastward slopes on the top surface of the mounds suggest rotation of half grabens, making the style of deformation within the mounds reminiscent of domino faulting (Barr, 1987). The normal faults within the mounds do not extend upwards into the overburden. The overburden onlaps the fault scarps (e.g. (iii) on Fig. 5-4), and this is indicative that these faults formed while the mound was exposed on the seabed.

The dip of the normal faulting is unusually low for normal fault zones, with the dips of the normal faults being an average of 6.3° in Mound BCF. This suggests that at the time of faulting the mound was weakly brittle or weakly ductile, which may have been partly or entirely due to high fluid pore pressure (Axen, 1992).

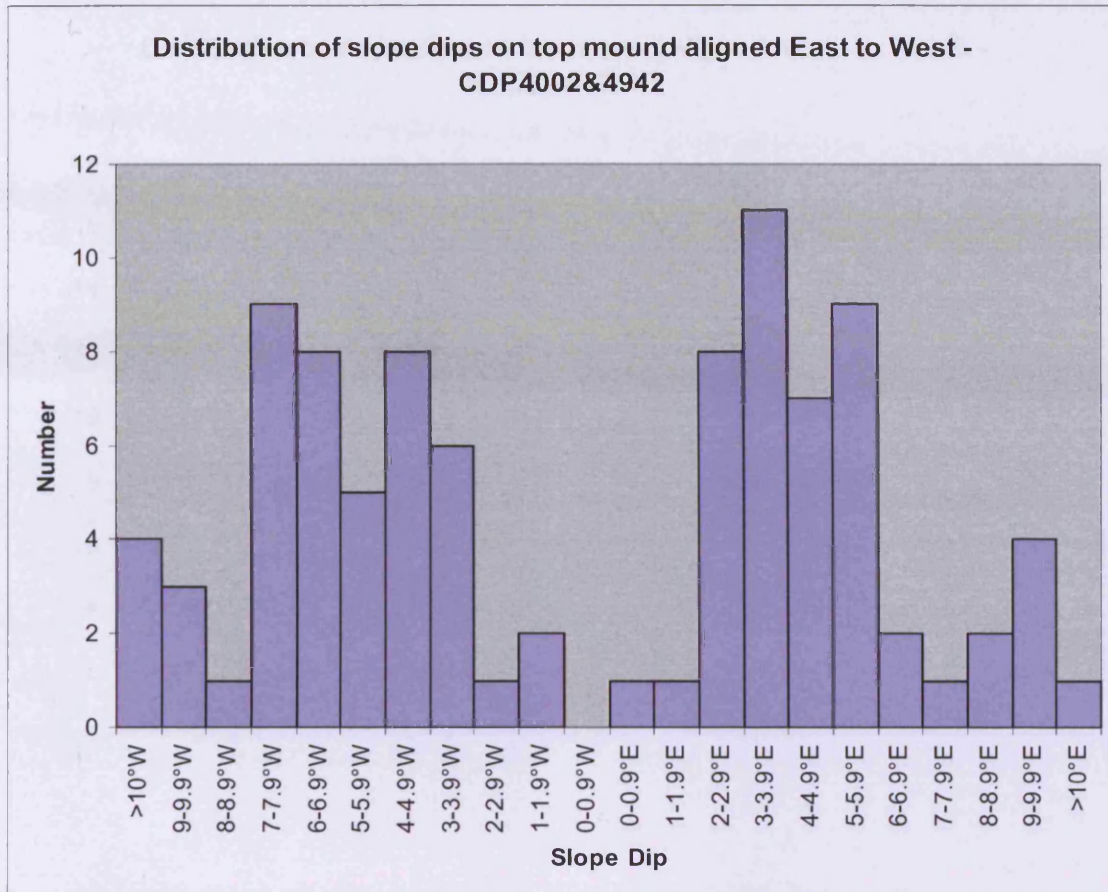


Fig. 5-16: Distribution of slope dips measured on lines with an east to west orientation. See Table A4- 45, Table A4- 46, Table A4- 49 and Table A4- 50 for data.

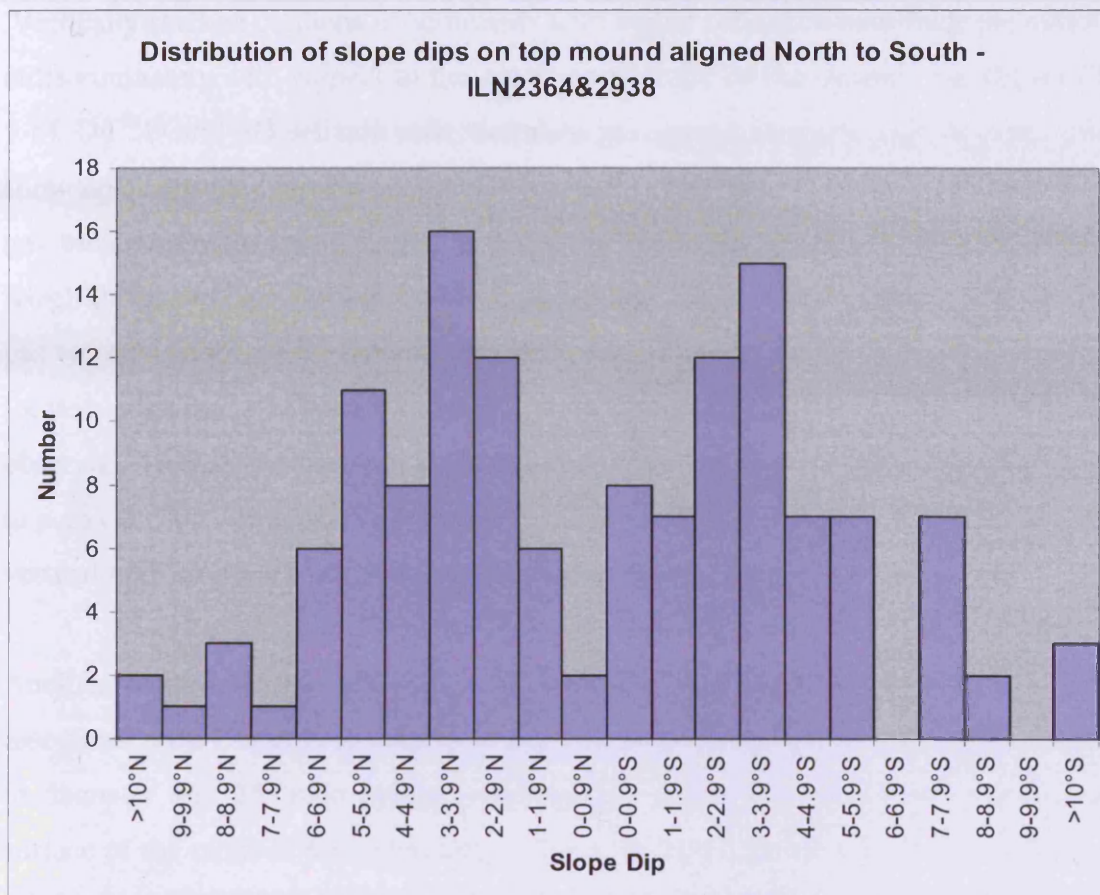


Fig. 5-17: Distribution of slope dips measured on lines with an north to south orientation. See Table A4- 47, Table A4- 48, Table A4- 51 and Table A4- 52 for data.

Vertically stacked columns of sediments with higher reflection amplitude are situated indiscriminately with respect to the outer morphology of the mound (e.g. (ii) on Fig. 5-8). On 2D and 3D seismic reflection data gas escape conduits such as pipes often show up as vertical narrow amplitude anomalies, with the reflection amplitude of the gas escape conduit being higher than the reflection amplitude of the sediments in which the gas escape conduit is found, which may indicate gas charging adjacent to a gas escape conduit (c.f. Løseth et al., 2009, Fig. 5.19). In the portion of Mound BCF located adjacent to Crater B narrow vertical high amplitude anomalies are also observed. These would require further testing to be evidence of gas charging adjacent to a gas escape conduit after Løseth et al. (2009), as the seismic data are noisy, and vertical high amplitude anomalies could represent artefacts.

Another feature of the topography of Mound A and the portion of Mound BCF associated with Crater B is a series of circular conically shaped features 250 to 500 m in diameter and 25 m in height superimposed on top of the geometry of the top surface of the mounds described above. These features, clearly visible on a time map of a portion of the top surface of Mound BCF (Fig. 5-20), are spaced at intervals of approximately 500 m, and are located on the crests of ridges on the top surface of the mound (Fig. 5-20). The conically shaped features are not interpreted as mud volcanoes related to emplacement of the ooze, because there is no evidence of a central vent.

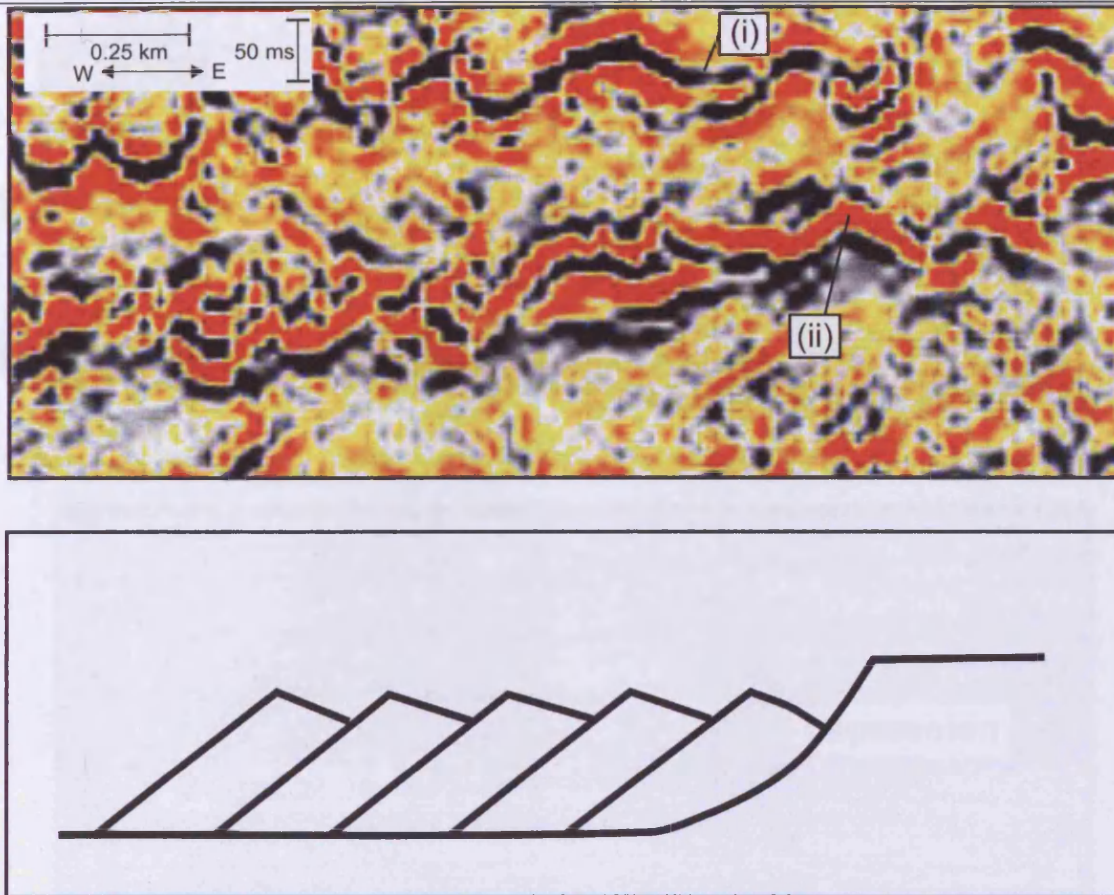


Fig. 5-18: (Top) A close up of the mound in Fig. 5-3. (Bottom) After Barr (1987). (i) trough on top surface of Mound. Westward dipping plane in Mound intersects top surface of mound here. (ii) Ridge on bottom surface of mound. Westward dipping plane inside mound intersects bottom surface of mound here.

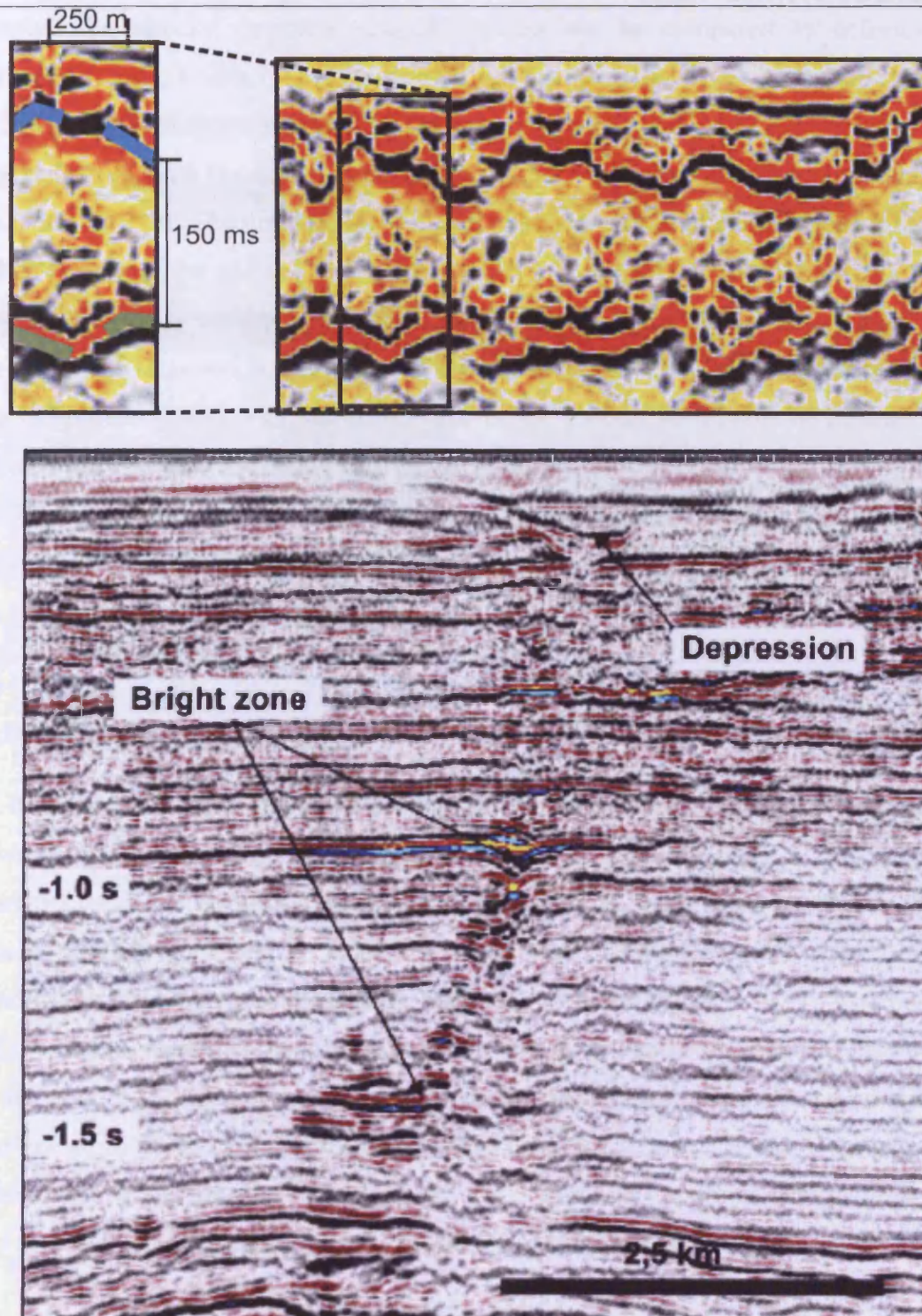


Fig. 5-19: A comparison of a gas escape conduit inside a mound (top), and a gas escape conduit utilising a fault (Løseth et al. 2009). The amplitude anomaly on the top figures may be due to gas charging.

Instead the circular conically shaped features can be compared to deformation associated with Raleigh Taylor instability. The top surfaces of sedimentary units which have undergone Raleigh Taylor instability are characterised by a ridge and spoke pattern, with the spokes being regularly spaced in a square or hexagonal pattern (e.g. Ribe, 1998). The distribution of the circular shaped features on the top surface of Slide W is irregular and not so similar to the layout of spokes which develops when a sedimentary body undergoes Rayleigh Taylor instability in perfectly isotropic stress conditions. It is noted however that in nature that Rayleigh Taylor instability related upwelling associated with subsurface salt in the Zagros Mountains of Iran and the Zeichstein Basin in Germany has an irregular pattern (Jackson et al., 1990, Ribe, 1998, Trusheim, 1960), similar to what is observed here, therefore Mound B may have undergone Raleigh Taylor instability.

5.5 Solsikke Survey

5.5.1 Description of Mound

A mound is located in the south eastern portion of the Solsikke Survey (Fig. 5-21). This mound is part of the mound named as Mound GJ in Chapter 4. The Solsikke survey covers the north eastern portion of this mound, in the vicinity of Crater J, a small portion of which is imaged on the unconformity separating the Brygge Formation from the Naust Formation underneath Mound GJ (Fig. 5-22). The portion of the mound described here extends north eastwards and south eastwards from this crater (Fig. 5-21). Crater J is filled by Slide W, and Mound GJ is located on the top surface of Slide W (Fig. 5-22 and Fig. 5-23). As with Mound B, the top surface of Mound GJ is an acoustically soft seismic reflection and the basal surface of Mound GJ is an acoustically hard seismic reflection (Fig. 5-22 and Fig. 5-23).

5.5.1.1 Well calibration of Mound

Mound GJ is penetrated by well 6403/10-U1 in the Solsikke Survey (Fig. 5-21), and this allows an investigation of the similarities and differences between the Brygge Formation and the sediments that form the mounds in this region. Sidewall cuttings from this well show that the mound consists of very sandy biosiliceous ooze. The

Brygge Formation, from which the mounds are sourced (Riis et al., 2005) (Chapter 4), but which has not been removed at the locality of the well, consists of ooze containing pyrite, carbonate and mica. Slide W in this region contains silt and mica.

A petrophysical log suite was obtained in well 6403/10-U1. Geophysical results suggest that the density of the ooze mound varies between 1.25 and 1.45 g/cm³, and that the porosity of the mound varies between 50 and 80 %. The density of Slide W varies between 1.95 and 2.05 g/cm³, and the porosity of Slide W is between 0 and 15 %. The density of the in situ Brygge Formation is consistently 1.45 g/cm³, and its porosity is consistently 60 %.

It has been previously observed that the volume of the mounds is frequently larger than that of the craters from which they are sourced (see above, Chapter 4). The well data obtained from well 6403/10-U1 makes it possible to explore why this might be. The well data shows that key differences between Mound GJ and the Brygge Formation from which the mound is sourced are that the mound consists of very sandy ooze, whereas the Brygge Formation consists of ooze, with a rare pyrite and carbonate. The mound also shows a greater variation in porosity and density than the Brygge Formation from which the mound is sourced. During the process of ooze extrusion sediments may be removed from Slide W. It may be that the ooze interacts and mixes with the sediments within Slide W, giving rise to a sandy ooze mound with variable density and porosity. This would explain why the mounds increase in volume. Alternatively the portion of Mound GJ sampled by the well may have been sampled from a sandier portion of the Brygge Formation not sampled by the well. It is also possible that water was added to the ooze during extrusion.

Another difference between the portion of the ooze mound sampled by 6403/10-U1 and the Brygge Formation sampled in this well is that rare pyrite and carbonate are sampled in the Brygge Formation but not in the mound. This material may be mixed into Slide W, or left as a residue at the base of a crater.

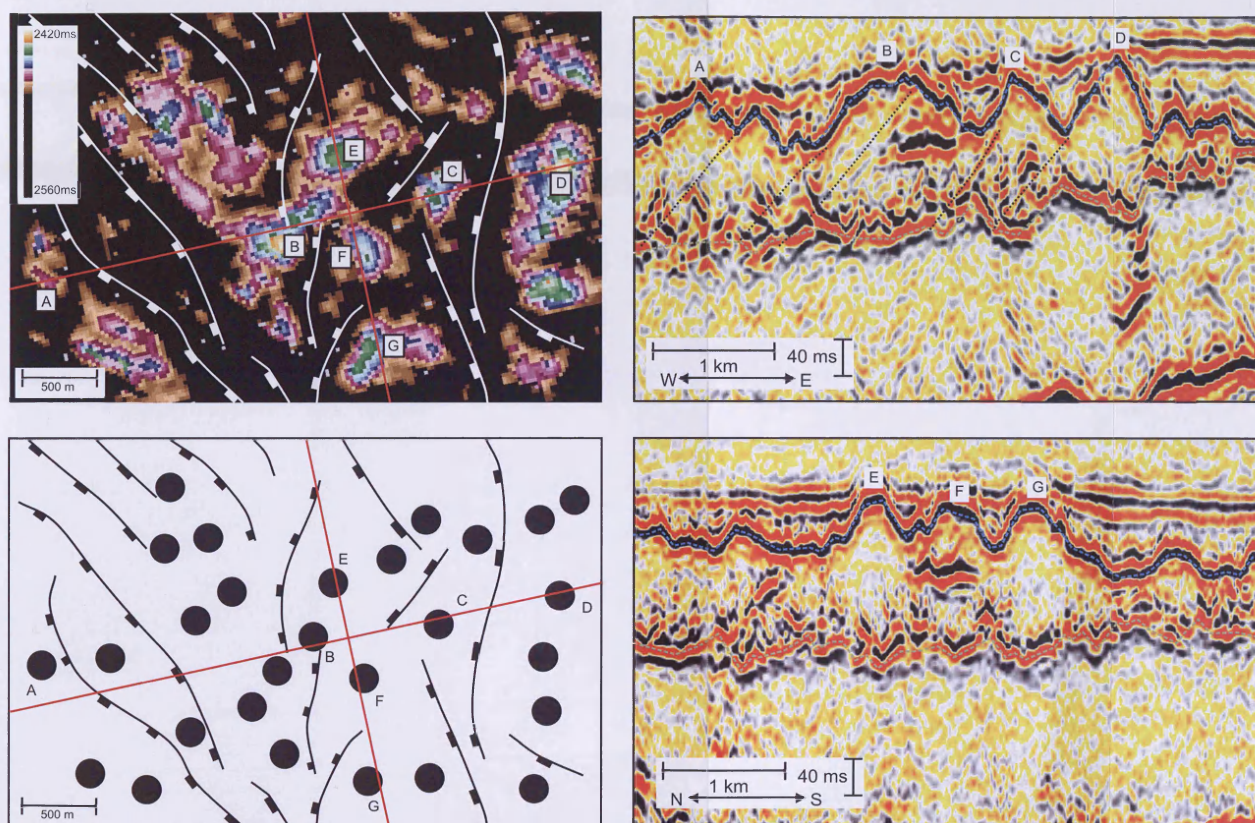


Fig. 5-20: Detailed map and sections through a portion of Mound BCF, showing the detailed topography of the top surface of the mound. Selected peaks are labelled A-F. (Top left) A time map of the top surface of the portion of Mound BCF associated with Crater B. See Fig. 5-13 for location. (Bottom left) An interpreted sketch map of (Top left). The black circles indicate the location of conical features on the top surface of Mound BCF. (Top right) A west to east cross section through the area mapped to the left. Interpreted shear zones are interpreted by a black dotted line. (Bottom right) A north to south cross section through the area mapped to the left.

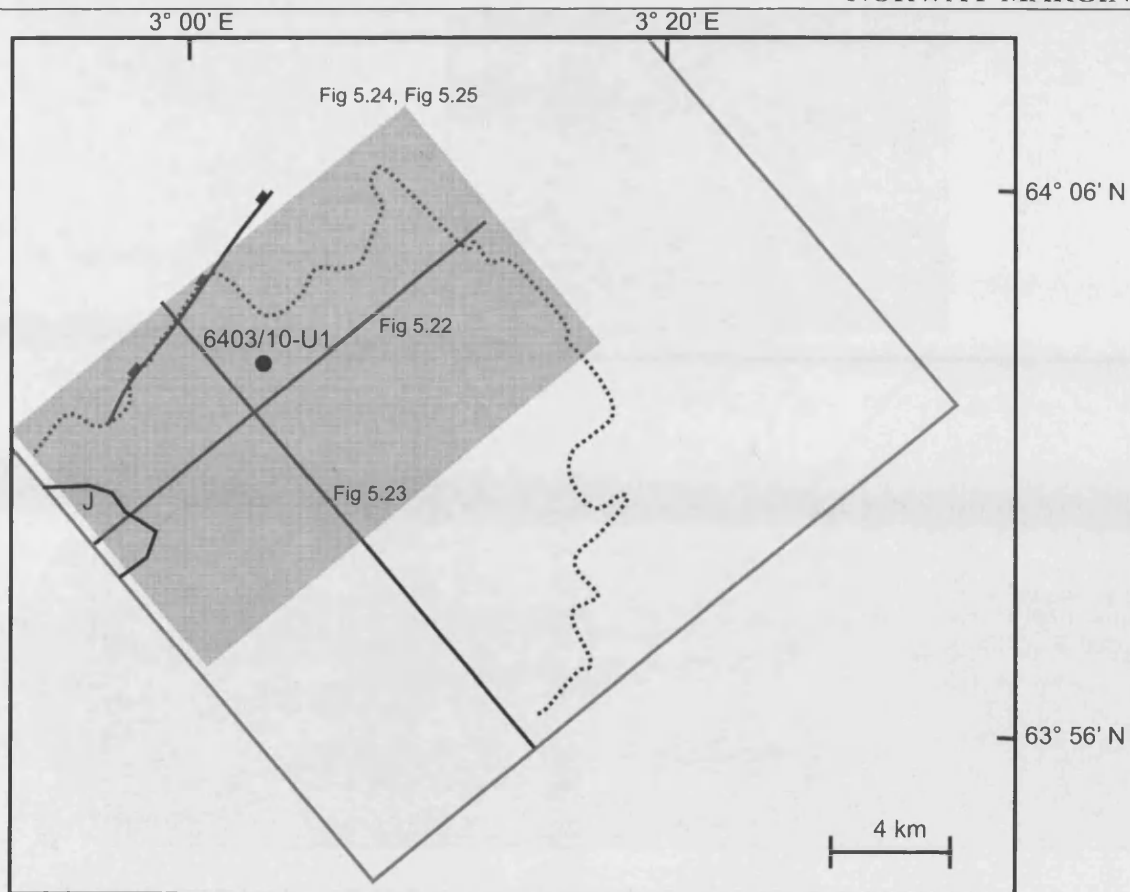


Fig. 5-21: A map of a portion of Mound GJ associated with Crater J in the Solsikke Survey highlighting the location of figures pertaining to Mound GJ. The location of the sidewall of Crater J is delineated by a solid line, and the location of the edge of the portion of Mound GJ associated with Crater B is delineated by a dotted line.

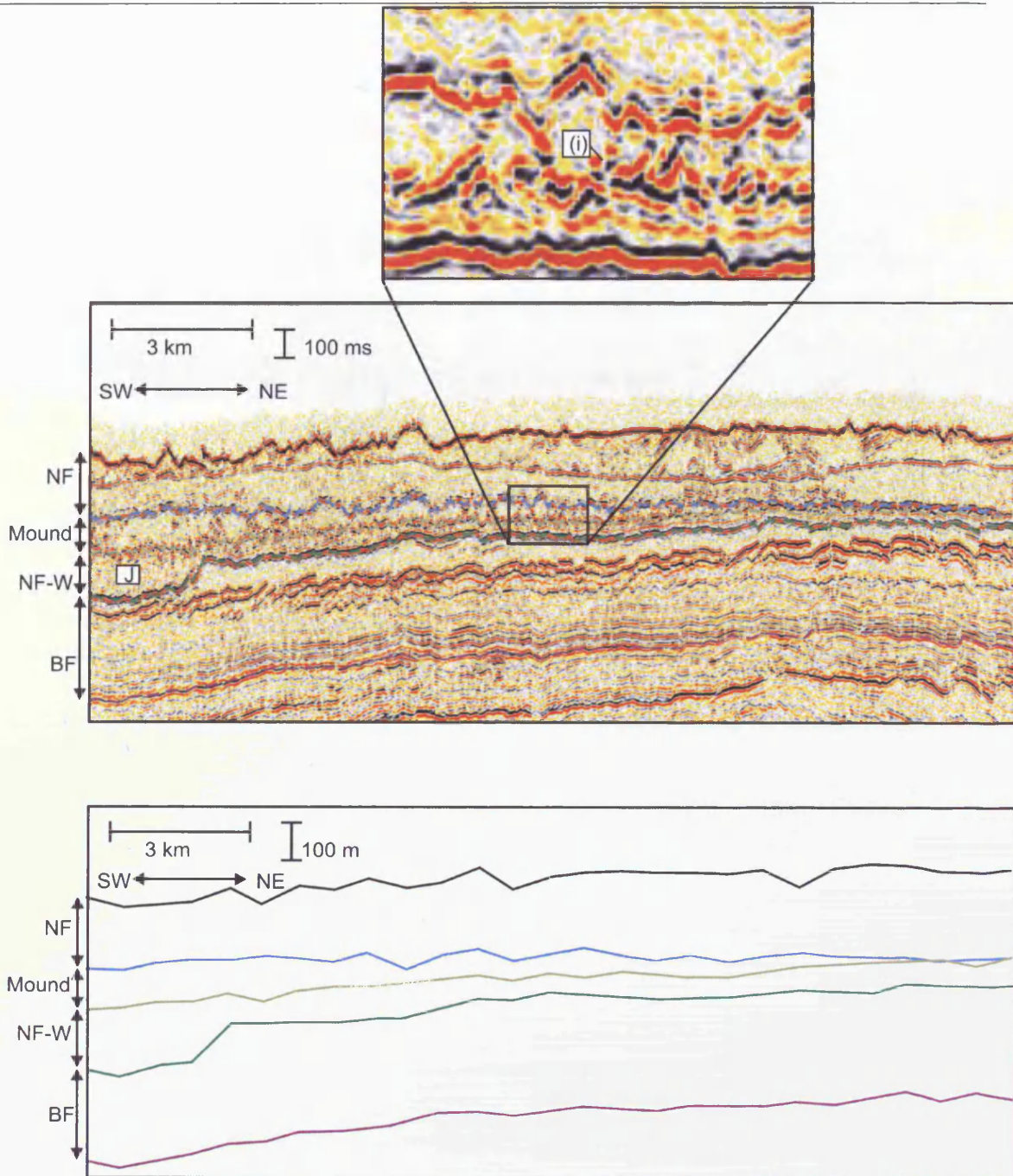


Fig. 5-22: A crossline in time through Mound GJ. A smoothed depth section is also displayed. See Fig. 5-21 for location. NF: Naust Formation, NF-W: Naust Formation W, BF: Brygge Formation. The opal A/CT boundary is indicated by a dotted line. (i) Dipping plane linking a trough on the top surface of Mound GJ to a ridge on the bottom surface of Mound GJ

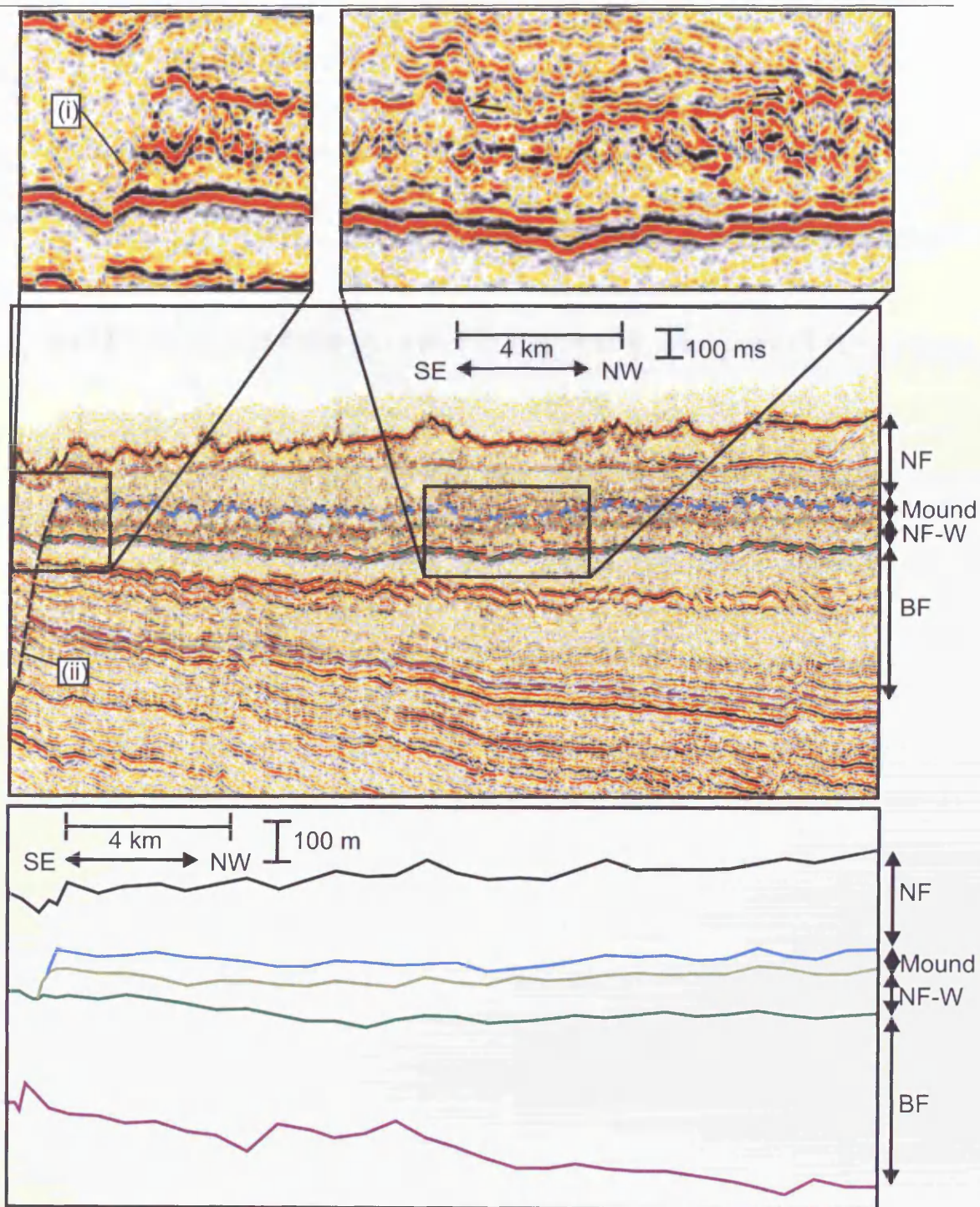


Fig. 5-23: A crossline in time through Mound GJ. A smoothed depth section is also displayed. See Fig. 5-21 for location. NF: Naust Formation, NF-W: Naust Formation W, BF: Brygge Formation. The opal A/CT boundary is indicated by a dotted line. (i) Truncation of internal sediments of Slide W. (ii) Normal fault which delineates the boundary of Mound GJ in this area.

5.5.1.2 External Morphology

The cross sectional morphology of the portion of Mound GJ described here is more complex than that of Mounds A and B. While Mounds A and B displayed localised thickness variations, the trend was that the mounds were thickest in the centre and thinnest at the edges, pinching out onto the top surface of Slide W. While the portion of Mound GJ described here thins to its north eastern and south western margin, the mound is at its thickest at its north western margin (Fig. 5-23), with cross sections showing the mound to be 100 m thick at this margin (Fig. 5-23).

The thickening towards the north western edge of Mound GJ (which is the upslope limit of the mound, Fig. 5-23) is interpreted to be evidence of mound incision or erosion by a later slide, which would make the north western edge of the portion of Mound GJ described here an erosive boundary. The truncation of the internal reflections of Slide W beneath the north western edge of the mound against internal reflections of a later slide (e.g. (i) on Fig. 5-23) supports this interpretation. It is unlikely that the thickening observed at the north western edge of Mound GJ is primary, because this would require the upslope movement of a large volume of remobilised sediment from the current centre of the mound to the edges of the current mound, which is not observed elsewhere (e.g. Mound A and Mound BCF). This incision of Mound GJ occurs along the line of a north east – south west trending normal fault which dips north westwards and pierces the overburden (Fig. 5-21, (ii) on Fig. 5-23), and it is considered that this fault may have represented a zone of weakness that was easily incised.

Like Mounds A and BCF, the top and basal surfaces of mound GJ are characterised by a series of ridges and troughs, with ridges on the top surface being correlated vertically with troughs on the bottom surface. The mounds and troughs on the top surface of Mound BCF are arranged regularly and trend in an approximately north to south direction, however the ridges and troughs on the top surface of Mound GJ imaged in the Solsikke survey display no preferred orientation, being more circular than elongate (e.g. (i) on Fig. 5-24). As with Mound B, we interpret the ridges and troughs on the top surface and basal surface of the mounds, with an approximate correlation between ridges on the top surface and troughs on the basal surface of the

mound, as evidence of extension. In addition to this, there are some areas in Mound GJ where the top surface of the mound is essentially flat, whereas ridges and troughs continue to be imaged on the basal surface of the mound (Fig. 5-23). This is further evidence that the ridges and troughs on the basal surface of the mound are real. It has been noted above that the north western edge of Mound GJ is incised by a later slide. The geometry described here of the mound having a flat top and irregular base may also be because of incision of the later slide into ridges on the top surface of the mound.

5.5.1.3 Internal Geometry of Mound GJ

A similarity to the mound associated with crater B are a series of vertically aligned packages of higher amplitude sediments within Mound GJ, and the dissection of Mound GJ by shallowly dipping low amplitude planes (e.g. (i) on Fig. 5-22). The shallow dipping planes with low reflection amplitude are similar to those described at Mound B above, linking a ridge on the top surface of Mound GJ with an adjacent trough on the basal surface of the mound (e.g. (i) on Fig. 5-22). The shallow dipping high amplitude planes linking ridges on the top surface of the mound with adjacent troughs on the basal surface of the mound are interpreted as low angle normal faults (see above). As with Mound B described above, these do not extend upwards into the overburden and later sediments onlap the fault scarps (e.g. Fig. 5-23), suggesting that the faulting was active when the mound was exposed at the seabed. As above, the vertical high amplitude anomalies within the mounds are interpreted as gas escape conduits.

5.5.2 Description of Craters

The craters located in the Solsikke survey were labelled as Craters H and I in Chapter 4 above. These craters, located in the north western portion of the Solsikke survey, were distinguished from many of the other craters described above because they are not filled by Slide W and are not associated with ooze mounds. They are however filled by the same slide that incises Mound GJ (see above).

5.5.2.1 External Morphology and Burial of Craters H and I

Craters H and I are defined in a similar manner to Crater B above. The basal surface of Craters H and I is a soft reflection, which is a boundary between the Brygge

Formation below and the Naust Formation above. The sides of the craters are defined by the truncation of internal seismic reflections of the Brygge Formation against internal reflections of the Naust formation (e.g. (i) on Fig. 5-26).

Craters H and I are different however to Crater B above, in that they are not fully enclosed features. The north western edge of Crater H and the north eastern edge of Crater I open into a larger and deeper erosive feature (Fig. 5-25), with the internal sediments of Craters H and I being adjacent to sediments which fill the deeper erosive feature (e.g. (i) on Fig. 5-27). The erosive feature (Fig. 5-25) is known as the Solsikke Trough, a feature which may have been carved out by the Holocene Storegga Slide (Haflidason et al., 2004).

The slide that fills Craters H and I is not the same slide that fills the Solsikke Trough. Craters H, I and the area not incised by the Solsikke Trough are buried by two slide deposits which are separated by a high amplitude hard reflection (Fig. 5-26 and Fig. 5-27). The bottom slide to bury Craters H and I is the same slide which incises Mound GJ above (Fig. 5-28). The upper slide to bury Craters H and I is the Holocene Storegga Slide. There is only one slide deposit imaged within the Solsikke Trough (Fig. 5-26 and Fig. 5-27), and, being exposed at the seabed, this is interpreted as the Storegga Slide.

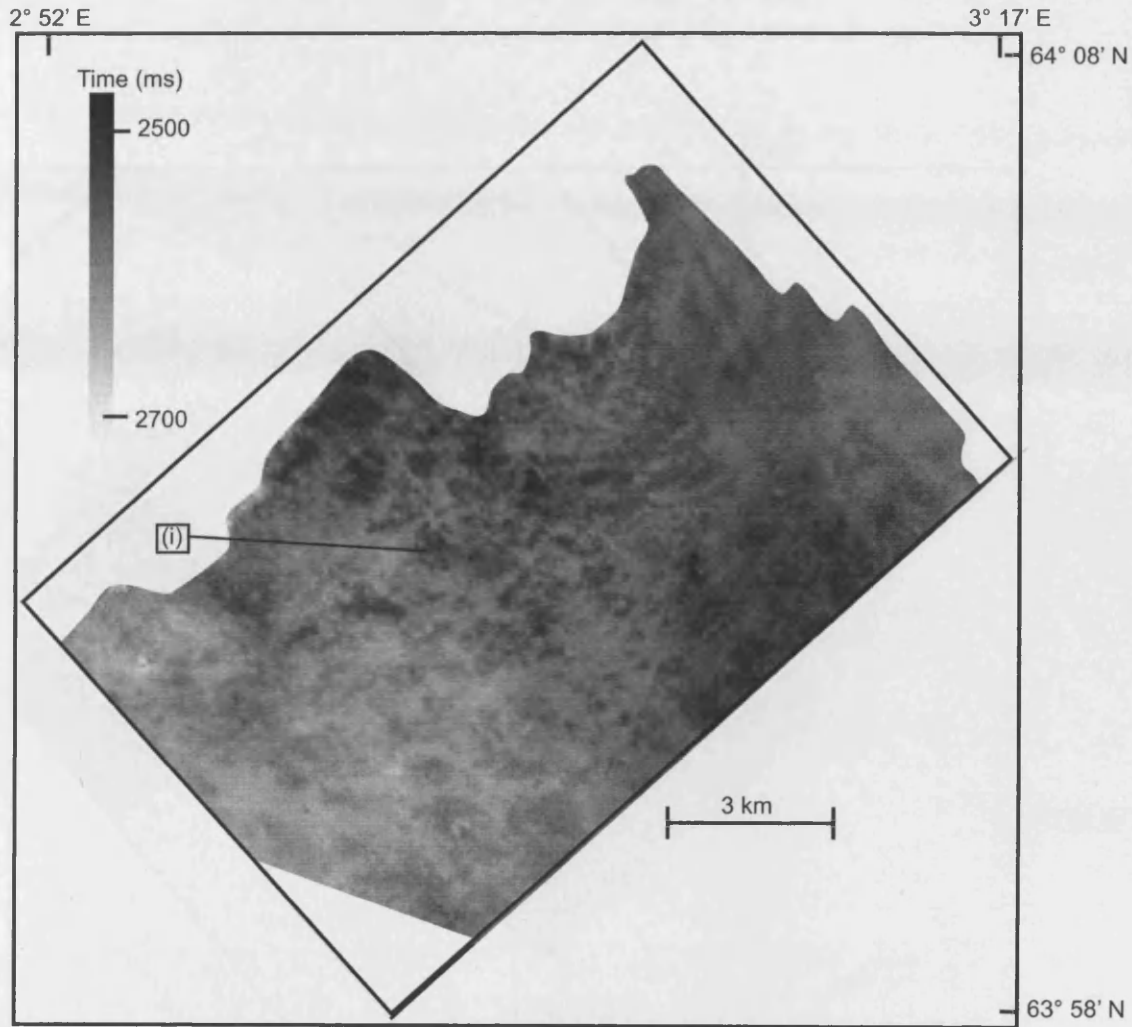


Fig. 5-24: A time map of the top surface of Mound GJ. See Fig. 5-21 for location. (i) A non-elongate ridge on the top surface of Mound GJ.

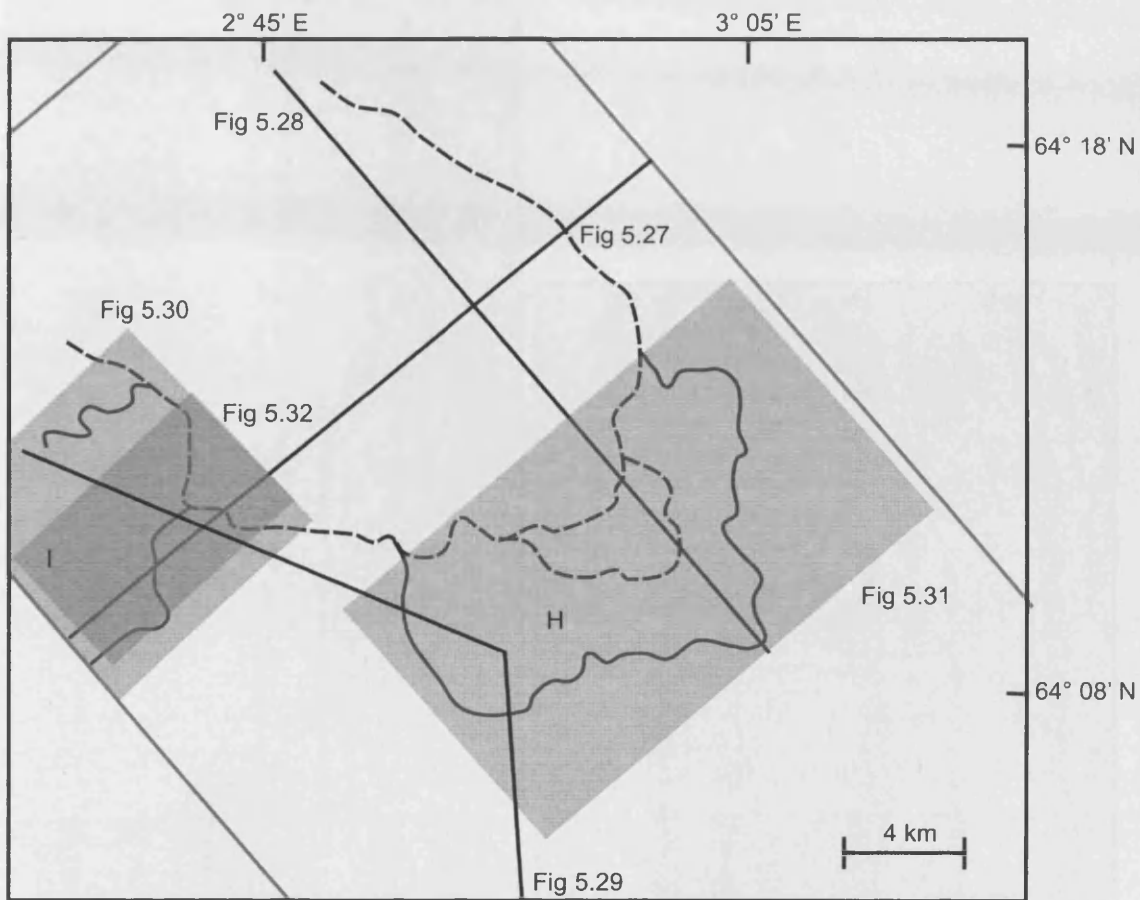


Fig. 5-25: A map of a Craters H and I in the Solsikke Survey highlighting the location of figures pertaining to Craters H and I. The location of the sidewall of Craters H and I is delineated by a solid line, and the location of the sidewalls of the Solsikke Trough are delineated by a dashed line.

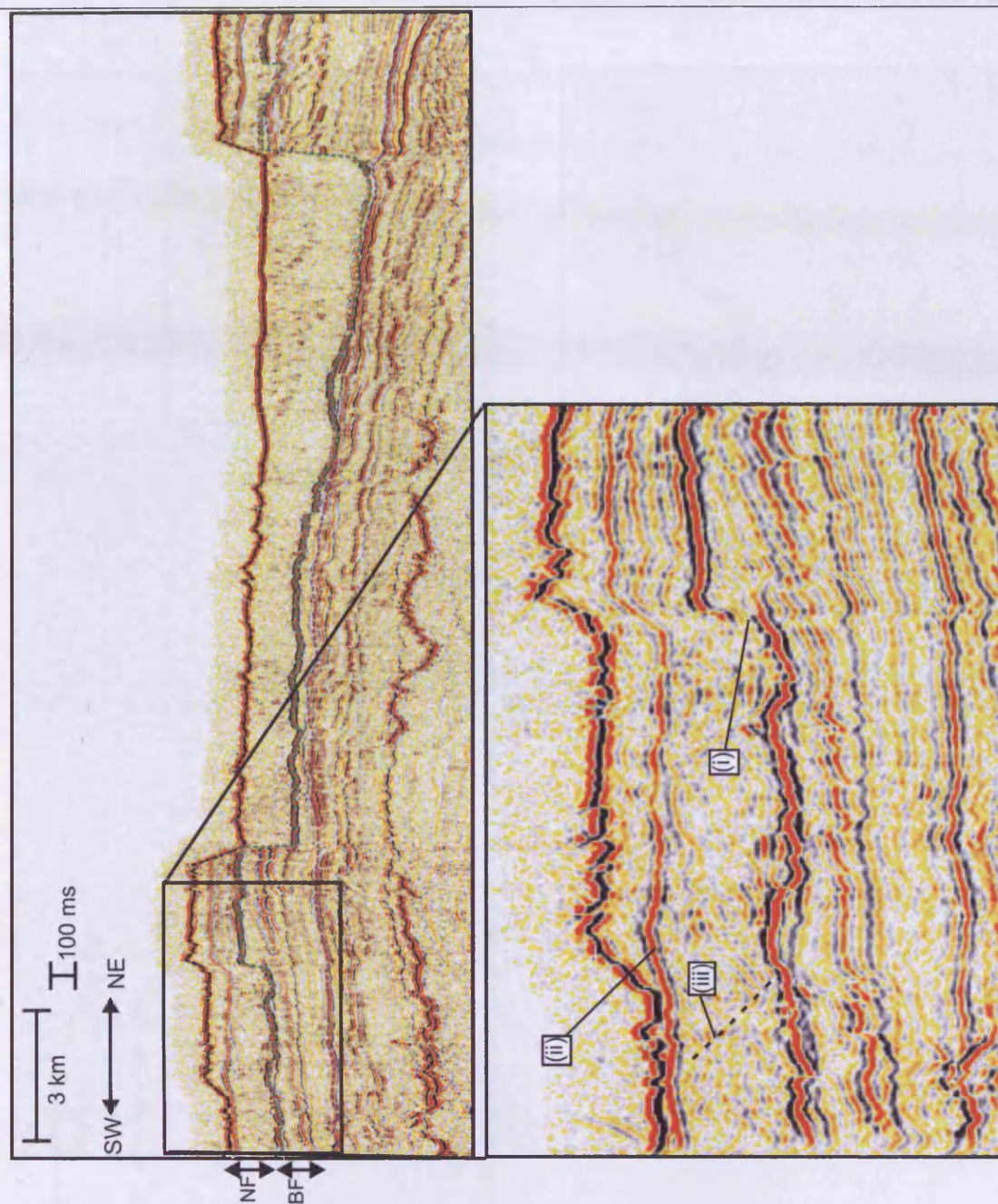


Fig. 5-26: A crossline in time through Crater I. See Fig. 5-25 for location. NF: Naust Formation, BF: Brygge Formation. (i) Truncation of Brygge Formation sediments at the edge of Crater I. (ii) A hard reflection with high reflection amplitude, separating the Storegga Slide above from the slide which fills Crater I below.

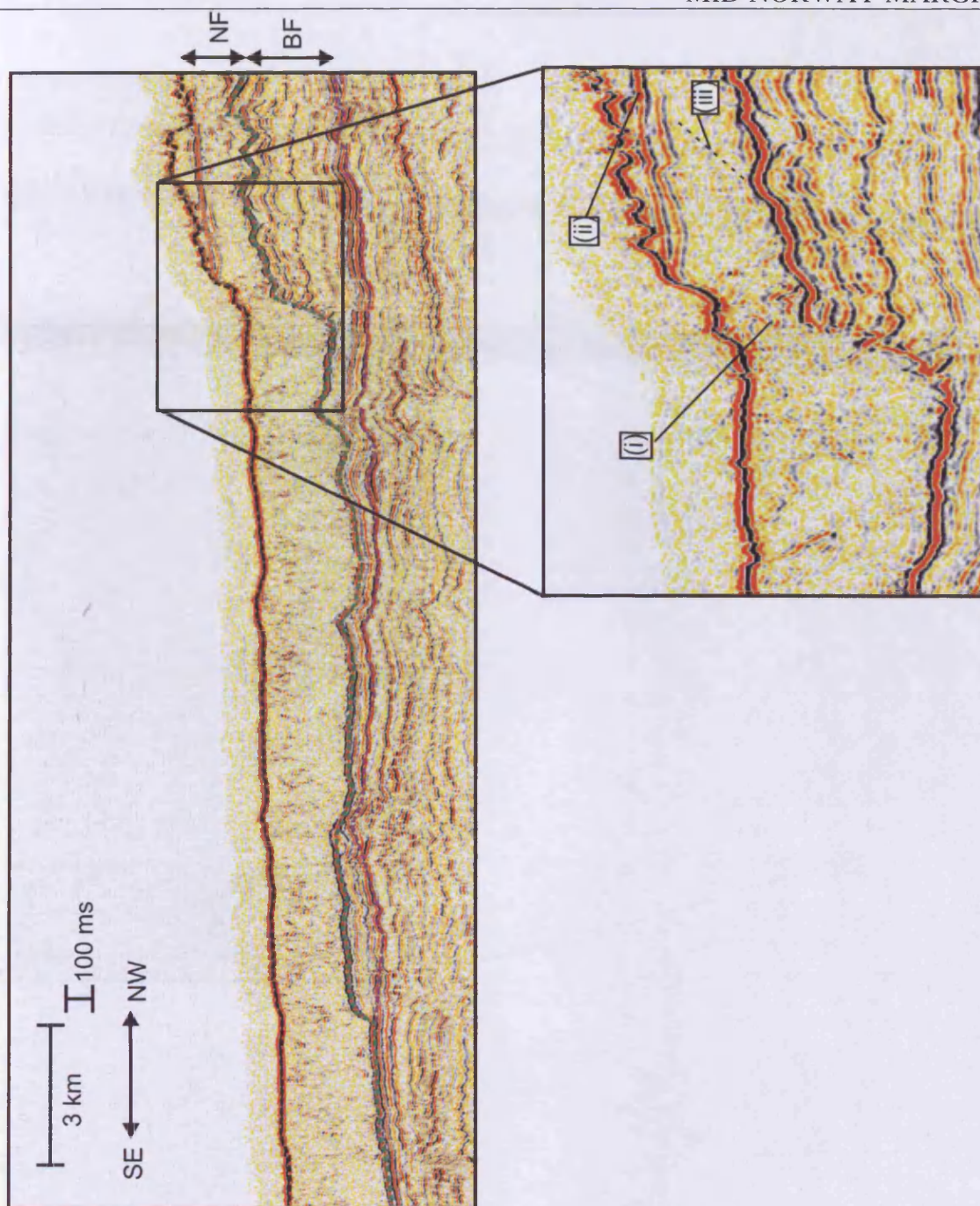


Fig. 5-27: A crossline in time through Crater H. See Fig. 5-25 for location. NF: Naust Formation, BF: Brygge Formation. (i) Truncation of Brygge Formation sediments at the edge of Crater H against the fill of the Solsikke Trough. (ii) A hard reflection with high reflection amplitude, separating the Storegga Slide above from the slide which fills Crater I below. (iii) Plane with eastward component of dip in the fill of Crater H.

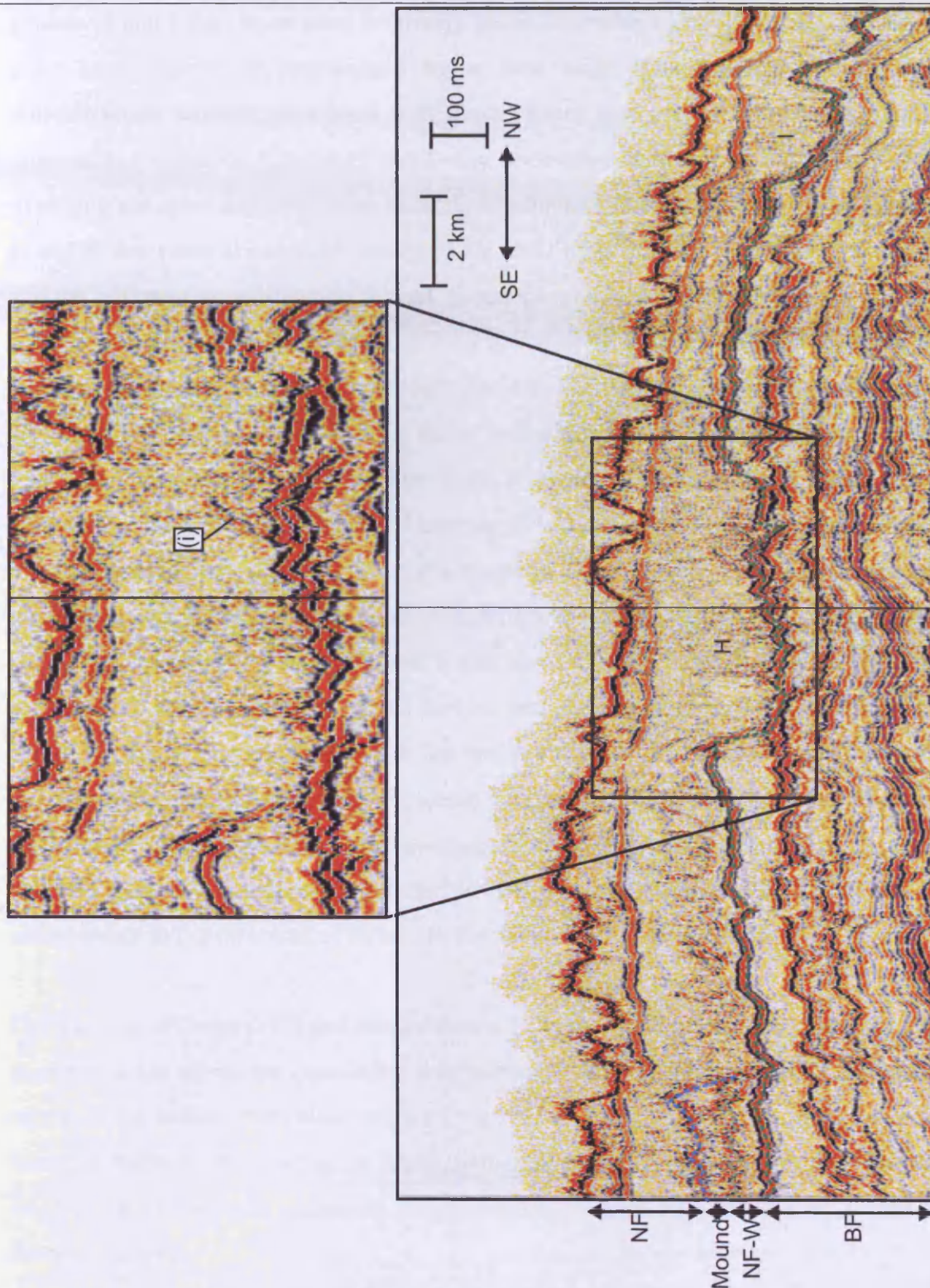


Fig. 5-28: A crossline in time through Mound GJ and Crater H. See Fig. 5-25, Fig. 5-29 and Fig. 5-30 for location. NF: Naust Formation, NF-W: Naust Formation W, BF: Brygge Formation. (i) Plane with eastward component of dip in the fill of Crater H.

Craters H and I may have been originally associated with an earlier slide, which has since been eroded or remobilised by a later slide. The absence of sediment remobilisation mounds associated with these craters may represent evidence of this process. For example, Craters H and I may once have been buried by Slide W and overlying sediment remobilisation mounds in a manner similar to the burial of Craters A and B described above, with another later slide incising and remobilising Slide W and the sediment remobilisation mound. Evidence which would support this is that the Slide which does fill Craters H and I does incise Slide W (Fig. 5-23). The burial of Craters H and I by Slide W is however considered unlikely. In the region of Mound GJ (described above) Slide W thins north westwards over the Solsikke Dome (Fig. 5-23), and therefore it is likely that Slide W would thin to zero thickness south eastwards of Crater H and Crater I. However it is not precluded that Craters H and I were associated with a slide event subsequent to Slide W and were also associated with sediment remobilisation mounds, which have since been incised by a more recent slide. The opening of Craters H and I into the Solsikke Trough suggests that the sediments in which Craters H and I formed were incised by the Storegga Slide. In particular, the location of Crater H at the upslope limit of the Solsikke Trough, raises the possibility that incision of the Solsikke Trough may have initiated at the locality of Crater H. This would require the Storegga Slide to incise downwards into the slide that buries Crater H, and to then incise downwards into the crater floor of Crater H and to incise in the direction of flow into the north western sidewall of Crater H.

The incision of Craters H, I and the sediments in which these craters are incised by the Storegga Slide raises the possibility that sediment remobilisation mounds emplaced on top of the bottom most slide to bury Craters H and I may have been incised by the Storegga Slide. This would be an alternative explanation of why these craters are not overlain or linked with sediment remobilisation mounds like Craters A, B and J described above.

5.5.2.2 Basal Surface and Internal fill of Craters H and I

The basal surface of both Craters H and I exhibits irregular topography. In addition to a trace of the polygonal faulting which deforms the Brygge formation in this area (Chapter 2 & 3) (Berndt et al., 2003, Cartwright and Dewhurst, 1998, Hustoft et al.,

2007), short lineations of up to 1000 m in length are observed (Fig. 5-29). These lineations are aligned in a south east to north west orientation, a similar orientation to the Solsikke Trough in this area. The lineations on the basal surfaces of Craters H and I are shorter than but otherwise similar to those observed on the basal surface of Crater B, and are therefore interpreted similarly as scour marks.

Despite being filled by a later slide, the internal geometry of the fill within Crater H and Crater I is similar in some respects to that described within Crater B described above. The fill of Crater B was distinguished on a coherency slice by lineations with spacing of 200 m, the strike of which varied between being north to south and south east to north west. In both Crater H and Crater I similarly spaced lineations are distinguished on coherency slices (Fig. 5-30 and Fig. 5-31). In Crater H the strike of these varies between east to west and north east to south west (Fig. 5-30). In Crater I the strike of the internal fabric varies between north to south and north east to south west (Fig. 5-31). Cross sections show that the dip of these planes has an easterly component (Fig. 5-26 and Fig. 5-28).

The generally eastward dipping planes that dissect the fills of Craters H and I are reminiscent of thrust faulting described at the northern edge of Slide W, and on this basis are interpreted as such. It should be noted that, unlike Craters A and B above, these thrust faults exhibit very low reflection amplitude, suggesting that the process of ooze removal from the crater floor was efficient here, or else that the slide deposit was deposited sometime after formation of the crater. Vertical amplitude anomalies such as those described in the internal fill of Craters A and B are not observed. These may have existed in an earlier slide deposit which may have buried craters H and I which may have later been incised by a later slide event.

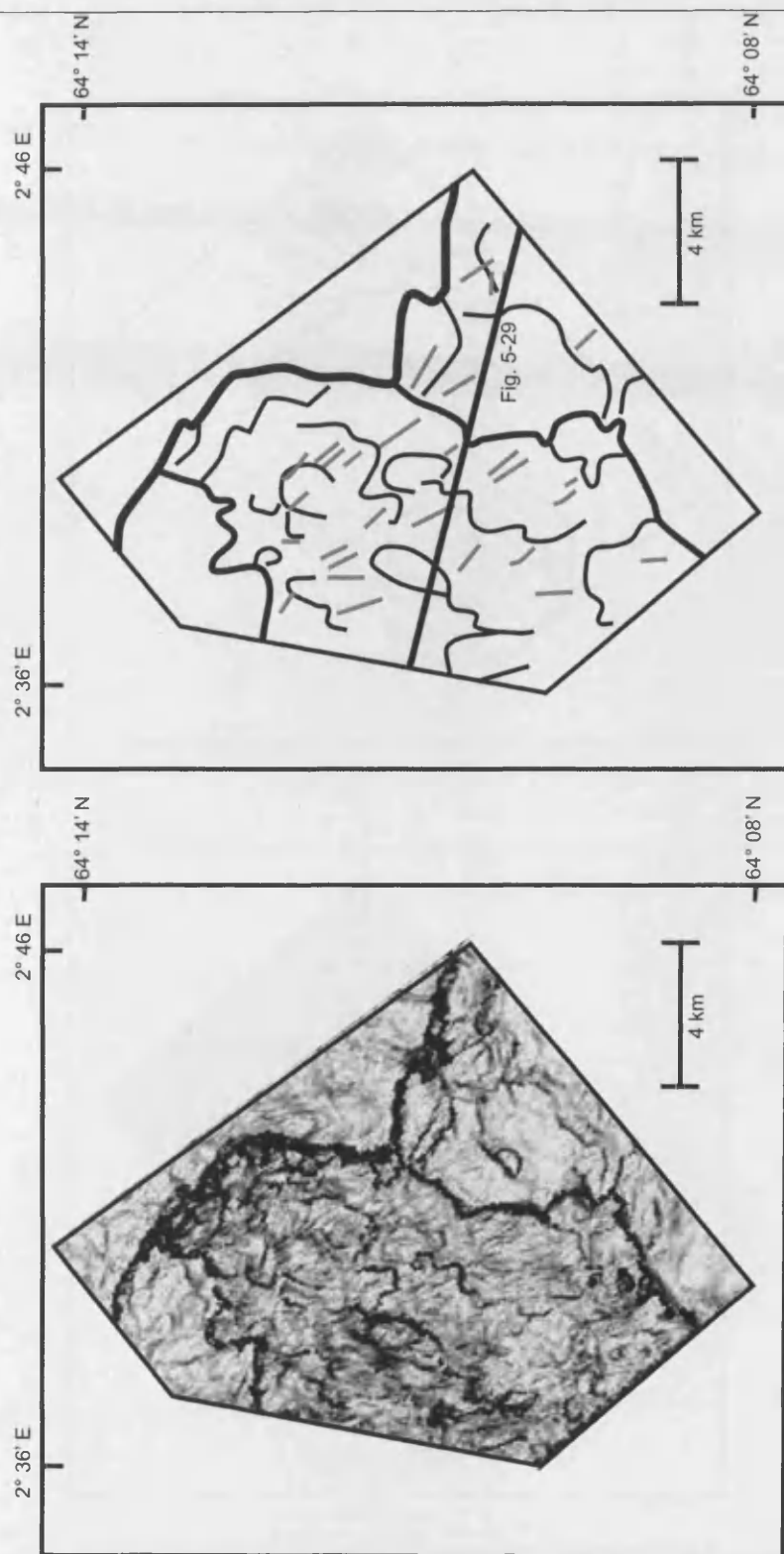


Fig. 5-29: A dip map of a portion of the basal surface of Crater I. For an exact location, see Fig. 5-25. (Top) Non-interpreted dip map. (Bottom) Sketch of dip map displayed above, highlighting important features. The sidewalls of Crater I are highlighted by a bold solid black line. The trace of polygonal faulting is delineated by a fine black line, and scour marks on the basal surface of crater B are highlighted by fine grey lines. Location of Fig. 5-28 is indicated.

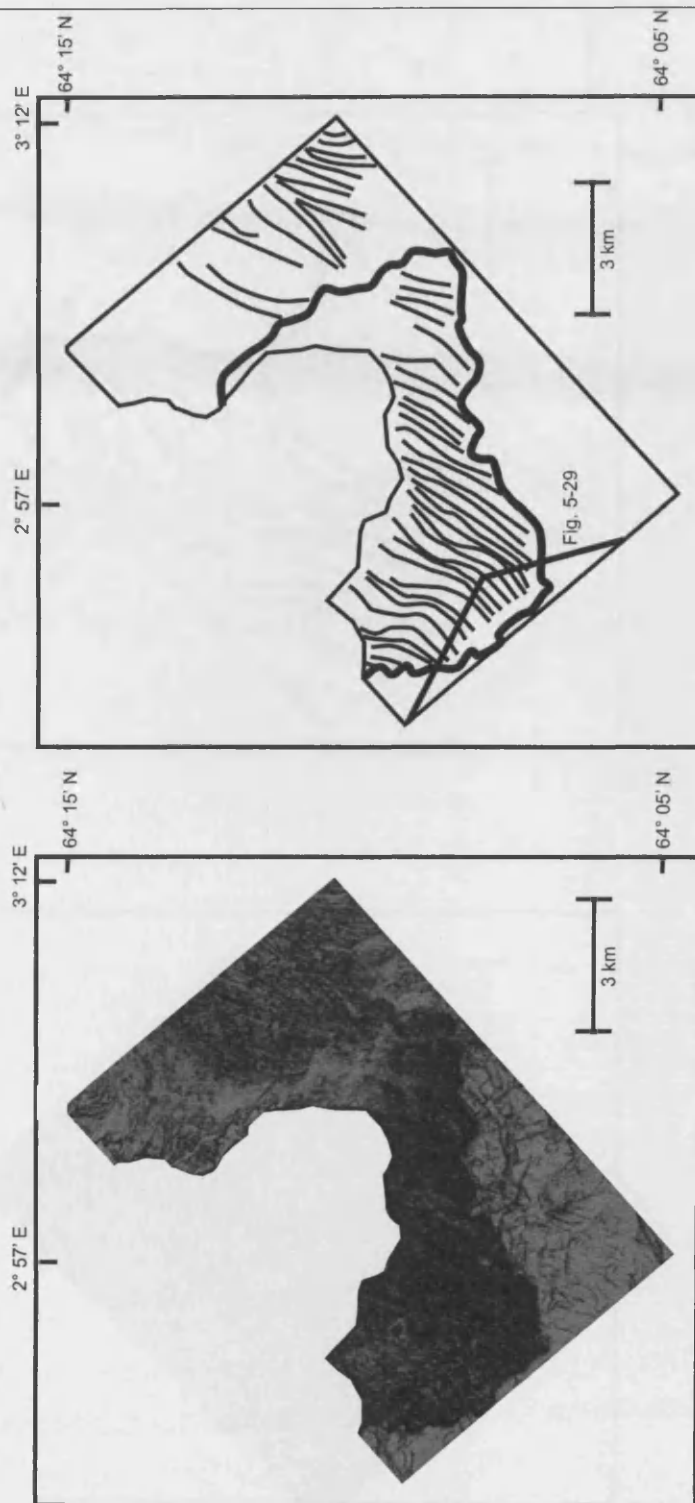


Fig. 5-30: (Top) A coherency slice, highlighting the internal geometry of Crater H. See Fig. 5-25 for location. (Bottom) A sketch, highlighting important features of the coherency slice in (Left). The sidewalls of Crater H are highlighted by a bold solid black line, lineations within the fill of Crater B are highlighted by fine black lines. Location of Fig. 5-28 is indicated.

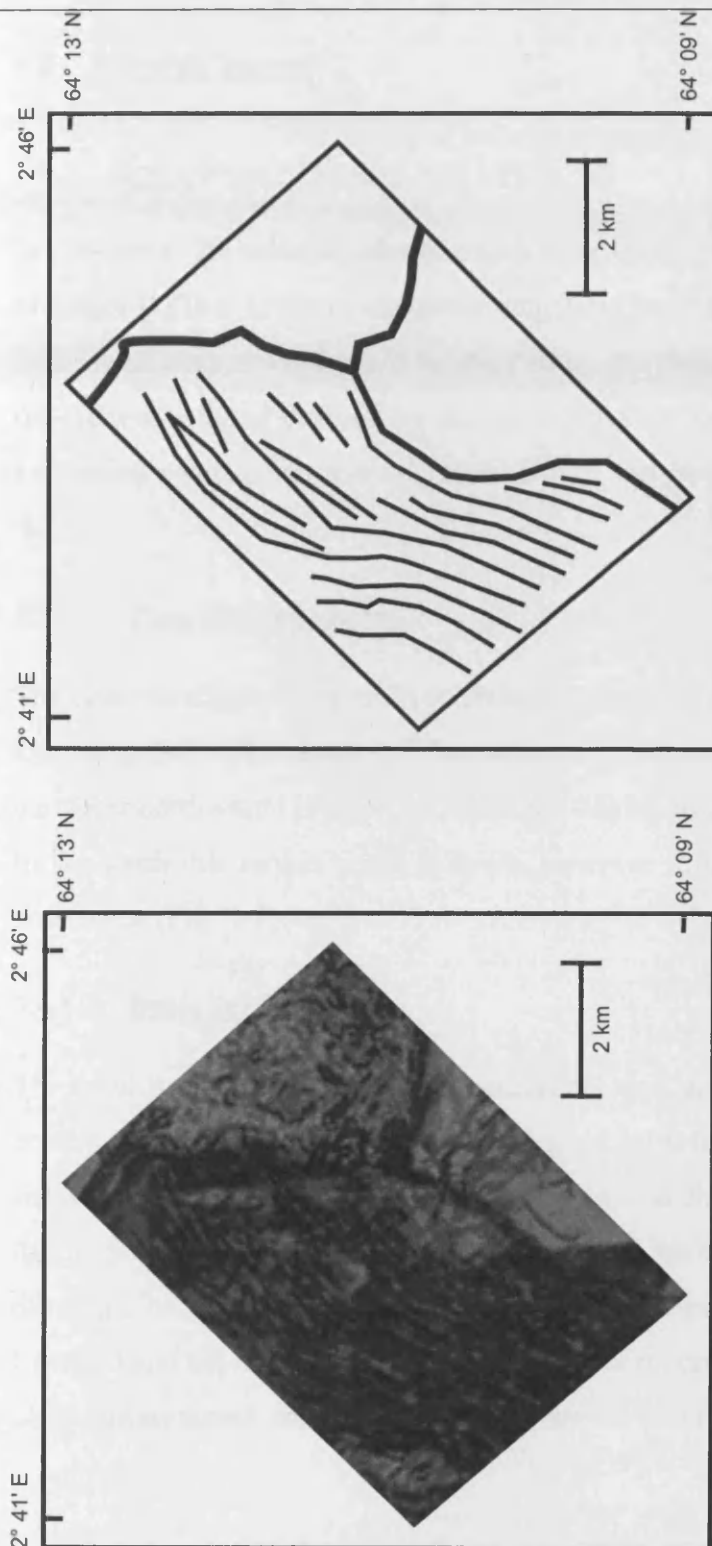


Fig. 5-31: (Top) A coherency slice, highlighting the internal geometry of Crater I. See Fig. 5-25 for location. (Bottom) A sketch, highlighting important features of the coherency slice in (Top). The sidewalls of Crater I are highlighted by a bold solid black line, lineations within the fill of Crater B are highlighted by fine black lines.

5.6 Edvarde Survey

5.6.1 Description of Crater and Crater fill

In Chapter 4, 2D seismic reflection data were used to describe the plan view geometry of Crater D. This crater is somewhat enigmatic because it is not filled by Slide W, and because no ooze mound could be mapped on 2D data. Crater D is fully enclosed, with the sidewalls being defined by the termination of internal reflections of the Brygge Formation against the internal reflections of the Naust Formation (Fig. 5-33 to Fig. 5-36).

5.6.1.1 Plan view geometry

The crater is aligned in a south south east – north north west orientation, and is 25 km long (Fig. 5-3). The crater is 7 km wide at its southern end, becoming progressively narrower northwards (Fig. 5-3). There is a dogleg in the eastern sidewall of the crater. In the south this strikes north to south, however further north it strikes south east to north west (Fig. 5-3)

5.6.1.2 Basal surface

The basal surface of Crater D is irregular, but similar to the basal surfaces of the other craters described above in this chapter. It is defined as a soft reflection which separates the Brygge Formation beneath from the Naust Formation above (Fig. 5-33 to Fig. 5-36). The trace of underlying polygonal faulting can be mapped on relief and dip maps of the crater (Fig. 5-37). A key difference between the basal surface of Crater D and the basal surfaces of other craters described in this chapter is an absence of lineations which are interpreted elsewhere as scour marks.

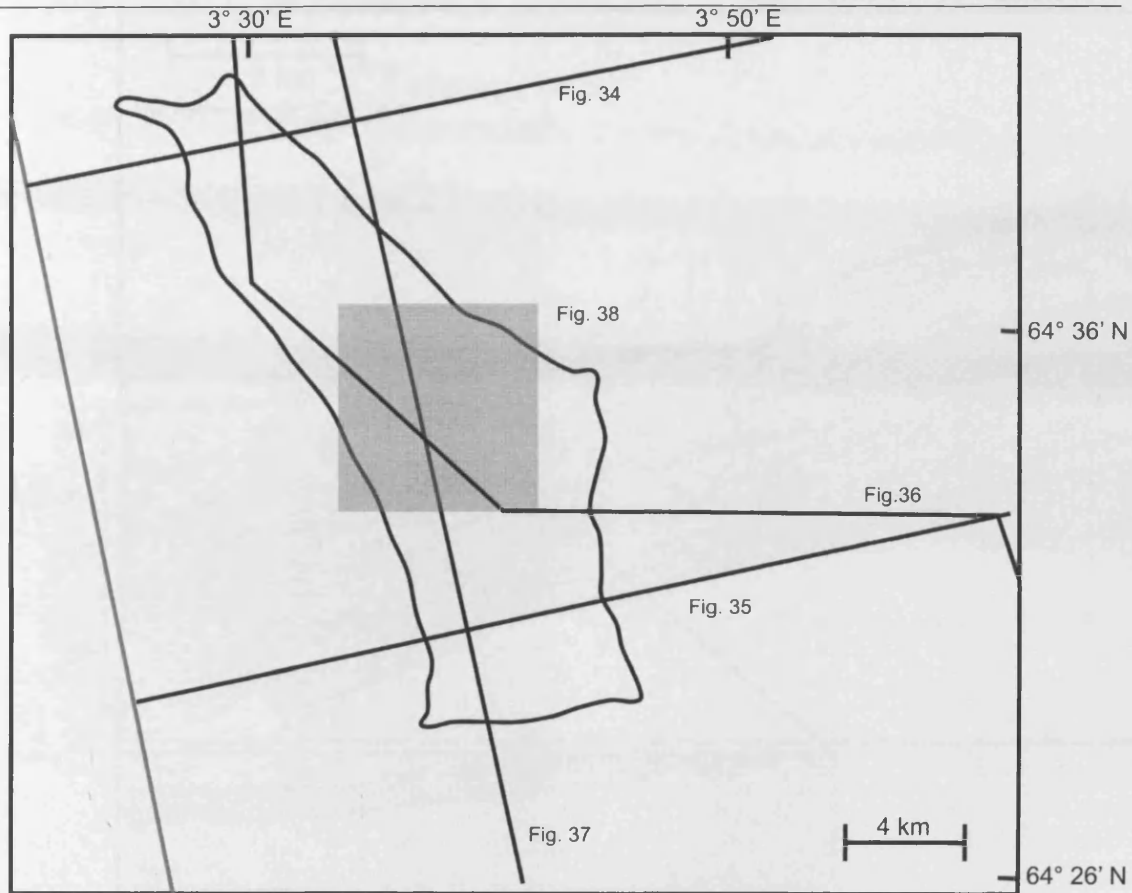


Fig. 5-32: A map of a Crater D and Mound D in the Edvarde Survey highlighting the location of figures pertaining to Crater D and Mound D. The location of the sidewall of Crater D is delineated by a solid line, and the location of the edge of Mound D is delineated by a dotted line.

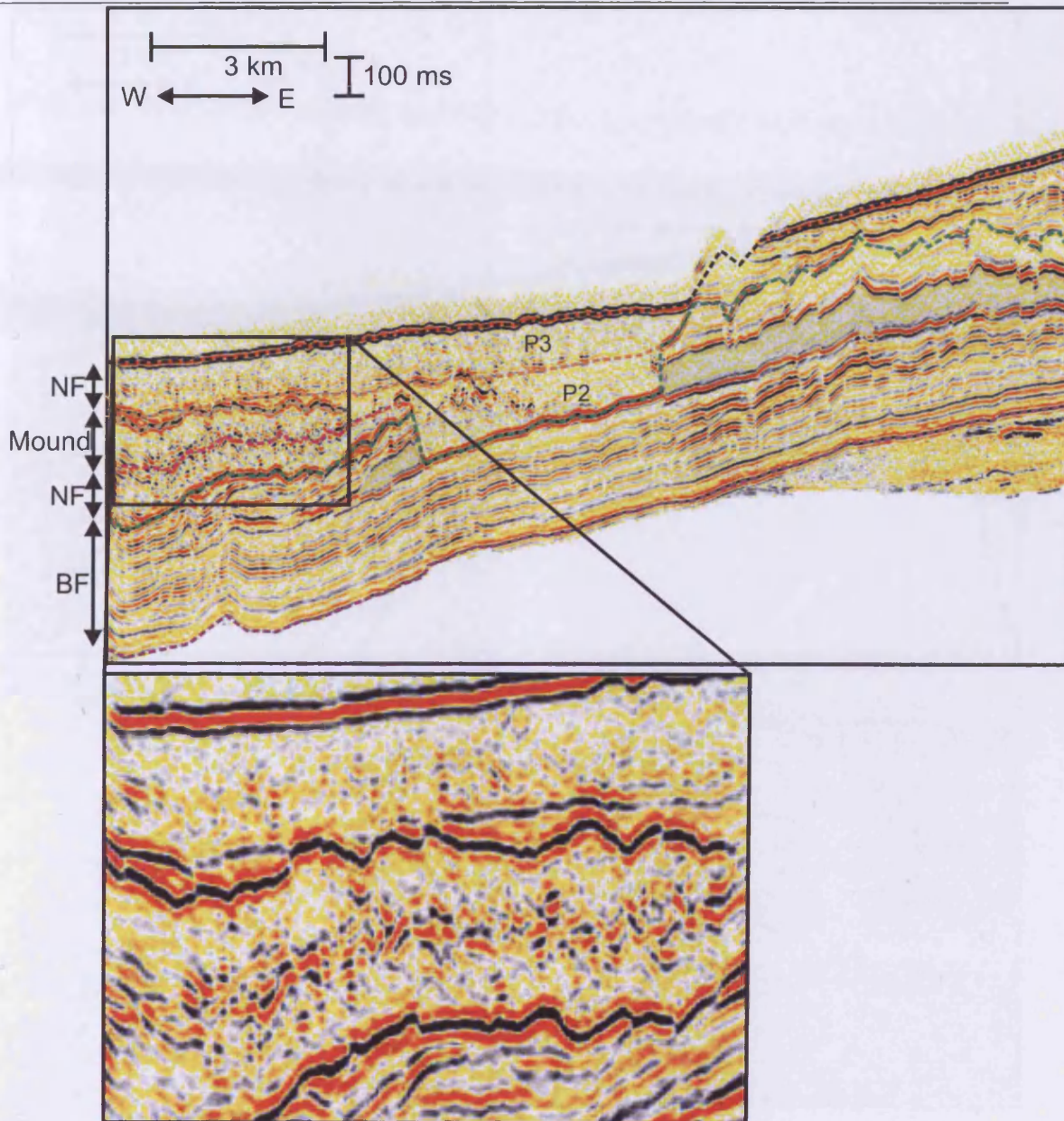


Fig. 5-33: A crossline in time through Crater D and Mound D. See Fig. 5-32 for location. NF: Naust Formation, BF: Brygge Formation, P2: Package 2, P3: Package 3. The lensoid shaped package is highlighted in transparent grey.

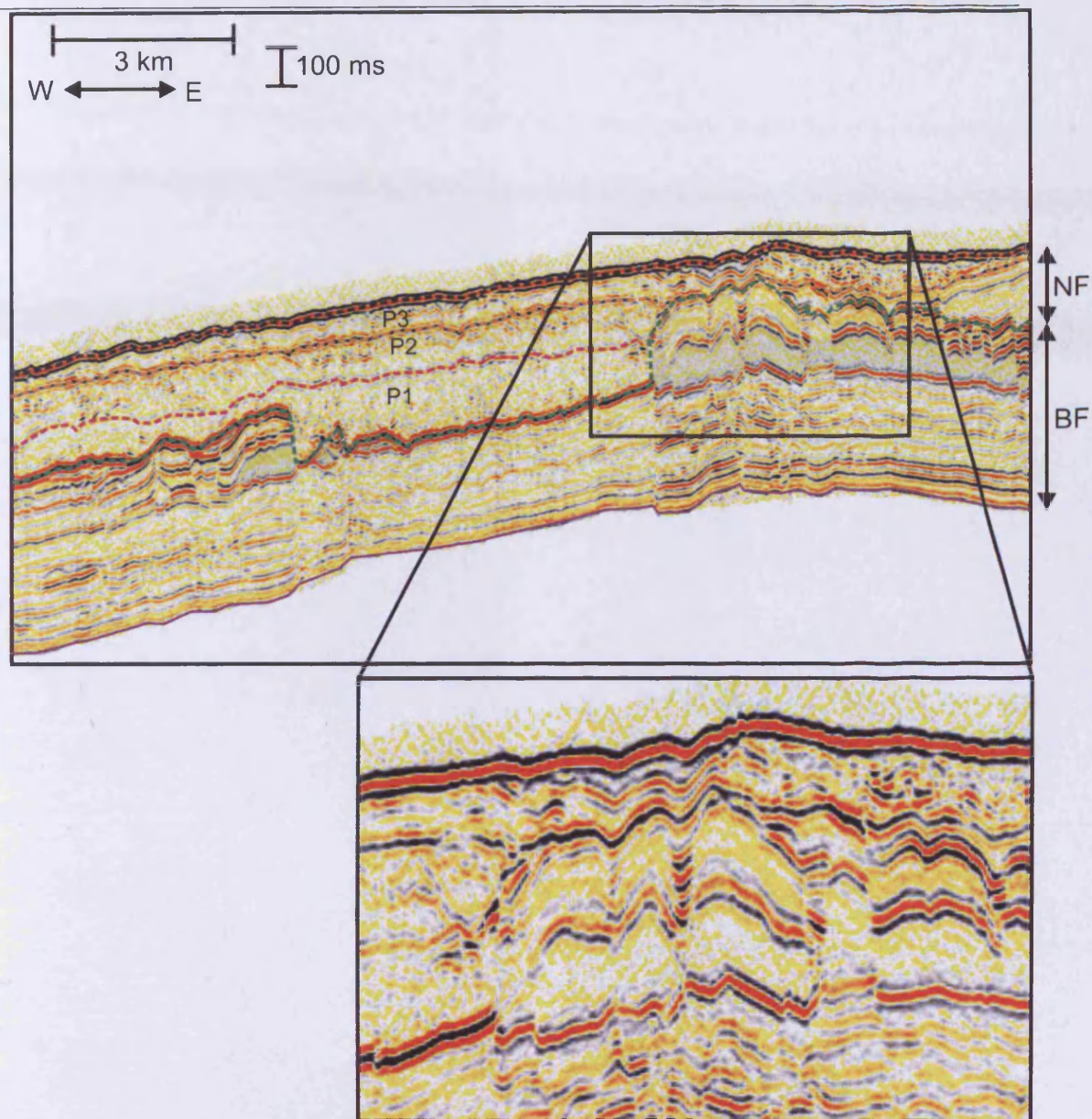


Fig. 5-34: A crossline in time through Crater D. See Fig. 5-32 for location. NF: Naust Formation, BF: Brygge Formation, P1: Package 1, P2: Package 2, P3: Package 3. The lensoid shaped package is highlighted in transparent grey.

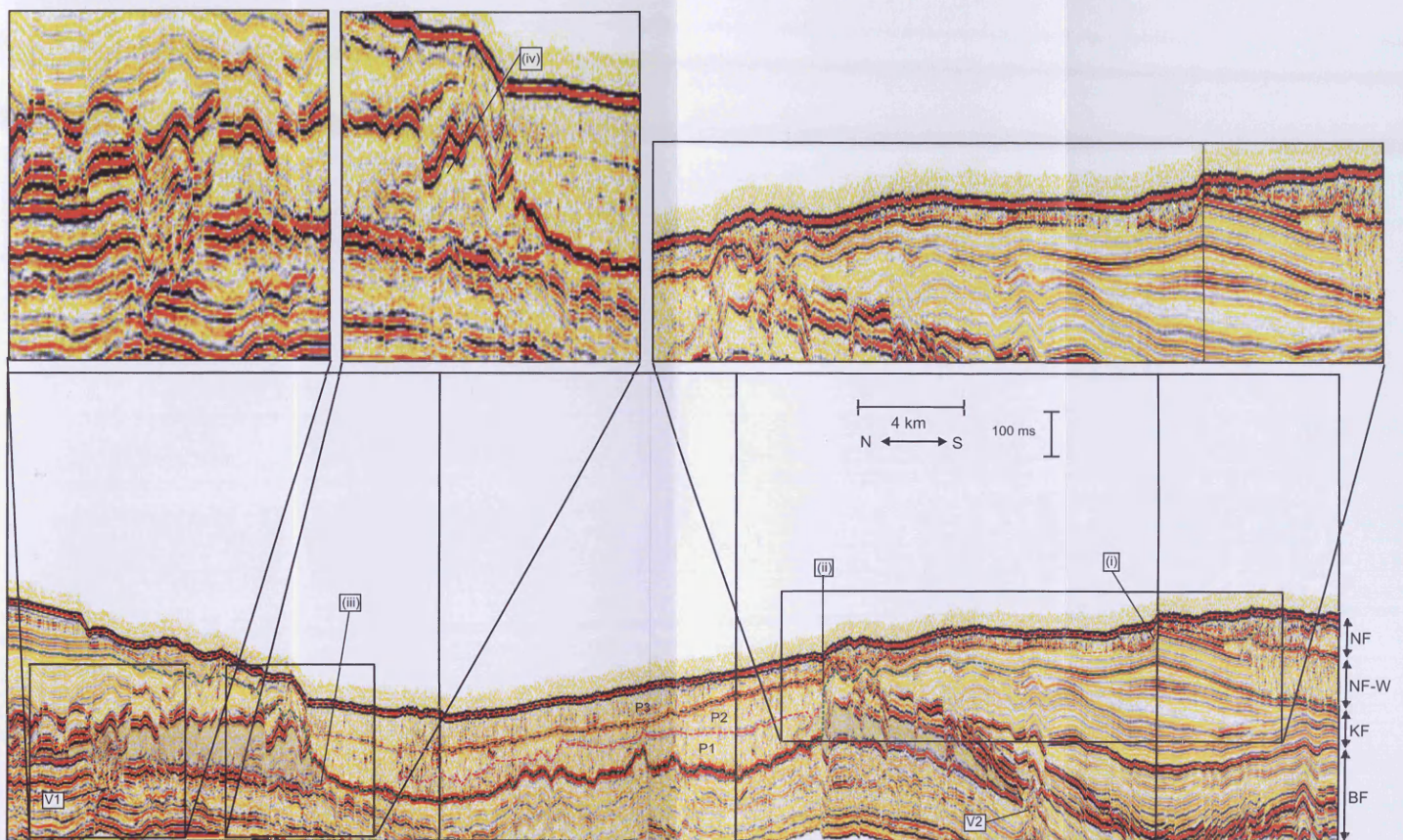


Fig. 5-35: A traverse in time through Crater D. See Fig. 5-32 for location. NF: Naust Formation, NF-W: Naust Formation W, KF: Kai Formation, BF: Brygge Formation, P1: Package 1, P2: Package 2, P3: Package 3. The lensoid shaped package is highlighted in transparent grey. (i) Incision of sediments that can be correlated with Slide W by the Storegga Slide. (ii) Sediments which can be correlated with Slide W truncated at edge of Crater D. (iii) Base of Lensoid shaped package (an opal A/CT boundary) cross cuts stratigraphy. (iv) Sediments of lensoid shaped package are domed between normal faults. V1 and V2: Vent complexes underneath lensoid shaped package.

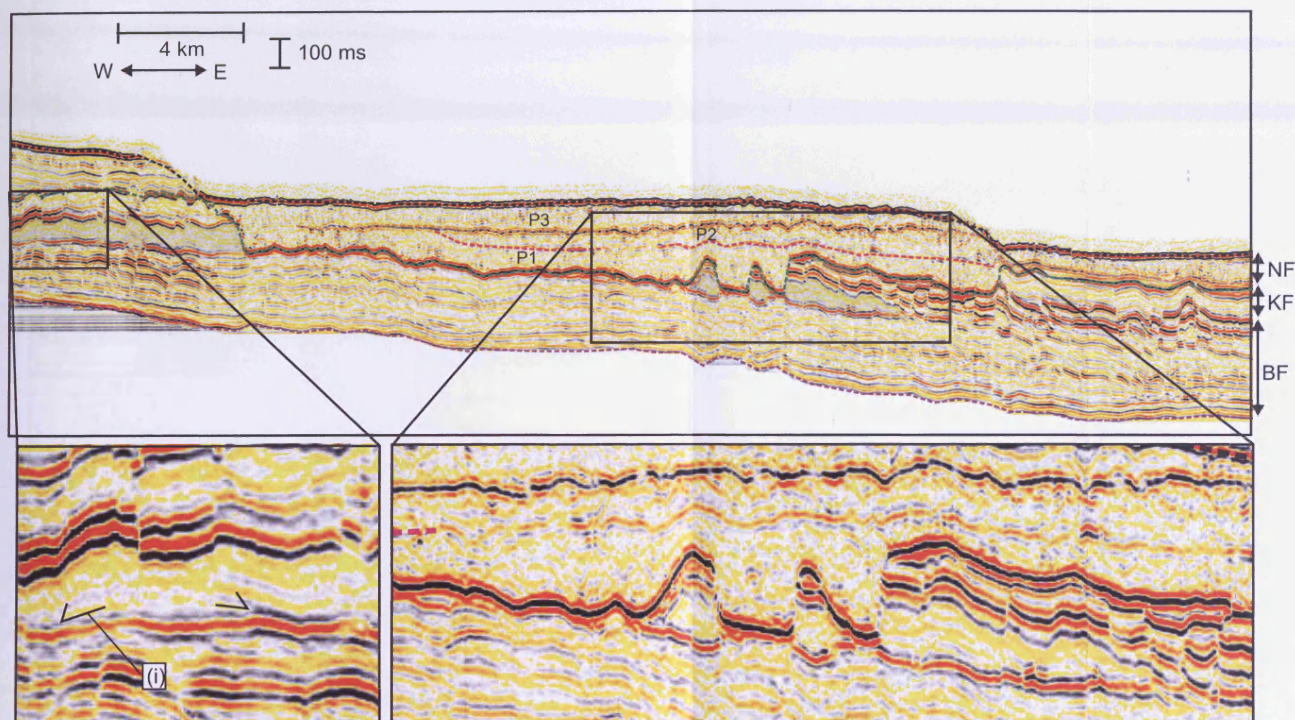


Fig. 5-36: An inline in time through Crater D. See Fig. 5-32 for location. NF: Naust Formation, KF: Kai Formation, BF: Brygge Formation, P1: Package 1, P2: Package 2, P3: Package 3. The lensoid shaped package is highlighted in transparent grey. (i) Downlap of sediments in lensoid shaped package onto opal A/CT boundary.

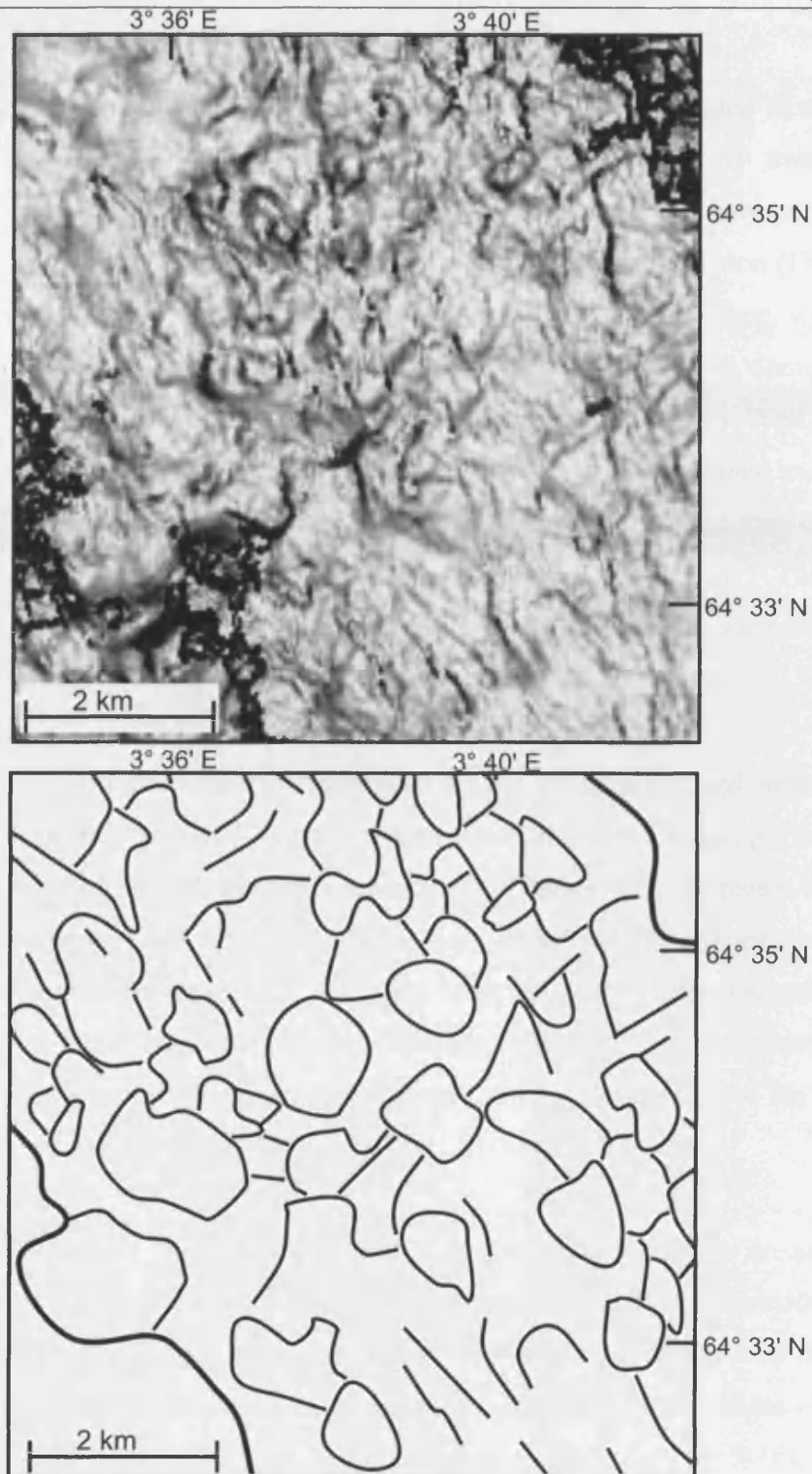


Fig. 5-37: A dip map of a portion of the basal surface of Crater D. For an exact location, see Fig. 5-32. (Top) Non-interpreted dip map. (Bottom) Sketch of dip map displayed above, highlighting important features. The sidewalls of Crater D are highlighted by a bold solid black line. The trace of polygonal faulting is delineated by a finer black line.

5.6.1.3 Sediments evacuated at Crater D

Sediments from the Brygge Formation have been evacuated from Crater D (Fig. 5-33 to Fig. 5-36), however sediments are also evacuated from a lensoid shaped stratigraphic package that is discontinuous and which is only mapped within the Møre Basin in the region of Crater D within the Brygge Formation (Fig. 5-33 to Fig. 5-36). This lensoid shaped package is centred on the Havsule Dome, with the package being thickest on the crest of the dome and pinching out on the dome flanks (Fig. 5-33 to Fig. 5-36). The lensoid shaped package is penetrated by Well 6403/6-1. While the package was not sampled, the geophysical data suite obtained in the package indicates that the package has a density of 2.1 g/cm^3 , slightly lower than the Brygge Formation above the package which has a density of 2.15 g/cm^3 . This indicates that the composition of this package is not too different from the composition of the rest of the Brygge Formation.

The bottom surface of the lensoid shaped package is a high amplitude hard reflection (Fig. 5-33 to Fig. 5-36) that is interpreted elsewhere as an opal A/CT boundary that is mapped beneath the other craters (e.g. Chapter 4). Underneath 90 % of the sediment body, the opal A/CT boundary is concordant with stratigraphy beneath the boundary; however the opal A/CT boundary cross cuts stratigraphy beneath the boundary at the north western corner of the sediment body (Fig. 5-35). Sediments from the lensoid shaped package are evacuated from Crater D downwards to the opal A/CT boundary (Fig. 5-33 to Fig. 5-36).

The upper surface of the lensoid shaped package is also an acoustically hard high amplitude reflection. On seismic reflection data internal reflections within this lensoid shaped package has anomalously low amplitude (Fig. 5-33 to Fig. 5-36). These reflections are semi-continuous, and, particularly at the edges of the sediment body, downlap onto the opal A/CT boundary (e.g. (i) on Fig. 5-36). Between the normal faults, which cut across the package, the interior reflections of the sediment body have a domed appearance (e.g. (iv) on Fig. 5-35).

The dip of reflections above the lensoid shaped package is greater than the dip of the reflections beneath the lensoid shaped package (Fig. 5-33 to Fig. 5-36). This might be

indicative of sediment above the lensoid shaped package collapsing into the lensoid shaped package, which would suggest that the lensoid shaped package was not able to support large loads and may have had low shear strength. However the lensoid shaped package is now cross cut by normal faulting, which suggests that the lensoid shaped package gained shear strength after burial, becoming more brittle, by a mechanism similar to dewatering. The deformation of the overburden extends upwards into a package of sediments that is correlated with Slide W (Fig. 5-35). This indicates that the deformation of the lensoid shaped package occurred at around this time.

A number of columnar features consisting of vertical stacks of disrupted reflections are observed beneath the lensoid shaped sediment package, with these features being terminated at the base of the lensoid shaped sediment package (e.g. V1 and V2 on Fig. 5-35). In geometry, these are similar to the vents in this area described by Svensen et al. (2003), and are therefore interpreted as such.

5.6.1.4 Burial of Crater D

Crater D is buried by three stratigraphic packages that can be delineated on 3D seismic reflection data (Fig. 5-33 to Fig. 5-36). Each of these packages is characterised by the internal reflections consisting of discontinuous low amplitude reflections (Fig. 5-33 to Fig. 5-36). Each package is bounded below and above by a continuous high amplitude reflection. The bottom most package to bury Crater D is bounded below by an acoustically soft reflection and above by an acoustically hard reflection, and is named Package 1 (Fig. 5-33 to Fig. 5-36). The middle package which buries Crater D is bounded by the acoustically hard reflection that is the upper boundary to Package 1, is bounded above by an acoustically soft reflection, and is named Package 2 (Fig. 5-33 to Fig. 5-36). The topmost package to bury Crater D is bounded below by the acoustically soft reflection which is the upper boundary of the middle package and is bounded above by the present day seabed, which is an acoustically hard reflection (Fig. 5-33 to Fig. 5-36). This is named Package 3.

The top surface of Package 1 is a semi-continuous lower amplitude reflection, which cannot be traced over ca 50 % of the crater (Fig. 5-38). A mound that is too small to be interpreted on 2D data is mapped pinching out onto this surface to the north west

of the crater, in a manner similar to the way that Mound B pinches out onto the top surface of Slide W. This mound, named Mound D, is up to 150 m thick (Fig. 5-33). The volume of Mound D is impossible to measure because it is located on the edge of the dataset, however the portion of Mound D within our dataset is miniscule compared to the amount of sediment that has been removed from the crater. Mound D is similar in its characteristics to Mound GJ, described above. The top surface of Mound D is characterised by a series of randomly arranged ridges and troughs (Fig. 5-33). Ridges on the top surface of the mound are associated with troughs on the basal surface of the mound (Fig. 5-33). The top surface of Mound D is overlapped by later sediments, suggesting that Mound D was emplaced at the seabed (Fig. 5-33).

Package 3 is exposed at the present day seabed. Lineations which strike from east to west above the southern portion of Crater D and which curve so that they strike parallel to the eastern sidewall of Crater D from south east to north west above the northern portion of Crater D are imaged on the basal surface of this package. These are interpreted as scour marks on the basal shear surface of the Storegga Slide (Fig. 5-39). This interpretation is confirmed by the mapping of similar lineations eastwards of Crater D on the basal shear surface of the Storegga Slide (Fig. 5-39).

Packages 1 and 2 are also interpreted as separate slides. This interpretation is primarily on the basis that both packages consist of internal discontinuous reflections with low reflection amplitude (e.g. Fig. 5-33 to Fig. 5-36), but the interpretation of these two features as separate slides as opposed to one slide is because of the mound on the top surface of package 1, which does not appear to be an intrusive feature in the middle of a slide consisting of packages 1 and 2 because of the lack of deformation of the package 2 above this feature.

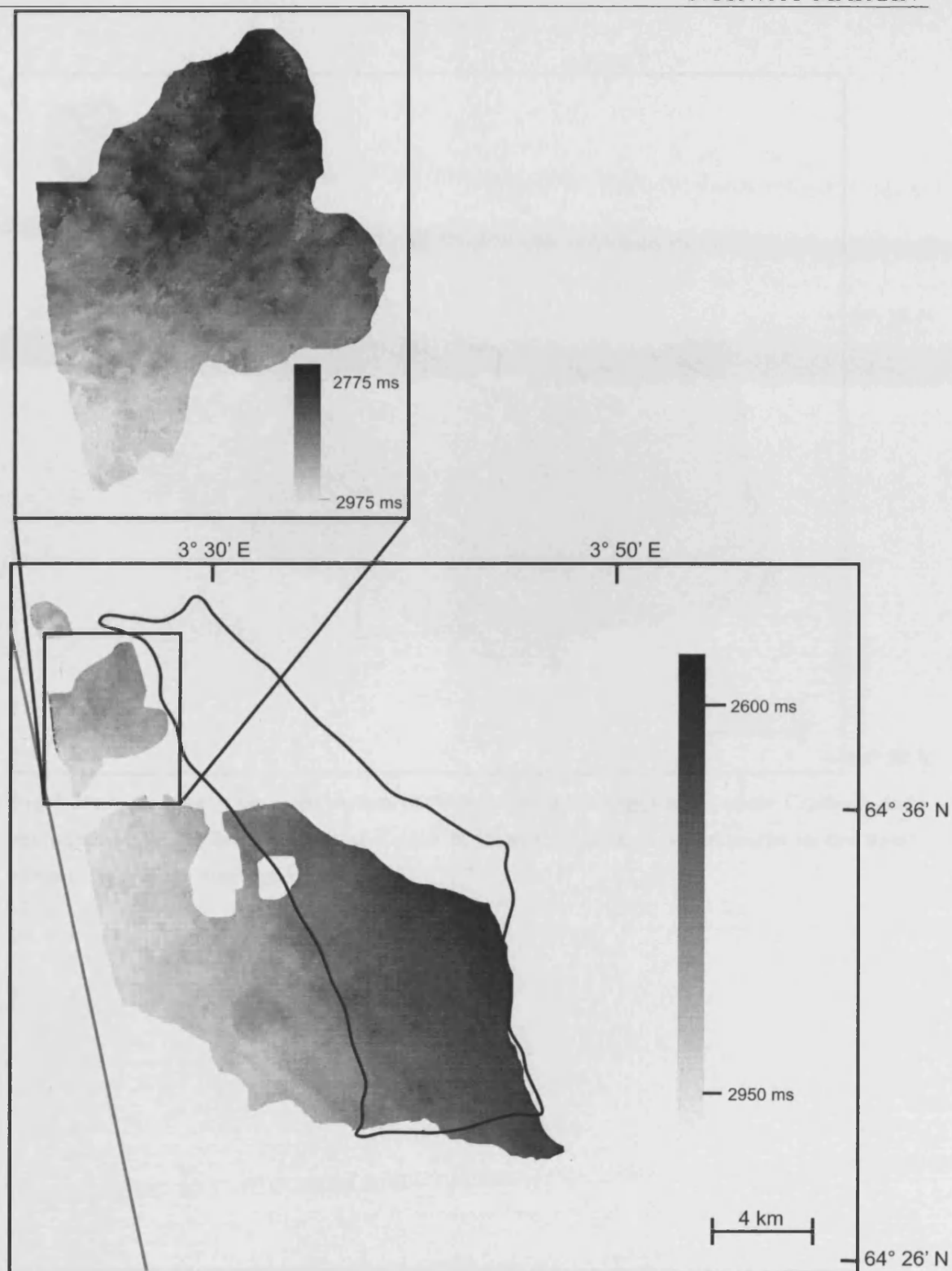


Fig. 5-38: A time map of the top surface of Package 1 in the area of Crater D. In the region of Mound D (shown in the insert), the top of Mound D is taken as the top of Package 1.

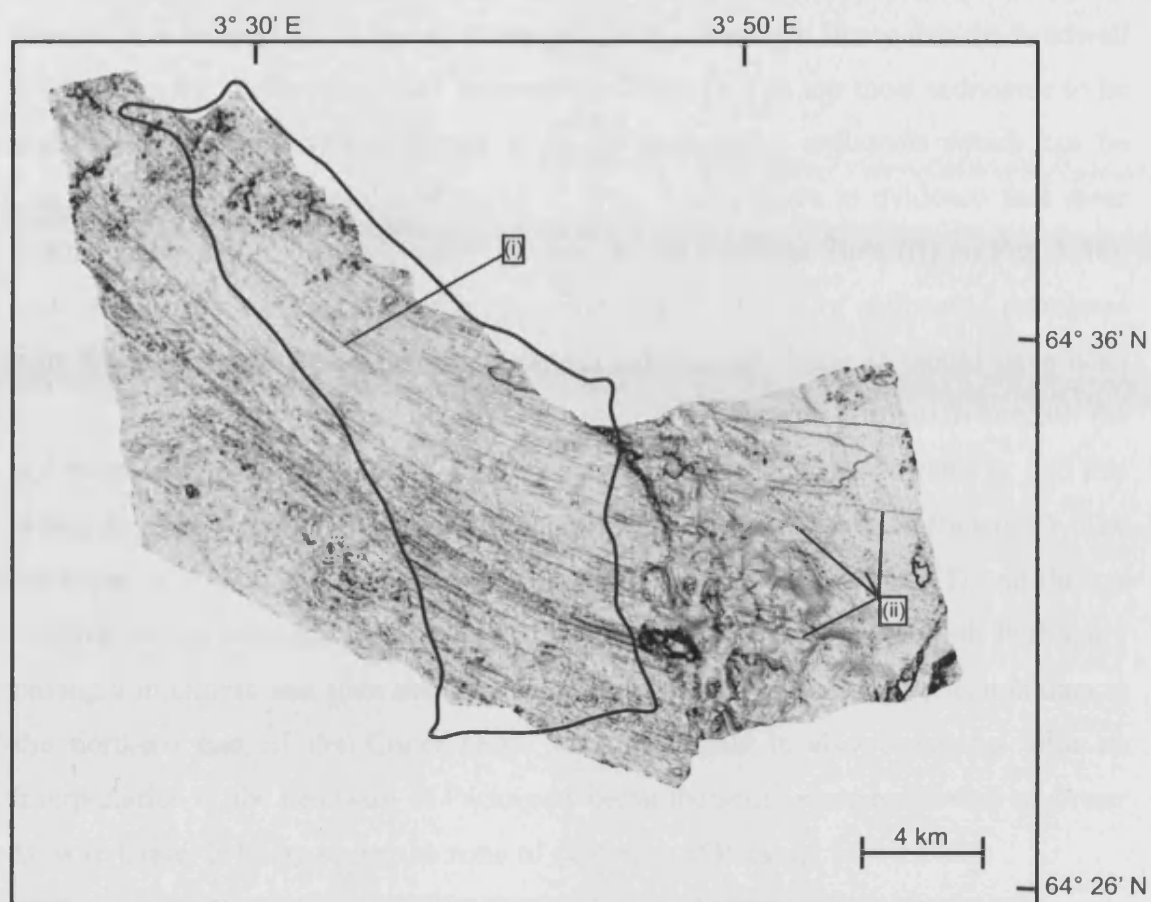


Fig. 5-39: A dip map of the basal surface of Package 3 (The Storegga Slide) above Crater D, and eastwards of the southern portion of Crater D. (i) and (ii) indicate scour marks on the Basal shear surface of the Storegga Slide.

Package 1 is of particular interest, because this slide fills Crater D, and because Mound D is on the top surface of Package 1. It is considered likely that the headwall of Package 1 is the south eastern sidewall of Crater D. The top most sediments to be truncated at the sidewall of Crater D is the package of sediments which can be correlated with the sidewalls of Slide W (Fig. 5-35). There is evidence that these sediments have been incised further upslope by the Storegga Slide ((i) on Fig. 5-36), and that therefore prior to the Storegga Slide the thickness of sediments correlated with Slide W truncated at the south eastern sidewall of Crater D would have been greater. The top of Package 1 is truncated against the Brygge Formation beneath the sediments correlated with Slide W at the south eastern sidewall of Crater D, and this would be consistent with Crater D being in the zone of depletion of Package 1. The thickness of Package 1 is thinner near the eastern sidewall of Crater D and thicker towards the western sidewall of Crater D (Fig. 5-33 and Fig. 5-34), with Package 1 having a thickness less than that which can be resolved on seismic reflection data at the northern end of the Crater (Fig. 5-33), and this is also consistent with an interpretation of the headwall of Package 1 being the south eastern sidewall of Crater D, with Crater D being under the zone of depletion of Package 1.

It is considered less likely that Package 1 is correlated with slides which occurred after Slide W which are incised further up the continental slope by the Storegga Slide, although this eventuality cannot be precluded. Had this been the case, it would have been more likely that the thickness of Package 1 in Crater D would have been thicker, and that the top surface of Package 1 would be truncated against the top surface of the south eastern sidewall. Mound D is not truncated or incised, and because Mound A is on the top surface of Package 1 it follows that Package 1 has not undergone significant incision by Package 2.

The observation that Package 1 is not incised and that the top surface of Package 1 is truncated close to the base of the eastern sidewall of Crater D demonstrates that the area mapped as Crater D underwent unloading during the formation of Crater D.

5.7 Synthesis

Craters A, B, D, H and I are features defined at the top of the Brygge Formation and the base of the Naust Formation. The sidewalls of these craters are defined as being a surface where internal reflections of the Brygge Formation are truncated against internal reflections of the Naust Formation.

Craters A, B, D, H and I are filled by Plio-Pleistocene slides which have occurred on the mid Norway margin. Craters A and B are filled by Slide W (Chapter 3). Craters H and I are filled by a slide which incises Slide W eastwards of Craters H and I. Crater D is filled by a slide, the timing of which with respect to Slide W is uncertain.

The fill of Craters A, B, H and I are characterised by a series of closely spaced shallowly dipping thrust faults with an easterly component of dip, demonstrating that these craters are formed in zone of accumulation of the slides which fill them. The spacing of these faults is c. 200 m and the average dip of these faults in Crater B is c. 11.2° , with a standard deviation of 2.1° . In craters A and B, fluid escape pipes are observed which exploit these thrust faults and cross cut these thrust faults. At crater D, the slide which first fills the crater is depleted, suggesting that this crater formed in the zone of depletion of this slide.

A relationship is observed at Craters A and B between the direction of flow of Slide W and the dip of the sidewalls of these craters. It is observed that sidewalls dipping downslope in the direction of movement of Slide W are shallowest, sidewalls dipping towards the headwall of Slide W are steeper, and that sidewalls dipping towards the lateral margins of Slide W are the steepest.

The base of Craters A, B, D, H and I can be defined as the basal shear surface of the slides which fill these craters. On the basal surface of Craters A, B, H and I scour marks trending c. east to west are observed c. 1 km long. On the basal surface of Crater B a rise which is reminiscent of a Roche Moutonnée is observed. The orientation of this rise would be consistent with abrasion of the shallower eastward dipping slope of the rise by Slide W.

Craters A, B and D are overlain by mounds of remobilised sediment which are emplaced on the top of the slides which fill these craters. The mounds associated with Craters A and B are emplaced in a topographical depression on the top surface of Slide W which is located over the western sidewalls of Craters A and B. The upper surface of the mounds which overlie Craters A and B is characterised by a series of c. north to south trending ridges which are correlated vertically with troughs on the basal surface of the mounds, and by a series of randomly distributed conical rises. These may represent Rayleigh Taylor Instability. These ridges and conical rises are onlapped by overlying sediments, suggesting emplacement of the mounds at the seabed. The internal geometry of the mounds which overlie Craters A and B are characterised by a series of interpreted shallowly dipping normal faults dipping westwards which link troughs on the top surface of these mounds with ridges on the basal surface of the mounds. The westward dipping slopes of the top surface of the mounds which overlie Craters A and B are on average steeper than the eastward dipping slopes of the mounds which overlie Craters A and B. The external and internal geometry of the mounds is consistent with necking, boudinage and extension of the mounds. The volume of the mound which overlies Crater A is larger than that of Crater A.

Part of a mound which overlies craters G and J (craters G and J are not covered by 3D data) is mapped. This mound is emplaced on the top surface of Slide W and is named Mound GJ. Mound GJ is essentially similar to the mounds which overlie Craters A and B, however differs in that there is no preferred orientation of ridges on the top surface of Mound GJ, that there is no preferred orientation of normal faults in Mound GJ, and that Mound GJ has been incised by the slide which fills Craters H and I (described above). Well evidence at Mound GJ suggests that during emplacement of this mound there may have been attrition of pyrite and carbonate at the base of Slide W or in the internal fill of Slide W, and that sediments within Slide W may have been mixed into the remobilised sediments.

5.8 Discussion

A key question posed at the beginning of this chapter is whether these craters form because of fluid flow from beneath (a bottom upwards hypothesis, Hypothesis A, Fig. 4-6), or whether the craters form due to loading of the Brygge Formation by slides

such as Slide W (a top downwards hypothesis, Hypothesis B, Fig. 4-7). The key to understanding whether these craters are formed because of fluid flow from below, potentially triggering the slide, lies in understanding whether remobilisation of ooze started before or after the start of sliding. The challenge is that any deformation associated with a remobilisation of ooze before the initiation of sliding may be overprinted by the slide process, meaning that any features described here may be overprinting original deformation structures, if they existed.

It is not considered likely that the craters were ever exposed on the seafloor. In Chapter 3 Slide W was described as likely having a minimal translation distance of under 10 km, being more akin in some respects to an area of in situ sediment remobilisation. Given that Craters A and B are located a minimum of 80 km from the toe region of Slide W, it follows that the site of Craters A and B would have been buried at the time of sliding. Other craters described here and in Chapter 4 are also some distance from the headwall region of Slide W (see Fig. 4.1 in Chapter 4). It has been established (Chapter 4, Riis et al., 2005) that mounds emplaced above craters on the top surface of the first slide to bury the craters are sourced from the Brygge Formation. If the ooze mounds are sourced from the craters, and if Slide W is not translated far (<10 km, Chapter 3), the ooze must have transposed strata, therefore it is considered impossible that the craters formed on the seabed and were buried before the occurrence of later slides.

5.8.1 Evaluation of Hypotheses A and B

Much of the evidence presented in this chapter could be argued to be in favour of either Hypothesis A or Hypothesis B. For example, Craters A, B, H and I exhibit scour marks on their basal surfaces, demonstrating that Slide W was translated across the basal surfaces of Craters A and B and that other slides were translated across the basal surface of Craters H and I. This could mean that the external morphology of craters such as Craters A, B, H and I was modified by later slides (consistent with Hypothesis A), or alternatively that later slides continued to translate across the crater floors of Craters A, B, H and I after loading and carving out the craters (consistent with Hypothesis B).

The incisions in the western sidewall of Crater B described above are in some ways reminiscent of the headwall and sidewalls of slides, and may represent collapse of the sidewalls into the area of the craters. For the crater wall to fail sediments adjacent to the crater wall must either be removed or undergo a change in physical properties such as undergoing liquefaction or fluidisation, so that sediments sourced from failure of the sidewall could displace sediments adjacent to the sidewall. Fluidisation and liquefaction would be in keeping with Hypothesis A. Alternatively the incisions on the western sidewall of Crater B could represent incision of the western sidewall of Crater B by Slide W after formation of the crater with incised ooze sediment being mixed into Slide W or remobilised to the surface, a scenario which could arise under Hypothesis A or Hypothesis B.

It has been demonstrated above that there is a good relationship between the morphology of Craters A and B and the flow direction of Slide W. A general rule is that sidewalls parallel to the flow direction of Slide W are steeper than sidewalls perpendicular to the flow direction of Slide W. This could imply steepening of lateral sidewalls by Slide W indicating erosion of the lateral sidewalls, or could represent abrasion of the western and eastern sidewalls of these craters, also indicating erosion. These would be especially compatible with Slide W loading and carving out the Craters (Hypothesis B), but it could also be compatible with Hypothesis A if Slide W merely modifies the morphology of the craters.

The observation of thrust faulting in the internal geometry of Craters A, B, H and I, and the idea that thrust faulting within the interior fill of Craters A and B may be exploited by hydrocarbon fluid flow, raises the possibility of liquefied sediment also using the thrust as a conduit to the surface. The thrust faults in the internal fill of Craters A and B would only form subsequent to the initiation of Slide W. Therefore if the thrust faults were exploited by liquefied sediment as a conduit to the surface, it is likely that liquefaction of the Brygge Formation would occur after the initiation of Slide W, suggesting a possible causal relationship between Slide W and liquefaction of the Brygge Formation. This would be consistent with Hypothesis B, but could also be consistent with Hypothesis A if liquefaction occurred prior to sliding and upwards remobilisation occurred after the initiation of sliding.

An important observation is that Crater D underwent unloading during crater formation. This contradicts Hypothesis B, which requires the Brygge Formation to be loaded by a slide to bring about liquefaction.

5.8.2 A new hypothesis

Neither Hypothesis A nor Hypothesis B satisfactorily explains the formation of craters and the remobilisation of ooze to mounds on the mid Norway margin. Any hypothesis developed to explain the formation of craters and remobilisation of ooze must account for the fact that it is necessary for ooze of the Brygge Formation to be transposed through the overlying Naust Formation, because the spacing of craters on the basal surface of Slide W and mounds on the top surface of Slide W (~40 km, Chapter 4) is far greater than the displacement of Slide W (< 10 km, Chapter 3). Here a new hypothesis, Hypothesis C, is developed and presented. Hypothesis C links the formation of craters and remobilisation of ooze to the dissociation of gas hydrate brought about by the rapid deposition of the Naust Formation on top of the Brygge Formation. Gas hydrate is formed on parts of the mid Norway margin at the present day; however it is believed that gas hydrate formation is currently inhibited because of the presence at the sea bed of sediments with poor porosity and permeability (Bünz et al., 2003). No direct evidence of gas hydrate at the present day is observed in the study area. Hypothesis C is not supported by direct evidence, and therefore Hypothesis C should be regarded as speculative and in further need of testing. Strengths and weaknesses of Hypothesis C will be highlighted in the following part of this chapter.

5.8.2.1 Gas Hydrates

Gas hydrate dissociation is well known to lead to destabilisation of large volumes of slope sediment (e.g. Kennett et al., 2003, McIver, 1982). Gas Hydrate dissociation has been implicated in the triggering of the Storegga Slide (e.g. Bryn et al., 2005a, Mienert et al., 2005). The conditions at the time of crater formation are therefore evaluated, to examine whether gas hydrate could have been present in sufficient quantities to warrant examination of dissociation as a potential trigger.

The sediments which comprise Slide W are correlated with a contourite sequence (Chapter 3), which has been identified as ideal for the formation of gas hydrate (Bünz et al., 2003). Rapid deposition of sediments which comprise Slide W between 4 Ma and 1.8 Ma (Chapter 2) would cause the base of the gas hydrate stability zone to shoal upwards. The consequent dissociation of gas hydrate to free gas could create overpressured conditions at the top of the Brygge Formation if a connected gas column would be able to form.

This system might be fed by advection of free gas from depth. The large accumulation of gas at the nearby Ormen Lange gas field suggests a significant source of thermogenic gas. The Upper Jurassic Spekk Formation has been identified as a potential source rock; although this may be overmature (e.g. Swiecicki et al., 1998). There may also be Upper Cretaceous oil source intervals (e.g. Brekke et al., 1999). Continued advection of gas from depth, which is believed to be the source for gas hydrate formation on the mid Norway margin (Bünz et al., 2003), would contribute to the overpressured conditions. This overpressure would persist until the free gas could escape into the ocean atmosphere system, and it is hypothesised that this may be at the time of failure of Slide W and crater formation. These ideas are tested, using craters A and B as a case study.

In order to understand how the theoretical position of the base of the Gas Hydrate Stability Zone relates to the regional opal A/CT boundary, the depositional thickness of the Brygge Formation above the arrested opal A/CT transition in the areas of Craters A and B must be calculated accurately. It is also important to know the depositional thickness of Slide W in the area of craters A and B to understand accurately the relationship between migration of the base of the Gas Hydrate Stability Zone and sedimentation between 4 Ma and 1.8 Ma. The compaction of sediments on the mid Norway margin is estimated using the formula:

$$C = (1 - \Phi_i) / (1 - \Phi_f) [1] \text{ (Berner, 1980)}$$

where Φ_i is the initial porosity, and Φ_f is the formation porosity.

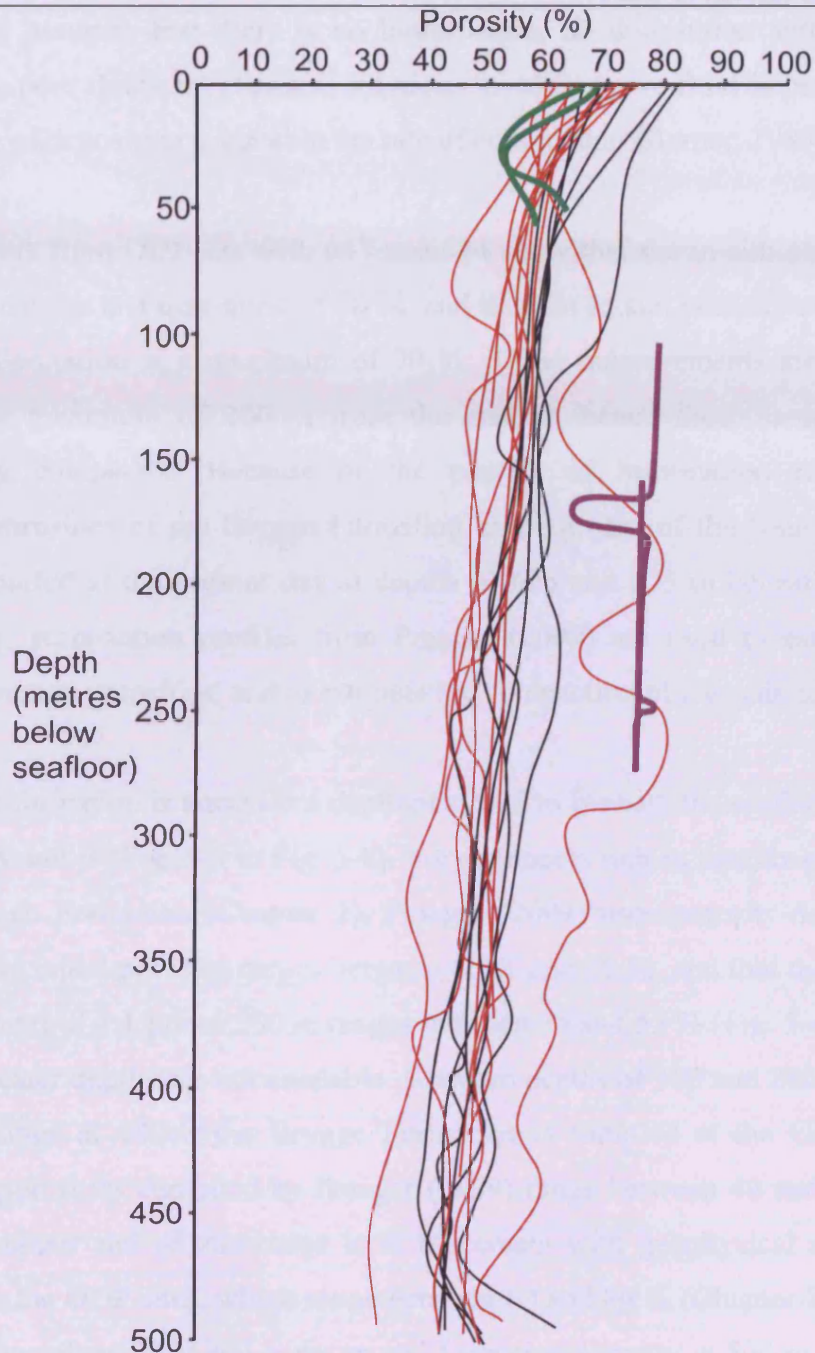


Fig. 5-40: Best fit porosity-depth profiles from Praeger (2009), taken from ODP Site 717, Indian Ocean; ODP Site 900, Iberia margin; ODP Site 931, Amazon Fan; ODP Site 935, Amazon Fan; ODP Site 944, Amazon Fan; ODP Site 976, western Mediterranean; ODP Site 977, western Mediterranean; ODP Site 979, Western Mediterranean; ODP Site 985, North Atlantic; ODP Site 986, North Atlantic; ODP Site 1079, West Africa; ODP Site 1146, South China Sea; ODP Site 1148, South China Sea; ODP Site 1245, Cascadia Margin; and ODP Site 1324, Gulf of Mexico. Ooze rich lithologies are indicated in black and clay/silt/sand rich lithologies are indicated in red. Superimposed on the data are porosity depth profiles for sediments correlated with the Naust Formation (green) and the Brygge Formation (purple) at ODP sites 642 and 643, compiled from Hempel et al. (1989)

Formula [1] assumes that there is no bioturbation, no dissolution and removal of sediment by pore fluids, no chemical reactions involving pore fluid or bulk solid, and that the rate of deposition is equal to the rate of compaction (Berner, 1980).

Measurements from ODP site 642, 643 and 644 show that the in-situ porosity of the Brygge Formation is a maximum of 80 %, and that the in-situ porosity of the base of the Naust Formation is a maximum of 70 %. These measurements are taken from sediments a maximum of 200 m from the seabed; hence these samples are not significantly compacted. Because of the paucity of information regarding the formation porosities of the Brygge Formation and the base of the Naust Formation, which are buried at the present day at depths of 625 and 475 m beneath the seabed respectively, compaction profiles from Praeger (2009) are used to estimate likely current formation porosities, and to estimate the compaction of the sediments.

The Brygge formation is buried at a depth of c. 625 m beneath the seafloor in the area of Craters A and B (Fig. 5-3 to Fig. 5-8). For sediments rich in nanofossil ooze, such as the Brygge Formation (Chapter 2), Praeger (2009) uses porosity-depth plots to show that the initial porosity ranges between 65 % and 80 %, and that the porosity of these sediments at a depth of 500 m ranges between 35 and 55 % (Fig. 5-40). Porosity values at greater depths are not available. Between depths of 100 and 280 m, which is the depth range at which the Brygge Formation is sampled at the ODP holes in Chapter 2, porosities compiled by Praeger (2009) range between 40 and 80 % (Fig. 5-40). The upper end of this range is in agreement with geophysical and sampled porosities at the ODP sites, which range between 60 and 80 % (Chapter 2, Fig. 5-40). Therefore the values for initial porosity and formation porosity at 500 m burial depth from Praeger (2009) are substituted into expression [1] to find the uncompacted thickness of the Brygge Formation. It is found that these sediments have undergone compaction ranging between 0.33 and 0.77. Given that the sampled porosities of the Brygge formation lie at the upper end of the range of ooze rich sediments described by Praeger (2009) (Fig. 5-40), compaction is likely to be at the upper end of this range. This means that the original uncompacted thickness of the Brygge Formation would lie within a range between 195 m and 455 m, lying close to the bottom end of this range.

The Naust Formation is buried approximately 475 m beneath the seafloor in the area of Craters A and B (Fig. 5-3 to Fig. 5-8). For more clay rich sediments, such as those found at the base of the Naust Formation (Chapter 2), porosity-depth plots compiled by Praeger (2009) show that at 475 m the porosity of these sediments varies between 25 % and 60 %, and that the initial porosity of these sediments varies between 80 % and 60 % (Fig. 5-40). From 0 to 50 m depth, the depth at which the Naust Formation is sampled at the ODP sites described in Chapter 2, the porosities compiled by Praeger (2009) for more clay rich sediments are between 30 and 80 %, which agrees with a range of 50 to 70 % found at the ODP sites described in Chapter 2 (Fig. 5-40). Therefore values for initial porosity and formation porosity at 475 m burial depth from Praeger (2009) can be substituted into expression [1] above. It is found that these sediments have undergone compaction ranging between 0.27 and 0.73, which would imply that the uncompacted depth of the Naust W at the base of the Naust Formation would lie within a range between 205 m and 555 m.

The likely thickness of the gas hydrate stability zone before, during and after Slide W will be dependent on temperature, and therefore on the geothermal gradient (e.g. Dickens, 2001). The present day geothermal gradient on the mid Norway margin is modelled using the current position of the base of the gas hydrate stability zone to the north of the study area, and is found to be between 51.5 °C/km and 55.8 °C/km (Bouriak et al., 2000). This unusually high geothermal gradient may represent thinning of the continental crust in this area (Olafsson et al., 1992). A lower figure of between 31 and 53 °C/km has been put forward as a geothermal gradient in this region (Neagu et al., in press); however these lower values are derived from uncorrected bottom borehole temperatures, hence the higher geothermal gradient suggested by Bouriak et al. (2001) is preferred.

The thickness of the gas hydrate stability zone is dependent on pressure and therefore will be constrained by water depth (e.g. Dickens, 2001, Fig. 5-41). The current water depth in the vicinity of Craters A and B is 1500 m. The onset of northern hemisphere glaciation is often cited as occurring between 2.6 and 2.7 Ma on the basis of Ice Rafted Debris (Hjelstuen et al., 2005, Jansen et al., 2000), which is in the middle of the period during which the sediments that comprise Slide W were deposited. From

3.2 Ma to 1.8 Ma $\delta^{18}\text{O}$ records in the North Atlantic show that sea level dropped by 40 m (Fig 5-42, Sosdian and Rosenthal, 2009).

The depth of the gas hydrate stability field will also be affected by bottom water temperature, so it is important to consider how bottom water temperature might have changed between 4 Ma and 1.8 Ma. Between 17 and 16 Ma the seabed temperature at high latitude was 5 – 6 °C warmer than at the present day (Savin et al., 1975). Since then there have been two periods of climatic deterioration – from 15 to 12 Ma, and from 4 to 2 Ma (Fig. 5-43, Wright and Miller, 1996). Global temperature has decreased from 5 Ma during the second period of climatic deterioration to the present by 3.5 °C (Lear et al., 2003). Wright and Miller (1996) show that $\delta^{18}\text{O}$ increased from 2 to 2.9 from 15 to 12 Ma, and that $\delta^{18}\text{O}$ increased from 2.9 to 4 from 4 to 2 Ma (Fig. 5-43, Wright and Miller, 1996). Northern Component Water flux increased at 12.5 Ma (Fig. 5-43, Wright and Miller, 1996), it has been estimated that the initiation of the onset of deep water circulation through the Faeroe-Shetland Basin caused seabed temperatures to reduce by 3 – 4 °C (Coachman and Aagaard, 1974). There was a significant increase in Northern Component Water flux from 4 to 3 Ma (Fig. 5-43, Wright and Miller, 1996) during the period of climatic deterioration from 4 to 2 Ma, this may have caused further cooling of temperature at the seabed. A Mg/Ca record at mid latitudes in the North Atlantic from Sosdian and Rosenthal (2009) shows cooling from 5 – 2 °C from 3.2 to 1.8 Ma (Fig. 5-44).

Graphs showing the likely depth of the gas hydrate stability zone beneath the seafloor at 4 Ma and the depth of the gas hydrate zone beneath the seafloor at 1.8 Ma after deposition of the sediments that comprise Slide W are plotted after Dickens (2001) in order to test the hypothesis that the base of the gas hydrate zone shoaled upwards towards the boundary between the Brygge Formation and the Naust Formation during the deposition of sediments that comprise Slide W (Fig. 5-41).

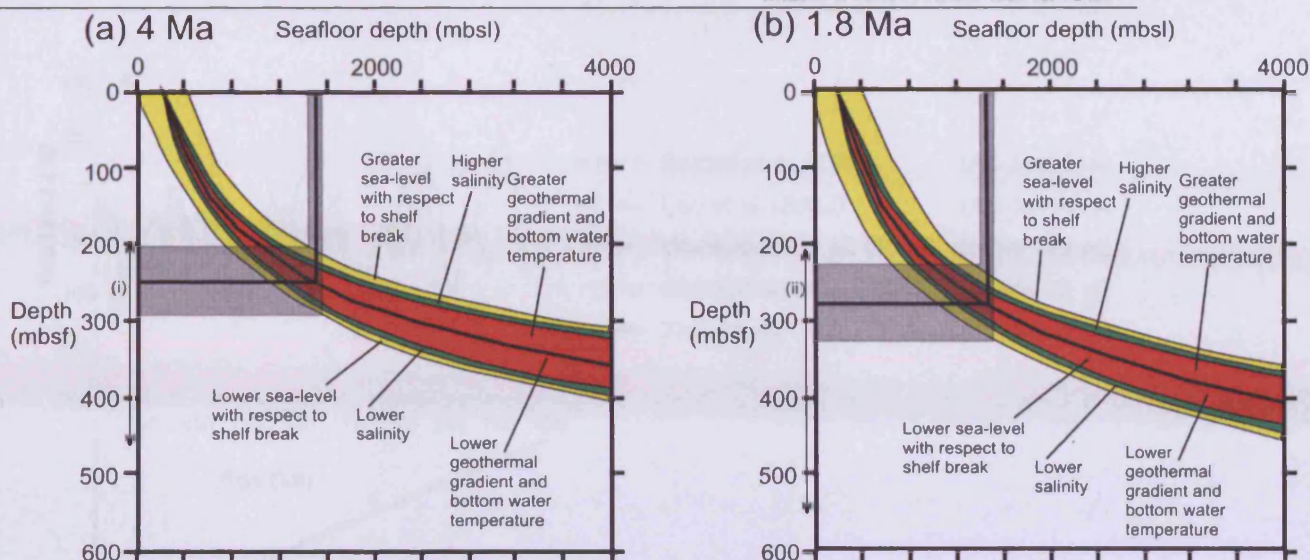


Fig. 5-41: After Dickens et al. (2001). (a) Graph of seafloor depth vs. depth of the base of the gas hydrate zone beneath the seafloor at 4 Ma before deposition of Naust W sediments. Sources of uncertainty are indicated, and are relative to the assumed conditions (see text). (i) Range of the thickness of the depth beneath the sea floor of the opal A/CT transition. (b) Graph of seafloor depth vs. depth of the base of the gas hydrate zone beneath the seafloor at 1.8 Ma after deposition of Naust W sediments. Sources of uncertainty are indicated, and are relative to the assumed conditions (see text). (ii) Range of the thickness of the depth beneath the sea floor of the boundary between the Naust Formation and the Brygge Formation.

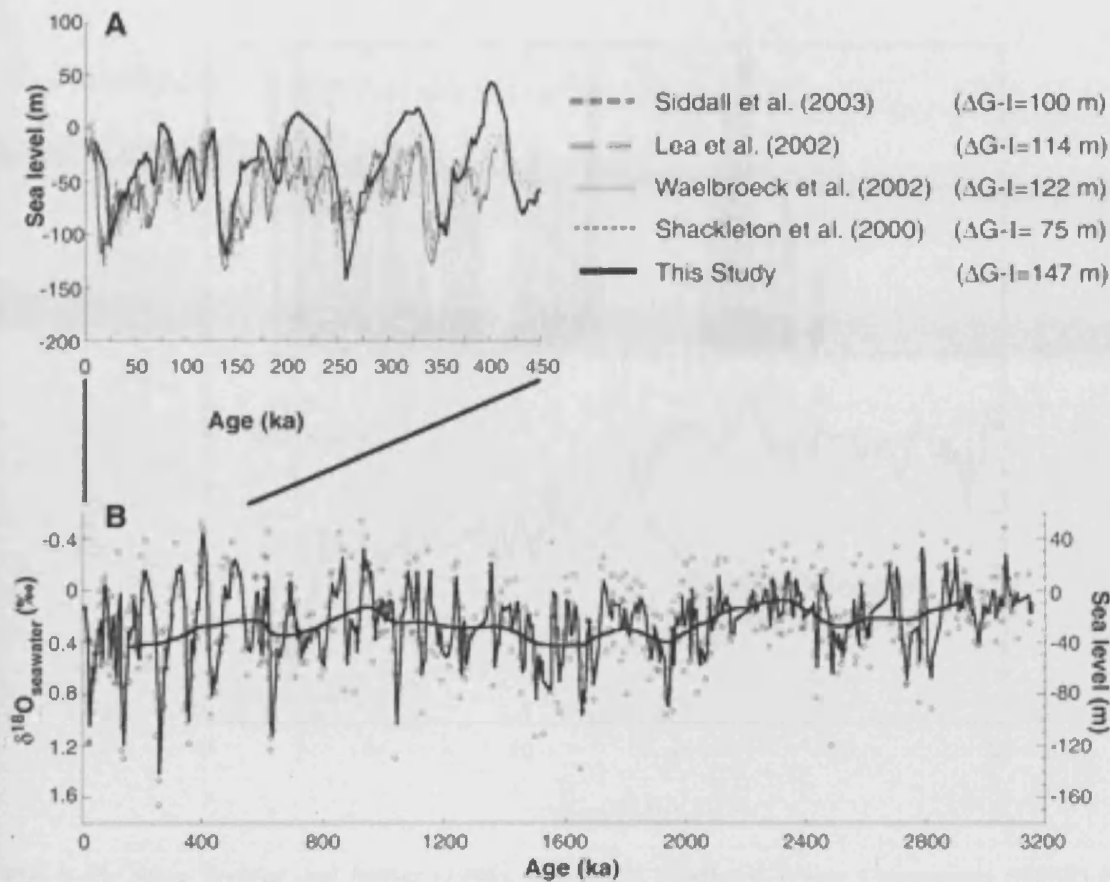


Fig. 5-42: After Sosdian and Rosenthal (2009). $\delta^{18}O$ records for the North Atlantic, indicating eustatic sea level change from 3.2 Ma to the present.

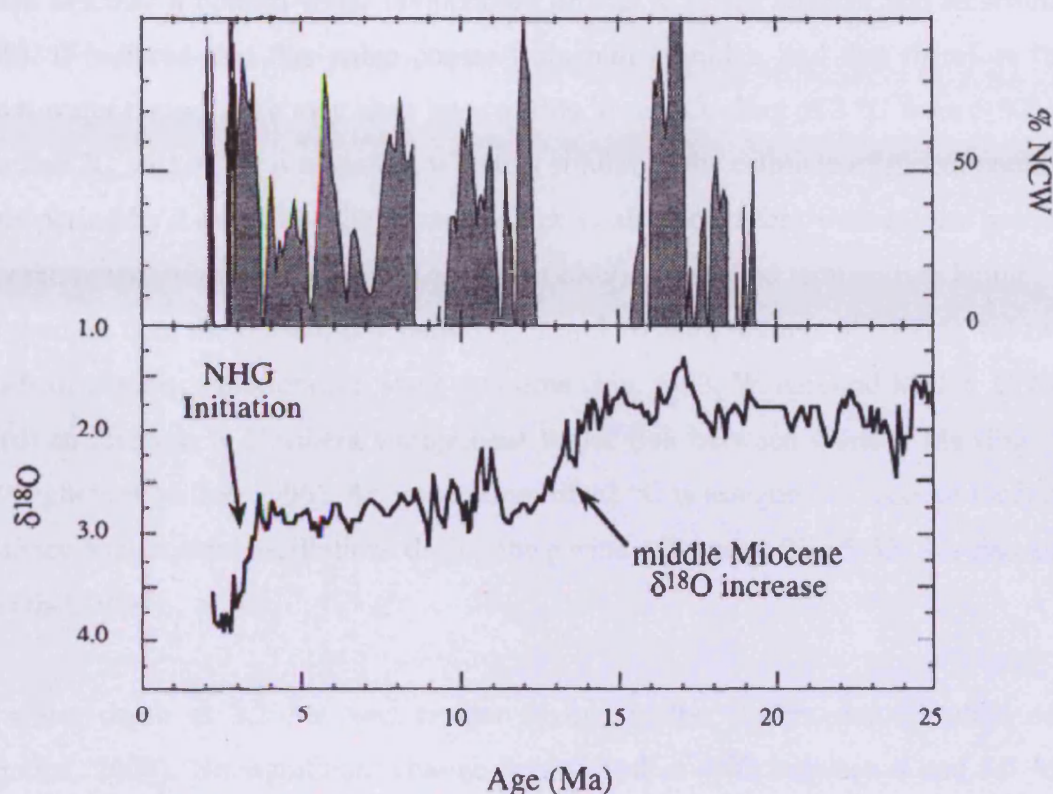


Fig. 5-43: After Wright and Miller (1996). Record of Northern Water Component (NCW) flux (obtained by recording benthic foraminiferal $\delta^{13}\text{C}$ changes in the southern ocean relative to change in North Atlantic and Pacific records) and of $\delta^{18}\text{O}$ (obtained from Benthic Foraminifera) between 25 Ma and 2.5 Ma (the record from 2.5 Ma to the present is not shown due to high frequency variations). NHG: Northern Hemisphere Glaciation. Two periods of climatic deterioration are observed between 15 and 12 Ma, and between 4 and 2 Ma. An increase in NCW flux is observed at 12.5 Ma, and between 4 and 3 Ma.

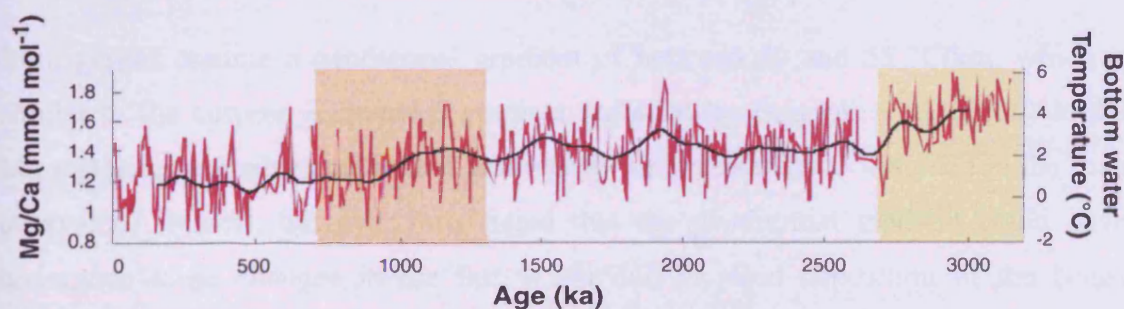


Fig. 5-44: After Sosdian and Rosenthal (2009). Mg/Ca record from the North Atlantic (DSP Site 607, approx 40 °N and 35 °W), indicating changes in bottom water temperature from 3.2 Ma to the present.

The graph showing the likely depth of the base of the Gas Hydrate Stability Zone at 1.8 Ma assumes a bottom water temperature of $\sim 2^\circ\text{C}$, after Sosdian and Rosenthal (2009). It is noted that this value comes from mid latitudes, and that therefore the bottom water temperature may have been a little lower. Cooling of 3°C from 5°C at 4 Ma to 2°C at 1.8 Ma is assumed, which is similar to the estimate of global cooling in this period by Lear et al. (2003), and which is also consistent with (a) the bottom temperature record of Sosdian and Rosenthal (2009), (b) seabed temperature being $5 - 6^\circ\text{C}$ warmer than the present day between 17 and 16 Ma (Savin et al., 1975), (c) two periods of climatic deterioration since this time (Fig. 5-43, Wright and Miller, 1996), and (d) an increase in Northern Component Water flux between 4 and 3 Ma (Fig. 5-43, Wright and Miller, 1996). An uncertainty of $\pm 2^\circ\text{C}$ is assigned to account for high frequency temperature oscillations during the period of interest (Fig 5-42, Sosdian and Rosenthal, 2009)

The water depth at 3.2 Ma was similar to that at the current day (Sosdian and Rosenthal, 2009). No significant change is observed in $\delta^{18}\text{O}$ between 4 and 3.5 Ma (Fig. 5-43, Wright and Miller, 1996), suggesting that there was no significant change in eustatic sea level during this time. Therefore the current day water depth of 1500 m is assumed for 4 Ma. A water depth of 1460 m is estimated at 1.8 Ma from $\delta^{18}\text{O}$ records in the North Atlantic (Sosdian and Rosenthal, 2009). An uncertainty of ± 40 m is assigned to account for high frequency oscillations of sea level during the period of interest (Fig 5-42, Sosdian and Rosenthal, 2009).

Both graphs assume a geothermal gradient of between 50 and $55^\circ\text{C}/\text{km}$, which is similar to the current geothermal gradient recorded by Bouriak et al. (2000) in the Møre Basin. A similar geothermal gradient to the present day is assumed in the time interval of interest, however it is noted that the geothermal gradient could have undergone large changes in the last 4 Ma due to rapid deposition of the Naust Formation. A key issue which remains to be resolved is the competition between the rate of deposition, the rate of heating and the slope of the gas hydrate phase boundary. A weakness of Hypothesis C is the assumption that heat flow in the Møre Basin is able to adjust to rapid deposition of the Naust Formation, and this part of the hypothesis would require further testing and refinement.

Other important factors that have been identified which may affect the depth of the gas hydrate stability zone are the salinity of the body of water in which sediments are deposited and the sea level depth at the continental shelf (Dickens et al., 2001). Salinity is assumed to be close to current day conditions, however this assumption also requires further testing and refinement. The depth of the continental shelf is related to sea level changes, because the craters occupy a similar position with respect to the continental shelf through the period of interest. The given uncertainty reflects the uncertainty in sea levels given above. The uncertainties associated with salinity and the depth of the continental shelf are also displayed on the graphs.

The graphs displayed in Fig. 5-41 demonstrate that the predicted base of the gas hydrate stability zone at 4 Ma is 245 m below the seafloor, with an uncertainty of ± 45 m. This overlaps with the calculated range of depths of the opal A/CT boundary beneath the seabed at 4 Ma before deposition of the sediments that fail as Slide W, which is calculated to be in the range 195 and 445 m (see above). The graphs displayed in Fig. 5-41 also show that the predicted base of the gas hydrate stability zone at 1.8 Ma is between 225 m and 325 m. This overlaps with the range of depths calculated for the boundary between the Naust Formation and Brygge Formation at 1.8 Ma, which is calculated to be at the lower end of the range between 205 and 555 m (see above). These findings are consistent with the hypothesis that the failure of Slide W and the formation of Craters may be related to the base of the gas hydrate stability zone shoaling towards the boundary between the Brygge Formation and the Naust Formation at 1.8 Ma.

Free gas at the base of the gas hydrate stability zone would occupy a reservoir bounded beneath by the opal A/ CT boundary and bounded above by the base of the Gas Hydrate Zone and the base of the Naust Formation at 1.8 Ma. It is considered that clay in the Brygge Formation allows polygonal faults to provide a sideways lateral seal (c.f. Bouvier et al., 1989), although this requires further work to establish whether this could be the case.

5.8.2.2 Fluidisation or Liquefaction of the Brygge Formation

Sediments may be remobilised from the base of the craters to the top of a slide which fills the craters by a process which may involve liquefaction and fluidisation of sediments at the floor of the craters (Riis et al., 2005).

Fluidisation occurs when the fluid drag force of an ascending fluid is equal to or exceeds the weight of individual particles in a sediment body (Maltman and Bolton, 2003). Fluidisation is most likely to occur in sediment bodies consisting of cohesionless granular material (Owen, 2003). Fluidisation can result in sorting of granular sediments, and can also result in the upward transportation of sediments (Owen, 2003).

Liquefaction occurs when the pore fluid pressure in a sediment body equals the normal stress across solid contacts, such that the grain weight is supported by the pore fluid (Owen, 2003).

As a sediment body such as the Brygge formation undergoes burial, it will compact if drainage is good and pore fluids can drain away, with the effective stress (total stress minus pore pressure) of the sediment body increasing. If drainage is poor and pore fluid cannot drain away, the sediment body will maintain its depositional porosity and effective stress (Maltman and Bolton, 2003). Drainage is affected by factors such as whether the sediment body under consideration is surrounded by less permeable sediments, and whether voids in the sediment body are filled by sediments with a smaller grain size (Seed et al., 2001).

To decrease the effective stress of a sediment body such as the Brygge Formation so that grain weight can be increasingly supported by pore fluid, the pore pressure of the sediment body can be increased by the addition of pore fluid at a rate faster than the added pore fluid can be drained. This is known as overpressure (e.g. Bowers, 2002, Byerlee, 1990, Mann and Mackenzie, 1990, Osborne and Swarbrick, 1997, Westbrook and Smith, 1983). Alternatively lithostatic load can be removed. This will result in the sediment body becoming over consolidated (Maltman and Bolton, 2003).

A decrease in effective stress brought about by unloading is ruled out; because before the craters form Naust formation sediments were being deposited rapidly on top of the Brygge Formation. An increase in pore pressure brought about by the addition of fluid is a relevant factor to consider here, especially considering the likely dissociation of gas hydrate within Brygge Formation sediments and the addition of free gas from below (see Chapter 4). The dissociation of 1 m³ of gas hydrate at standard temperature and pressure will yield 0.8 m³ of water and 164 m³ of methane (Kvenvolden, 1993). If there is not sufficient pore space to store the excess gas within the Brygge Formation at formation fluid pressure, the methane will be compressed according to the ideal gas law into the available pore space at a greater pressure than the fluid pressure prior to the addition of gaseous methane. If the gas could form a connected gas column, an overpressure could develop due to gas buoyancy effects.

Overpressuring of the Brygge Formation due to the dissociation of gas hydrate requires that the Brygge Formation be effectively sealed so that fluid cannot be displaced from the reservoir by the addition of gaseous methane. It is shown in Chapter 2 above that the permeability coefficient of the Brygge Formation at a depth of 100 to 200 m below the seafloor ranges between 1×10^{-7} and 1×10^{-5} cm/s, and that the permeability coefficient of the base of the Naust Formation at a depth of 0 to 50 m beneath the seafloor ranges between 1×10^{-9} and 1×10^{-6} cm/s (Pittenger et al., 1989). Porosity-depth curves compiled by Praeger (2009) show that at 100 to 200 m burial the porosity of ooze-rich sediments such as the Brygge Formation will be 45 – 80 % (Fig. 5-40). Porosities at the upper end of this range are anticipated (see above). At depths of 300 m this porosity will be reduced by c. 5 - 10 % (Fig. 5-40). Data presented by Bryant (1981) suggests that for a porosity drop of c. 10%, the permeability coefficient will also drop by an order of magnitude. This means that the permeability of the Brygge Formation buried at 300 m before deposition of Naust Formation sediments would be between 1×10^{-8} and 1×10^{-5} cm/s. The porosity-depth curves compiled by Praeger (2009) show that for more clay rich sediments such as the Naust Formation, the porosity will be between 30 and 70 % at depths of 300 m, a reduction of c. 10 % from values obtained at the seabed (Fig. 5-40). Again, data presented by Bryant (1981) shows that this will be linked with a permeability coefficient drop of one order of magnitude, which means that at the base of the Naust

Formation at the time of crater formation, the permeability coefficient of the Naust Formation will be between 1×10^{-10} and 1×10^{-7} cm/s.

These permeability coefficients translate (Bryant et al., 1981) to permeabilities of 1×10^{-2} to 10 mD for the Brygge Formation and of 1×10^{-4} to 1×10^{-1} mD for the Naust Formation. The permeability coefficients quoted here do not take into account the effect of gas hydrate, which would act to further reduce the permeability of the sediments (Johnson et al., 2010, Kvenvolden, 1999, Nimblett and Ruppel, 2003). Bryant (1981) considers sediments with permeabilities under 1×10^{-2} mD to be impermeable for all practical purposes. Thus the base of the Naust Formation could be considered impermeable.

There are various categories of loading events that can then bring about liquefaction of sediments. These include monotonic external short lived events such as igneous emplacement, footsteps and meteorite impacts, and monotonic external short lived cyclic events such as surface waves and seismic waves brought about by earthquakes (Maltman and Bolton, 2003, Seed et al., 2001). Large sediment bodies are particularly prone to liquefaction during earthquakes, because the drainage distance will be large (Seed et al., 2001). Loading may be of an external long-lived nature, such as persistent sedimentation or tectonic stresses (Maltman and Bolton, 2003). Loading can come about by internal processes such as mineral dehydration, gas expansion and aquathermal effects (Maltman and Bolton, 2003). Loading can also come about as a result of fluid movements, such as externally sourced fluid pulses and seepage (Maltman and Bolton, 2003).

Mechanisms for loading the Brygge Formation to bring about liquefaction in the study area around the time of slope failures such as Slide W are considered. There is no evidence for igneous emplacement, meteorite impacts, mineral dehydration and aquathermal effects. The application of a stress by loading by the addition of sediments to the sedimentary column during sliding (c.f. Riis et al., 2005) is considered unlikely, because Crater D is located in the headwall region of the slide on top of which ooze incised from the crater is emplaced and therefore undergoes unloading during crater formation. In many of the craters (A, B, E, F, G, H, I, J and

K) it is considered unlikely that liquefaction of the Brygge Formation is brought about by undermining (c.f. Bull et al., 2009b), because there is no evidence of removal of part of the sidewall of the crater by slides which might release confining pressure. A shear stress might be applied by an earthquake, however this is considered unlikely because sediments are only known to liquefy due to earthquakes in the shallow subsurface (Obermeier, 1996).

Given that it is possible that there is pore pressure build up in the Brygge Formation due to the dissociation of gas hydrate and the creation of an overpressured gas column, it is considered that this pore pressure might increase until it becomes equal to lithostatic pressure. This would lead to fracturing of the overburden, which would resolve the overpressure (c.f. Flemings et al., 2003). Venting of overpressured gas is associated with slope instability (Tréhu et al., 2004), therefore it is possible that venting of overpressured gas may trigger Slide W and other slides on the mid Norway margin by the destabilising of sediments on the continental slope. Liquefaction of the Brygge Formation would be driven by gas expansion during venting or by incorporation of the Brygge Formation in to the subsequent slide and translation.

If overpressure build up is not sufficient to fracture the overburden and initiate sliding, it is possible that sliding may be initiated in the area of the craters because of overpressure build up in the Brygge Formation. This would reduce the shear strength of the Brygge Formation in the area of the craters, increasing the likelihood of slope failure (c.f. slope failure described in the Norwegian Channel by Davies and Clark, 2006). The overpressured sediments of the Brygge Formation would then be incorporated into a slide as a detachment unit, which would then be liquefied due to translation (Davies and Clark, 2006).

5.8.2.3 Remobilisation of the Brygge Formation

Once liquefied, the sediments of the Brygge Formation would be remobilised to the top of the slide, either through faults developing in the internal geometry of the slide (c.f. Davies and Clark, 2006), or, alternatively, through vents developed during fracturing of the overburden because of overpressure build-up due to gas hydrate dissociation. Emplacement of the ooze mounds will be quick with respect to regional

sedimentation, because the ooze mounds pinch out on a single horizon (Chapter 4). It is not clear how long emplacement of the mounds takes in absolute terms.

The liquefaction of Brygge Formation ooze would indicate that as this ooze is remobilised to the surface it is in a liquid state, and the accumulation of Mounds A and BCF in depressions forming on the top surface of Slide W indicates possible detachment of Mounds A and BCF. However the mounds are cross cut by normal faulting, indicating that the remobilised ooze later lost liquidity and underwent extension. Because of the disruption apparent in the internal architecture of Slide W, it is not possible to be definitive about whether the slide is incised by the mound or not. However detachment of mounds from Slide W would imply that incision would be possible. The normal faulting which cross cuts the mounds does not extend into the overburden, and therefore it is possible to constrain the timing of the loss of liquidity of the ooze mounds and the normal faulting as occurring when the ooze mounds were exposed at the seabed. The normal faulting may extend into Slide W beneath the mounds (e.g. (viii) on Fig. 5-3), and this could explain the basal topography of the mounds. An example of a process that could bring about a decrease in volume leading to normal faulting, and which could explain a transition of the mound such that it lost its liquid properties, would be dewatering.

5.8.2.4 Mounds post-emplacement

Mounds are likely to form good reservoirs subsequent to burial, making an accurate understanding of the internal geometry, external geometry and mechanism of formation of the mounds important. It is observed from Well 6403/10-U1 above that Mound GJ has a porosity of between 50 and 80 %, whereas the porosity of Slide W beneath is between 0 and 15 %. The porosity of the slides immediately above Mound GJ is between 0 and 20 %. This also indicates that if reservoir mounds are filled before the sediments which bury the reservoirs fail, it may be possible to remobilise ooze from the reservoirs in a manner similar to the remobilisation of ooze from the Brygge Formation at the bases of craters.

It was shown above that cylindrical conical features are superimposed on the top of the stretching geometries described on the top surface of mound BCF. Mound BCF may have undergone Rayleigh Taylor instability. This would be consistent with

density data, which suggests that the density of the Brygge Formation is less than the density of the Naust Formation (Chapter 2). Therefore the density of the mounds (which are sourced from the Brygge Formation) might be less than the density of the sediments of the Naust Formation above and below the mound. These conditions would be ideal for Rayleigh Taylor Instability, which can form when density inversion is present (e.g. Conrad and Molnar, 1997, Davies et al., 1999).

5.8.2.5 Crater A

It was shown above that the geometry of the top surface of Slide W in the fill of Crater A could occur if sediments from Slide W were mixed into Slide Y below, a process considered unlikely because of the continuity of the reflection of the top surface of Slide Y. Alternatively; it was shown that the location of Crater A may have been almost entirely buried by Slide Y. If Crater A were almost entirely buried by Slide Y, a mechanism by which the observed geometry may come about is as follows. Sediment in the western region of Crater A in the Brygge Formation may liquefy through the mechanisms described above. This liquefied sediment would then be remobilised to the surface. Confining pressure on Brygge Formation ooze sediments located beneath Slide Y would be released in a manner similar to that described by Bull et al (2009b), causing Brygge Formation sediments beneath Slide Y to be expelled horizontally and remobilised to the surface. This would undermine Slide Y, causing Slide Y to collapse backwards into the forming crater, causing Slide Y sediments to collapse progressively towards the eastern sidewall of Crater A.

5.8.2.6 Significance of opal A/CT boundary

The slope failure described by Davies and Clark (2006) is associated with the migration of an active opal A/CT boundary upwards. This is associated with porosity reduction, which indicates that fluid may be expelled upwards above this boundary (e.g. Chaika and Dvorkin, 2000, Davies et al., 2008). The hypothesis presented here is different from the system described by Davies and Clark (2006) because the source of fluid which fills the reservoir may be different. While an opal A/CT boundary underlies the mapping area described here, it is demonstrated in Chapter 3 above that this boundary arrested sometime before the emplacement of sediments that fail as Slide W at Craters A, B, C, E, F, G, J and K. However, it cannot be ruled out that the

density data, which suggests that the density of the Brygge Formation is less than the density of the Naust Formation (Chapter 2). Therefore the density of the mounds (which are sourced from the Brygge Formation) might be less than the density of the sediments of the Naust Formation above and below the mound. These conditions would be ideal for Rayleigh Taylor Instability, which can form when density inversion is present (e.g. Conrad and Molnar, 1997, Davies et al., 1999).

5.8.2.5 Crater A

It was shown above that the geometry of the top surface of Slide W in the fill of Crater A could occur if sediments from Slide W were mixed into Slide Y below, a process considered unlikely because of the continuity of the reflection of the top surface of Slide Y. Alternatively; it was shown that the location of Crater A may have been almost entirely buried by Slide Y. If Crater A were almost entirely buried by Slide Y, a mechanism by which the observed geometry may come about is as follows. Sediment in the western region of Crater A in the Brygge Formation may liquefy through the mechanisms described above. This liquefied sediment would then be remobilised to the surface. Confining pressure on Brygge Formation ooze sediments located beneath Slide Y would be released in a manner similar to that described by Bull et al (2009b), causing Brygge Formation sediments beneath Slide Y to be expelled horizontally and remobilised to the surface. This would undermine Slide Y, causing Slide Y to collapse backwards into the forming crater, causing Slide Y sediments to collapse progressively towards the eastern sidewall of Crater A.

5.8.2.6 Significance of opal A/CT boundary

The slope failure described by Davies and Clark (2006) is associated with the migration of an active opal A/CT boundary upwards. This is associated with porosity reduction, which indicates that fluid may be expelled upwards above this boundary (e.g. Chaika and Dvorkin, 2000, Davies et al., 2008). The hypothesis presented here is different from the system described by Davies and Clark (2006) because the source of fluid which fills the reservoir may be different. While an opal A/CT boundary underlies the mapping area described here, it is demonstrated in Chapter 3 above that this boundary arrested sometime before the emplacement of sediments that fail as Slide W at Craters A, B, C, E, F, G, J and K. However, it cannot be ruled out that the

water and methane from which gas hydrate might form in the Brygge Formation is sourced previously from the upwards migrating opal A/CT boundary. Indeed, it is possible that there may be some sort of interaction between the upwards migrating opal A/CT boundary and the base of the gas hydrate zone, particularly as the fossilised opal A/CT boundary may have coincided with the base of the gas hydrate stability zone around the time of formation of the craters described here. This would merit further investigation.

5.8.3 Summary of Hypothesis C

A new hypothesis which would explain the formation of the craters is presented in Fig. 5-45 and summarised below.

- (1) The development of a gas hydrate zone is dependent on advection of gas from depth, possibly through the hydrothermal vent complexes described in Chapter 4 (Fig. 5-45A).
- (2) During deposition of the Naust Formation on top of the Brygge Formation, the boundary of the gas hydrate stability zone shoals upwards, leading to dissociation of gas hydrate into methane and water. This process could increase pore pressure within the Brygge Formation if methane is able to form an interconnected gas column (Fig. 5-45A & D).
- (3) Overpressure build up in the Brygge Formation may lead to venting of overpressured gas. In this scenario, liquefaction of the Brygge Formation during the formation of craters may be driven by gas expansion during venting or by the assimilation and translation of the Brygge Formation within a subsequent slide (Fig. 5-45B).
- (4) Alternatively, overpressure build up will result in a reduction of shear strength within the Brygge Formation, which may prime or trigger a slide (c.f. Davies and Clark, 2006). Where craters form, the Brygge Formation becomes a detachment unit for the slide, and is liquefied due to translation (Fig. 5-45B).
- (5) Craters may form at different times in different locations (Fig. 5-45B & E).

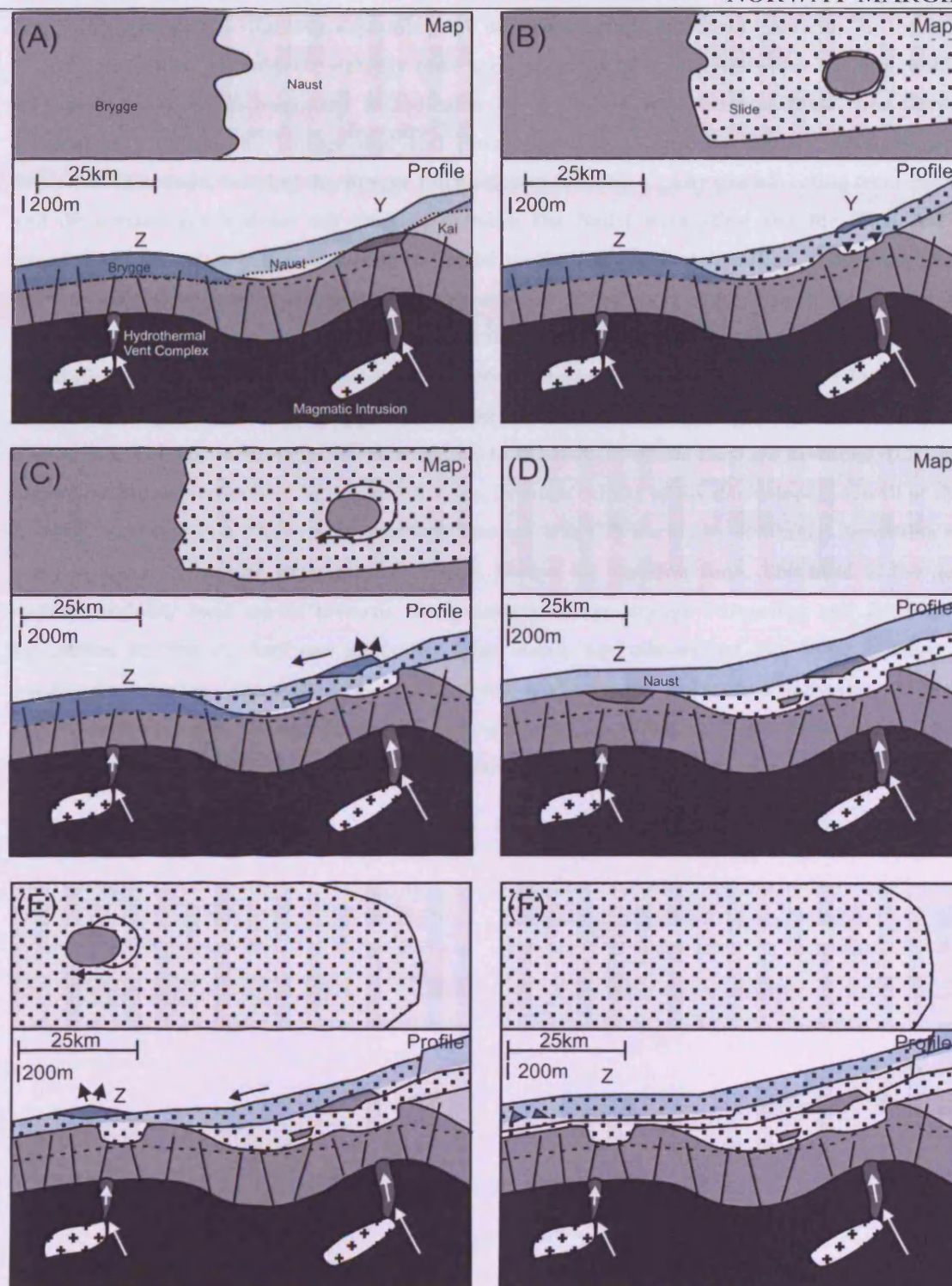


Fig. 5-45: Schematic hypothesis explaining the development of craters and mounds on the mid Norway margin. A gas hydrate stability zone is represented by transparent blue shading, and a stationary Opal A/CT boundary is indicated by a dashed line. Normal faults are shown schematically within the Brygge and Kai Formations. (A) Naust Formation sediments are deposited on a slope, burying the Brygge Formation at location Y. Any gas advecting from depth and dissociated gas hydrate are trapped between the Naust Formation and the Opal A/CT boundary. A possible gas reservoir is indicated in the Brygge Formation at Y by dark grey shading. (B) Naust Formation sediments deposited at Y fail as a slide. This could be due to overpressure build up within the Brygge Formation leading to fracturing of the overburden, destabilising sediments on the slope. Alternatively the host sediments of the reservoir indicated in (A) are incorporated into the slide as a detachment unit and undergo liquefaction due to translation. The host sediments are remobilised to the seabed, where they are extruded. (C) The mound on the seabed moves further down slope. Possible failure of the downslope sidewall of the crater is indicated. (D) The system described in steps A to C is buried by continued deposition of sediments. At site Z, the Brygge Formation is buried for the first time. The base of the gas hydrate stability zone moves towards the boundary of the Brygge Formation and the Naust Formation at Site Z. Any gas advecting from depth and dissociated gas hydrate form a potentially overpressured gas reservoir at the top of the Brygge Formation, indicated by dark grey shading. (E) Process described at Y in steps A to C repeated at Z. (F) Later slide incises downwards into slide which buries crater at Z, removing ooze mound.

- (6) Ooze liquefied at the crater floor ascends through the moving slide which buries the crater formation site, possibly due to its low density (Riis et al., 2005), either exploiting faults developing within the slide or vents as a flow conduit to reach the surface. At the seabed, ooze is emplaced (Fig. 5-45B, C & E) in depressions that form on the top surface of the slide which buries the forming crater (e.g. Mounds A and B which occupy large depressions on the top surface of Slide W above the western margin of Craters A and B).
- (7) After emplacement and before burial the mounds lose their liquid properties, undergoing extension by normal faulting which might be related to volumetric contraction. A process that might give rise to this loss in liquid properties and volumetric contraction would be dewatering (indicated by c. vertical black arrows on Fig. 5-45C & E).
- (8) After burial mounds may act as good reservoirs, given a source of fluid and an impermeable seal. Potentially, craters could be formed in the mounds by a similar mechanism to those which form at the top of the Brygge Formation, with a shoaling Opal A/CT transition leading to dissociation of gas hydrate and the build up of overpressure in the mound. Mounds may undergo Rayleigh Taylor instability if they are buried by a sedimentary sequence which has a high density than the sediments which make up the mounds. The mounds may be partly or fully incised (Fig. 5-45F) by later slides (i.e. Mound GJ).

6 DISCUSSION

6.1 Wider significance of craters on the mid Norway margin

It was shown in Chapter 4 that the craters described in this thesis are located on the contact between the Eocene to Oligo-Miocene Brygge Formation and the Pliocene to Pleistocene Naust Formation. Ooze evacuated from the craters is emplaced as mounds on the top surface of the first large scale slide to occur in the Pliocene and Pleistocene on this margin, Slide W, which is located at the base of the Naust Formation (Chapter 3). The idea that the formation of craters and emplacement of mounds triggered slides, such as Slide W (Chapter 3), was considered possible in Chapter 4. Findings from Chapter 5 suggest that triggering of slides by crater formation is possible. If Hypothesis C presented in Chapter 5 accurately describes the formation of craters, the principle significance of the formation of craters and emplacement of mounds lies in that they may represent a history of slides and gas hydrate dissociation on the mid Norway margin.

The formation of craters and emplacement of mounds on the mid Norway margin may have resulted in significant methane release to the ocean atmosphere system. The mass of methane which would have been released to the ocean atmosphere system is calculated, using the volume of Crater A calculated in Chapter 5, and the volumes of the other craters calculated in Chapter 4. Firstly, the mass of methane released due to the formation of craters on the basal shear surface of Slide W is calculated. Secondly, the mass of methane released from craters H and I on the Solsikke Dome which are buried by a later slide is calculated. Finally, the mass of methane released due to the formation of Crater D is calculated.

6.1.1 Volume of methane released from craters

The total volume of the craters on the basal shear surface of Slide W is 975 km³, although this may represent an overestimate (Chapter 5). It is shown above using compaction profiles from Praeger (2009) and Hempel et al. (1989) that the porosity of the Brygge Formation buried at a depth of c. 300 m would be between 35 and 75 %, with the porosity of the Brygge Formation likely lying at the upper end of this range (Fig. 5-40). The Brygge Formation sediments sampled at ODP sites have porosities at

the upper end of those predicted by Praeger (2009), therefore a range of porosities from 50 to 75 % is used to calculate the quantity of methane which might be released to the ocean / atmosphere system. The pore volume of the craters on the basal shear plane of Slide W would have been between 490 and 736 km³. At the Blake Ridge, the percentage of pore volume occupied by gas hydrates varies between 0 % and 9 % in the lower portion of the gas hydrate stability zone, with an estimate of 2.3 % given for the average percentage of pore volume occupied by gas hydrate over almost the entire gas hydrate stability zone at the Blake Ridge (Table 6-1). Noting that the gas hydrate at the Blake Ridge is sourced primarily from biogenic methane (Borowski et al., 1996, Brooks et al., 1983, Claypool and Kaplan, 1974, Claypool and Threlkeld, 1983, Paull et al., 2000) and that the source of methane in the study area may be thermogenic (Chapter 4), the latter value is taken as an indicative value for the mid Norway margin, to estimate how much methane may have been released into the atmosphere, given dissociation of gas hydrate during crater formation. The volume of gas hydrate at the sites of the craters on the basal shear surface of Slide W will therefore be up to between 11 and 17 km³. At standard temperature and pressure, this would give rise to up to between 1838 and 2758 km³ of methane (Kvenvolden, 1993). At standard temperature and pressure, the density of methane is 1.819 kg/m³. The mass of methane released to the ocean atmosphere system due to the formation of craters on the basal surface of Slide W would therefore be between 3.3 and 4.8 GT, which is approximately 0.9 – 1.4 times the quantity of methane currently in the atmosphere (3.6 GT, e.g. Whiticar, 1990). A similar calculation for Craters H and I (which are both incised by the Solsikke trough, Chapter 5) suggests that at least between 0.06 GT and 0.08 GT of methane would have been released to the ocean/atmosphere system during formation of Craters H and I (1.5 – 2.3 % of methane currently in the atmosphere), and that between 0.25 and 0.37 GT of methane would have been released to the ocean/atmosphere system during formation of Crater D (6.9 – 10.2 % of methane currently in the atmosphere).

| <u>Reference</u> | <u>Method</u> | <u>Estimate of pore volume occupied by gas hydrate at Blake Ridge</u> | <u>Depth range of estimate</u> |
|--------------------------------|--|--|---|
| Holbrook et al. (1996) | P-wave velocity | 2 – 7 % | 200 – 450 m below sea floor |
| Dickens et al. (1997) | Direct in-situ measurements | 0 - 9 % | 190 – 450 m below sea floor |
| Egeberg and Dickens, (1999) | Pore water Cl ⁻ concentrations | 2.3 % (average value) | 24 – 452 m below sea floor |

Table 6-1: Estimates of the percentage of pore space in the gas hydrate stability zone occupied by gas hydrate at the Blake Ridge.

6.2 Comparative study area: The Blake Ridge Depression

6.2.1 Description

One of the most puzzling aspects of this research is to explain why such large craters of this type have only been documented offshore Norway. The closest analogue to the Norwegian craters is perhaps the Blake Ridge Depression, on Hydrate Ridge offshore the eastern USA (Fig. 6-1, Fig. 6-2). The Blake Ridge Depression is about 38 by 18 km in extent defined at the seabed as a depression ~ 100 m deep, with the basal surface of the depression having a relief of ~ 100 m (Fig. 6-2, Holbrook et al., 2002).

The Blake Ridge Depression has been interpreted in two different ways. The earlier interpretation is that the Blake Ridge Depression is a collapse structure (Dillon et al., 1998). Faults which disrupt the sea floor and sole out or terminate about 40 – 500 m below the sea floor at the base of the gas hydrate stability zone are interpreted (Dillon et al., 1998). Many of these faults are interpreted as normal faults, however reverse faults are also interpreted (Dillon et al., 1998). Folds are mapped, with some folds converting into faults, sediment diapirs and deposits of sediments erupted onto the seafloor are also interpreted (Dillon et al., 1998). The faults in the western part of the depression trend south / south east to north / north west (Dillon et al., 1998).

The latter interpretation is that the Blake Ridge Depression consists of a series of sediment waves (Holbrook et al., 2002). Evidence cited in support of this interpretation are the stratal geometries in the depression, which include sigmoidal shapes and climbing crests; the lack of stratal continuity across features previously interpreted as faults, including erosion of underlying strata and the thinning of overlying strata towards the unconformities; the shallow dip (2 – 7°) of the discontinuities interpreted as faults above, much shallower than numerous high angle faults (with a dip of 50°) interpreted beneath the depression; and seabed scarps which do not extend into the subsurface (Holbrook et al., 2002). It is noted that the ridges are 5 to 10 km long, 1 – 3 km apart, and are orientated north west – south east, with wave crests typically reaching 75 m and sometimes reaching 150 m above troughs (Holbrook et al., 2002).

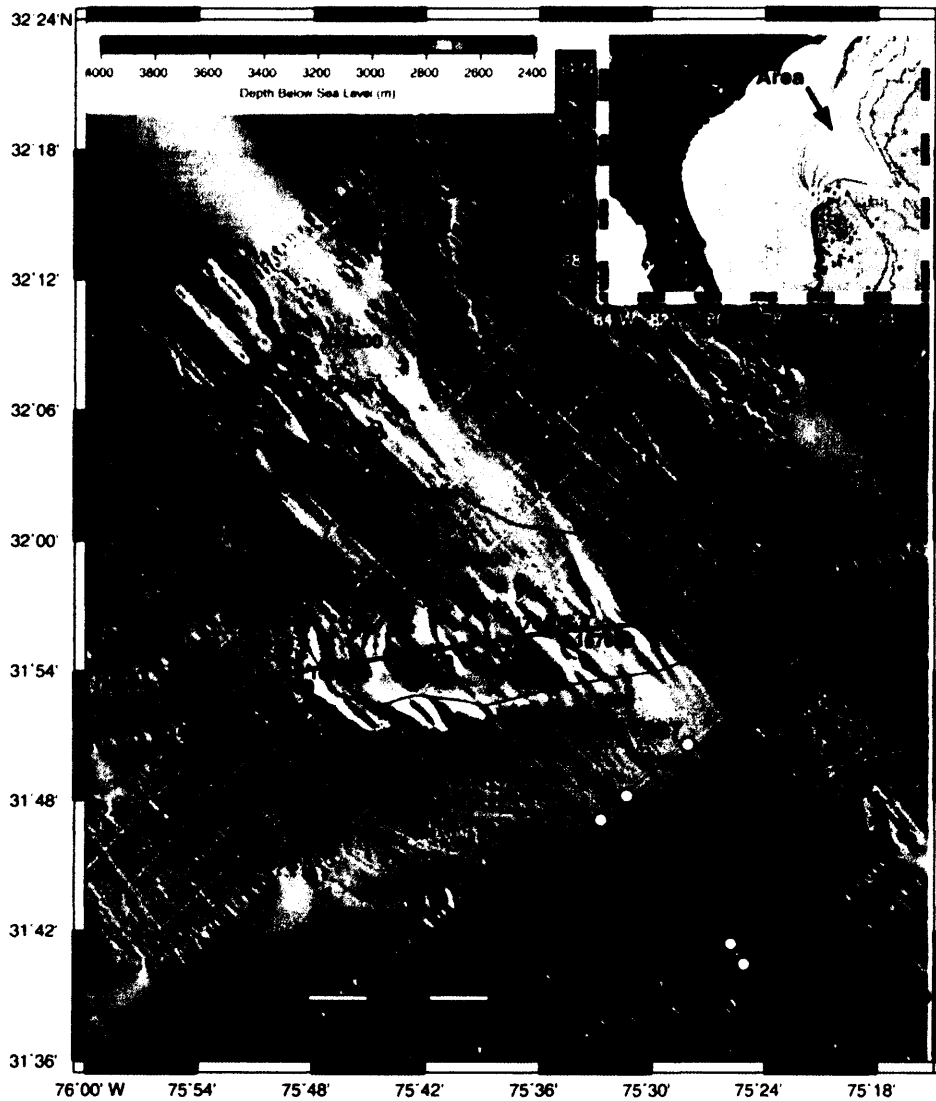


Fig. 6-1: From Holbrook et al. (2002). A map of the Blake Ridge Depression (BRD), showing the location of the seismic lines in Fig. 6-2.

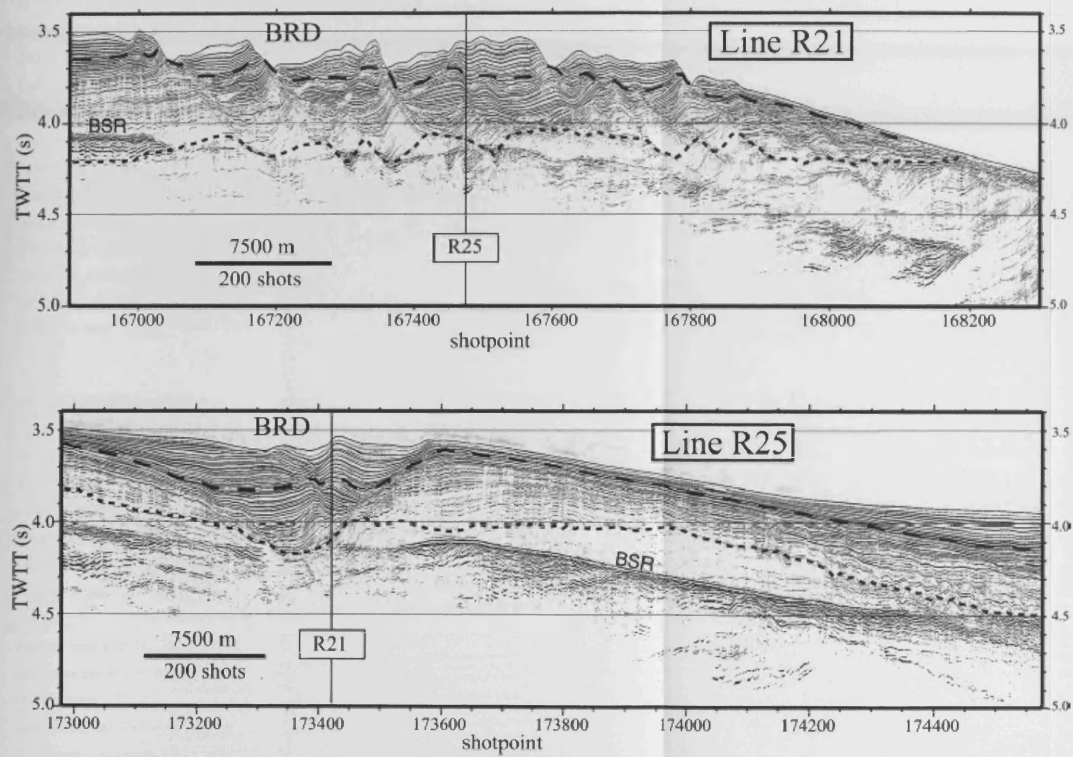


Fig. 6-2: From Holbrook et al. (2002). Seismic reflection data illustrating the Blake Ridge Depression (BRD). See Fig. 6-1 for location. The dotted reflection is the 3.3 Ma marker, the dashed line is the 1.6 Ma marker. TWTT: two-way travel time. BSR: Bottom simulating reflector.

proportion of biosiliceous microfossils in the clay sediments at the Blake Ridge are variable (Paull and Matsumoto, 2000), with the carbonate content being up to 25 % (Kraemer et al., 2000).

The size of the Blake Ridge Depression and the craters described in this thesis are in the same order of magnitude. The craters described in this thesis being up to 80 km in diameter and 200 m deep (Chapter 4). The Blake Ridge Depression is 38 by 18 km in extent and 100 m deep (Holbrook et al., 2002).

At both the Blake Ridge Depression and at the craters on the mid Norway margin there are permeable pathways connecting sediments at depth to the seabed. At the Blake Ridge Depression, there is some disagreement as to whether sediments at depth are linked to the seabed faults (Dillon et al., 1998, Dillon et al., 2001) or the boundaries between sediment waves (Holbrook et al., 2002). On the mid Norway margin the internal structure of the slides which fill the craters consists of a series of closely spaced faults which may be exploited by fluid flow (Chapter 5).

Perhaps the most important similarity between the Blake Ridge Depression and the craters described in this thesis lies in a potential link to dissociation of gas hydrate and the formation of gas reservoirs at depth trapped by a shoaling gas hydrate stability zone. At the Blake Ridge Depression, rapid sedimentation (see above) would lead to rapid shoaling of the gas hydrate stability zone (Holbrook et al., 2002), with reservoirs of free gas being accumulated at the base of the gas hydrate stability zone before being lost to the ocean-atmosphere system (Dillon et al., 1998, Dillon et al., 2001, Holbrook et al., 2002). Hypothesis C presented in Chapter 5 suggests that shoaling of the gas hydrate stability zone during deposition of the sediments that fail as Slide W may have led to the creation of free gas reservoirs in the sediments in which the craters form.

There are also a number of differences between the Blake Ridge Depression and the craters described in this thesis. Perhaps the most significant difference lies in the arrangement of sediments at the two sites. On the mid Norway margin there is a clearly stratified arrangement of sediments, with low permeability clay sediments overlying very permeable and porous sediments consisting of biosiliceous

microfossils (Chapter 2). At the Blake Ridge Depression, such a clearly stratified arrangement of sediments is not present (e.g. Kraemer et al., 2000), with the sediments showing only a little heterogeneity (e.g. Paull and Matsumoto, 2000)

Another significant difference between the Blake Ridge Depression and the craters on the mid Norway margin described in this thesis lies in the evidence of significant remobilisation of sediment from the subsurface to the seabed. On the mid Norway margin this evidence is ubiquitous on seismic reflection data (e.g. Chapters 4 and 5), although it is important to note that at some craters, for example Crater E, the apparent volume of sediment extruded as mounds is considerably less than the volume of the sediment missing from the crater (e.g. Chapter 4). At the Blake Ridge Depression there is evidence of remobilisation of sediment to the seabed and of the formation of mounds (Dillon et al., 1998). However 2D profiles show that the volume of sediment extruded is small. There may be significant seafloor erosion of sediments at the Blake Ridge Depression (Holbrook et al., 2002, Hornbach et al., 2008); therefore at the Blake Ridge Depression it is possible that any extruded sediment from depth may be eroded. It is also possible that the Blake Ridge Depression no sediment was extruded, and that the depression exists as a consequence of seafloor erosion (e.g. Holbrook et al., 2002, Hornbach et al., 2008).

6.3 Are the craters pockmarks?

The craters described in this thesis might be considered as giant pockmarks, in that they represent depressions on the top of the Brygge Formation. Some of the craters described (e.g. Crater A) have aspect ratios that lie within the range suggested for pockmarks by Stewart (1999). The craters described in this thesis are located in an area of significant vertical fluid advection (Chapter 4), and may be associated with the release of methane to the ocean/atmosphere system (see above).

The mechanism by which the craters in this thesis formed according to Hypothesis C presented in Chapter 5 may be similar in some respects to the mechanism by which pockmarks form. Pockmarks form by the accumulation of shallow reservoirs of overpressured fluid. The pressure of the fluid becomes similar to lithostatic pressure. Hydro fracturing occurs and a pockmark or small crater is formed (Hovland and Judd, 1988). According to the hypothesis presented in Chapter 5 the craters described in this

thesis could also be formed by the build up of overpressure in the subsurface, which may fracture the overburden.

The craters described in this thesis however are also dissimilar to pockmarks in many respects. A distinguishing feature of pockmarks is that pockmarks form on the seabed (e.g. Hovland and Judd, 1988). The craters described in this thesis, however, formed in the subsurface (e.g. Chapter 5), which means that the craters described in this thesis are very different from pockmarks. Furthermore, the craters described in this thesis are filled exclusively by slides, and are associated with mounds of remobilised ooze which are emplaced above the slide which buries the craters (Chapters 4 and 5). Mounds of remobilised sediment have not been described above pockmarks. Another difference between the craters described in this thesis and pockmarks is the respective sizes of pockmarks and the craters. The largest pockmarks yet described are around 5 km in diameter (Cole et al., 2000), whereas the only the smallest craters have diameters of this magnitude (Chapters 4 and 5).

The craters described in this thesis are not considered to be related to pockmarks, primarily because of the significant diagnostic differences between the craters described in this thesis and pockmarks.

6.4 Are the mounds diapirs?

It was demonstrated in Chapter 5 above that mounds located above craters on the mid Norway margin consist of sediment evacuated from the craters. In the hypothesis presented in Chapter 5 shows that liquefied sediment rises to the seabed through vents or faults developing in the overburden which hitherto had acted as a seal, with the upward advection of liquefied sediment being driven by density inversion (Riis et al., 2005) and, potentially if the reservoir were overpressured before liquefaction, by the pressure difference between the liquefied sediment at depth and the pressure at the bottom of the water column.

Previously the mounds described in this thesis above craters were interpreted as diapirs. Diapirs have been defined as:

“Upward-directed, dome-like intrusion of a lighter rock mass, e.g. salt or granite, into a denser cover.” (Allaby and Allaby, 2003)

In some respects the mounds described in this thesis might be considered to be diapirs because a rock mass with lower density moves upwards into a denser cover (e.g. Chapter 5). There are however significant differences between the mounds described in this thesis and diapirs as defined above. Critically, the mounds are extruded on the seabed (Chapters 4 and 5), and are not intruded. Therefore, while the process may be diapiric, the mounds cannot be defined as diapirs.

6.5 Subsurface Gas Expulsion Structures

The craters described in this thesis were classified as “Evacuation Structures” by Riis et al. (2005). This classification was chosen, because sediments are evacuated from the craters because of loading by a slide and are emplaced on the seabed (Riis et al., 2005). However; a number of conclusions reached in this thesis make a new classification necessary. Firstly, Hypothesis C presented in Chapter 5 suggests that crater formation and mound emplacement could be driven by the shoaling of the base of a gas hydrate stability zone leading to formation of a potentially overpressured reservoir. Secondly, according to the same hypothesis, the formation of the craters and emplacement of mounds may have been associated with the release of a significant mass of methane to the ocean atmosphere system. Thirdly, the Blake Ridge Depression, which is not associated with significant evacuation of sediments like the craters described in this thesis, could be classified as a similar structure to the craters.

Assuming Hypothesis C is correct, the Blake Ridge Depression and the craters and mounds described in this thesis could be classified as Subsurface Gas Expulsion Structures. Subsurface Gas Expulsion Structures are defined as structures which form due to the expulsion of dissociated gas hydrate or dissociated gas hydrate and other free gas from a sealed reservoir in the shallow subsurface (e.g. < 500 m below the seabed) through fluid flow pathways which develop within the brittle seal (which buries the location of the reservoir before, during and after formation of the structure) to the ocean / atmosphere system.

Subsurface Gas Expulsion Structures could be confused with craters associated with mud volcanoes, particularly where the pipe or conduit of the mud volcano is associated with a gas hydrate stability zone (e.g. Ginsburg et al., 1999). However Subsurface Gas Expulsion Structures differ from craters associated with mud volcanoes because the gas source of these structures generally lies at depth (e.g. Ginsburg et al., 1999), and not in the shallow subsurface. It should be noted, however, that mud volcanoes in at least one area have been described which forms due to the dissociation of gas hydrate (e.g. Van Rensbergen et al., 2002), and these could also be defined as Subsurface Gas Expulsion Structures.

6.6 Where else could Subsurface Gas Expulsion Structures form?

Subsurface Gas Expulsion Structures are ubiquitous on the area of the mid Norway margin described in this thesis. There are a number of conditions which are present on the Blake Ridge and on the mid Norway margin which would be vital to the formation of Subsurface Gas Expulsion Structures elsewhere. Firstly, a source of methane is necessary to be frozen as gas hydrate. This might come about by bacterial methanogenesis (e.g. Blake Ridge, Borowski et al., 1996, Brooks et al., 1983, Claypool and Kaplan, 1974, Claypool and Threlkeld, 1983, Paull et al., 2000); alternatively this might come about by the advection of methane from depth (e.g. Chapter 4). Secondly, conditions such as seabed depth, bottom water temperature, salinity and geothermal gradient must be right to ensure the stability of gas hydrates at the seabed. Thirdly, there must be a reservoir in the shallow subsurface which is fed by the advection of methane from depth and / or by the dissociation of a shoaling gas hydrate stability zone. Fourthly, this reservoir must be sealed, either by less porous sediments or by a gas hydrate stability zone. Finally, conditions must exist to drive gas expulsion.

These conditions were present on the mid Norway margin when the craters formed and the mounds were emplaced. It was demonstrated in Chapter 4 that the mid Norway margin is a region of significant methane advection towards the seabed. It was shown in Chapter 5 that conditions were right when the craters formed for gas hydrate to be stable at the seabed. After burial, the Brygge Formation acted as an excellent reservoir for gas due to the exceptionally high porosity of the Brygge Formation. (Chapter 2). This reservoir would have been sealed by the base of a

shoaling gas hydrate stability zone (Chapter 5) or / and by the less porous and permeable sediments of the Naust Formation (Chapter 2 and 5).

The conditions necessary for Subsurface Gas Expulsion Structures are also present on the Blake Ridge. At the Blake Ridge there is significant bacterial methanogenesis which also acts as a source of methane (Borowski et al., 1996, Brooks et al., 1983, Claypool and Kaplan, 1974, Claypool and Threlkeld, 1983, Paull et al., 2000). Conditions are right for gas hydrate to be stable at the seabed. The geothermal gradient at the Blake Ridge is 40 °C/km (Ruppel et al., 1995), and the depth of the seabed at the Blake Ridge Depression is 2550 m (Holbrook et al., 2002). Under these conditions, a gas hydrate stability zone extending 500 m underneath the seabed is predicted (Dickens, 2001). Sediments on the Blake Ridge have a porosity of between 60 % and 70 % in the interval of interest (see above), and are therefore able to act as an effective reservoir.

Slopes on continental margins will be particularly “at risk” as regards the formation of Subsurface Gas Expulsion Structures, because conditions will be right for the rapid deposition of terrigenous sediment on the seafloor to trigger formation of Subsurface Gas Expulsion Structures. The formation of Subsurface Gas Expulsion Structures on the seafloor of deep oceans is considered less likely, because of slower deposition rates. Shallow continental shelves are also considered at low risk with regards to the formation of Subsurface Gas Expulsion Structures, because in shallow waters bottom water temperature will be too high for the formation of gas hydrates (Dickens, 2001).

It is also important to note that the conditions necessary for the formation of Subsurface Gas Expulsion Structures are unlikely to exist on other planets. Other planets may be cold enough at the surface to support the formation of gas hydrate at the surface (e.g. Mars, Pollack, 1978). However, on those planets and other bodies closest to Earth (the Moon, Mars and Venus), no current processes have been observed which could lead to the rapid deposition of sediments which could lead to a shoaling of the gas hydrate stability zone and dissociation of gas hydrate at depth, which is a pre-requisite for the formation of Subsurface Gas Expulsion Structures. It is possible, however, that these conditions existed in the past. For example, on Mars,

evidence of sedimentary rocks have been observed (Malin and Edgett, 2000), which suggest that sedimentary processes may have been active in the geological past.

6.7 Significance of Subsurface Gas Expulsion Structures

Subsurface Gas Expulsion Structures are significant; because they represent a way which has not been described previously by which dissociated gas hydrate can be moved from the base of a gas hydrate stability zone to the ocean atmosphere system, bypassing the gas hydrate stability zone which would otherwise act as a seal. According to the clathrate gun hypothesis (Kennett et al., 2003), changes in oceanic circulation towards the end of glacial periods may result in dissociation of gas hydrate at depth, which then triggers slides, allowing the dissociated gas hydrate to be released into the ocean atmosphere system, amplifying and accelerating global warming. This may have been particularly relevant in the Quaternary (Kennett et al., 2003). Subsurface Gas Expulsion Structures don't necessarily require global warming or changes in oceanic circulation. On the mid Norway margin, if Hypothesis C presented in Chapter 5 were to be true, steepening of the continental slope due to climatic deterioration (Chapter 3) may be sufficient to shoal the base of a gas hydrate stability zone (Chapter 5) and trigger or prime Slide W (Chapter 3), which in turn leads to the formation of craters and the emplacement of mounds (Chapters 4 and 5) and the release of a significant mass of methane to the ocean atmosphere system (see above).

Subsurface Gas Expulsion Structures could be considered geohazards in the sense that they may provide for a mechanism to transport large quantities of gas hydrate to be added to the ocean atmosphere. Areas particularly at risk would be those areas where there is rapid deposition of sediments, a plentiful supply of methane, and conditions favourable to the formation of gas hydrate. Continental slopes on passive continental margins could be considered especially at risk, because in such environments deposition of sediments will be rapid, methane can be readily supplied from bacterial activity and by advection from depth, and because conditions will be favourable to the development of gas hydrate.

The area studied in this thesis, despite being a passive continental slope setting, is considered to be at low risk with regards to the formation of Subsurface Gas

Expulsion Structures. The continental slope is currently believed to be stable (e.g. Nadim et al., 2005), and furthermore, gas hydrates are not able to form on the slope because the porosity of slide units on the margin is too low to support the development of gas hydrates (Bünz et al., 2003).

6.8 Further Work

Given that Subsurface Gas Expulsion Structures could potentially occur on other unstable continental margins, the work presented in this thesis adds an imperative to better understanding which continental slopes are at risk of failure. Areas of rapid sediment deposition should be analysed to consider the risk of the formation of Subsurface Gas Expulsion Structures. Areas with a particular risk of Subsurface Gas Expulsion Structure will be distinguished by:

- (a) an abundant methane supply from bacterial activity and / or advection of methane from depth.
- (b) conditions which ensure the stability of gas hydrate at the seabed.
- (c) sediments within 500 m of the seabed which are capable of forming a good reservoir.
- (d) rapid deposition of less porous sediments on more porous sediments, or rapid deposition of high porosity sediments leading to rapid shoaling of the base of the gas hydrate stability zone.

A better understanding of the likely consequences on global climate of the formation of Subsurface Gas Expulsion Structures is required. Further modelling is required to understand the likely consequence of the release of up to 5 GT of methane over a variety of timescales.

7 SUMMARY AND CONCLUSIONS

7.1 Previous work

A number of enigmatic craters up to tens of kilometres in diameter have recently been mapped on the mid Norway margin by Riis et al. (2005). Key findings are summarised.

- 1) The craters are mapped on the top of a regional Oligo-Miocene ooze formation and are filled by slides.
- 2) Mounds are mapped above the craters on the top surface of slides which fill the craters. Well data combined with the seismic characteristics of the mounds suggest that the mounds were remobilised from the crater floors. Onlap of the mounds by later sediments suggests that the mounds were emplaced on the seabed.
- 3) A hypothesis is proposed whereby the craters were formed by emplacement of slides onto the top of Oligo-Miocene ooze formations, which may have been overpressured. The loading of these Oligo-Miocene ooze formations at the seafloor or under shallow burial by sliding brings about liquefaction of the Oligo-Miocene ooze formations, which are then remobilised towards the seabed.

In this study the work of Riis et al. (2005) is built upon by use of an extensive suite of 2D and 3D seismic reflection data to carry out detailed mapping of slides, craters and mounds in the Møre Basin.

7.2 Conclusions from Chapter 3: Mapping of Slides

Two of the first slides to bury the top of Oligo-Miocene ooze formations in the Møre Basin were identified on seismic reflection data and mapped in this study, to better understand the dynamics of these movements.

- 1) The first slide to occur in the Møre Basin since Miocene times was a small scale slide that only covered a small portion of the top of the Oligo-Miocene ooze formation mapped by Riis et al. (2005). This first slide was named Slide Y. Palynological data shows that the sediments which comprise Slide Y were deposited in the late Pliocene from the Piacenzian to Gelasian (3.6 to 1.8 Ma). Failure could have occurred at any time during this time period.

- 2) The occurrence of Slide Y is linked temporally with the cessation of active normal faulting and the arrest of an opal A/CT transition in the Møre Basin. No causal relationship between the two events is identified.
- 3) The second slide is more significant areally, covering a large portion of the top of the Oligo-Miocene ooze formation mapped by Riis et al. (2005), and filling many craters identified at the top of the Oligo-Miocene ooze formation in the Møre Basin. This second slide, named Slide W, has a volume of over 4320 km³ and is equivalent in volume to the Holocene Tsunamgenic Storegga Slide, however unlike the Storegga Slide; Slide W was only translated by a few kilometres. Evidence in support of this conclusion includes the confinement of much of Slide W by the Faeroe Shetland Escarpment and a middle Miocene dome, and the observation that Slide W has a very small zone of depletion near the headwall and a very large zone of accumulation at the toe. Palynological data shows that the sediments that comprise Slide W were deposited in the Pliocene between the Late Zanclean and Gelasian (4.0-1.8 Ma). Failure of Slide W likely occurred at the end of this period.
- 4) There is a relationship between the oversteepening of the continental slope and the initiation of sliding in the Møre Basin.

7.3 Conclusions from Chapter 4: Regional mapping of craters and mounds

Regional mapping of craters and mounds located in the Møre Basin using 2D seismic reflection data was performed.

- 1) Eleven craters are mapped. It is found that all of the craters are incised in a sub-unit of the Brygge Formation which is dated using palynological data as being of early Eocene to Oligocene in age. More recent sediments are also incised at the sidewall of one of the craters. All of the craters are located on a surface which can be correlated to the failure plane of Slide W, however not all of the craters are filled by Slide W. It is found that many of the craters are located in the crestal regions of middle Miocene domes.
- 2) Six mounds are mapped in the vicinity of craters which are filled by Slide W. These all pinch out onto the top surface of Slide W, with the exception of mounds located at the edge of Slide W which pinches out onto a surface that can be correlated with the top surface of Slide W. The mounds are generally larger in volume than the craters they overlie, although there are two mounds

which are significantly smaller in volume than the crater they overlie. The seismic characteristics of the mounds suggest that the mounds are sourced from the floors of the craters, in agreement with previous work.

- 3) Craters which are filled by Slide W and overlain by mounds are dated as forming contemporaneously with failure of Slide W. It is not possible to constrain the time of formation of craters filled by other slides, because mounds are not mapped in the vicinity of craters filled by later slides on the top surfaces of the slides which fill these craters.
- 4) In the context of the subsurface fluid flow regime of the Møre Basin, two hypotheses are presented that could explain the formation of craters and the remobilisation of ooze to the seabed. In one hypothesis (Hypothesis A), a sudden eruption of fluid from depth fluidises and remobilises the early Eocene to Oligocene ooze, potentially triggering sliding. In the other hypothesis (Hypothesis B), continuous fluid flow from depth feeds reservoirs in the early Eocene to Oligocene ooze. Slide W loads overpressured reservoirs in the subsurface within the early Eocene to Oligocene, bringing about liquefaction and remobilisation of ooze to the seabed.

7.4 Conclusions from Chapter 5: Detailed mapping of craters and mounds

The detailed 3D geometries of craters and mounds located within the boundaries of 3D seismic reflection surveys in the Møre Basin are considered.

- 1) There is a relationship between the morphology of some of the craters and the flow direction of Slide W.
- 2) The slides which fill some of the craters located in 3D seismic reflection surveys in the Møre Basin are broken up by a series of closely spaced thrust faults (spacing is 200 m), which is consistent with thrusting of a slide in the zone accumulation. It is therefore possible that these craters were loaded by sliding. However, importantly, it is found that one crater is unloaded by sliding.
- 3) The external morphology of the mounds is reminiscent of sediment bodies which have undergone layer-parallel extension, with necking and shearing of the mounds being observed.
- 4) A regional Opal A/CT boundary is not considered to be a direct cause of crater formation. Evidence in support of this is the observation that the regional opal

A/CT transition arrested at the time of failure of Slide Y, which predates the formation of craters filled by Slide W.

- 5) Noting that the Plio-Pleistocene sediments which bury the early Eocene-Oligocene ooze at the sites of crater formation have a lower permeability and porosity than the early Eocene-Oligocene ooze, and noting that the depth of the gas hydrate stability zone at the time of failure of Slide W may coincide with the calculated thickness of Slide W in the vicinity of the craters, a new hypothesis is presented linking the formation of craters and the remobilisation of early Eocene to Oligocene ooze in the Møre Basin with the dissociation of gas hydrate.
- 6) According to the hypothetical hypothesis presented in Chapter 5, during rapid deposition of sediments burying the early Eocene to Oligocene ooze in the Møre Basin from 4 Ma to 1.8 Ma, the base of a gas hydrate stability zone shoals upwards towards the top of the early Eocene to Oligocene ooze. The dissociation of gas hydrate within the early Eocene to Oligocene ooze leads to the build up of pore pressure and the reduction of effective stress of the early Eocene to Oligocene ooze. The pore pressure could increase to lithostatic pressure, leading to fracturing of the overburden and venting of overpressured gas, followed by sliding of the overburden. Alternatively, the pore pressure in the Eocene to Oligocene ooze increases towards lithostatic pressure, priming or triggering a slope failure of the overburden. The overpressured Eocene to Oligocene ooze then becomes a detachment unit. Translation brings about liquefaction of Eocene to Oligocene ooze, which is incorporated into the slope failure.
- 7) According to the hypothetical hypothesis presented in Chapter 5, ooze is remobilised to the seabed through faults or vents which develop in the overburden. The emplacement of ooze will be rapid with respect to background sedimentation. Evidence in support of this includes the pinch out of the mounds on a single datum. It is not clear how quick the process of ooze emplacement is in absolute terms. Shortly after emplacement on the seabed, liquefied ooze loses its liquid properties and undergoes extension by shear and possible volumetric contraction. The ooze mounds may undergo Rayleigh Taylor instability, undergo liquefaction and remobilisation again in a process similar to the process described above, or be incised by a later slide.

7.5 Conclusions from Chapter 6: Subsurface gas expulsion structures

Up to 5 GT of methane may have been released into the ocean atmosphere system during formation of the craters and the remobilisation of ooze sediments to the seafloor, assuming the hypothesis presented in Chapter 5 accurately describes formation of the craters described in this thesis. The craters mapped in the Møre Basin are similar in some regards to the Blake Ridge Depression, where there is evidence that 0.6 GT of methane gas has bypassed a gas hydrate cap at the seabed and been vented to the ocean atmosphere system. Assuming Hypothesis C accurately describes the formation of the craters described in this thesis, the structures described in the Møre Basin and the Blake Ridge Depression could be classed as Subsurface Gas Expulsion Structures.

- 1) Subsurface Gas Expulsion Structures are considered to be significant, because they represent a manner by which significant quantities of methane can bypass the cap of a gas hydrate stability zone and be vented to the ocean-atmosphere system without a change in sea level or warming of global climate.
- 2) Continental margins should be considered at risk for the formation of Subsurface Gas Expulsion Structures where there is a plentiful supply of biogenic or thermogenic methane, where conditions are right for the formation of gas hydrate, where there is a capped reservoir at shallow depth and where there is rapid deposition at the seafloor leading to a rapid shoaling of the base of a gas hydrate stability zone.
- 3) The Møre Basin is currently considered to be at low risk as regards the formation of Subsurface Gas Expulsion Structures, because present day sediments at the seabed are not favourable to the formation of gas hydrate, and because the continental slope to the east of the Møre Basin is considered to be stable at the present day.
- 4) Further work is required to better understand the climatic effects of the release from Subsurface Gas Expulsion Structures of quantities of methane similar to the current quantity of methane in the atmosphere over a variety of geologically rapid timescales.

8 REFERENCES

ALLABY, A. & ALLABY, M. (2003) *Dictionary of Earth Sciences*, Oxford, Oxford University Press.

AXEN, G. J. (1992) Pore Pressure, Stress Increase, and Fault Weakening in Low-Angle Normal Faulting. *Journal of Geophysical Research - Solid Earth*, 97(B6), 8979–8991.

BARR, D. (1987) Lithospheric stretching, detached normal faulting and footwall uplift IN COWARD, M. P., DEWEY, J. F. & HANCOCK, P. L. (Eds.) *Continental Extensional Tectonics*. London, Geological Society.

BEN-DAVID, R., EYAL, Y., ZILBERMAN, E. & DOWMAN, D. (2002) Fluvial systems response to rift margin tectonics: Makhtesh Ramon area, southern Israel. *Geomorphology*, 45, 147-163.

BERG, K., SOLHEIM, A. & BRYN, P. (2005) The Pleistocene to recent geological development of the Ormen Lange area. *Marine and Petroleum Geology*, 22, 45-56.

BERNDT, C. (2005) Focused fluid flow in passive continental margins. *Philosophical Transactions of the Royal Society Series A*, 363, 2855-2871.

BERNDT, C., BÜNZ, S., CLAYTON, T., MIENERT, J. & SAUNDERS, M. (2004) Seismic character of bottom simulating reflectors: examples from the mid-Norwegian margin. *Marine and Petroleum Geology*, 21, 723-733.

BERNDT, C., BÜNZ, S. & MIENERT, J. (2003) Polygonal fault systems on the mid-Norwegian margin; a long-term source for fluid flow. IN VAN RENSBURG, P., HILLIS, R. R., MALTMAN, A. J. & MORLEY, C. K. (Eds.) *Subsurface sediment mobilization*. London, Geological Society.

BERNER, R. A. (1980) *Early Diagenesis a Theoretical Approach*, Princeton, NJ, Princeton University Press.

BEAUDOIN, A. B. & HEAD, M. J. (2004) Drawing a line in the sand: identifying and characterizing boundaries in the geological record. IN BEAUDOIN, A.B. & HEAD, M.J. (eds) *The Palynology and Micropalaeontology of Boundaries*. London, Geological Society.

BODREEL, L. O. & ANDERSEN, M. S. (1998) Tertiary compressional structures on the Faeroe–Rockall Plateau in relation to northeast Atlantic ridge-push and Alpine foreland stresses. *Tectonophysics*, 300, 13-28.

BOROWSKI, W. S., PAULL, C. K. & USSLER III, W. (1996) Marine pore-water sulfate profiles indicate in situ methane flux from underlying gas hydrate. *Geology*, 24, 655-658.

BOURIAK, S., VANNESTE, M. & SAOUTKINE, A. (2000) Inferred gas hydrates and clay diapirs near the Storegga Slide on the southern edge of the Vøring Plateau, offshore Norway. *Marine Geology*, 163, 125-148.

BOUVIER, J. D., KAARS-SIJPESTEIJN, C. H., KLUESNER, D. F., ONYEJEKWE, C. C. & VAN DER PAL, R. C. (1989) Three-Dimensional Seismic Interpretation and Fault Sealing Investigations, Nun River Field, Nigeria. *AAPG Bulletin*, 73, 1397-1414.

BOWERS, G. L. (2002) Detecting high overpressure. *The Leading Edge*, 21, 174-177.

BREKKE, H. (2000) The tectonic evolution of the Norwegian Sea Continental Margin with emphasis on the Vøring and Møre Basins. IN NØTTVEDT, A. (Ed.) *Dynamics of the Norwegian Margin*. London, Geological Society.

- BREKKE, H., DAHLGREN, S., NYLAND, B. & MAGNUS, C. (1999) The prospectivity of the Vøring and Møre basins on the Norwegian Sea continental margin. IN FLEET, A. J. & BOLDY, S. A. R. (Eds.) *Petroleum Geology of Northwest Europe - Proceedings of the 5th Conference*. Bath, The Geological Society.
- BROOKS, J. M., BERNARD, L. A., WEISENBERG, D. A., KENNICUTT II, M. C. & KVENVOLDEN, K. A. (1983) Molecular and isotopic compositions of hydrocarbons at Site 533. *Initial Reports*. US Government Printing Office.
- BROWN, A. R. (2004) *Interpretation of Three-Dimensional Seismic Data, Sixth ed*, Society Of Exploration Geophysicists.
- BRYANT, W. R., BENNETT, R. & KATHERMAN, C. (1981) Shear strength, consolidation, porosity, and permeability of oceanic sediments. IN EMILIANI, C. (Ed.) *The Sea*. New York, Wiley.
- BRYN, P., BERG, K., FORSBERG, C. F., SOLHEIM, A. & KVALSTAD, T. J. (2005a) Explaining the Storegga Slide. *Marine and Petroleum Geology*, 22, 11-19.
- BRYN, P., BERG, K., STOKER, M. S., HAFLIDASON, H. & SOLHEIM, A. (2005b) Contourites and their relevance for mass wasting along the mid-Norwegian Margin. *Marine and Petroleum Geology*, 22, 85-96.
- BULL, S., CARTWRIGHT, J. & HUUSE, M. (2009a) A review of kinematic indicators from mass-transport complexes using 3D seismic data. *Marine and Petroleum Geology*, 26, 1132-1151.
- BULL, S., CARTWRIGHT, J. A. & HUUSE, M. (2009b) A subsurface evacuation model for submarine slope failure. *Basin Research*, 21, 433-443.

- BÜNZ, S., MIENERT, J. & BERNDT, C. (2003) Geological controls on the Storegga gas-hydrate system of the mid-Norwegian continental margin. *Earth and Planetary Science Letters*, 209, 291-307.
- BÜNZ, S., MIENERT, J., BRYN, P. & BERG, K. (2005) Fluid flow impact on slope failure from 3D seismic data: a case study in the Storegga Slide. *Basin Research*, 17, 109-122.
- BYERLEE, J. (1990) Friction, overpressure and fault normal compression. *Geophysical Research Letters*, 17, 2109-2112.
- CARTWRIGHT, J. A. (2007) The impact of 3D seismic data on the understanding of compaction, fluid flow and diagenesis in sedimentary basins. *Journal of the Geological Society*, 164, 881-893.
- CARTWRIGHT, J. A. & DEWHURST, D. N. (1998) Layer-bound compaction faults in fine-grained sediments. *Geological Society of America Bulletin*, 110, 1242-1257.
- CERAMICOLA, S., STOKER, M. S., PRAEG, D., SHANNON, P. M., DE SANTIS, L., HOULT, R., HJELSTUEN, B. O., LABERG, S. & MATHIESEN, A. (2005) Anomalous Cenozoic subsidence along the 'passive' continental margin from Ireland to mid-Norway. *Marine and Petroleum Geology*, 22, 1045-1067.
- CHAIKA, C. & DVORKIN, J. (2000) Porosity Reduction During Diagenesis of Diatomaceous Rocks. *American Association of Petroleum Geologists Bulletin*, 84, 1173-1184.
- CLAYPOOL, G. E. & KAPLAN, I. R. (1974) The origin and distribution of methane in marine sediments. *Natural Gases in Marine Sediments*. New York, Plenum.

CLAYPOOL, G. E. & THRELKELD, C. N. (1983) Anoxic diagenesis and methane generation in sediments of the Blake Outer Ridge, Deep Sea Drilling Project, Site 533, Leg 76. *Initial Reports*. US Government Printing Office.

COACHMAN, L. K. & AAGAARD, K. (1974) Physical Oceanography of Arctic and Subarctic Seas. IN HERMAN, Y. (Ed.) *Marine Geology and Oceanography of the Arctic Seas*. Berlin, Springer-Verlag.

COLE, D., STEWART, S. A. & CARTWRIGHT, J. A. (2000) Giant irregular pockmark craters in the paleogene of the Outer Moray Firth Basin, UK North Sea. *Marine and Petroleum Geology*, 17, 563-577.

CONRAD, C. P. & MOLNAR, P. (1997) The growth of Rayleigh-Taylor-type instabilities in the lithosphere for various rheological and density structures. *Geophysical Journal International*, 129, 95-112.

COWAN, D. S. (1986) Structural styles in Mesozoic and Cenozoic mélanges in the western Cordillera of North America. *Geological Society of America Bulletin*, 96, 451-462.

DAHLGREN, K. I. T., VORREN, T. O. & LABERG, J. S. (2002) Late Quaternary glacial development of the mid-Norwegian margin—65 to 68°N. *Marine and Petroleum Geology*, 19, 1089-1113.

DALLAND, A., WORSLEY, D. & OFSTAD, K. (1988) *A Lithostratigraphic Scheme for the Mesozoic and Cenozoic Succession Offshore Mid- and Northern Norway*. NPD-Bulletin 4, Norwegian Petroleum Directorate.

DAVIES, R., CARTWRIGHT, J. & RANA, J. (1999) Giant hummocks in deep-water marine sediments: Evidence for large-scale differential compaction and density inversion during early burial. *Geology*, 27, 907-910.

DAVIES, R. J. & CARTWRIGHT, J. (2002) A fossilized Opal A to Opal C/T transformation on the northeast Atlantic margin: support for a significantly elevated palaeogeothermal gradient during the Neogene? *Basin Research*, 14, 467-486.

DAVIES, R. J. & CLARK, I. R. (2006) Submarine slope failure primed and triggered by silica and its diagenesis. *Basin Research*, 18, 339-350.

DAVIES, R. J., GOULTY, N. R. & MEADOWS, D. (2008) Fluid flow due to the advance of basin-scale silica reaction zones. *Geological Society of America Bulletin*, 120, 195-206.

DAVISON, I., INSLEY, M., HARPER, M., WESTON, P., BLUNDELL, D., MCCLAY, K. & QUALLINGTON, A. (1993) Physical modelling of overburden deformation around salt diapirs. *Tectonophysics*, 228, 255-274.

DICKENS, G. R. (2001) The potential volume of oceanic methane hydrates with variable external conditions *Organic Geochemistry*, 32, 1179-1193.

DICKENS, G. R., PAULL, C. K. & WALLACE, P. (1997) Direct measurement of in situ methane quantities in a large gas-hydrate reservoir. *Nature*, 385, 426-428.

DILLON, W. P., DANFORTH, W. W., HUTCHINSON, D. R., DRURY, R. M., TAYLOR, M. H. & BOOTH, J. S. (1998) Evidence for faulting related to dissociation of gas hydrate and release of methane off the southeastern United State. IN HENRIET, J. P. & MIENERT, J. (Eds.) *Gas hydrates: Relevance to world margin stability and climate change*. London, Geological Society.

DILLON, W. P., NEALON, J. W., TAYLOR, M. H., LEE, M. W., DRURY, R. M. & ANTON, C. H. (2001) Seafloor collapse and methane venting associated with gas hydrate on the Blake Ridge—Causes and implications to seafloor stability and methane release. IN PAULL, C. K. & DILLON, W. P. (Eds.) *Natural gas hydrates: Occurrence, distribution, and detection*.

DORÉ, A. & LUNDIN, E. R. (1996) Cenozoic compressional structures on the NE Atlantic margin: nature, origin, and potential significance for hydrocarbon exploration. *Petroleum Geoscience*, 2, 299-311.

DORÉ, A., LUNDIN, E. R., KUSZNIR, N. J. & PASCAL, C. (2008) Potential mechanisms for the genesis of Cenozoic domal structures on the NE Atlantic margin: pros, cons and some new ideas. IN JOHNSON, H., DORÉ, A., GATLIFF, R. W., HOLDSWORTH, R., LUNDIN, E. R. & RITCHIE, J. D. (Eds.) *The Nature and Origin of Compression in Passive Margins*. London, Geological Society.

DRUITT, T. H. & FRANCAVIGLIA, V. (1992) Caldera formation on Santorini and the physiography of the islands in the late Bronze Age. *Bulletin of Volcanology*, 54, 484-493.

EGEBERG, P. K. & DICKENS, G. R. (1999) Thermodynamic and pore water halogen constraints on gas hydrate distribution at ODP Site 997 (Blake Ridge) *Chemical Geology*, 153, 53-79.

ELDHOLM, O., THIEDE, J., TAYLOR, E., BARTON, C., BJØRKLUND, K., BLEIL, U., CIESIELSKI, P., DESPRAIRIES, A., DONNALLY, D., FROGET, C., GOLL, R., HENRICH, R., JAMNSEN, E., KRISSEK, L., KVENVOLDEN, K., LEHURAY, A., LOVE, D., LYSNE, P., MCDONALD, T., MUDIE, P., OSTERMAN, L., PARSON, L., PHILLIPS, J. D., PITTENGER, A., QVALE, G., SCHÖNHARTING, G. & VIERECK, L. (1987) *Proceedings of the Ocean Drilling Program, Scientific Results*, College Station, Texas, Ocean Drilling Program.

EVANS, D., HARRISON, Z., SHANNON, P. M., LABERG, J. S., NIELSEN, T., AYERS, S., HOLMES, R., HOULT, R. J., LINDBERG, B., HAFLIDASON, H., LONG, D., KUIJPERS, A., ANDERSEN, E. S. & BRYN, P. (2005) Paleoslides and other mass failures of Pliocene to Pleistocene age along the Atlantic continental margin of NW Europe. *Marine and Petroleum Geology*, 22, 1131-1148.

- EVANS, D., KING, E. L., KENYON, N. H., BRETT, C. & WALLIS, D. (1996) Evidence for long-term instability in the Storegga Slide region off western Norway. *Marine Geology*, 130, 281-292.
- FLEMINGS, P. B., LIU, X. & WINTERS, W. J. (2003) Critical pressure and multiphase flow in Blake Ridge gas hydrates. *Geology*, 31, 1057-1060.
- FORSBERG, C. F. & LOCAT, J. (2005) Mineralogical and microstructural development of the sediments on the Mid-Norwegian margin. *Marine and Petroleum Geology*, 22, 109-122.
- FOWLER, C. M. R. (2005) *The Solid Earth - An Introduction to Global Geophysics*, 2nd Edition. Cambridge, UK, Cambridge University Press.
- FREY-MARTINEZ, J., CARTWRIGHT, J. & JAMES, D. (2006) Frontally confined versus frontally emergent submarine landslides: A 3D seismic characterisation. *Marine and Petroleum Geology*, 23, 585-604.
- FREY MARTINEZ, J., CARTWRIGHT, J. & HALL, B. (2005) 3D seismic interpretation of slump complexes: examples from the continental margin of Israel. *Basin Research*, 17, 83-108.
- GARDNER, G. H. F., GARDNER, L. W. & GREGORY, A. R. (1974) Formation velocity and density - the diagnostic basics for stratigraphic traps. *Geophysics*, 39, 770-780.
- GAUER, P., KVALSTAD, T. J., FORSBERG, C. F., BRYN, P. & BERG, K. (2005) The last phase of the Storegga Slide: simulation of retrogressive slide dynamics and comparison with slide-scar morphology. *Marine and Petroleum Geology*, 22, 171-178.

- GAY, A. & BERNDT, C. (2007) Cessation/reactivation of polygonal faulting and effects on fluid flow in the Vøring Basin, Norwegian Margin. *Journal of the Geological Society*, 164, 129-141.
- GAY, A., LOPEZ, M., COCHONAT, P. & SERMONDADAZ (2004) Polygonal faults-furrows system related to early stages of compaction - upper Miocene to recent sediments of the Lower Congo Basin. *Basin Research*, 16, 101-116.
- GEE, M. J. R., GAWTHORPE, R. L. & FRIEDMANN, J. S. (2005) Giant striations at the base of a submarine landslide. *Marine Geology*, 214, 287-294.
- GINSBURG, G. D., MILKOV, A. V., SOLOVIEV, V. A., EGOROV, A. V., CHERKASHEV, G. A., VOGT, P. R., CRANE, K., LORENSON, T. D. & KHUTORSKOY, M. D. (1999) Gas hydrate accumulation at the Håkon Mosby Mud Volcano *Geo-Marine Letters*, 19, 57-67.
- HAFLIDASON, H., AARSETH, I., HAUGEN, J. E., SEJRUP, H. P., LOVLIE, R. & REITHER, E. (1991) Quaternary stratigraphy of the Draugen area, Mid-Norwegian Shelf. *Marine Geology*, 101, 125-145.
- HAFLIDASON, H., GRAVDAL, A. & SEJRUP, H. P. (2003) The northern Storegga slide escarpment—Morphology and features. IN MIENERT, J. & WEAVER, P. (Eds.) *European margin sediment dynamics, side-scan sonar and seismic images*. Berlin-Heidelberg, Springer-Verlag.
- HAFLIDASON, H., LIEN, R., SEJRUP, H. P., FORSBERG, C. F. & BRYN, P. (2005) The dating and morphometry of the Storegga Slide. *Marine and Petroleum Geology* 22, 123-136.
- HAFLIDASON, H., SEJRUP, H. P., NYGÅRD, A., MIENERT, J., BRYN, P., LIEN, R., FORSBERG, C. F., BERG, K. & MASSON, D. (2004) The Storegga Slide: architecture, geometry and slide development. *Marine Geology*, 213, 201-234.

- HART, B. S. (1999) Definition of subsurface stratigraphy, structure and rock properties from 3-D seismic data.
- HEIN, J. R., SCHOLL, D. W., BARRON, J. A., JONES, M. G. & MILLER, J. (1978) Diagenesis of late Cenozoic diatomaceous deposits and formation of the bottom-simulating reflector in the southern Bering Sea. *Sedimentology*, 25, 155-181.
- HEMPEL, P., MAYER, L., TAYLOR, E., BOHRMANN, G. & PITTENGER, A. (1989) The influence of biogenic silica on seismic lithostratigraphy at ODP sites 642 and 643, Eastern Norwegian Sea. IN ELDHOLM, O., THIEDE, J. & TAYLOR, E. (Eds.) *Proceedings of the Ocean Drilling Program, Scientific Results*. College Station, Texas, Ocean Drilling Program.
- HILDEBRAND, A. R., PENFIELD, G. T., KRING, D. A., PILKINGTON, M., CAMARGO Z., A., JACOBSEN, S. B. & BOYNTON, W. V. (1991) Chicxulub Crater: A possible Cretaceous/Tertiary boundary impact crater on the Yucatán Peninsula, Mexico. *Geology* 19, 867-871.
- HJELSTUEN, B. O., ELDHOM, O. & SKOGSEID, J. (1997) Vøring Plateau diapir fields and their structural and depositional settings. *Marine Geology*, 144, 22-57.
- HJELSTUEN, B. O., SEJRUP, H. P., HAFLIDASON, H., NYGÅRD, A., CERAMICOLA, S. & BRYN, P. (2005) Late Cenozoic glacial history and evolution of the Storegga Slide area and adjacent slide flank regions, Norwegian continental margin. *Marine and Petroleum Geology*, 22, 57-69.
- HOLBROOK, W. S., HOSKINS, H., WOOD, W. T., STEPHEN, R. A., LIZARRALDE, D. & PARTY, L. S. (1996) Methane Hydrate and Free Gas on the Blake Ridge from Vertical Seismic Profiling. *Science*, 273, 1840-1843.

HOLBROOK, W. S., LIZARRALDE, D., PECHER, I. A., GORMAN, A. R., HACKWITH, K. L., HORNBACH, M. & SAFFER, D. (2002) Escape of methane gas through sediment waves in a large methane hydrate province. *Geology*, 30, 467-470.

HORNBACH, M. J., SAFFER, D. M., HOLBROOK, W. S., VAN AVENDONK, H. J. A. & GORMAN, A. R. (2008) Three-dimensional seismic imaging of the Blake Ridge methane hydrate province: Evidence for large, concentrated zones of gas hydrate and morphologically driven advection. *Journal of Geophysical Research*, 113, B07101.

HOVLAND, M. (2008) *Deep-Water Coral Reefs : Unique Biodiversity Hot-Spots*, Chichester, UK, Praxis Publishing.

HOVLAND, M. & JUDD, A. G. (1988) *Seabed Pockmarks and Seepages : Impact on Geology, Biology and the Marine Environment*, London / Dordrecht / Boston, Graham and Trotman.

HOVLAND, M., NYGAARD, E. & THORBJØRNSSEN, S. (1998) Piercement shale diapirism in the deep-water Vema Dome area, Vøring basin, offshore Norway. *Marine and Petroleum Geology*, 15, 191-201.

HUSTOFT, S., MIENERT, J., BÜNZ, S. & NOUZÉ, H. (2007) High-resolution 3D-seismic data indicate focussed fluid migration pathways above polygonal fault systems of the mid-Norwegian margin. *Marine Geology*, 245, 89-106.

HUVENNE, V. A. I., CROKER, P. F. & HENRIET, J. P. (2002) A refreshing 3D view of an ancient sediment collapse and slope failure. *Terra Nova*, 14, 33-40.

JACKSON, M. P. A., CRAIG, C. H., GANSSER, A., STOCKLIN, J. & TALBOT, C. J. (1990) *Salt diapirs of the Great Kavir, Central Iran*, Geological Society of America.

JAMES BROWN, R., STEWART, R. R., GAISER, J. E. & LAWTON, D. C. (2000) An acquisition polarity standard for multicomponent seismic data. *CREWES Research Report, Volume 12*.

JAMTVEIT, B., SVENSEN, H., PODLADCHIKOV, Y. Y. & PLANKE, S. (2004) Hydrothermal vent complexes associated with sill intrusions in sedimentary basins. IN BREITKREUZ, C. & PETFORD, N. (Eds.) *Physical Geology of High-Level Magmatic Systems*. London, Geological Society.

JANSEN, E., FRONVAL, T., RACK, F. & CHANNELL, J. E. T. (2000) Pliocene-Pleistocene ice rafting history and cyclicity in the Nordic Seas during the last 3.5 Myr. *Paleoceanography*, 15, 709-721.

JOHNSON, A., PATIL, S. & DANDEKAR, A. (2010) Experimental investigation of gas–water relative permeability for gas hydrate bearing sediments from Mount Elbert gas hydrate stratigraphic test well, Alaska North Slope *Marine and Petroleum Geology*, in press.

JORDT, H., FALEIDE, J. I., BJØRLYKKE, K. & IBRAHIM, M. T. (1995) Cenozoic sequence stratigraphy in the Central and Northern North Sea: tectonic development, sediment distribution and provenance areas. *Marine and Petroleum Geology*, 12, 845-879.

JUDD, A. & HOVLAND, M. (2007) *Seabed Fluid Flow : The Impact on Geology, Biology and the Marine Environment*, Cambridge, Cambridge University Press.

KEARY, P., BROOKS, M. & HILL, I. (2002) *An introduction to geophysical exploration*, Blackwell Science.

KENNETT, J. P., CANNARIATO, K. G., HENDY, I. L. & BEHL, R. J. (2003) *Methane Hydrates in Quaternary Climate Change - The Clathrate Gun Hypothesis*, Washington, American Geophysical Union.

- KING, E. L., SEJRUP, H. P., HAFLIDASON, H., ELVERHOI, A. & AARSETH, I. (1996) Quaternary seismic stratigraphy of the North Sea Fan: glacially-fed gravity flow aprons, hemipelagic sediments, and large submarine slides. *Marine Geology*, 130, 293-315.
- KJELDSTAD, A., SKOGSEID, J., LANGTANGEN, H. P., BJØRLYKKE, K. & HØEG, K. (2003) Differential loading by prograding sedimentary wedges on continental margins: An arch-forming mechanism. . *Journal of Geophysical Research*, 108(B1), 2036.
- KRAEMER, L. M., OWEN, R. M. & DICKENS, G. R. (2000) Lithology of the upper gas hydrate zone, Blake Outer Ridge: a link between diatoms, porosity, and gas hydrate. IN MILLER, C. M. & RIEGEL, R. (Eds.) *Gas Hydrate Sampling on the Blake Ridge and Carolina Rise - Scientific Results*. College Station, Texas, Ocean Drilling Program.
- KVALSTAD, T. J., ANDRESEN, L., FORSBERG, C. F., BERG, K., BRYN, P. & WANGEN, M. (2005) The Storegga slide: evaluation of triggering sources and slide mechanics. *Marine and Petroleum Geology*, 22, 245-256.
- KVENVOLDEN, K. (1999) Potential effects of gas hydrate on human welfare. *Proceedings of the National Academy of Sciences of the United States of America*, 96, 3420-3426.
- KVENVOLDEN, K. A. (1993) Gas Hydrates - Geological Perspective and Global Change. *Reviews of Geophysics*, 31, 173-187.
- LEAR, C. H., ROSENTHAL, Y. & WRIGHT, J. D. (2003) The closing of a seaway: ocean water masses and global climate change *Earth and Planetary Science Letters*, 210, 425-436.

- LIGER-BELAIR, G. (2005) The Physics and Chemistry behind the Bubbling Properties of Champagne and Sparkling Wines: A State-of-the-Art Review. *Journal of Agricultural and Food Chemistry*, 53, 2788-2802.
- LØSETH, H., GADING, M. & WENSAAS, L. (2009) Hydrocarbon leakage interpreted on seismic data *Marine and Petroleum Geology*, 26, 1304-1319
- LØSETH, H. & HENRIKSEN, S. (2005) A mid to late Miocene compression phase along the Norwegian passive margin. IN DORÉ, A. & VINING, B. (Eds.) *Petroleum Geology: North-West Europe and Global Perspectives, Proceedings of the 6th Petroleum Geology Conference*. London, Geological Society.
- LUNDIN, E. & DORÉ, A. G. (2002) Mid-Cenozoic post-breakup deformation in the 'passive' margins bordering the Norwegian–Greenland Sea. *Marine and Petroleum Geology*, 19, 77-93.
- MALIN, M. C. & EDGETT, K. S. (2000) Sedimentary Rocks of Early Mars. *Science*, 290, 1927-1937.
- MALTMAN, A. J. (1994) *The Geological Deformation of Sediments*, London, Chapman and Hall.
- MALTMAN, A. J. & BOLTON, A. (2003) How sediments become mobilized. IN VAN RENSBURG, P., HILLIS, R. R., MALTMAN, A. J. & MORLEY, C. K. (Eds.) *Subsurface Sediment Mobilization*. London, Geological Society.
- MANN, D. M. & MACKENZIE, A. S. (1990) Prediction of pore fluid pressures in sedimentary basins. *Marine and Petroleum Geology*, 7, 55-65.
- MARTIN, V., NETO, D., CHEYRON, C., THORE, P. & PARÉ, A. (2010) Well-to-seismic tie method in complex imaging areas - Examples in the deep offshore subsalt Angola domain. *The Leading Edge*, 29, 1028-1037.

- MCIVER, R. D. (1982) Role of Naturally Occurring Gas Hydrates in Sediment Transport. *AAPG Bulletin*, 66, 789-792.
- MIENERT, J., VANNESTE, M., BÜNZ, S., ANDREASSEN, K., HAFLIDASON, H. & SEJRUP, H. P. (2005) Ocean warming and gas hydrate stability on the mid-Norwegian margin at the Storegga Slide. *Marine and Petroleum Geology*, 22, 233-244.
- MÖLLER, N., GJELBERG, J. G., MARTINSEN, O., CHARNOCK, M. A., FÆRSETH, R. B., SPERREVIK, S. & CARTWRIGHT, J. A. (2004) A geological model for the Ormen Lange hydrocarbon reservoir. *Norwegian Journal of Geology*, 84, 169-190.
- MOSCARDELLI, L. & WOOD, L. (2008) New classification system for mass transport complexes in offshore Trinidad. *Basin Research*, 20, 73-98.
- MULDER, T. & COCHONAT, P. (1996) Classification of offshore mass movements. *Journal of Sedimentary Research*, 66, 43-57.
- NADIM, F., KVALSTAD, T. J. & GUTTORMSEN, T. (2005) Quantification of risks associated with seabed instability at Ormen Lange *Marine and Petroleum Geology*, 22, 311-318.
- NEAGU, R. C., CARTWRIGHT, J., DAVIES, R. & JENSEN, L. (IN PRESS) Fossilisation of a silica diagenesis reaction front on the mid-Norwegian margin. *Marine and Petroleum Geology*.
- NEAGU, R. C., CARTWRIGHT, J. & DAVIES, R. (2010) Measurement of diagenetic compaction strain from quantitative analysis of fault plane dip. *Journal of Structural Geology*, 32, 641-655.

NICHOLS, R. J. (1995) The liquefaction and remobilization of sandy sediments. IN HARTLEY, A. J. & PROSSER, D. J. (Eds.) *Characterization of Deep Marine Clastic Systems*. London, Geological Society.

NIMBLETT, J. & RUPPEL, C. (2003) Permeability evolution during the formation of gas hydrates in marine sediments. *Journal of Geophysical Research*, 108.

OBERMEIER, S. F. (1996) Use of liquefaction-induced features for paleoseismic analysis — An overview of how seismic liquefaction features can be distinguished from other features and how their regional distribution and properties of source sediment can be used to infer the location and strength of Holocene paleo-earthquakes. *Engineering Geology*, 44, 1-76.

OKADA, H. (2000) Neogene and Quaternary calcareous nannofossils from the Blake Ridge, Sites 994, 995, and 997 IN MILLER, C. M. & RIEGEL, R. (Eds.) *Gas Hydrate Sampling on the Blake Ridge and Carolina Rise - Scientific Results*. College Station, Texas, Ocean Drilling Program.

OLAFSSON, I., SUNDVOR, E., ELDHOLM, O. & GRUE, K. (1992) Møre Margin: Crustal structure from analysis of Expanded Spread Profiles *Marine Geophysical Researches*, 14, 137-162.

OSBORNE, M. J. & SWARBRICK, R. E. (1997) Mechanisms for generating overpressure in sedimentary basins: A re-evaluation. *AAPG Bulletin*, 81, 1023-1041.

OWEN, G. (2003) Load structures: gravity-driven sediment mobilization in the shallow subsurface. IN VAN RENSBURG, P., HILLIS, R. R., MALTMAN, A. J. & MORLEY, C. K. (Eds.) *Shallow Subsurface Sediment Mobilization*. London, Geological Society.

PAULL, C. K., LORENSON, T. D., BOROWSKI, W. S., USSLER III, W., OLSEN, K. & RODRIGUEZ, N. M. (2000) Isotopic composition of CH₄, CO₂ species, and

sedimentary organic matter within samples from the Blake Ridge: Gas source implications. IN MILLER, C. M. & RIEGEL, R. (Eds.) *Gas Hydrate Sampling on the Blake Ridge and Carolina Rise - Scientific Results*. College Station, Texas, Ocean Drilling Program.

PAULL, C. K. & MATSUMOTO, R. (2000) Leg 164 overview. IN MILLER, C. M. & RIEGEL, R. (Eds.) *Gas Hydrate Sampling on the Blake Ridge and Carolina Rise - Scientific Results*. College Station, Texas, Ocean Drilling Program.

PITTENGER, A., TAYLOR, E. & BRYANT, W. R. (1989) The influence of biogenic silica on the geotechnical stratigraphy of the Vøring Plateau, Norwegian Sea. IN ELDHOLM, O., THIEDE, J. & TAYLOR, E. (Eds.) *Proceedings of the Ocean Drilling Program, Scientific Results*. College Station, Texas, Ocean Drilling Program.

PLANKE, S., RASMUSSEN, T., REY, S. S. & MYKLEBUST, R. (2005) Seismic characteristics and distribution of volcanic intrusions and hydrothermal vent complexes in the Vøring and Møre basins. IN DORÉ, A. & VINING, B. A. (Eds.) *Petroleum Geology: North-West Europe and Global Perspectives—Proceedings of the 6th Petroleum Geology Conference*. London, Geological Society.

PLANKE, S., SKOGSEID, J. & ELDHOLM, O. (1991) Crustal Structure off Norway, 62° to 70° north. *Tectonophysics*, 189, 91-107.

POLLACK, J. B. (1978) Climatic Change on the Terrestrial Planets. *Icarus*, 37, 479-533.

PRAEGER, T. (2009) Heterogeneities in fine grained slope systems and their impact on seal quality. *School of Earth and Ocean Sciences*. Cardiff, Cardiff University.

RIBE, N. M. (1998) Spouting and planform selection in the Rayleigh Taylor instability of miscible viscous fluids. *Journal of Fluid Mechanics*, 377, 27-45.

- RIIS, F., BERG, K., CARTWRIGHT, J., EIDVIN, T. & HANSCH, K. (2005) Formation of large, crater evacuation structures in ooze sediments in the Norwegian Sea. Possible implications for the development of the Storegga Slide. *Marine and Petroleum Geology*, 22, 257-273.
- RISE, L., OTTESEN, D., BERG, K. & LUNDIN, E. (2005) Large-Scale development of the mid-Norwegian margin during the last 3 million years. *Marine and Petroleum Geology*, 22, 33-44.
- RISE, L., OTTESEN, D., LONGVA, O., SOLHEIM, A., ANDERSEN, E. S. & AYERS, S. (2006) The Sklinnadjupet slide and its relation to the Elsterian glaciation on the mid-Norwegian margin. *Marine and Petroleum Geology*, 23, 569-583.
- RUPPEL, C., VON HERZEN, R. P. & BONNEVILLE, A. (1995) Heat flux through an old (~175 Ma) passive margin, offshore southeastern U.S.A. *Journal of Geophysical Research*, 100, 20037-20057.
- SAVIN, S., DOUGLAS, R. G. & STEHLI, F. G. (1975) Tertiary marine paleotemperatures. *Geological Society of America Bulletin*, 86, 1499-1510.
- SEED, R. B., CETIN, K. O., MOSS, R. E. S., KAMMERER, A. M., WU, J., PESTANA, J. M. & RIEMER, M. F. (2001) Recent advances in soil liquefaction engineering and seismic site response evaluation. *Fourth International Conference on Recent Advances in Geotechnical Earthquake Engineering and Soil Dynamics and Symposium in Honor of Professor W.D. Liam Fynn*. San Diego, California.
- SEJRUP, H. P., LARSEN, E., LANDVIK, J., KING, E. L., HAFLIDASON, H. & NESJE, A. (2000) Quaternary glaciations in southern Fennoscandia: evidence from southwestern Norway and the northern North Sea region. *Quaternary Science Reviews*, 19, 667-685.

SHERIFF, R. E. & GELDART, L. P. (1995) *Exploration Seismology*, Cambridge, Cambridge University Press.

SKOGSEID, J. & ELDHOLM, O. (1989) Vøring Plateau continental margin: seismic interpretation, stratigraphy and vertical movements. IN ELDHOLM, O., THIEDE, J. & TAYLOR, E. (Eds.) *Proceedings of the Ocean Drilling Program, Scientific Results*. College Station, Texas, Ocean Drilling Program.

SKOGSEID, J., PEDERSEN, T. & LARSEN, V. B. (1992) Vøring Basin: subsidence and tectonic evolution. IN LARSEN, R. M., BREKKE, H., LARSEN, B. T. & TALLERAAS, E. (Eds.) *Structural and Tectonic Modelling and its Application to Petroleum Geology*, Norwegian Petroleum Society.

SKOGSEID, J., PLANKE, S., FALEIDE, J. I., PEDERSEN, T., ELDHOLM, O. & NEVERDEL, F. (2000) NE Atlantic continental rifting and volcanic margin formation. IN NØTTVEDT, A. (Ed.) *Dynamics of the Norwegian Margin*. London, Geological Society.

SMYTHE, D. K., CHALMERS, J. A., SKUCE, A. G., DOBINSON, A. & MOULD, A. S. (1983) Early opening history of the North Atlantic — I. Structure and origin of the Faeroe—Shetland Escarpment. *Geophysical Journal International*, 72, 373–398.

SOLHEIM, A., BERG, K., FORSBERG, C. F. & BRYN, P. (2005) The Storegga Slide complex: repetitive large scale sliding with similar cause and development. *Marine and Petroleum Geology*, 22, 97–107.

SOSDIAN, S. & ROSENTHAL, Y. (2009) Deep-Sea Temperature and Ice Volume Changes Across the Pliocene-Pleistocene Climate Transitions. *Science*, 325, 306–310.

STAGG, H. M. J. (1985) The structure and origin of Prydz Bay and MacRobertson Shelf, east Antarctica. *Tectonophysics*, 114, 315–340.

STEWART, S. A. (1999) Seismic interpretation of circular geological structures *Petroleum Geoscience*, 5, 273-285.

STOKER, M. S., PRAEG, D., HJELSTUEN, B. O., LABERG, J. S., NIELSON, T. & SHANNON, P. M. (2005) Neogene stratigraphy and the sedimentary and oceanographic development of the NW European Atlantic margin. *Marine and Petroleum Geology*, 22, 977-1005.

STRACHAN, L. J. (2002) Slump-initiated and controlled syndepositional sandstone remobilization: an example from the Namurian of County Clare, Ireland. *Sedimentology*, 49, 25-41.

STRATAGEM (2003) Stoker, M.S. (Compiler). Neogene evolution of the glaciated European margin. A Product of the EC-supported STRATAGEM Project.

STUEVOLD, L. M., FAERSETH, R. B., ARNESEN, L., CARTWRIGHT, J. & MOLLER, N. (2003) Polygonal faults in the Ormen Lange Field, More basin, offshore Mid Norway. IN VAN RENSBERGEN, P., HILLIS, R. R., MALTMAN, A. J. & MORLEY, C. K. (Eds.) *Subsurface sediment mobilization*. London, Geological Society of London.

STUEVOLD, L. M., SKOGSEID, J. & ELDHOLM, O. (1992) Post-Cretaceous uplift events on the Vøring continental margin. *Geology*, 20, 919-922.

SUGDEN, D. E., GLASSER, N. & CLAPPERTON, C. M. (1992) Evolution of Large Roches Moutonnées *Geografiska Annaler*, 74, 253-264.

SUGDEN, D. E. & JOHN, B. S. (1976) *Glaciers and landscape: a geomorphological approach*, London, England, Edward Arnold.

SVENSEN, H., PLANKE, S., JAMTVEIT, B. & PEDERSEN, T. (2003) Seep carbonate formation controlled by hydrothermal vent complexes: a case study from the Vøring Basin, the Norwegian Sea. *Geo-Marine Letters*, 23, 351-358.

SVENSEN, H., PLANKE, S., MALTHER-SØRENSEN, A., JAMTVEIT, B., MYKLEBUST, R., EIDEM, T. R. & REY, S. S. (2004) Release of methane from a volcanic basin as a mechanism for initial Eocene global warming. *Nature*, 429, 542-545.

SWIECICKI, T., GIBBS, P. B., FARROW, G. E. & COWARD, M. P. (1998) A tectonostratigraphic framework for the Mid-Norway region. *Marine and Petroleum Geology*, 15, 245-276.

TALWANI, M., UDINTSEV, G., BJØRKLUND, K., CASTON, V. N. D., FAAS, R. W., KHARIN, G. N., MORRIS, D. A., MÜLLER, C., NILSEN, T. H., VAN HINTE, J., WARNKE, D. A. & WHITE, S. M. (1976) *Initial reports of the Deep Sea Drilling Project*, Washington, US Government Printing Office.

THYBERG, B. I., JORDT, H., BJØRLYKKE, K. & FALEIDE, J. I. (2000) Relationships between sequence stratigraphy, mineralogy and geochemistry in Cenozoic sediments of the northern North Sea. IN NOTTVEDT, A. (Ed.) *Dynamics of the Norwegian Margin*. London, The Geological Society of London.

TRÉHU, A. M., LONG, P. E., TORRES, M. E., BOHRMANN, G., RACK, F. R., COLLET, T. S., GOLDBERG, D. S., MILKOV, A. V., RIEDEL, M., SCHULTHEISS, P., BANGS, N. L., BARR, S. R., BOROWSKI, W. S., CLAYPOOL, G. E., DELWICHE, M. E., DICKENS, G. R., GRACIA, E., GUERIN, G., HOLLAND, M., JOHNSON, J. E., LEE, Y.-J., LIU, C.-S., SU, X., TEICHERT, B., TOMARU, H., VANNESTE, M., WATANABLE, M. & WEINBERGER, J. L. (2004) Three-dimensional distribution of gas hydrate beneath southern Hydrate Ridge: constraints from ODP Leg 204. *Earth and Planetary Science Letters*, 222, 845-862.

- TRUSHEIM, F. (1960) Mechanism of salt migration in northern Germany. *AAPG Bulletin*, 44, 1519-1540.
- VÅGNES, E., GABRIELSEN, R. H. & HAREMO, P. (1998) Late Cretaceous-Cenozoic intraplate contractional deformation at the Norwegian continental shelf: timing, magnitude and regional implications. *Tectonophysics*, 300, 29-46.
- VAN RENSBERGEN, P., DE BATIST, M., KLERKX, J., HUS, R., POORT, J., VANNESTE, M., GRANIN, N., KHLYSTOV, O. & KRINITSKY, P. (2002) Sublacustrine mud volcanoes and methane seeps caused by dissociation of gas hydrates in Lake Baikal. *Geology*, 30, 631-634.
- VARNES, D. J. (1978) Slope movement types and processes. IN SCHUSTER, R. L. & KRIZEK, R. J. (Eds.) *Landslides, Analysis and Control*. Washington D.C., National Academy of Sciences.
- VOLPI, V., CAMERLENGHI, A., HILLENBRAND, C.-D., REBESCO, M. & IVALDI, R. (2003) Effects of biogenic silica on sediment compaction and slope stability on the Pacific margin of the Antarctic Peninsular. *Basin Research*, 15, 339-363.
- WESTBROOK, G. K. & SMITH, M. J. (1983) Long décollements and mud volcanoes: Evidence from the Barbados Ridge Complex for the role of high pore-fluid pressure in the development of an accretionary complex. *Geology*, 11, 279
- WHITICAR, M. J. (1990) A geochemical perspective of natural gas and atmospheric methane. *Advances in Organic Geochemistry*, 16, 531-547.
- WOODCOCK, N. H. (1979) The use of slump structures as paleoslope orientation estimators. *Sedimentology*, 26, 83-99.

WRIGHT, J. D. & MILLER, K. G. (1996) Control of North Atlantic deep-water circulation by the Greenland-Scotland Ridge. *Paleoceanography*, 11, 157-170.

YILMAZ, Ö. & DOHERTY, S. M. (2001) *Seismic Data Analysis: Processing, Inversion and Interpretation of Seismic Data*. Tulsa, OK, Society of Exploration Geophysicists.

APPENDIX A1: ADDITIONAL EVIDENCE IN SUPPORT OF FINDINGS OF CHAPTER 2

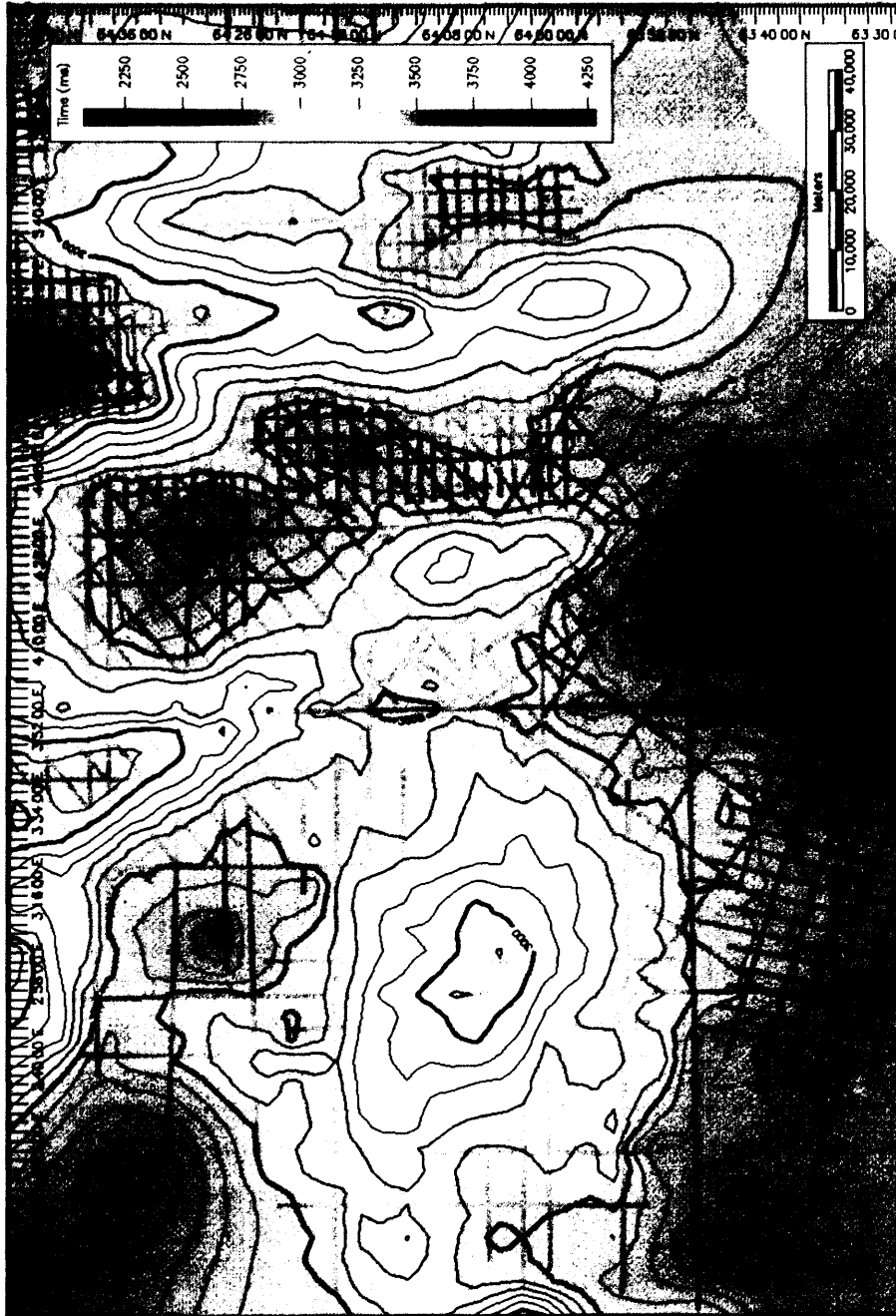


Fig. A1- 1: Two way travel time map of base Brygge Reflection

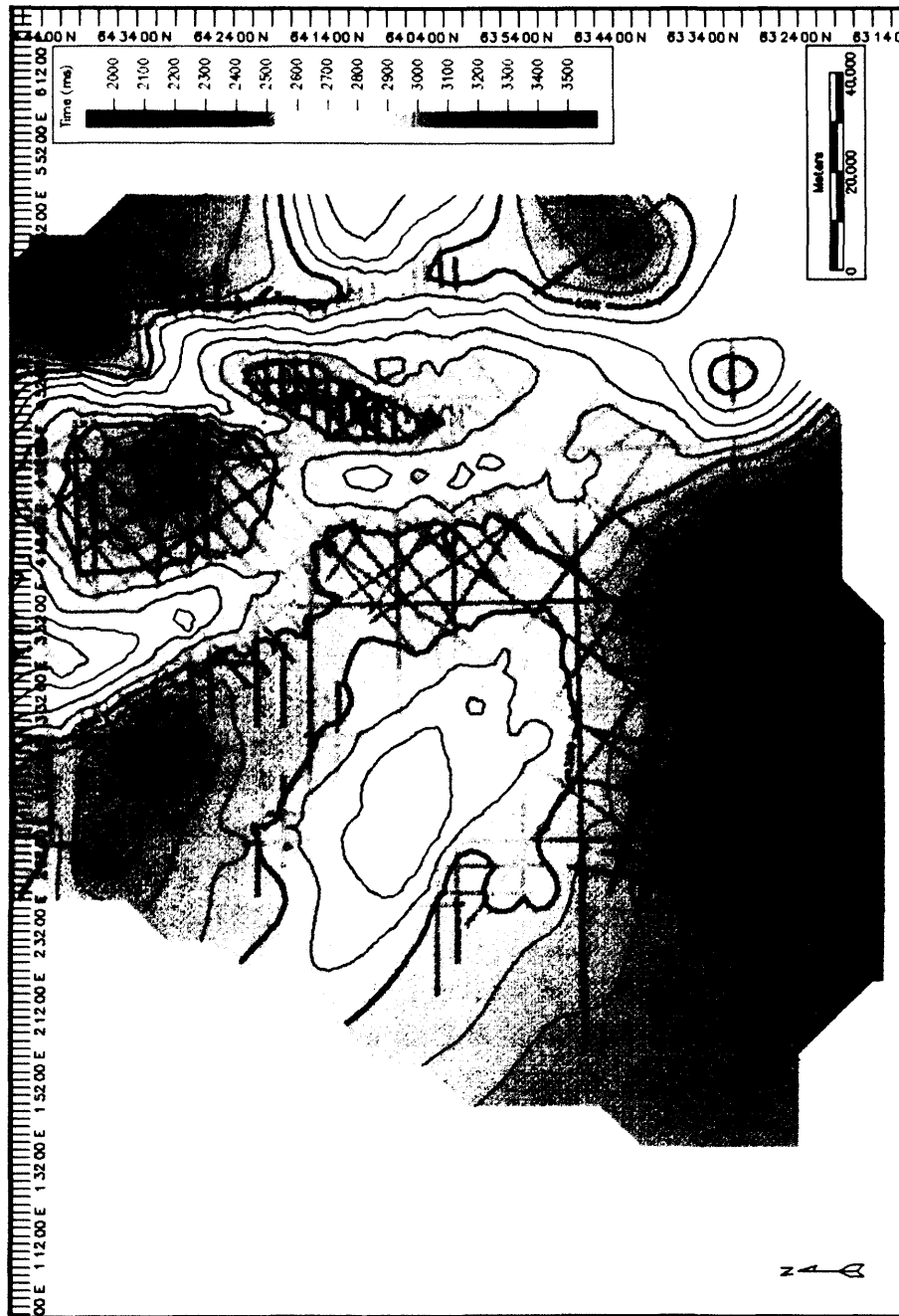


Fig. A1- 2: Two way travel time map of Top Brygge Unit I (early Eocene reflection)

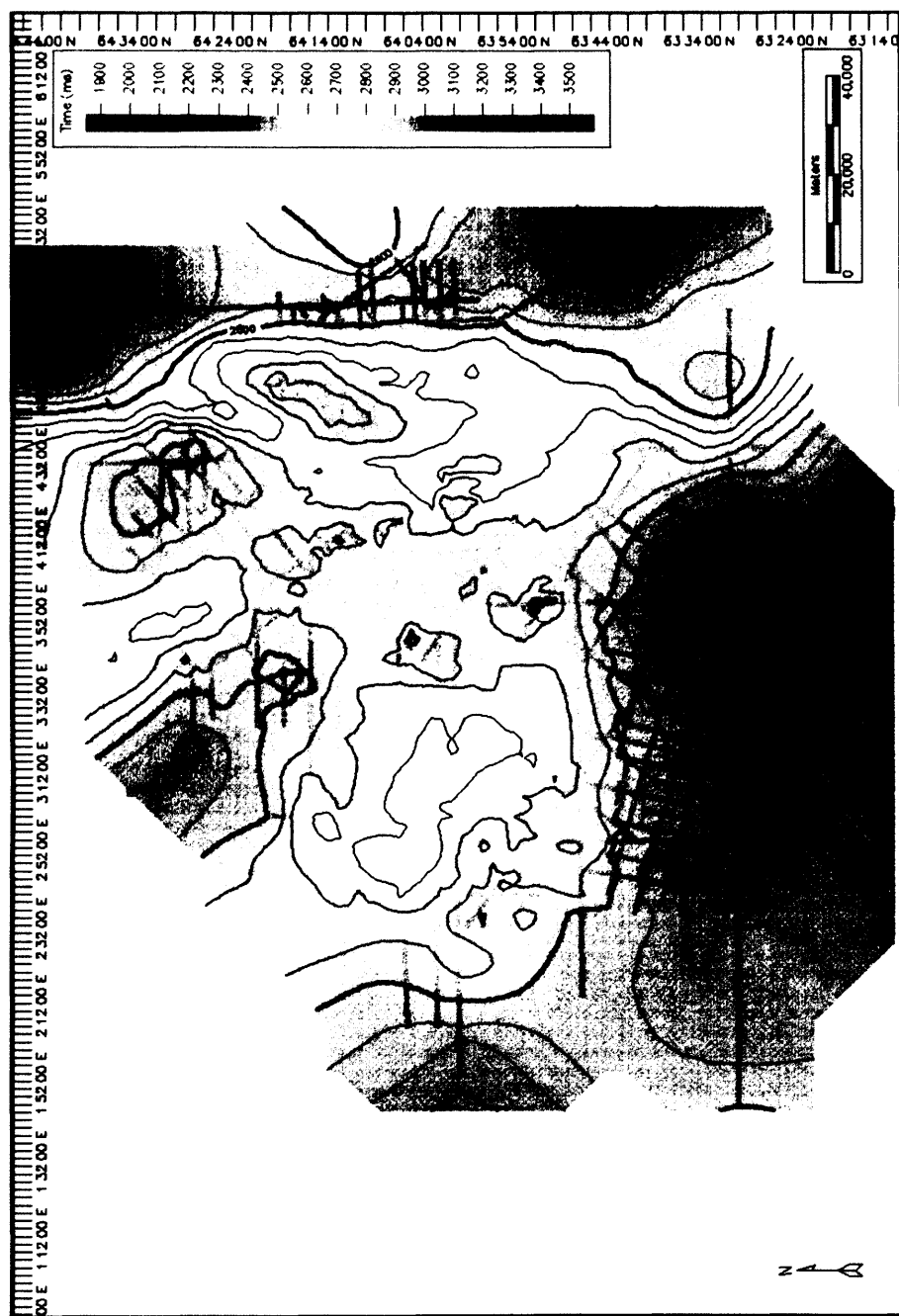


Fig. A1- 3: Two way travel time map of Top Brygge Unit II (Oligocene reflection)

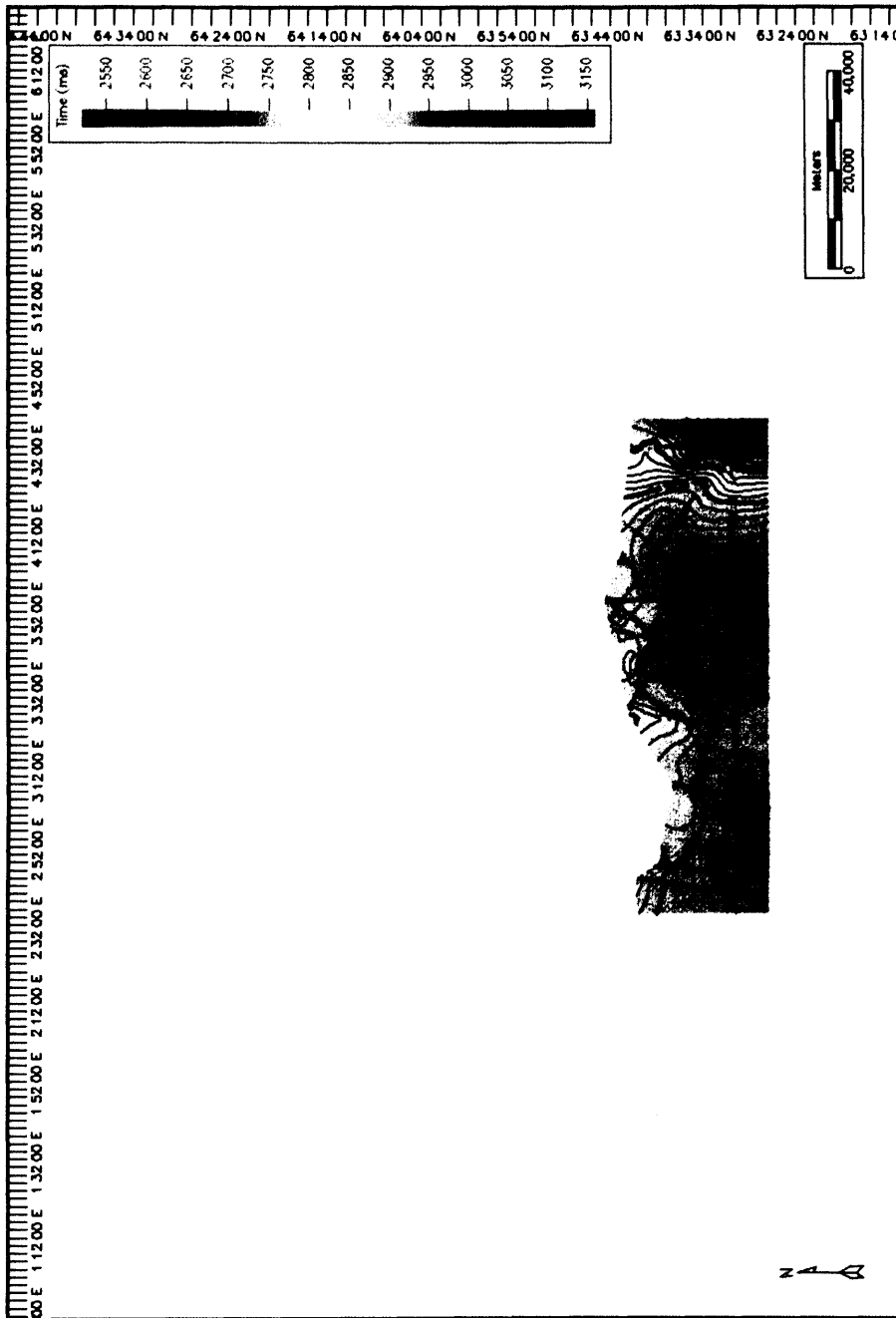


Fig. A1- 4: Two way travel time map of Top Brygge III in south of study area (Oligocene reflection)

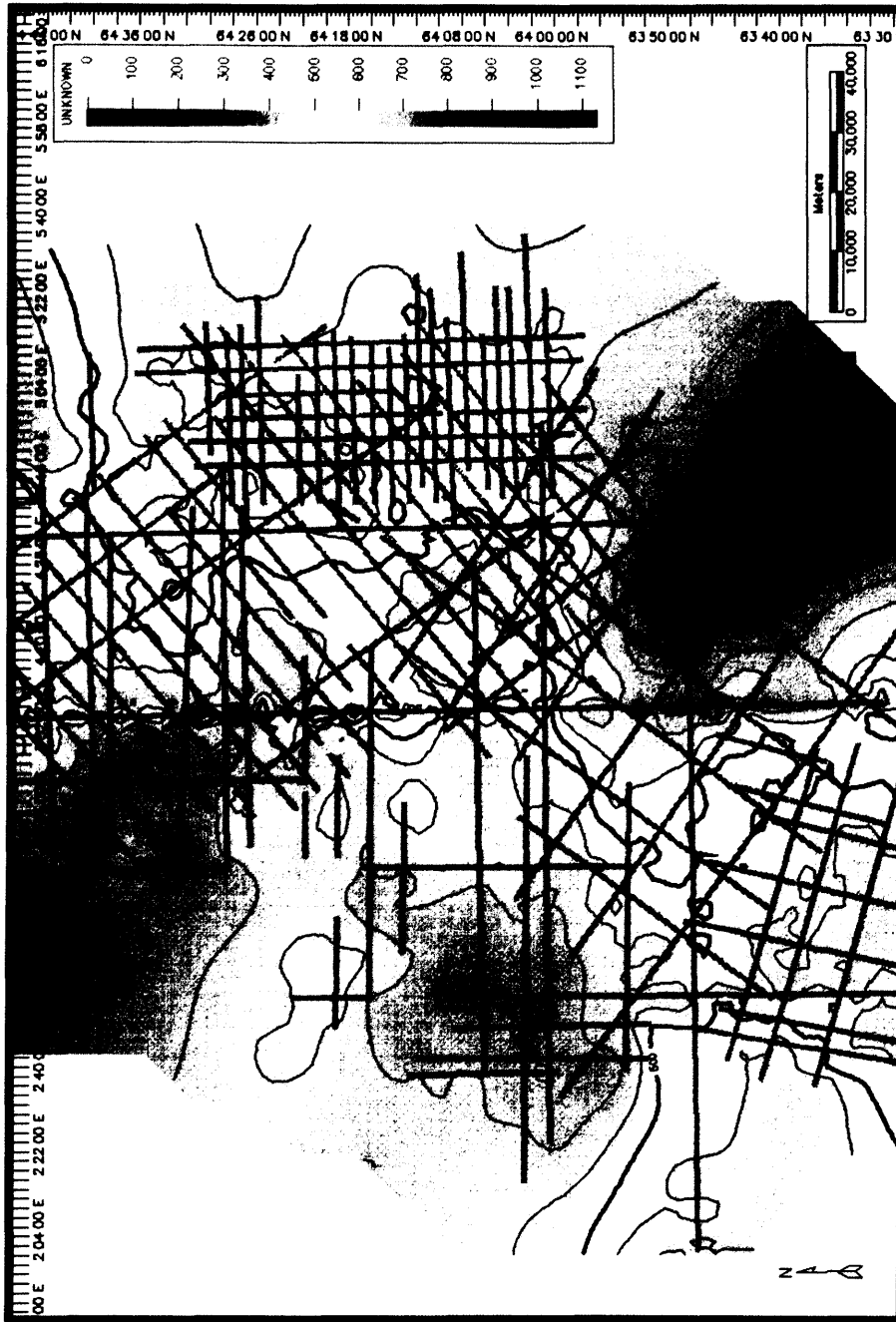


Fig. A1- 5: Two way travel time isochron map of Brygge Formation Unit I.

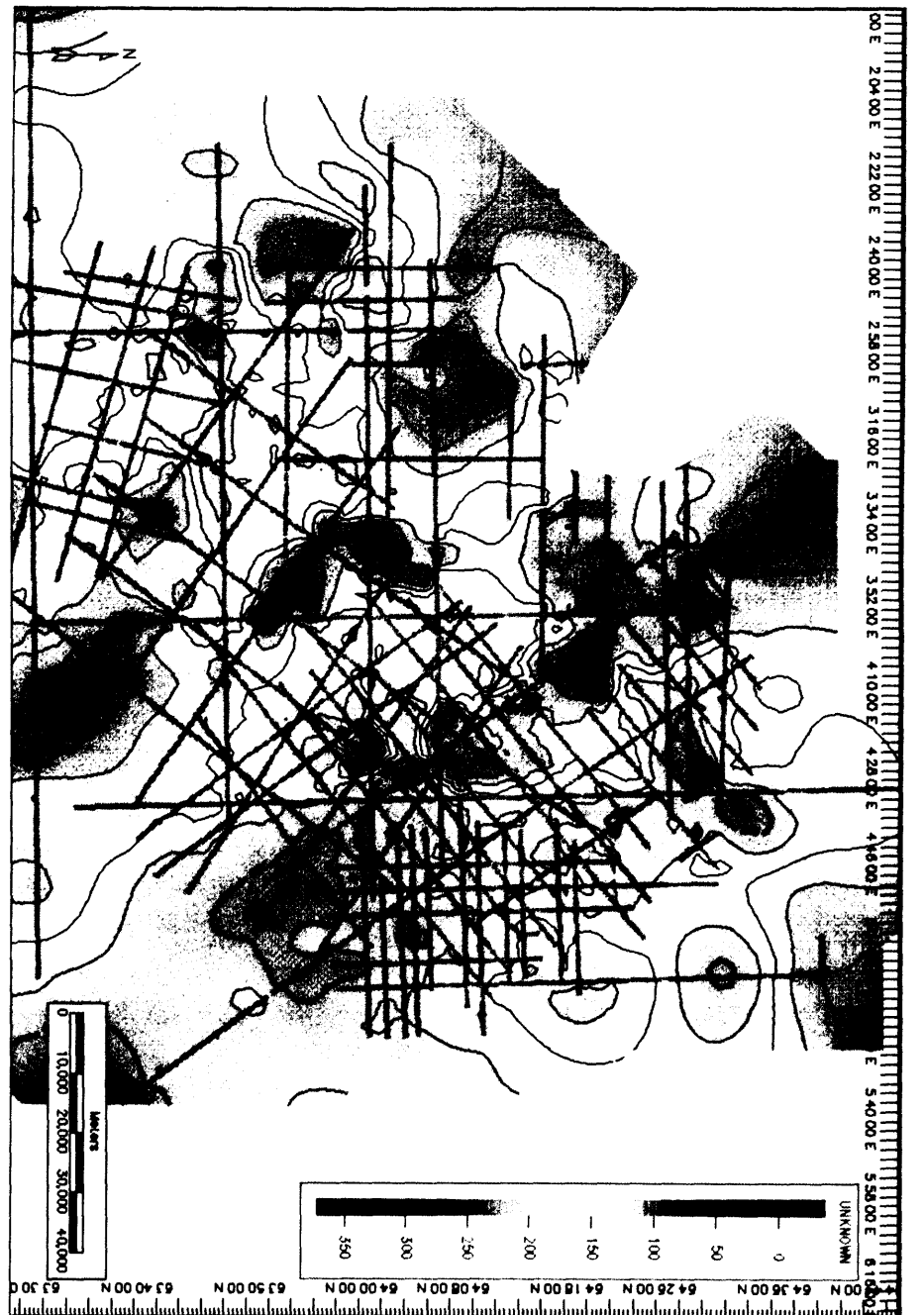


Fig. A1-6: Two way travel time isochron map of Brygge Formation Unit II.

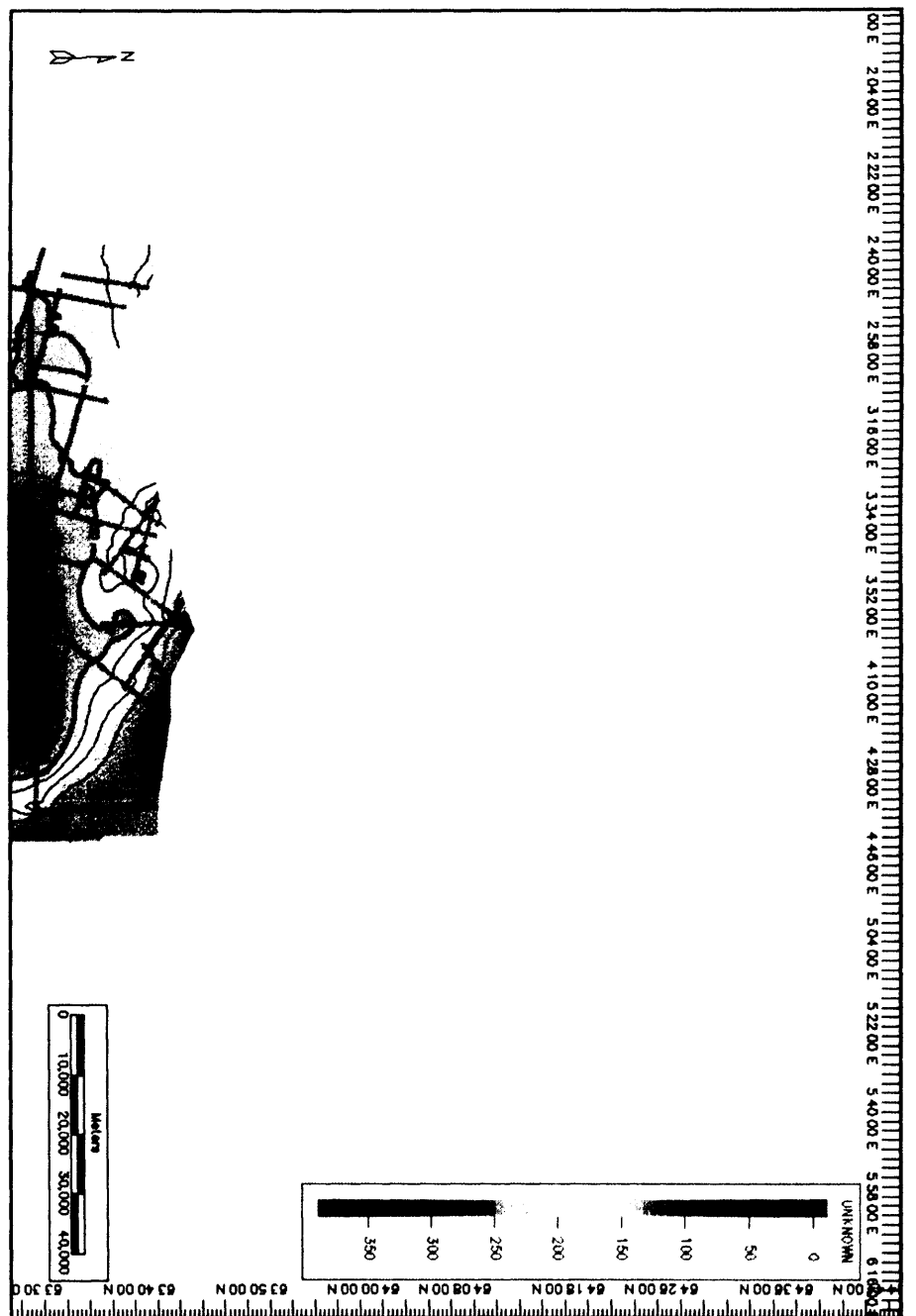


Fig. A1-7: Two way travel time isochron map of Brygge Formation Unit III.

APPENDIX A2: ADDITIONAL EVIDENCE IN SUPPORT OF FINDINGS OF CHAPTER 3

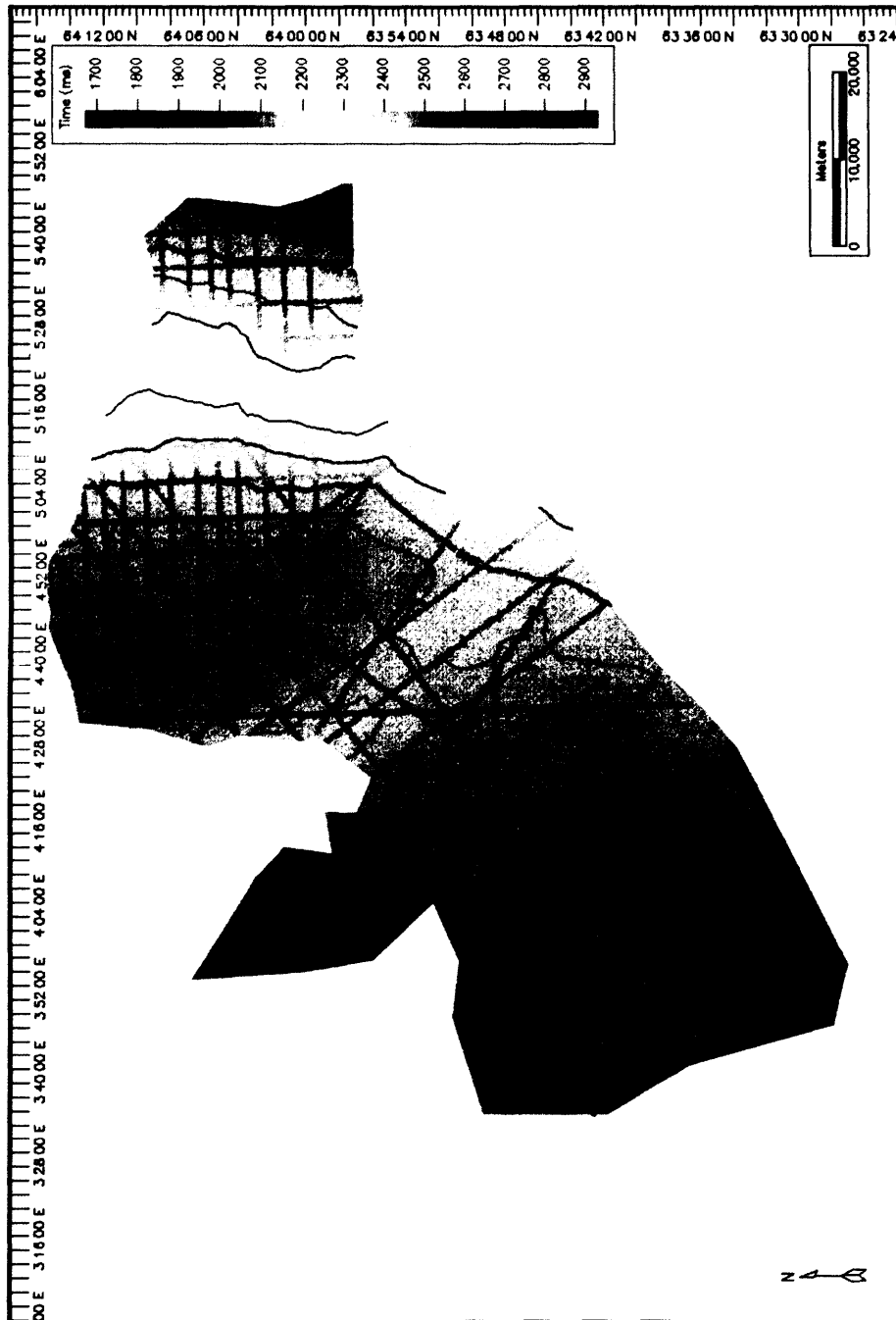


Fig. A2- 1: Two way travel time map of basal shear surface of Slide Y, compiled from 2D seismic reflection data.

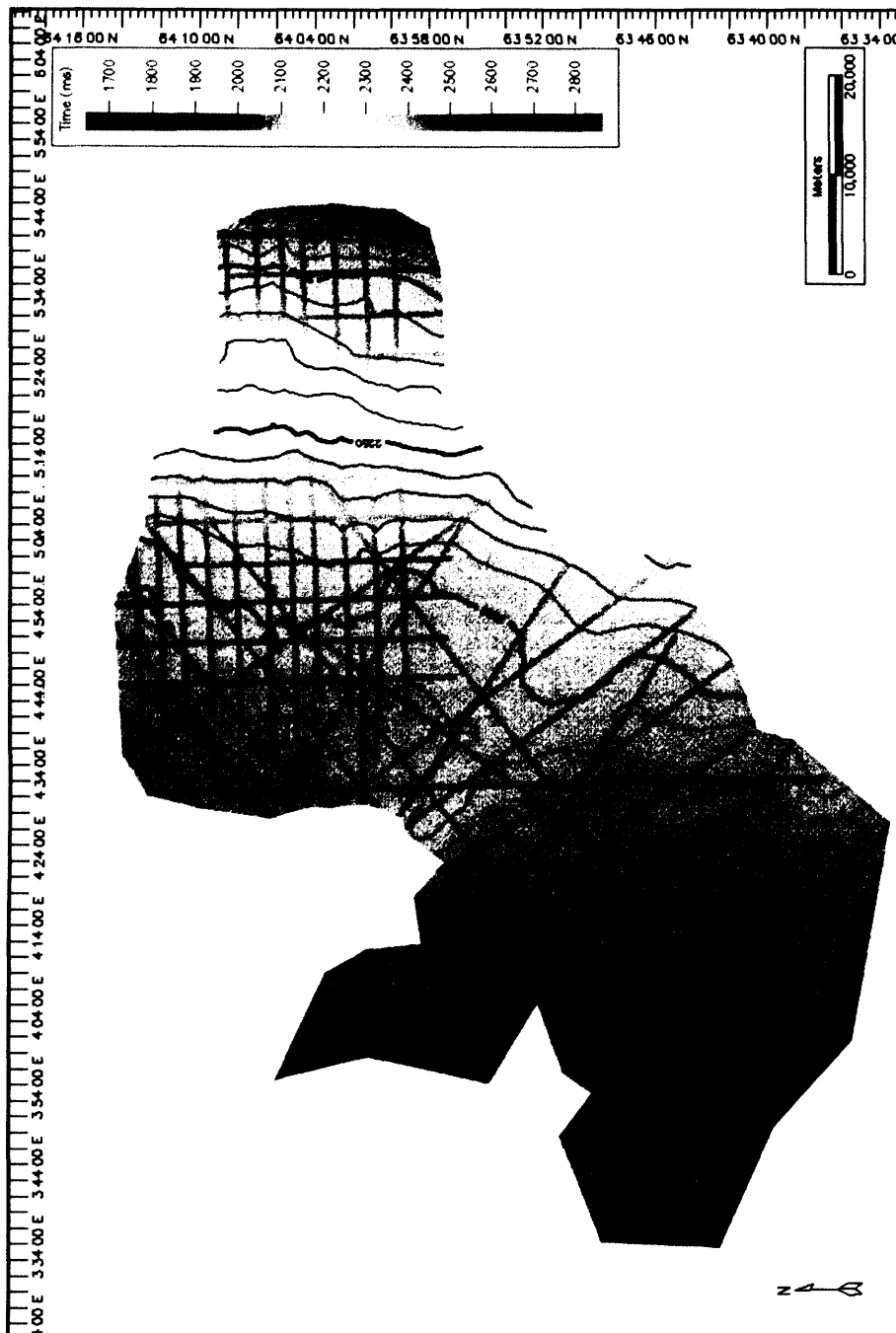


Fig. A2- 2: Two way travel time map of top surface of Slide Y, compiled from 2D seismic reflection data.

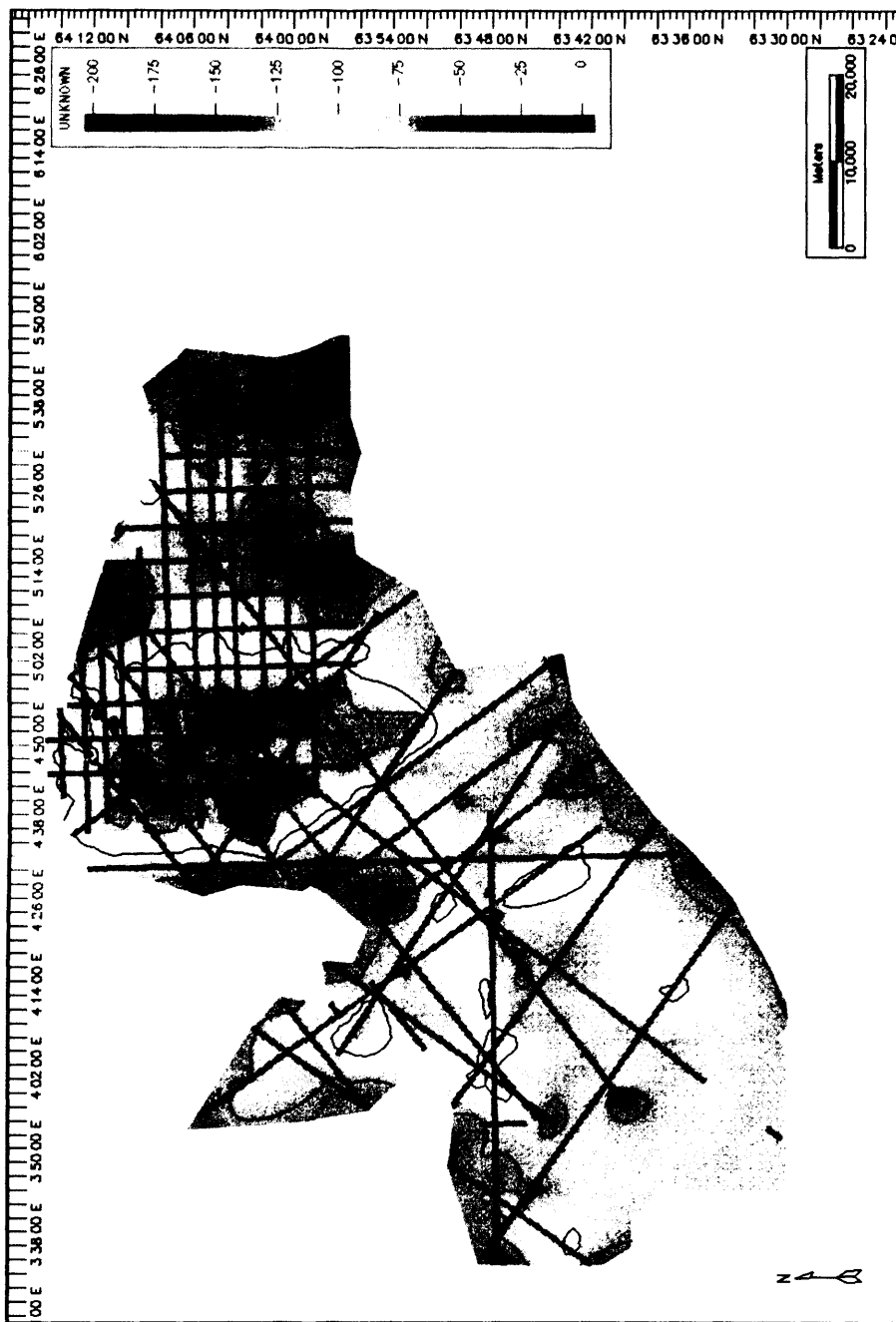


Fig. A2- 3: Two way travel time isochron map of Slide Y, compiled from 2D seismic reflection data.

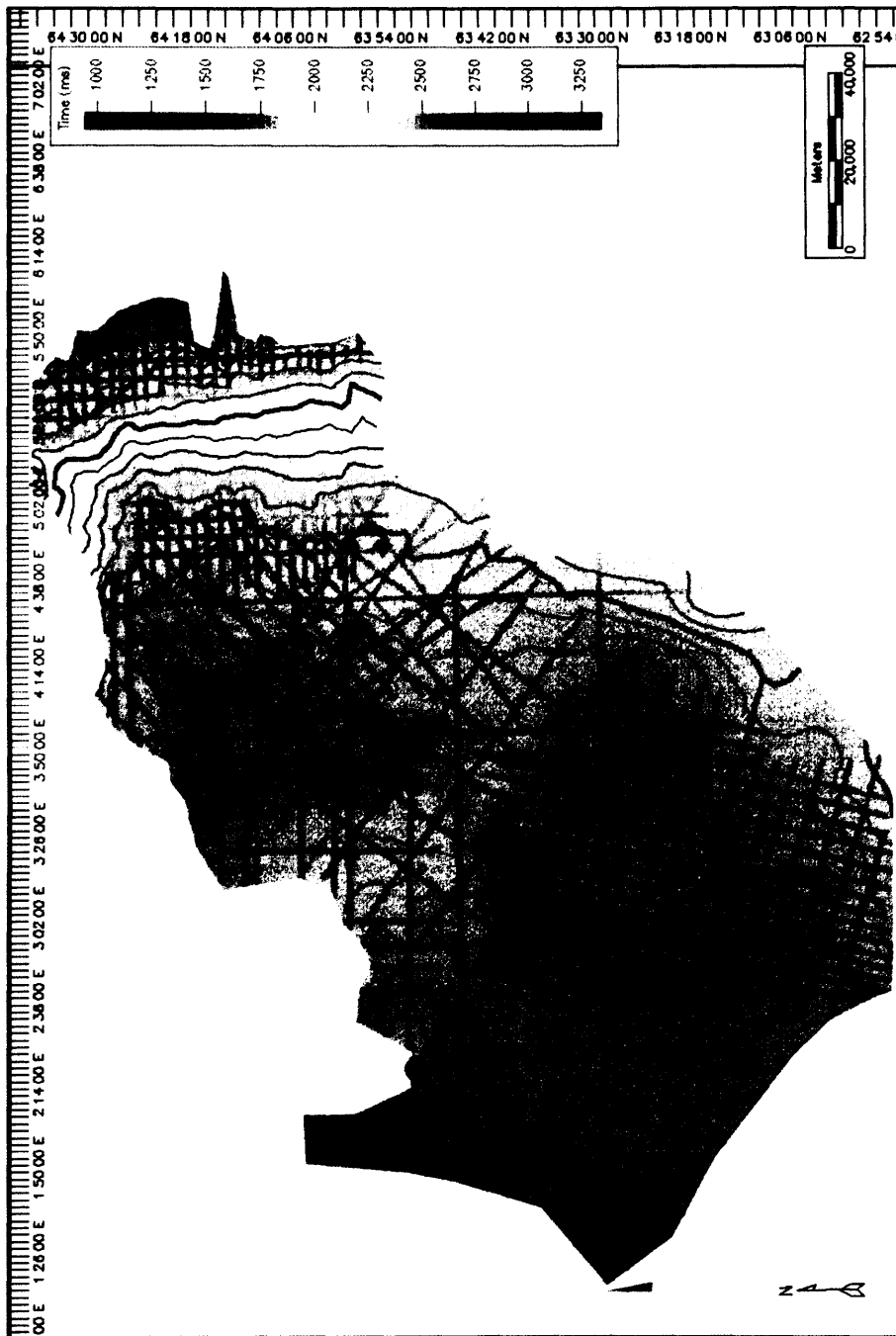


Fig. A2- 4: Two way travel time map of basal shear surface of Slide W, compiled from 2D seismic reflection data.

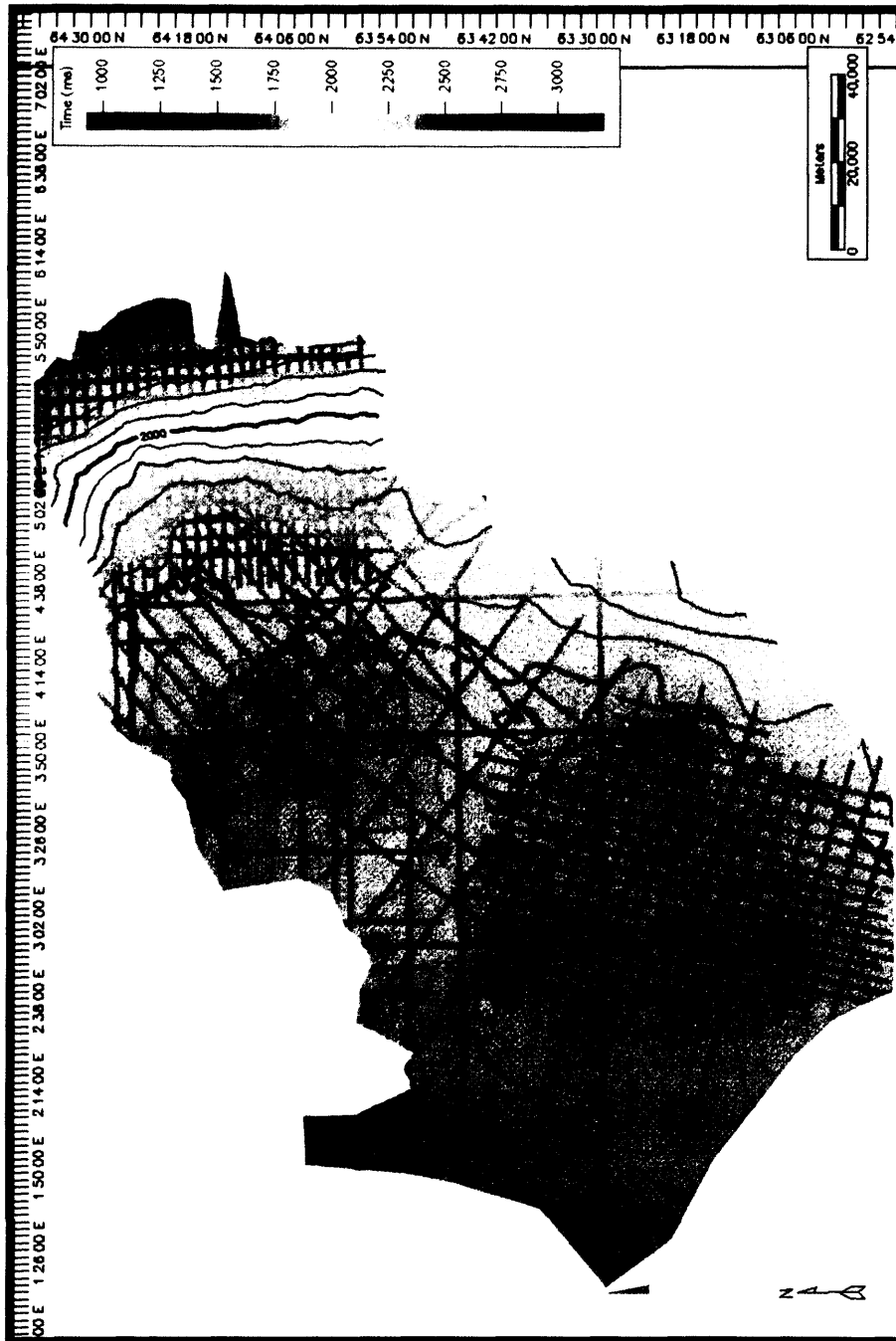


Fig. A2- 5: Two way travel time map of top surface of Slide W, compiled from 2D seismic reflection data.

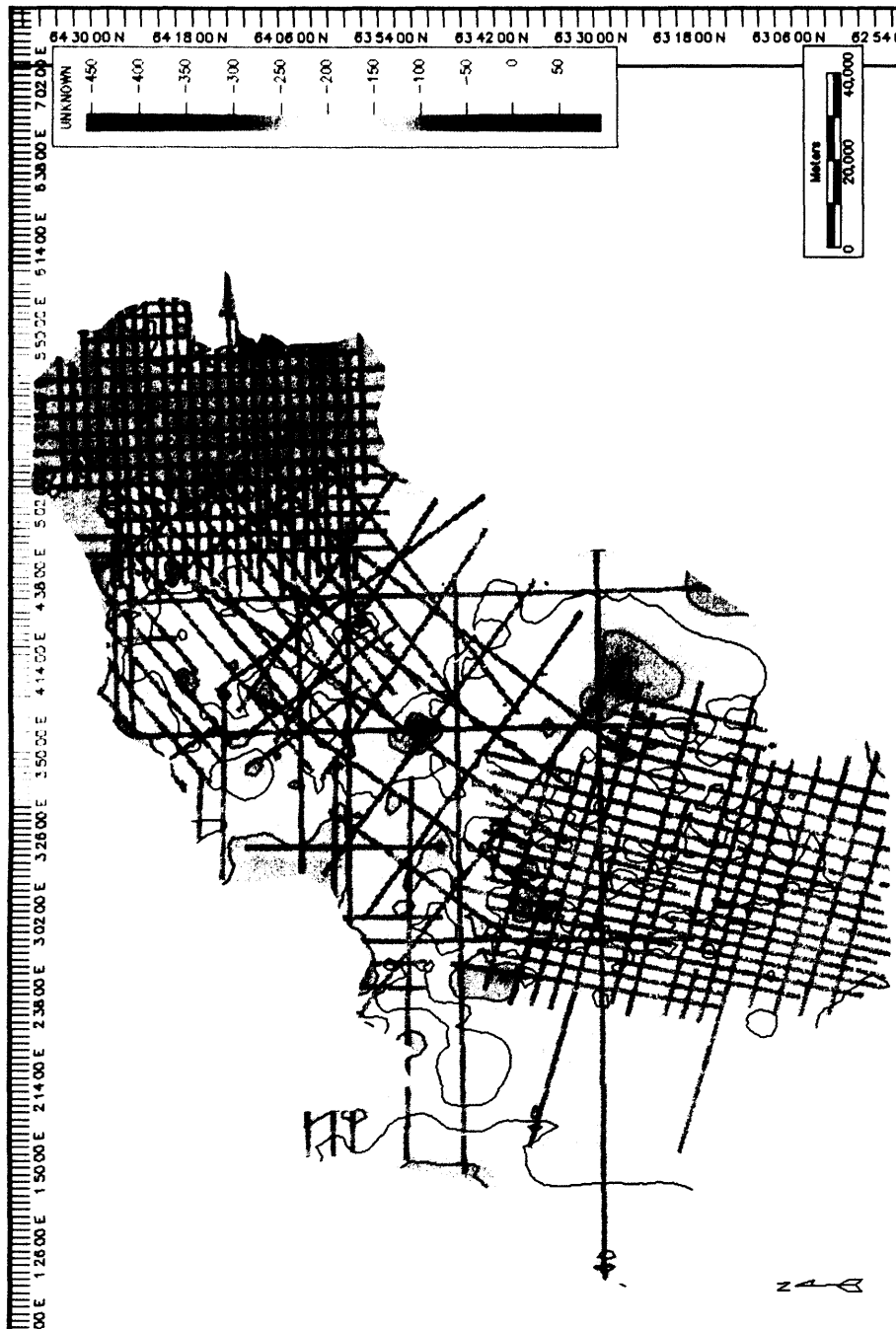


Fig. A2- 6: Two way travel time isochron map of Slide W, compiled from 2D seismic reflection data.

APPENDIX A3: ADDITIONAL EVIDENCE IN SUPPORT OF FINDINGS OF CHAPTER 4

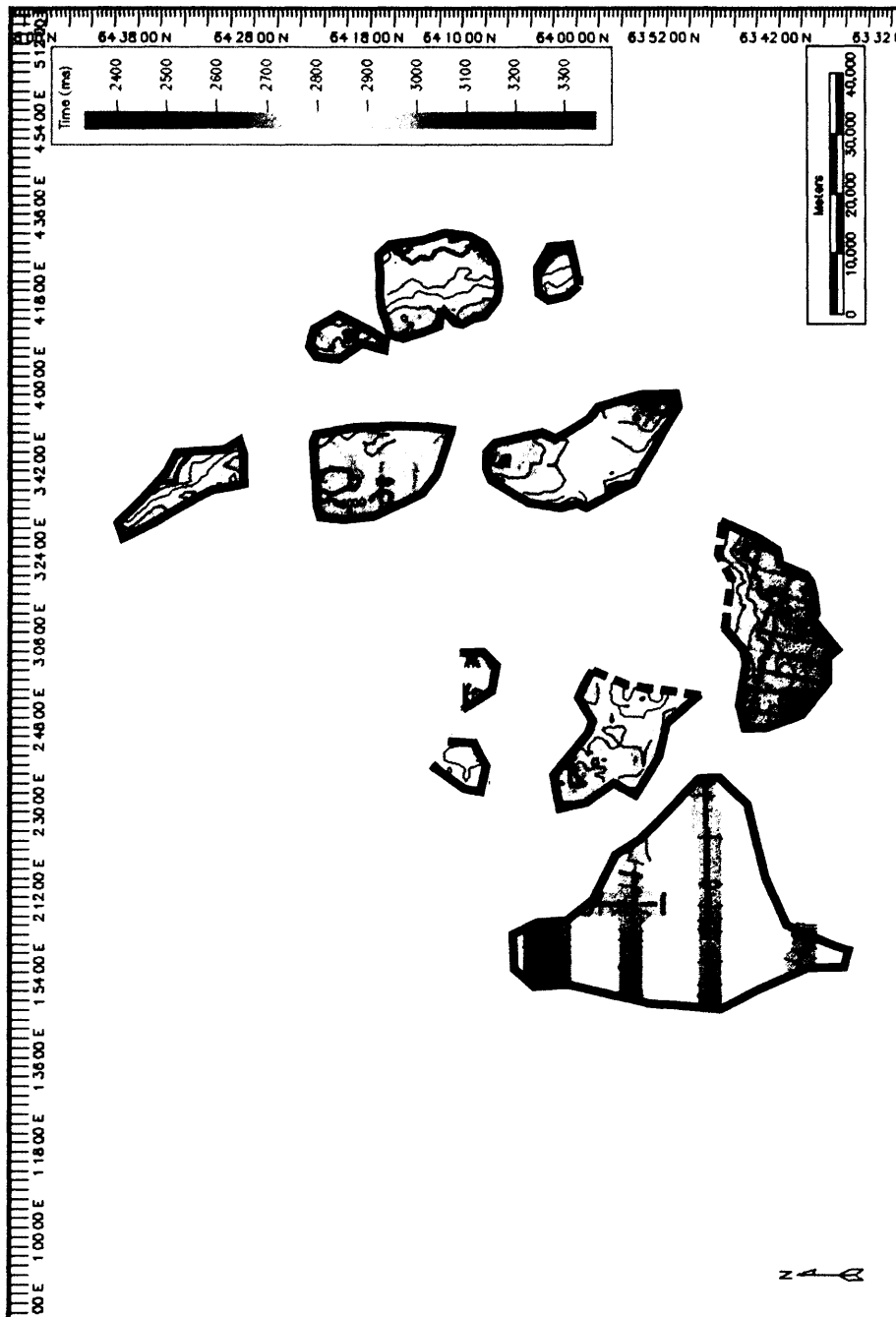


Fig. A3- 1: Two way travel time map of base of craters, compiled from 2D seismic reflection data.

APPENDIX A4: ADDITIONAL EVIDENCE IN SUPPORT OF FINDINGS OF CHAPTER 5

Data used for depth conversions

CDP 4002 Havsule

| Shot Point | Time pick of seabed (ms) | Time pick of top Slide W and top mound (ms) | Time pick of top Slide W and base mound (ms) | Time pick of base Slide W (ms) | Time pick of base Brygge (ms) |
|------------|--------------------------|---|--|--------------------------------|-------------------------------|
| 5 | -2046 | -2594 | -2594 | -2846 | -3430 |
| 25 | -2044 | -2578 | -2578 | -2840 | -3426 |
| 50 | -2054 | -2584 | -2584 | -2828 | -3410 |
| 75 | -2072 | -2582 | -2582 | -2808 | -3404 |
| 100 | -2060 | -2574 | -2574 | -2806 | -3380 |
| 115 | -2076 | -2576 | -2576 | -2796 | -3366 |
| 116 | -2076 | -2576 | -2576 | -2796 | -3376 |
| 125 | -2075 | -2558 | -2596 | -2789 | -3371 |
| 150 | -2074 | -2540 | -2616 | -2780 | -3366 |
| 175 | -2108 | -2528 | -2610 | -2774 | -3374 |
| 200 | -2106 | -2514 | -2624 | -2762 | -3368 |
| 225 | -2098 | -2486 | -2598 | -2740 | -3358 |
| 225 | -2098 | -2486 | -2598 | -2740 | -3358 |
| 226 | -2098 | -2488 | -2598 | -2888 | -3328 |
| 250 | -2106 | -2488 | -2636 | -2894 | -3308 |
| 275 | -2100 | -2470 | -2612 | -2870 | -3298 |
| 300 | -2116 | -2478 | -2592 | -2862 | -3294 |
| 325 | -2100 | -2516 | -2574 | -2846 | -3258 |
| 350 | -2100 | -2484 | -2558 | -2820 | -3246 |
| 375 | -2096 | -2490 | -2558 | -2814 | -3230 |
| 400 | -2088 | -2482 | -2558 | -2806 | -3198 |
| 407 | -2088 | -2512 | -2512 | -2802 | -3202 |
| 408 | -2088 | -2512 | -2512 | -2802 | -3192 |
| 425 | -2088 | -2512 | -2512 | -2796 | -3172 |
| 450 | -2084 | -2502 | -2502 | -2774 | -3174 |
| 475 | -2076 | -2490 | -2490 | -2758 | -3164 |
| 500 | -2072 | -2490 | -2490 | -2750 | -3164 |
| 525 | -2052 | -2490 | -2490 | -2746 | -3156 |
| 550 | -2036 | -2478 | -2478 | -2728 | -3148 |
| 575 | -2020 | -2480 | -2480 | -2726 | -3156 |
| 600 | -2012 | -2476 | -2476 | -2720 | -3112 |
| 625 | -2006 | -2474 | -2474 | -2714 | -3124 |
| 650 | -1992 | -2480 | -2480 | -2698 | -3136 |
| 675 | -1990 | -2476 | -2476 | -2702 | -3140 |
| 683 | -1982 | -2484 | -2484 | -2704 | -3164 |
| 684 | -1982 | -2484 | -2484 | -2604 | -3204 |
| 700 | -1976 | -2480 | -2480 | -2612 | -3208 |
| 725 | -1972 | -2472 | -2472 | -2624 | -3222 |
| 750 | -1968 | -2458 | -2458 | -2650 | -3240 |
| 775 | -1956 | -2458 | -2458 | -2658 | -3270 |
| 800 | -1960 | -2454 | -2454 | -2678 | -3316 |

| | | | | | |
|-----|-------|-------|-------|-------|-------|
| 825 | -1948 | -2454 | -2454 | -2700 | -3344 |
|-----|-------|-------|-------|-------|-------|

Table A4- 1: CDP 4002 Havsule – Time picks of selected horizons.

| Shot Point | Calculated depth to seabed (m) | Calculated depth to top Slide W and top mound (m) | Calculated depth to top Slide W and base mound (m) | Calculated depth to base Slide W (m) | Calculated depth to base Brygge (m) |
|------------|--------------------------------------|--|--|--|---|
| 5 | -1596 | -2067 | -2067 | -2334 | -2858 |
| 25 | -1594 | -2054 | -2054 | -2331 | -2856 |
| 50 | -1602 | -2058 | -2058 | -2316 | -2838 |
| 75 | -1616 | -2055 | -2055 | -2294 | -2828 |
| 100 | -1607 | -2049 | -2049 | -2295 | -2809 |
| 115 | -1619 | -2050 | -2050 | -2282 | -2793 |
| 116 | -1619 | -2050 | -2050 | -2282 | -2802 |
| 125 | -1618 | -2034 | -2065 | -2269 | -2791 |
| 150 | -1618 | -2019 | -2080 | -2253 | -2779 |
| 175 | -1644 | -2006 | -2072 | -2245 | -2783 |
| 200 | -1643 | -1994 | -2082 | -2228 | -2772 |
| 225 | -1636 | -1970 | -2061 | -2211 | -2765 |
| 225 | -1636 | -1970 | -2061 | -2211 | -2765 |
| 226 | -1636 | -1972 | -2061 | -2368 | -2762 |
| 250 | -1643 | -1971 | -2091 | -2364 | -2735 |
| 275 | -1638 | -1956 | -2071 | -2344 | -2728 |
| 300 | -1650 | -1962 | -2054 | -2340 | -2727 |
| 325 | -1638 | -1996 | -2043 | -2330 | -2700 |
| 350 | -1638 | -1968 | -2028 | -2305 | -2687 |
| 375 | -1635 | -1974 | -2029 | -2300 | -2673 |
| 400 | -1629 | -1968 | -2029 | -2291 | -2643 |
| 407 | -1629 | -1993 | -1993 | -2300 | -2659 |
| 408 | -1629 | -1993 | -1993 | -2300 | -2650 |
| 425 | -1629 | -1993 | -1993 | -2294 | -2631 |
| 450 | -1625 | -1985 | -1985 | -2273 | -2632 |
| 475 | -1619 | -1975 | -1975 | -2259 | -2623 |
| 500 | -1616 | -1976 | -1976 | -2251 | -2622 |
| 525 | -1600 | -1977 | -1977 | -2248 | -2616 |
| 550 | -1588 | -1968 | -1968 | -2233 | -2609 |
| 575 | -1576 | -1971 | -1971 | -2232 | -2617 |
| 600 | -1569 | -1969 | -1969 | -2227 | -2578 |
| 625 | -1565 | -1967 | -1967 | -2221 | -2589 |
| 650 | -1554 | -1974 | -1974 | -2204 | -2597 |
| 675 | -1552 | -1970 | -1970 | -2209 | -2602 |
| 683 | -1546 | -1978 | -1978 | -2211 | -2623 |
| 684 | -1546 | -1978 | -1978 | -2105 | -2643 |
| 700 | -1541 | -1975 | -1975 | -2115 | -2649 |
| 725 | -1538 | -1968 | -1968 | -2129 | -2665 |
| 750 | -1535 | -1957 | -1957 | -2160 | -2689 |
| 775 | -1526 | -1958 | -1958 | -2169 | -2718 |
| 800 | -1529 | -1954 | -1954 | -2191 | -2763 |
| 825 | -1519 | -1955 | -1955 | -2215 | -2792 |

Table A4- 2: CDP 4002 Havsule – Calculated depths to selected horizons.

ILN 2634 Havsule

| Shot Point | Time pick of seabed (ms) | Time pick of top Slide W and top mound (ms) | Time pick of top Slide W and base mound (ms) | Time pick of base Slide W (ms) | Time pick of base Brygge (ms) |
|------------|--------------------------|---|--|--------------------------------|-------------------------------|
| 825 | -1984 | -2526 | -2526 | -2690 | -3296 |
| 850 | -2026 | -2526 | -2526 | -2690 | -3280 |
| 875 | -2018 | -2526 | -2526 | -2692 | -3272 |
| 900 | -2042 | -2532 | -2532 | -2700 | -3286 |
| 925 | -2084 | -2534 | -2534 | -2700 | -3296 |
| 930 | -2094 | -2514 | -2560 | -2698 | -3300 |
| 935 | -2092 | -2504 | -2572 | -2700 | -3308 |
| 940 | -2094 | -2502 | -2592 | -2846 | -3270 |
| 950 | -2094 | -2518 | -2588 | -2850 | -3276 |
| 975 | -2102 | -2514 | -2588 | -2814 | -3284 |
| 1000 | -2100 | -2510 | -2578 | -2832 | -3280 |
| 1025 | -2110 | -2494 | -2590 | -2830 | -3274 |
| 1050 | -2116 | -2488 | -2604 | -2876 | -3278 |
| 1075 | -2114 | -2462 | -2596 | -2860 | -3268 |
| 1100 | -2122 | -2462 | -2616 | -2846 | -3268 |
| 1125 | -2120 | -2492 | -2600 | -2852 | -3246 |
| 1150 | -2122 | -2490 | -2598 | -2856 | -3236 |
| 1175 | -2140 | -2468 | -2602 | -2856 | -3234 |
| 1200 | -2148 | -2476 | -2604 | -2838 | -3246 |
| 1225 | -2156 | -2474 | -2608 | -2864 | -3248 |
| 1250 | -2156 | -2508 | -2586 | -2824 | -3262 |
| 1275 | -2168 | -2432 | -2658 | -2896 | -3264 |
| 1288 | -2180 | -2414 | -2668 | -2900 | -3276 |
| 1300 | -2174 | -2436 | -2660 | -2890 | -3282 |
| 1312 | -2180 | -2494 | -2630 | -2860 | -3264 |
| 1325 | -2178 | -2524 | -2626 | -2854 | -3258 |
| 1350 | -2192 | -2562 | -2596 | -2870 | -3280 |
| 1375 | -2194 | -2558 | -2624 | -2880 | -3294 |
| 1400 | -2212 | -2578 | -2610 | -2856 | -3288 |
| 1425 | -2224 | -2564 | -2618 | -2886 | -3304 |
| 1450 | -2248 | -2558 | -2604 | -2882 | -3304 |
| 1475 | -2238 | -2560 | -2614 | -2874 | -3320 |
| 1500 | -2240 | -2550 | -2616 | -2882 | -3316 |
| 1525 | -2244 | -2586 | -2586 | -2898 | -3330 |
| 1550 | -2264 | -2584 | -2614 | -2912 | -3316 |
| 1575 | -2280 | -2600 | -2600 | -2904 | -3314 |
| 1600 | -2278 | -2604 | -2604 | -2898 | -3334 |
| 1625 | -2234 | -2586 | -2586 | -2882 | -3338 |
| 1650 | -2300 | -2578 | -2578 | -2878 | -3328 |
| 1675 | -2296 | -2596 | -2596 | -2898 | -3336 |
| 1700 | -2304 | -2602 | -2602 | -2884 | -3344 |
| 1710 | -2320 | -2614 | -2614 | -2886 | -3336 |
| 1715 | -2336 | -2616 | -2616 | -2814 | -3366 |
| 1725 | -2338 | -2610 | -2610 | -2824 | -3370 |
| 1750 | -2340 | -2614 | -2614 | -2820 | -3360 |

Table A4- 3: ILN 2634 Havsule – Time picks of selected horizons.

| Shot Point | Calculated depth to seabed (m) | Calculated depth to top Slide W and top mound (m) | Calculated depth to top Slide W and base mound (m) | Calculated depth to base Slide W (m) | Calculated depth to base Brygge (m) |
|------------|--------------------------------------|---|--|---|--|
| 825 | -1547 | -2014 | -2014 | -2187 | -2731 |
| 850 | -1580 | -2011 | -2011 | -2184 | -2713 |
| 875 | -1574 | -2011 | -2011 | -2187 | -2707 |
| 900 | -1593 | -2014 | -2014 | -2192 | -2717 |
| 925 | -1625 | -2013 | -2013 | -2188 | -2723 |
| 930 | -1633 | -1995 | -2032 | -2178 | -2717 |
| 935 | -1632 | -1986 | -2041 | -2177 | -2722 |
| 940 | -1633 | -1984 | -2057 | -2326 | -2706 |
| 950 | -1633 | -1998 | -2055 | -2332 | -2714 |
| 975 | -1639 | -1994 | -2054 | -2293 | -2714 |
| 1000 | -1638 | -1991 | -2046 | -2314 | -2716 |
| 1025 | -1646 | -1976 | -2054 | -2308 | -2706 |
| 1050 | -1650 | -1971 | -2064 | -2352 | -2712 |
| 1075 | -1649 | -1948 | -2056 | -2336 | -2701 |
| 1100 | -1655 | -1948 | -2072 | -2315 | -2694 |
| 1125 | -1654 | -1974 | -2061 | -2327 | -2681 |
| 1150 | -1655 | -1972 | -2059 | -2332 | -2673 |
| 1175 | -1669 | -1951 | -2060 | -2328 | -2667 |
| 1200 | -1675 | -1958 | -2061 | -2308 | -2674 |
| 1225 | -1682 | -1955 | -2063 | -2334 | -2678 |
| 1250 | -1682 | -1985 | -2047 | -2299 | -2692 |
| 1275 | -1691 | -1918 | -2100 | -2352 | -2682 |
| 1288 | -1700 | -1902 | -2107 | -2352 | -2689 |
| 1300 | -1696 | -1921 | -2102 | -2345 | -2697 |
| 1312 | -1700 | -1971 | -2080 | -2324 | -2686 |
| 1325 | -1699 | -1997 | -2079 | -2320 | -2682 |
| 1350 | -1710 | -2028 | -2056 | -2345 | -2713 |
| 1375 | -1711 | -2024 | -2078 | -2349 | -2720 |
| 1400 | -1725 | -2040 | -2066 | -2326 | -2714 |
| 1425 | -1735 | -2027 | -2071 | -2354 | -2729 |
| 1450 | -1753 | -2020 | -2057 | -2351 | -2730 |
| 1475 | -1746 | -2023 | -2066 | -2341 | -2741 |
| 1500 | -1747 | -2014 | -2067 | -2349 | -2738 |
| 1525 | -1750 | -2045 | -2045 | -2375 | -2762 |
| 1550 | -1766 | -2041 | -2065 | -2381 | -2743 |
| 1575 | -1778 | -2054 | -2054 | -2375 | -2743 |
| 1600 | -1777 | -2057 | -2057 | -2368 | -2759 |
| 1625 | -1742 | -2045 | -2045 | -2358 | -2767 |
| 1650 | -1794 | -2033 | -2033 | -2351 | -2754 |
| 1675 | -1791 | -2049 | -2049 | -2368 | -2761 |
| 1700 | -1797 | -2053 | -2053 | -2352 | -2764 |
| 1710 | -1809 | -2063 | -2063 | -2350 | -2754 |
| 1715 | -1822 | -2063 | -2063 | -2272 | -2767 |
| 1725 | -1824 | -2058 | -2058 | -2284 | -2774 |
| 1750 | -1825 | -2061 | -2061 | -2279 | -2763 |

Table A4- 4: ILN 2634 Havsule – Calculated depths to selected horizons.

CDP 4942 Havsule

| Shot Point | Time pick of seabed (ms) | Time pick of top Slide W and top mound (ms) | Time pick of top Slide W and base mound (ms) | Time pick of base Slide W (ms) | Time pick of base Brygge (ms) |
|------------|--------------------------|---|--|--------------------------------|-------------------------------|
| 5 | -2174 | -2568 | -2678 | -2820 | -3380 |
| 25 | -2208 | -2568 | -2696 | -2828 | -3400 |
| 50 | -2240 | -2560 | -2688 | -2830 | -3404 |
| 75 | -2246 | -2552 | -2686 | -2844 | -3420 |
| 100 | -2232 | -2534 | -2704 | -2840 | -3412 |
| 125 | -2248 | -2532 | -2680 | -2848 | -3422 |
| 150 | -2258 | -2574 | -2684 | -2834 | -3420 |
| 175 | -2256 | -2562 | -2680 | -2826 | -3410 |
| 180 | -2254 | -2584 | -2676 | -2974 | -3400 |
| 200 | -2256 | -2580 | -2676 | -2942 | -3352 |
| 225 | -2256 | -2550 | -2664 | -2948 | -3370 |
| 250 | -2256 | -2544 | -2664 | -2936 | -3356 |
| 275 | -2250 | -2526 | -2620 | -2934 | -3338 |
| 300 | -2244 | -2532 | -2618 | -2892 | -3332 |
| 325 | -2244 | -2526 | -2614 | -2874 | -3322 |
| 335 | -2242 | -2564 | -2564 | -2878 | -3310 |
| 340 | -2234 | -2568 | -2568 | -2880 | -3298 |
| 350 | -2216 | -2570 | -2570 | -2866 | -3294 |
| 375 | -2188 | -2556 | -2556 | -2858 | -3274 |
| 400 | -2184 | -2562 | -2562 | -2840 | -3242 |
| 425 | -2178 | -2558 | -2558 | -2820 | -3248 |
| 450 | -2170 | -2544 | -2544 | -2808 | -3238 |
| 475 | -2168 | -2542 | -2542 | -2790 | -3250 |
| 500 | -2156 | -2540 | -2540 | -2778 | -3248 |
| 525 | -2138 | -2526 | -2526 | -2768 | -3252 |
| 550 | -2132 | -2520 | -2520 | -2770 | -3242 |
| 575 | -2072 | -2512 | -2512 | -2758 | -3242 |
| 600 | -2040 | -2502 | -2502 | -2740 | -3254 |
| 625 | -2022 | -2494 | -2494 | -2736 | -3258 |
| 650 | -2022 | -2498 | -2498 | -2744 | -3258 |
| 675 | -2012 | -2492 | -2492 | -2738 | -3266 |
| 700 | -2006 | -2484 | -2484 | -2736 | -3274 |
| 725 | -1986 | -2488 | -2488 | -2734 | -3280 |
| 750 | -1984 | -2488 | -2488 | -2772 | -3266 |
| 770 | -1982 | -2486 | -2486 | -2776 | -3280 |
| 775 | -1980 | -2484 | -2484 | -2664 | -3332 |
| 800 | -1974 | -2486 | -2486 | -2676 | -3360 |
| 825 | -1972 | -2484 | -2484 | -2694 | -3372 |

Table A4- 5: CDP 4942 Havsule – Time picks of selected horizons.

| Shot Point | Calculated depth to seabed (m) | Calculated depth to top Slide W and top mound (m) | Calculated depth to top Slide W and base mound (m) | Calculated depth to base Slide W (m) | Calculated depth to base Brygge (m) |
|------------|--------------------------------------|--|--|--|---|
| 5 | -1696 | -2035 | -2123 | -2274 | -2776 |
| 25 | -1722 | -2032 | -2135 | -2275 | -2788 |
| 50 | -1747 | -2023 | -2126 | -2276 | -2791 |
| 75 | -1752 | -2015 | -2123 | -2290 | -2807 |
| 100 | -1741 | -2001 | -2138 | -2282 | -2795 |
| 125 | -1753 | -1998 | -2117 | -2295 | -2809 |
| 150 | -1761 | -2033 | -2122 | -2281 | -2806 |
| 175 | -1760 | -2023 | -2118 | -2273 | -2796 |
| 180 | -1758 | -2042 | -2116 | -2432 | -2813 |
| 200 | -1760 | -2038 | -2116 | -2397 | -2765 |
| 225 | -1760 | -2013 | -2105 | -2405 | -2783 |
| 250 | -1760 | -2007 | -2104 | -2392 | -2769 |
| 275 | -1755 | -1992 | -2068 | -2400 | -2763 |
| 300 | -1750 | -1998 | -2067 | -2357 | -2752 |
| 325 | -1750 | -1993 | -2064 | -2339 | -2741 |
| 335 | -1749 | -2026 | -2026 | -2358 | -2745 |
| 340 | -1742 | -2030 | -2030 | -2360 | -2735 |
| 350 | -1728 | -2033 | -2033 | -2346 | -2730 |
| 375 | -1707 | -2023 | -2023 | -2343 | -2716 |
| 400 | -1703 | -2029 | -2029 | -2323 | -2683 |
| 425 | -1699 | -2026 | -2026 | -2303 | -2687 |
| 450 | -1693 | -2014 | -2014 | -2294 | -2679 |
| 475 | -1691 | -2013 | -2013 | -2275 | -2688 |
| 500 | -1682 | -2012 | -2012 | -2264 | -2685 |
| 525 | -1668 | -2001 | -2001 | -2257 | -2691 |
| 550 | -1663 | -1997 | -1997 | -2261 | -2684 |
| 575 | -1616 | -1995 | -1995 | -2255 | -2689 |
| 600 | -1591 | -1989 | -1989 | -2240 | -2701 |
| 625 | -1577 | -1983 | -1983 | -2239 | -2707 |
| 650 | -1577 | -1987 | -1987 | -2247 | -2708 |
| 675 | -1569 | -1982 | -1982 | -2243 | -2716 |
| 700 | -1565 | -1976 | -1976 | -2243 | -2725 |
| 725 | -1549 | -1981 | -1981 | -2241 | -2731 |
| 750 | -1547 | -1981 | -1981 | -2282 | -2724 |
| 770 | -1546 | -1980 | -1980 | -2286 | -2738 |
| 775 | -1544 | -1978 | -1978 | -2168 | -2767 |
| 800 | -1540 | -1980 | -1980 | -2181 | -2794 |
| 825 | -1538 | -1979 | -1979 | -2201 | -2809 |

Table A4- 6: CDP 4942 Havsule – Calculated depths to selected horizons.

ILN 2398 Havsule

| Shot Point | Time pick of seabed (ms) | Time pick of top Slide W and top mound (ms) | Time pick of top Slide W and base mound (ms) | Time pick of base Slide W (ms) | Time pick of base Brygge (ms) |
|------------|--------------------------|---|--|--------------------------------|-------------------------------|
| 825 | -1998 | -2506 | -2560 | -2738 | -3334 |
| 850 | -1984 | -2542 | -2542 | -2732 | -3318 |
| 875 | -2022 | -2550 | -2550 | -2740 | -3328 |
| 900 | -2036 | -2552 | -2552 | -2744 | -3332 |
| 925 | -2038 | -2560 | -2560 | -2750 | -3334 |
| 945 | -2076 | -2560 | -2560 | -2754 | -3342 |
| 950 | -2030 | -2538 | -2580 | -2750 | -3338 |
| 975 | -2086 | -2540 | -2600 | -2764 | -3348 |
| 1000 | -2120 | -2524 | -2600 | -2752 | -3366 |
| 1025 | -2102 | -2516 | -2608 | -2760 | -3344 |
| 1030 | -2102 | -2544 | -2610 | -2900 | -3304 |
| 1050 | -2118 | -2536 | -2636 | -2928 | -3314 |
| 1075 | -2116 | -2516 | -2634 | -2960 | -3320 |
| 1100 | -2132 | -2486 | -2636 | -2860 | -3332 |
| 1105 | -2132 | -2492 | -2638 | -2864 | -3332 |
| 1110 | -2116 | -2488 | -2642 | -2770 | -3350 |
| 1125 | -2140 | -2500 | -2648 | -2776 | -3368 |
| 1150 | -2144 | -2500 | -2664 | -2780 | -3368 |
| 1155 | -2146 | -2522 | -2668 | -2914 | -3348 |
| 1175 | -2156 | -2532 | -2662 | -2914 | -3306 |
| 1200 | -2162 | -2534 | -2664 | -2928 | -3330 |
| 1225 | -2170 | -2564 | -2660 | -2914 | -3336 |
| 1250 | -2188 | -2518 | -2692 | -2918 | -3334 |
| 1275 | -2190 | -2562 | -2660 | -2898 | -3344 |
| 1295 | -2198 | -2578 | -2686 | -2908 | -3354 |
| 1300 | -2200 | -2576 | -2690 | -2812 | -3384 |
| 1325 | -2204 | -2540 | -2708 | -2826 | -3410 |
| 1350 | -2222 | -2532 | -2696 | -2820 | -3420 |
| 1355 | -2224 | -2538 | -2682 | -2820 | -3422 |
| 1360 | -2222 | -2542 | -2702 | -2990 | -3358 |
| 1375 | -2226 | -2540 | -2702 | -2956 | -3384 |
| 1400 | -2228 | -2514 | -2698 | -2956 | -3390 |
| 1425 | -2244 | -2558 | -2688 | -2940 | -3368 |
| 1450 | -2248 | -2560 | -2662 | -2824 | -3416 |
| 1475 | -2250 | -2566 | -2676 | -2824 | -3394 |
| 1480 | -2254 | -2590 | -2670 | -2944 | -3352 |
| 1500 | -2262 | -2536 | -2684 | -2950 | -3348 |
| 1510 | -2260 | -2560 | -2666 | -2920 | -3358 |
| 1515 | -2260 | -2560 | -2664 | -2818 | -3378 |
| 1525 | -2270 | -2520 | -2662 | -2820 | -3384 |
| 1545 | -2272 | -2544 | -2682 | -2824 | -3378 |
| 1550 | -2274 | -2546 | -2664 | -2942 | -3360 |
| 1575 | -2284 | -2558 | -2658 | -2934 | -3368 |
| 1600 | -2296 | -2552 | -2654 | -2924 | -3358 |
| 1625 | -2306 | -2572 | -2652 | -2922 | -3360 |
| 1650 | -2354 | -2576 | -2658 | -2932 | -3362 |
| 1675 | -2356 | -2556 | -2662 | -2938 | -3362 |
| 1690 | -2352 | -2584 | -2640 | -2916 | -3358 |
| 1695 | -2360 | -2574 | -2644 | -2816 | -3396 |
| 1700 | -2368 | -2568 | -2642 | -2816 | -3404 |

| | | | | | |
|------|-------|-------|-------|-------|-------|
| 1725 | -2368 | -2592 | -2640 | -2834 | -3396 |
| 1750 | -2360 | -2610 | -2644 | -2830 | -3394 |

Table A4- 7: ILN 2398 Havsule – Time picks of selected horizons.

| Shot Point | Calculated depth to seabed (m) | Calculated depth to top Slide W and top mound (m) | Calculated depth to top Slide W and base mound (m) | Calculated depth to base Slide W (m) | Calculated depth to base Brygge (m) |
|------------|--------------------------------------|--|--|--|---|
| 825 | -1558 | -1996 | -2039 | -2227 | -2762 |
| 850 | -1547 | -2028 | -2028 | -2229 | -2754 |
| 875 | -1577 | -2031 | -2031 | -2232 | -2760 |
| 900 | -1588 | -2032 | -2032 | -2235 | -2762 |
| 925 | -1590 | -2039 | -2039 | -2240 | -2763 |
| 945 | -1619 | -2036 | -2036 | -2241 | -2768 |
| 950 | -1583 | -2021 | -2054 | -2234 | -2761 |
| 975 | -1627 | -2018 | -2066 | -2240 | -2763 |
| 1000 | -1654 | -2001 | -2063 | -2223 | -2774 |
| 1025 | -1639 | -1996 | -2070 | -2231 | -2754 |
| 1030 | -1639 | -2020 | -2073 | -2380 | -2742 |
| 1050 | -1652 | -2012 | -2092 | -2401 | -2747 |
| 1075 | -1650 | -1995 | -2090 | -2435 | -2757 |
| 1100 | -1663 | -1968 | -2089 | -2326 | -2749 |
| 1105 | -1663 | -1973 | -2090 | -2330 | -2749 |
| 1110 | -1650 | -1971 | -2095 | -2230 | -2750 |
| 1125 | -1669 | -1979 | -2098 | -2234 | -2764 |
| 1150 | -1672 | -1979 | -2111 | -2234 | -2761 |
| 1155 | -1674 | -1997 | -2115 | -2375 | -2765 |
| 1175 | -1682 | -2005 | -2110 | -2377 | -2728 |
| 1200 | -1686 | -2006 | -2111 | -2391 | -2751 |
| 1225 | -1693 | -2032 | -2109 | -2378 | -2756 |
| 1250 | -1707 | -1991 | -2131 | -2370 | -2743 |
| 1275 | -1708 | -2028 | -2107 | -2359 | -2759 |
| 1295 | -1714 | -2041 | -2129 | -2363 | -2763 |
| 1300 | -1716 | -2040 | -2131 | -2261 | -2773 |
| 1325 | -1719 | -2008 | -2144 | -2269 | -2792 |
| 1350 | -1733 | -2000 | -2132 | -2263 | -2801 |
| 1355 | -1735 | -2005 | -2121 | -2267 | -2807 |
| 1360 | -1733 | -2008 | -2138 | -2442 | -2772 |
| 1375 | -1736 | -2006 | -2137 | -2406 | -2790 |
| 1400 | -1738 | -1984 | -2132 | -2405 | -2794 |
| 1425 | -1750 | -2020 | -2125 | -2392 | -2776 |
| 1450 | -1753 | -2022 | -2104 | -2276 | -2806 |
| 1475 | -1755 | -2027 | -2116 | -2272 | -2783 |
| 1480 | -1758 | -2047 | -2112 | -2402 | -2767 |
| 1500 | -1764 | -2000 | -2119 | -2401 | -2758 |
| 1510 | -1763 | -2021 | -2106 | -2375 | -2768 |
| 1515 | -1763 | -2021 | -2105 | -2268 | -2770 |
| 1525 | -1770 | -1986 | -2100 | -2267 | -2773 |
| 1545 | -1772 | -2006 | -2117 | -2268 | -2764 |
| 1550 | -1774 | -2008 | -2103 | -2397 | -2772 |
| 1575 | -1781 | -2017 | -2098 | -2390 | -2779 |
| 1600 | -1791 | -2011 | -2093 | -2379 | -2768 |
| 1625 | -1799 | -2028 | -2092 | -2378 | -2770 |
| 1650 | -1836 | -2027 | -2093 | -2383 | -2769 |

| | | | | | |
|------|-------|-------|-------|-------|-------|
| 1675 | -1838 | -2010 | -2095 | -2387 | -2767 |
| 1690 | -1834 | -2034 | -2079 | -2371 | -2768 |
| 1695 | -1841 | -2025 | -2081 | -2263 | -2783 |
| 1700 | -1847 | -2019 | -2079 | -2263 | -2790 |
| 1725 | -1847 | -2040 | -2078 | -2284 | -2788 |
| 1750 | -1841 | -2056 | -2083 | -2280 | -2786 |

Table A4- 8: ILN 2398 Havsule – Calculated depths to selected horizons.**CDP 2920 Havsule**

| Shot Point | Time pick of seabed (ms) | Time pick of top Slide W and top mound (ms) | Time pick of top Slide W and base mound (ms) | Time pick of base Slide W (ms) | Time pick of base Brygge (ms) |
|------------|--------------------------|---|--|--------------------------------|-------------------------------|
| 25 | -2026 | -2564 | -2564 | -2830 | -3548 |
| 50 | -2014 | -2524 | -2572 | -2820 | -3516 |
| 75 | -2136 | -2518 | -2560 | -2786 | -3562 |
| 100 | -2000 | -2470 | -2582 | -2790 | -3582 |
| 125 | -2012 | -2494 | -2610 | -2788 | -3584 |
| 150 | -1980 | -2492 | -2560 | -2742 | -3570 |
| 175 | -2034 | -2472 | -2618 | -2750 | -3568 |
| 200 | -2006 | -2462 | -2588 | -2716 | -3542 |
| 215 | -2002 | -2438 | -2616 | -2714 | -3540 |
| 230 | -1996 | -2442 | -2604 | -2842 | -3488 |
| 250 | -1960 | -2406 | -2604 | -2842 | -3464 |
| 275 | -1962 | -2386 | -2580 | -2836 | -3432 |
| 300 | -1920 | -2390 | -2572 | -2828 | -3388 |
| 325 | -1938 | -2380 | -2544 | -2802 | -3352 |
| 350 | -1942 | -2414 | -2528 | -2800 | -3330 |
| 375 | -1912 | -2422 | -2478 | -2770 | -3290 |
| 400 | -1922 | -2434 | -2478 | -2766 | -3258 |
| 425 | -1914 | -2440 | -2440 | -2750 | -3222 |
| 450 | -1904 | -2440 | -2440 | -2750 | -3218 |
| 475 | -1904 | -2438 | -2438 | -2742 | -3188 |
| 500 | -1892 | -2428 | -2428 | -2744 | -3158 |
| 520 | -1894 | -2430 | -2430 | -2738 | -3126 |
| 535 | -1896 | -2424 | -2424 | -2562 | -3184 |
| 550 | -1890 | -2406 | -2406 | -2554 | -3176 |
| 575 | -1888 | -2402 | -2402 | -2558 | -3186 |
| 600 | -1886 | -2412 | -2412 | -2572 | -3200 |

Table A4- 9: CDP 2920 Havsule – Time picks of selected horizons.

| Shot Point | Calculated depth to seabed (m) | Calculated depth to top Slide W and top mound (m) | Calculated depth to top Slide W and base mound (m) | Calculated depth to base Slide W (m) | Calculated depth to base Brygge (m) |
|------------|--------------------------------|---|--|--------------------------------------|-------------------------------------|
| 25 | -1580 | -2043 | -2043 | -2325 | -2968 |
| 50 | -1571 | -2010 | -2048 | -2311 | -2935 |
| 75 | -1666 | -1995 | -2029 | -2268 | -2963 |
| 100 | -1560 | -1964 | -2055 | -2275 | -2985 |
| 125 | -1569 | -1984 | -2078 | -2266 | -2980 |

| | | | | | |
|-----|-------|-------|-------|-------|-------|
| 150 | -1544 | -1985 | -2040 | -2232 | -2975 |
| 175 | -1586 | -1963 | -2081 | -2221 | -2954 |
| 200 | -1565 | -1957 | -2059 | -2194 | -2935 |
| 215 | -1561 | -1937 | -2080 | -2184 | -2925 |
| 230 | -1557 | -1941 | -2071 | -2323 | -2902 |
| 250 | -1529 | -1913 | -2072 | -2324 | -2882 |
| 275 | -1530 | -1895 | -2052 | -2323 | -2857 |
| 300 | -1498 | -1902 | -2049 | -2320 | -2822 |
| 325 | -1512 | -1892 | -2024 | -2297 | -2790 |
| 350 | -1515 | -1921 | -2013 | -2301 | -2776 |
| 375 | -1491 | -1930 | -1975 | -2284 | -2750 |
| 400 | -1499 | -1940 | -1975 | -2280 | -2721 |
| 425 | -1493 | -1946 | -1946 | -2273 | -2697 |
| 450 | -1485 | -1946 | -1946 | -2274 | -2694 |
| 475 | -1485 | -1945 | -1945 | -2266 | -2666 |
| 500 | -1476 | -1937 | -1937 | -2271 | -2642 |
| 520 | -1477 | -1939 | -1939 | -2264 | -2612 |
| 535 | -1479 | -1933 | -1933 | -2079 | -2637 |
| 550 | -1474 | -1918 | -1918 | -2075 | -2632 |
| 575 | -1473 | -1915 | -1915 | -2080 | -2643 |
| 600 | -1471 | -1924 | -1924 | -2093 | -2656 |

Table A4- 10: CDP 2920 Havsule – Calculated depths to selected horizons.**ILN 2574 Havsule**

| Shot Point | Time pick of seabed (ms) | Time pick of top Slide W and top mound (ms) | Time pick of top Slide W and base mound (ms) | Time pick of base Slide W (ms) | Time pick of base Brygge (ms) |
|------------|--------------------------|---|--|--------------------------------|-------------------------------|
| 800 | -2004 | -2532 | -2532 | -2696 | -3318 |
| 775 | -2004 | -2510 | -2548 | -2704 | -3316 |
| 750 | -2026 | -2466 | -2572 | -2698 | -3320 |
| 725 | -2020 | -2484 | -2558 | -2686 | -3312 |
| 700 | -2012 | -2458 | -2550 | -2670 | -3318 |
| 690 | -2004 | -2476 | -2546 | -2660 | -3298 |
| 675 | -1982 | -2456 | -2564 | -2828 | -3300 |
| 650 | -1922 | -2460 | -2572 | -2870 | -3292 |
| 625 | -1972 | -2448 | -2554 | -2840 | -3304 |
| 600 | -1978 | -2404 | -2594 | -2858 | -3366 |
| 575 | -1960 | -2406 | -2604 | -2842 | -3344 |
| 550 | -1962 | -2368 | -2632 | -2824 | -3358 |
| 525 | -1966 | -2446 | -2530 | -2816 | -3352 |
| 500 | -1974 | -2390 | -2566 | -2836 | -3398 |
| 475 | -1940 | -2396 | -2576 | -2830 | -3360 |
| 450 | -1976 | -2414 | -2560 | -2858 | -3378 |
| 425 | -1990 | -2450 | -2546 | -2830 | -3400 |
| 410 | -1978 | -2412 | -2564 | -2834 | -3388 |
| 400 | -1974 | -2450 | -2530 | -2664 | -3398 |
| 375 | -1990 | -2488 | -2488 | -2660 | -3416 |
| 350 | -1980 | -2488 | -2488 | -2664 | -3390 |
| 325 | -2101 | -2482 | -2482 | -2664 | -3406 |
| 300 | -2012 | -2484 | -2484 | -2670 | -3428 |
| 275 | -2016 | -2490 | -2490 | -2680 | -3460 |
| 250 | -2042 | -2490 | -2490 | -2684 | -3528 |
| 225 | -2062 | -2480 | -2480 | -2694 | -3540 |

Table A4- 11: ILN 2574 Havsule – Time picks of selected horizons.

| Shot Point | Calculated depth to seabed (m) | Calculated depth to top Slide W and top mound (m) | Calculated depth to top Slide W and base mound (m) | Calculated depth to base Slide W (m) | Calculated depth to base Brygge (m) |
|------------|--------------------------------------|--|--|--|---|
| 800 | -1563 | -2017 | -2017 | -2191 | -2749 |
| 775 | -1563 | -1999 | -2029 | -2194 | -2743 |
| 750 | -1580 | -1959 | -2044 | -2178 | -2735 |
| 725 | -1576 | -1975 | -2035 | -2170 | -2731 |
| 700 | -1569 | -1953 | -2027 | -2154 | -2735 |
| 690 | -1563 | -1969 | -2026 | -2146 | -2718 |
| 675 | -1546 | -1954 | -2041 | -2320 | -2743 |
| 650 | -1499 | -1962 | -2052 | -2368 | -2746 |
| 625 | -1538 | -1948 | -2033 | -2336 | -2752 |
| 600 | -1543 | -1909 | -2063 | -2342 | -2797 |
| 575 | -1529 | -1913 | -2072 | -2324 | -2774 |
| 550 | -1530 | -1880 | -2093 | -2296 | -2775 |
| 525 | -1533 | -1946 | -2014 | -2317 | -2797 |
| 500 | -1540 | -1898 | -2040 | -2325 | -2829 |
| 475 | -1513 | -1906 | -2051 | -2319 | -2795 |
| 450 | -1541 | -1918 | -2036 | -2351 | -2817 |
| 425 | -1552 | -1948 | -2025 | -2326 | -2837 |
| 410 | -1543 | -1916 | -2039 | -2325 | -2821 |
| 400 | -1540 | -1949 | -2014 | -2156 | -2814 |
| 375 | -1552 | -1981 | -1981 | -2163 | -2840 |
| 350 | -1544 | -1982 | -1982 | -2168 | -2819 |
| 325 | -1639 | -1967 | -1967 | -2159 | -2824 |
| 300 | -1569 | -1975 | -1975 | -2172 | -2852 |
| 275 | -1572 | -1980 | -1980 | -2181 | -2881 |
| 250 | -1593 | -1978 | -1978 | -2183 | -2940 |
| 225 | -1608 | -1968 | -1968 | -2194 | -2953 |

Table A4- 12: ILN 2574 Havsule – Calculated depths to selected horizons.

CDP 4972 Solsikke

| Shot Point | Time pick of seabed (ms) | Time pick of top Slide W and top mound (ms) | Time pick of top Slide W and base mound (ms) | Time pick of base Slide W (ms) | Time pick of base Brygge (ms) |
|------------|-----------------------------|--|---|--------------------------------------|-------------------------------------|
| 1000 | -2400 | -2608 | -2738 | -2878 | -3132 |
| 975 | -2428 | -2612 | -2730 | -2894 | -3146 |
| 950 | -2422 | -2590 | -2712 | -2870 | -3130 |
| 925 | -2408 | -2580 | -2710 | -2858 | -3112 |
| 900 | -2372 | -2578 | -2686 | -2754 | -3090 |
| 875 | -2420 | -2572 | -2710 | -2770 | -3088 |
| 850 | -2364 | -2572 | -2672 | -2746 | -3056 |
| 825 | -2378 | -2584 | -2662 | -2742 | -3048 |
| 800 | -2340 | -2552 | -2658 | -2730 | -3042 |
| 775 | -2372 | -2602 | -2644 | -2732 | -3018 |
| 750 | -2346 | -2562 | -2634 | -2704 | -2996 |

| | | | | | |
|-----|-------|-------|-------|-------|-------|
| 725 | -2302 | -2534 | -2618 | -2668 | -2990 |
| 700 | -2370 | -2582 | -2640 | -2686 | -3010 |
| 675 | -2334 | -2560 | -2616 | -2664 | -2992 |
| 650 | -2318 | -2538 | -2624 | -2672 | -2982 |
| 625 | -2312 | -2558 | -2606 | -2668 | -2980 |
| 600 | -2320 | -2574 | -2614 | -2676 | -2984 |
| 575 | -2318 | -2560 | -2626 | -2674 | -2974 |
| 550 | -2324 | -2578 | -2622 | -2674 | -2970 |
| 525 | -2308 | -2558 | -2608 | -2664 | -2974 |
| 500 | -2364 | -2554 | -2596 | -2650 | -2970 |
| 475 | -2306 | -2556 | -2588 | -2648 | -2964 |
| 450 | -2288 | -2562 | -2574 | -2648 | -2940 |
| 425 | -2294 | -2562 | -2574 | -2624 | -2930 |
| 400 | -2314 | -2570 | -2570 | -2630 | -2950 |
| 375 | -2320 | -2566 | -2590 | -2640 | -2936 |
| 350 | -2308 | -2564 | -2564 | -2632 | -2946 |

Table A4- 13: CDP 4972 Solsikke – Time picks of selected horizons.

| Shot Point | Calculated depth to seabed (m) | Calculated depth to top Slide W and top mound (m) | Calculated depth to top Slide W and base mound (m) | Calculated depth to base Slide W (m) | Calculated depth to base Brygge (m) |
|------------|--------------------------------------|--|--|--|---|
| 1000 | -1872 | -2051 | -2156 | -2304 | -2532 |
| 975 | -1894 | -2052 | -2147 | -2321 | -2547 |
| 950 | -1889 | -2034 | -2132 | -2299 | -2532 |
| 925 | -1878 | -2026 | -2131 | -2288 | -2515 |
| 900 | -1850 | -2027 | -2114 | -2186 | -2488 |
| 875 | -1887 | -2018 | -2130 | -2193 | -2478 |
| 850 | -1844 | -2023 | -2104 | -2182 | -2460 |
| 825 | -1855 | -2032 | -2095 | -2180 | -2454 |
| 800 | -1825 | -2008 | -2093 | -2169 | -2449 |
| 775 | -1850 | -2048 | -2082 | -2175 | -2431 |
| 750 | -1830 | -2016 | -2074 | -2148 | -2410 |
| 725 | -1795 | -1995 | -2063 | -2116 | -2404 |
| 700 | -1848 | -2031 | -2078 | -2126 | -2417 |
| 675 | -1820 | -2015 | -2060 | -2111 | -2405 |
| 650 | -1808 | -1997 | -2067 | -2117 | -2395 |
| 625 | -1803 | -2015 | -2054 | -2119 | -2399 |
| 600 | -1809 | -2028 | -2060 | -2126 | -2402 |
| 575 | -1808 | -2016 | -2069 | -2120 | -2389 |
| 550 | -1813 | -2031 | -2067 | -2122 | -2387 |
| 525 | -1800 | -2015 | -2056 | -2115 | -2393 |
| 500 | -1844 | -2007 | -2041 | -2098 | -2385 |
| 475 | -1799 | -2014 | -2040 | -2103 | -2386 |
| 450 | -1785 | -2020 | -2030 | -2108 | -2370 |
| 425 | -1789 | -2020 | -2030 | -2082 | -2357 |
| 400 | -1805 | -2025 | -2025 | -2089 | -2375 |
| 375 | -1809 | -2021 | -2041 | -2093 | -2359 |
| 350 | -1800 | -2020 | -2020 | -2092 | -2374 |

Table A4- 14: CDP 4972 Solsikke – Calculated depths to selected horizons.

ILN 3174 Solsikke

| Shot Point | Time pick of seabed (ms) | Time pick of top Slide W and top mound (ms) | Time pick of top Slide W and base mound (ms) | Time pick of base Slide W (ms) | Time pick of base Brygge (ms) |
|------------|--------------------------|---|--|--------------------------------|-------------------------------|
| 1300 | -2375 | -2661 | -2661 | -2661 | -2965 |
| 1305 | -2387 | -2660 | -2660 | -2660 | -2969 |
| 1310 | -2394 | -2663 | -2663 | -2663 | -2989 |
| 1315 | -2411 | -2671 | -2671 | -2671 | -2922 |
| 1320 | -2427 | -2688 | -2688 | -2688 | -2940 |
| 1325 | -2439 | -2688 | -2688 | -2688 | -2957 |
| 1330 | -2425 | -2637 | -2637 | -2669 | -2966 |
| 1335 | -2406 | -2591 | -2609 | -2665 | -2974 |
| 1340 | -2415 | -2541 | -2603 | -2670 | -2980 |
| 1350 | -2348 | -2543 | -2595 | -2661 | -2981 |
| 1375 | -2381 | -2562 | -2614 | -2672 | -2995 |
| 1400 | -2356 | -2552 | -2608 | -2660 | -3011 |
| 1425 | -2354 | -2544 | -2625 | -2674 | -3010 |
| 1450 | -2375 | -2562 | -2650 | -2691 | -3039 |
| 1475 | -2354 | -2562 | -2631 | -2698 | -3043 |
| 1500 | -2335 | -2568 | -2630 | -2695 | -3085 |
| 1525 | -2367 | -2587 | -2640 | -2711 | -3012 |
| 1550 | -2337 | -2583 | -2644 | -2726 | -3025 |
| 1575 | -2308 | -2564 | -2626 | -2721 | -3039 |
| 1600 | -2329 | -2569 | -2638 | -2737 | -3032 |
| 1625 | -2319 | -2577 | -2646 | -2720 | -3000 |
| 1650 | -2272 | -2566 | -2610 | -2698 | -3036 |
| 1675 | -2316 | -2566 | -2632 | -2710 | -3068 |
| 1700 | -2334 | -2596 | -2638 | -2726 | -3096 |
| 1725 | -2326 | -2584 | -2614 | -2716 | -3114 |
| 1750 | -2336 | -2580 | -2624 | -2712 | -3120 |
| 1775 | -2304 | -2562 | -2620 | -2704 | -3108 |
| 1800 | -2272 | -2540 | -2604 | -2702 | -3112 |
| 1825 | -2302 | -2548 | -2598 | -2694 | -3118 |
| 1850 | -2298 | -2544 | -2604 | -2690 | -3122 |
| 1875 | -2302 | -2556 | -2598 | -2698 | -3130 |
| 1900 | -2298 | -2554 | -2600 | -2696 | -3146 |
| 1925 | -2286 | -2522 | -2578 | -2682 | -3158 |
| 1950 | -2266 | -2540 | -2580 | -2690 | -3174 |
| 1975 | -2280 | -2550 | -2600 | -2702 | -3136 |
| 2000 | -2260 | -2524 | -2598 | -2692 | -3160 |
| 2025 | -2236 | -2532 | -2574 | -2682 | -3152 |

Table A4- 15: ILN 3174 Solsikke – Time picks of selected horizons.

| Shot Point | Calculated depth to seabed (m) | Calculated depth to top Slide W and top mound (m) | Calculated depth to top Slide W and base mound (m) | Calculated depth to base Slide W (m) | Calculated depth to base Brygge (m) |
|------------|--------------------------------------|--|--|--|---|
| 1300 | -1852 | -2099 | -2099 | -2099 | -2371 |
| 1305 | -1862 | -2097 | -2097 | -2097 | -2374 |
| 1310 | -1867 | -2099 | -2099 | -2099 | -2391 |
| 1315 | -1880 | -2104 | -2104 | -2104 | -2329 |
| 1320 | -1893 | -2118 | -2118 | -2118 | -2343 |
| 1325 | -1902 | -2117 | -2117 | -2117 | -2358 |
| 1330 | -1891 | -2074 | -2074 | -2108 | -2374 |
| 1335 | -1877 | -2036 | -2050 | -2110 | -2387 |
| 1340 | -1884 | -1992 | -2042 | -2113 | -2391 |
| 1350 | -1831 | -1999 | -2041 | -2111 | -2398 |
| 1375 | -1857 | -2013 | -2055 | -2116 | -2406 |
| 1400 | -1838 | -2006 | -2051 | -2106 | -2421 |
| 1425 | -1836 | -2000 | -2065 | -2117 | -2418 |
| 1450 | -1852 | -2013 | -2084 | -2128 | -2440 |
| 1475 | -1836 | -2015 | -2071 | -2142 | -2451 |
| 1500 | -1821 | -2022 | -2072 | -2141 | -2490 |
| 1525 | -1846 | -2035 | -2078 | -2153 | -2423 |
| 1550 | -1823 | -2034 | -2084 | -2170 | -2438 |
| 1575 | -1800 | -2020 | -2070 | -2171 | -2456 |
| 1600 | -1817 | -2023 | -2079 | -2183 | -2448 |
| 1625 | -1809 | -2031 | -2086 | -2165 | -2416 |
| 1650 | -1772 | -2025 | -2061 | -2154 | -2457 |
| 1675 | -1806 | -2022 | -2075 | -2157 | -2478 |
| 1700 | -1820 | -2046 | -2080 | -2173 | -2505 |
| 1725 | -1814 | -2036 | -2060 | -2168 | -2525 |
| 1750 | -1822 | -2032 | -2067 | -2161 | -2526 |
| 1775 | -1797 | -2019 | -2066 | -2155 | -2517 |
| 1800 | -1772 | -2003 | -2054 | -2158 | -2526 |
| 1825 | -1795 | -2007 | -2048 | -2149 | -2529 |
| 1850 | -1792 | -2004 | -2052 | -2143 | -2531 |
| 1875 | -1795 | -2014 | -2048 | -2154 | -2541 |
| 1900 | -1792 | -2013 | -2050 | -2151 | -2555 |
| 1925 | -1783 | -1986 | -2031 | -2141 | -2568 |
| 1950 | -1767 | -2003 | -2035 | -2152 | -2586 |
| 1975 | -1778 | -2011 | -2051 | -2159 | -2548 |
| 2000 | -1763 | -1990 | -2050 | -2149 | -2569 |
| 2025 | -1744 | -1999 | -2033 | -2147 | -2568 |

Table A4- 16: ILN 3174 Solsikke – Calculated depths to selected horizons.

Data used to compile dip of thrust faults**CDP 4942**

| Horizontal Distance (m) | Vertical Distance (m) | Dip (°) |
|-------------------------|-----------------------|---------|
| 525 | 151 | 16.1 |
| 825 | 186 | 12.7 |
| 925 | 193 | 11.8 |
| 175 | 35 | 11.3 |
| 375 | 71 | 10.7 |
| 300 | 71 | 13.3 |
| 425 | 94 | 12.5 |
| 500 | 106 | 11.9 |
| 500 | 108 | 12.2 |
| 425 | 88 | 11.7 |
| 700 | 107 | 8.7 |
| 350 | 66 | 10.6 |
| 350 | 74 | 11.9 |
| 625 | 135 | 12.2 |
| 675 | 123 | 10.3 |
| 625 | 95 | 8.7 |
| 800 | 104 | 7.4 |
| 525 | 85 | 9.2 |
| 250 | 76 | 16.9 |
| 650 | 130 | 11.3 |
| 575 | 92 | 9.1 |

Table A4- 17: CDP 4942 – Raw data pertaining to measurement of dip of thrust faults.**CDP 4002**

| Horizontal Distance (m) | Vertical Distance (m) | Dip (°) |
|-------------------------|-----------------------|---------|
| 450 | 73 | 9.2 |
| 700 | 113 | 9.2 |
| 650 | 114 | 10.0 |
| 825 | 158 | 10.8 |
| 525 | 113 | 12.2 |
| 750 | 124 | 9.4 |
| 475 | 85 | 10.1 |
| 625 | 131 | 11.9 |
| 625 | 107 | 9.7 |
| 375 | 81 | 12.3 |
| 350 | 81 | 13.1 |

Table A4- 18: CDP 4002 – Raw data pertaining to measurement of dip of thrust faults.

Data used to compile dips of crater sidewalls**Crater A – Westward dipping sidewalls**

| Horizontal Distance (m) | Vertical Distance (m) | Dip (°) |
|-------------------------|-----------------------|---------|
| 250 | 157 | 32.1 |
| 250 | 133 | 28.1 |
| 250 | 93 | 20.4 |
| 400 | 208 | 27.5 |
| 300 | 182 | 31.2 |
| 300 | 165 | 28.8 |
| 425 | 154 | 20.0 |
| 550 | 135 | 13.8 |
| 250 | 140 | 29.2 |
| 325 | 172 | 27.9 |
| 350 | 165 | 25.2 |
| 350 | 189 | 28.4 |
| 350 | 199 | 29.6 |
| 400 | 197 | 26.2 |
| 250 | 157 | 32.1 |
| 375 | 166 | 23.9 |
| 250 | 177 | 35.2 |
| 350 | 194 | 28.9 |
| 325 | 180 | 29.0 |
| 300 | 203 | 34.1 |
| 175 | 186 | 46.8 |

Table A4- 19: Data used to compile average dip of westward dipping sidewall of Crater A.**Crater A – Eastward dipping sidewalls**

| Horizontal Distance (m) | Vertical Distance (m) | Dip (°) |
|-------------------------|-----------------------|---------|
| 450 | 208 | 24.8 |
| 450 | 182 | 22.0 |
| 200 | 157 | 38.1 |
| 275 | 153 | 29.2 |
| 200 | 133 | 33.7 |
| 150 | 117 | 38.1 |
| 325 | 156 | 25.6 |
| 250 | 142 | 29.6 |
| 300 | 145 | 25.8 |
| 250 | 74 | 16.5 |
| 400 | 162 | 22.0 |
| 250 | 146 | 30.3 |
| 325 | 156 | 25.6 |
| 275 | 161 | 30.3 |
| 300 | 165 | 28.8 |
| 325 | 190 | 30.4 |
| 175 | 142 | 39.0 |
| 175 | 144 | 39.4 |
| 325 | 164 | 26.8 |
| 300 | 184 | 31.5 |
| 225 | 165 | 36.3 |

Table A4- 20: Data used to compile average dip of eastward dipping sidewall of Crater A.

Crater A – Southward dipping sidewalls

| Horizontal Distance (m) | Vertical Distance (m) | Dip (°) |
|-------------------------|-----------------------|---------|
| 375 | 212 | 29.4 |
| 300 | 191 | 32.5 |
| 275 | 176 | 32.6 |
| 300 | 178 | 30.6 |
| 200 | 176 | 41.3 |
| 200 | 180 | 42.0 |
| 175 | 185 | 46.6 |
| 175 | 165 | 43.3 |
| 100 | 191 | 62.4 |
| 225 | 172 | 37.5 |
| 225 | 164 | 36.1 |
| 325 | 186 | 29.8 |
| 250 | 171 | 34.4 |
| 225 | 160 | 35.4 |
| 200 | 140 | 34.9 |
| 100 | 168 | 59.3 |
| 225 | 152 | 34.1 |

Table A4- 21: Data used to compile average dip of southward dipping sidewall of Crater A.**Crater A – Northward dipping sidewalls**

| Horizontal Distance (m) | Vertical Distance (m) | Dip (°) |
|-------------------------|-----------------------|---------|
| 150 | 171 | 48.8 |
| 100 | 165 | 58.8 |
| 300 | 199 | 33.5 |
| 275 | 195 | 35.3 |
| 200 | 199 | 44.8 |
| 150 | 187 | 51.3 |
| 275 | 180 | 33.2 |
| 225 | 196 | 41.0 |
| 100 | 176 | 60.3 |
| 375 | 169 | 24.3 |
| 375 | 106 | 15.8 |
| 600 | 108 | 10.2 |
| 225 | 79 | 19.4 |
| 350 | 114 | 18.1 |
| 500 | 188 | 20.6 |
| 350 | 169 | 25.8 |

Table A4- 22: Data used to compile average dip of northward dipping sidewall of Crater A.**Crater B – Westward dipping sidewalls**

| Horizontal Distance (m) | Vertical Distance (m) | Dip (°) |
|-------------------------|-----------------------|---------|
| 150 | 102 | 34.1 |
| 150 | 103 | 34.4 |
| 150 | 77 | 27.2 |
| 75 | 53 | 35.2 |
| 100 | 71 | 35.3 |
| 125 | 96 | 37.6 |
| 125 | 71 | 29.6 |
| 175 | 83 | 25.2 |
| 275 | 127 | 24.8 |

| | | |
|-----|-----|------|
| 200 | 105 | 27.6 |
| 200 | 105 | 27.6 |
| 150 | 99 | 33.5 |
| 200 | 92 | 24.7 |
| 225 | 97 | 23.4 |
| 200 | 104 | 27.4 |
| 175 | 76 | 23.5 |
| 275 | 129 | 25.1 |
| 250 | 126 | 26.7 |
| 250 | 112 | 24.2 |
| 200 | 118 | 30.6 |
| 125 | 90 | 35.7 |
| 100 | 98 | 44.5 |
| 225 | 97 | 23.4 |
| 250 | 73 | 16.3 |
| 150 | 120 | 38.6 |
| 325 | 108 | 18.4 |
| 350 | 190 | 28.5 |
| 425 | 188 | 23.9 |
| 425 | 179 | 22.8 |
| 500 | 172 | 19.0 |
| 400 | 160 | 21.8 |
| 475 | 173 | 20.1 |
| 325 | 164 | 26.8 |
| 275 | 159 | 30.0 |
| 325 | 179 | 28.8 |
| 250 | 132 | 27.9 |
| 225 | 136 | 31.2 |
| 200 | 105 | 27.6 |
| 275 | 120 | 23.5 |
| 275 | 121 | 23.7 |
| 275 | 127 | 24.8 |
| 250 | 117 | 25.2 |
| 225 | 127 | 29.4 |
| 275 | 127 | 24.8 |
| 275 | 131 | 25.5 |
| 250 | 134 | 28.3 |
| 200 | 142 | 35.3 |
| 100 | 113 | 48.5 |
| 125 | 106 | 40.2 |
| 275 | 118 | 23.3 |
| 225 | 139 | 31.6 |
| 175 | 136 | 37.9 |
| 250 | 90 | 19.8 |

Table A4- 23: Data used to compile average dip of westward dipping sidewall of Crater B.

Crater B – Southward dipping sidewalls

| Horizontal Distance (m) | Vertical Distance (m) | Dip (°) |
|-------------------------|-----------------------|---------|
| 100 | 96 | 43.9 |
| 175 | 96 | 28.8 |
| 75 | 90 | 50.2 |
| 50 | 103 | 64.0 |
| 150 | 116 | 37.8 |
| 100 | 78 | 38.1 |
| 175 | 97 | 29.1 |
| 300 | 97 | 18.0 |
| 150 | 72 | 25.6 |
| 150 | 83 | 28.8 |
| 125 | 60 | 25.8 |
| 125 | 68 | 28.4 |
| 625 | 80 | 7.3 |
| 150 | 67 | 24.0 |
| 225 | 99 | 23.8 |
| 75 | 37 | 26.3 |
| 150 | 66 | 23.6 |
| 125 | 54 | 23.3 |
| 100 | 59 | 30.6 |
| 50 | 43 | 40.9 |
| 375 | 85 | 12.7 |
| 400 | 68 | 9.6 |
| 150 | 71 | 25.3 |
| 125 | 69 | 28.8 |
| 100 | 68 | 34.1 |
| 75 | 30 | 21.6 |
| 75 | 70 | 43.0 |
| 100 | 91 | 42.3 |
| 175 | 88 | 26.6 |

Table A4- 24: Data used to compile average dip of southward dipping sidewall of Crater B

Crater B – Northward dipping sidewalls

| Horizontal Distance (m) | Vertical Distance (m) | Dip (°) |
|-------------------------|-----------------------|---------|
| 300 | 156 | 27.4 |
| 250 | 170 | 34.3 |
| 225 | 169 | 37.0 |
| 350 | 149 | 23.1 |
| 150 | 83 | 28.8 |
| 100 | 128 | 52.0 |
| 125 | 166 | 53.0 |
| 400 | 169 | 22.9 |
| 75 | 138 | 61.4 |
| 300 | 182 | 31.2 |
| 125 | 177 | 54.7 |
| 100 | 156 | 57.3 |
| 175 | 164 | 43.1 |
| 275 | 170 | 31.8 |
| 75 | 106 | 54.7 |
| 350 | 153 | 23.7 |
| 250 | 147 | 30.5 |
| 125 | 162 | 52.3 |
| 325 | 166 | 27.1 |
| 400 | 161 | 21.9 |
| 125 | 153 | 50.8 |
| 150 | 141 | 43.2 |
| 150 | 161 | 47.0 |
| 175 | 177 | 45.3 |
| 50 | 191 | 75.4 |

Table A4- 25: Data used to compile average dip of northward dipping sidewall of Crater B.**Crater B – Incision 1 – Westward dipping sidewalls**

| Horizontal Distance (m) | Vertical Distance (m) | Dip (°) |
|-------------------------|-----------------------|---------|
| 350 | 168 | 25.7 |
| 250 | 129 | 27.3 |
| 275 | 96 | 19.2 |
| 200 | 67 | 18.6 |

Table A4- 26: Data used to compile average dip of westward dipping sidewall of Incision 1 of Crater B.**Crater B – Incision 1 – Southward dipping sidewalls**

| Horizontal Distance (m) | Vertical Distance (m) | Dip (°) |
|-------------------------|-----------------------|---------|
| 625 | 151 | 13.6 |
| 100 | 90 | 42.0 |
| 150 | 116 | 37.8 |

Table A4- 27: Data used to compile average dip of southward dipping sidewall of Incision 1 of Crater B.**Crater B – Incision 1 – Northward dipping sidewalls**

| Horizontal Distance (m) | Vertical Distance (m) | Dip (°) |
|-------------------------|-----------------------|---------|
|-------------------------|-----------------------|---------|

| | | |
|-----|-----|------|
| 175 | 146 | 39.9 |
| 125 | 120 | 43.9 |
| 500 | 160 | 17.8 |

Table A4- 28: Data used to compile average dip of northward dipping sidewall of Incision 1 of Crater B.

Crater B – Incision 2 – Westward dipping sidewalls

| Horizontal Distance (m) | Vertical Distance (m) | Dip (°) |
|-------------------------|-----------------------|---------|
| 250 | 128 | 27.1 |
| 250 | 109 | 23.5 |
| 275 | 147 | 28.1 |
| 200 | 114 | 29.7 |
| 200 | 113 | 29.5 |

Table A4- 29: Data used to compile average dip of westward dipping sidewall of Incision 2 of Crater B.

Crater B – Incision 2 – Southward dipping sidewalls

| Horizontal Distance (m) | Vertical Distance (m) | Dip (°) |
|-------------------------|-----------------------|---------|
| 175 | 88 | 26.6 |
| 225 | 106 | 25.2 |
| 150 | 103 | 34.4 |
| 75 | 114 | 56.7 |

Table A4- 30: Data used to compile average dip of southward dipping sidewall of Incision 2 of Crater B.

Crater B – Incision 2 – Northward dipping sidewalls

| Horizontal Distance (m) | Vertical Distance (m) | Dip (°) |
|-------------------------|-----------------------|---------|
| 300 | 154 | 27.2 |
| 75 | 171 | 66.4 |
| 75 | 149 | 63.3 |
| 75 | 144 | 62.5 |

Table A4- 31: Data used to compile average dip of northward dipping sidewall of Incision 2 of Crater B.

Crater B – Incision 3 – Westward dipping sidewalls

| Horizontal Distance (m) | Vertical Distance (m) | Dip (°) |
|-------------------------|-----------------------|---------|
| 150 | 115 | 37.6 |
| 250 | 129 | 27.3 |
| 250 | 126 | 26.7 |
| 150 | 85 | 29.4 |

Table A4- 32: Data used to compile average dip of westward dipping sidewall of Incision 3 of Crater B.**Crater B – Incision 3 – Southward dipping sidewalls**

| Horizontal Distance (m) | Vertical Distance (m) | Dip (°) |
|-------------------------|-----------------------|---------|
| 175 | 107 | 31.4 |
| 200 | 110 | 28.8 |
| 50 | 86 | 59.7 |
| 225 | 99 | 23.8 |

Table A4- 33: Data used to compile average dip of southward dipping sidewall of Incision 3 of Crater B.**Crater B – Incision 3 – Northward dipping sidewalls**

| Horizontal Distance (m) | Vertical Distance (m) | Dip (°) |
|-------------------------|-----------------------|---------|
| 100 | 125 | 51.3 |
| 200 | 126 | 32.2 |
| 225 | 124 | 28.8 |
| 300 | 193 | 32.7 |
| 600 | 173 | 16.1 |
| 350 | 178 | 26.9 |
| 225 | 128 | 29.6 |

Table A4- 34: Data used to compile average dip of northward dipping sidewall of Incision 3 of Crater B.**Crater B – Incision 4 – Westward dipping sidewalls**

| Horizontal Distance (m) | Vertical Distance (m) | Dip (°) |
|-------------------------|-----------------------|---------|
| 175 | 97 | 29.1 |

Table A4- 35: Data used to compile average dip of westward dipping sidewall of Incision 4 of Crater B.

Crater B – Incision 4 – Southward dipping sidewalls

| Horizontal Distance (m) | Vertical Distance (m) | Dip (°) |
|-------------------------|-----------------------|---------|
| 125 | 105 | 40.0 |
| 125 | 118 | 43.5 |
| 250 | 126 | 26.7 |
| 250 | 125 | 26.5 |
| 200 | 124 | 31.8 |
| 150 | 105 | 34.9 |

Table A4- 36: Data used to compile average dip of southward dipping sidewall of Incision 4 of Crater B.

Crater B – Incision 4 – Northward dipping sidewalls

| Horizontal Distance (m) | Vertical Distance (m) | Dip (°) |
|-------------------------|-----------------------|---------|
| 175 | 130 | 36.6 |
| 150 | 144 | 43.8 |
| 125 | 158 | 51.6 |
| 250 | 131 | 27.7 |
| 150 | 131 | 41.2 |

Table A4- 37: Data used to compile average dip of northward dipping sidewall of Incision 4 of Crater B.

Crater B – Incision 5 – Westward dipping sidewalls

| Horizontal Distance (m) | Vertical Distance (m) | Dip (°) |
|-------------------------|-----------------------|---------|
| 250 | 125 | 26.5 |
| 250 | 136 | 28.6 |
| 200 | 143 | 35.5 |
| 550 | 134 | 13.7 |
| 1000 | 133 | 7.6 |
| 375 | 115 | 17.1 |

Table A4- 38: Data used to compile average dip of westward dipping sidewall of Incision 5 of Crater B.

Crater B – Incision 5 – Southward dipping sidewalls

| Horizontal Distance (m) | Vertical Distance (m) | Dip (°) |
|-------------------------|-----------------------|---------|
| 75 | 120 | 57.9 |
| 250 | 127 | 26.9 |
| 200 | 97 | 25.9 |

Table A4- 39: Data used to compile average dip of southward dipping sidewall of Incision 5 of Crater B.

Crater B – Incision 5 – Northward dipping sidewalls

| Horizontal Distance (m) | Vertical Distance (m) | Dip (°) |
|-------------------------|-----------------------|---------|
|-------------------------|-----------------------|---------|

| | | |
|-----|-----|------|
| 375 | 140 | 20.4 |
| 225 | 122 | 28.4 |
| 250 | 128 | 27.1 |
| 50 | 131 | 69.1 |
| 175 | 127 | 36.0 |
| 150 | 120 | 38.6 |
| 150 | 124 | 39.5 |
| 200 | 135 | 34.1 |
| 200 | 144 | 35.7 |

Table A4- 40: Data used to compile average dip of northward dipping sidewall of Incision 5 of Crater B.

Crater B – Mini crater – Westward dipping sidewalls

| Horizontal Distance (m) | Vertical Distance (m) | Dip (°) |
|-------------------------|-----------------------|---------|
| 250 | 173 | 34.8 |
| 450 | 190 | 22.9 |
| 350 | 182 | 27.5 |
| 400 | 173 | 23.4 |
| 250 | 190 | 37.3 |

Table A4- 41: Data used to compile average dip of westward dipping sidewall of mini crater on basal surface of Crater B.

Crater B – Mini crater – Eastward dipping sidewalls

| Horizontal Distance (m) | Vertical Distance (m) | Dip (°) |
|-------------------------|-----------------------|---------|
| 200 | 72 | 19.8 |
| 575 | 42 | 4.2 |
| 175 | 72 | 22.3 |
| 175 | 38 | 12.3 |
| 325 | 76 | 13.2 |

Table A4- 42: Data used to compile average dip of eastward dipping sidewall of mini crater on basal surface of Crater B.

Crater B – Mini crater – Southward dipping sidewalls

| Horizontal Distance (m) | Vertical Distance (m) | Dip (°) |
|-------------------------|-----------------------|---------|
| 175 | 72 | 22.3 |
| 200 | 110 | 28.8 |
| 150 | 68 | 24.3 |
| 150 | 63 | 22.9 |

Table A4- 43: Data used to compile average dip of southward dipping sidewall of mini crater on basal surface of Crater B.

Crater B – Mini crater – Northward dipping sidewalls

| Horizontal Distance (m) | Vertical Distance (m) | Dip (°) |
|-------------------------|-----------------------|---------|
| 350 | 199 | 29.6 |
| 275 | 118 | 23.3 |
| 125 | 55 | 23.8 |
| 100 | 68 | 34.1 |
| 250 | 38 | 8.7 |

Table A4- 44: Data used to compile average dip of northward dipping sidewall of mini crater on basal surface of Crater B.

Data used to compile dip of top surface of ooze mounds**CDP 4002 – Westward dipping slopes**

| Horizontal Distance (m) | Vertical Distance (m) | Dip (°) |
|-------------------------|-----------------------|---------|
| 150 | 16 | 6.0 |
| 125 | 7 | 3.2 |
| 125 | 14 | 6.3 |
| 75 | 10 | 7.2 |
| 125 | 3 | 1.2 |
| 75 | 10 | 7.2 |
| 50 | 4 | 4.6 |
| 75 | 6 | 4.2 |
| 150 | 11 | 4.1 |
| 50 | 5 | 5.4 |
| 75 | 8 | 6.4 |
| 75 | 9 | 6.8 |
| 50 | 3 | 3.6 |
| 75 | 13 | 9.6 |
| 50 | 10 | 10.8 |
| 150 | 20 | 7.7 |
| 125 | 13 | 6.0 |
| 75 | 12 | 9.1 |
| 200 | 25 | 7.2 |
| 75 | 10 | 7.8 |
| 150 | 14 | 5.4 |
| 125 | 8 | 3.6 |
| 125 | 19 | 8.6 |
| 50 | 5 | 5.4 |
| 50 | 8 | 9.0 |
| 250 | 31 | 7.0 |
| 75 | 8 | 6.4 |
| 75 | 6 | 4.2 |
| 75 | 7 | 5.4 |

Table A4- 45: Data used to compile average dip of westward dipping slopes on the top of ooze mounds – CDP 4002.

CDP 4002 – Eastward dipping slopes

| Horizontal Distance (m) | Vertical Distance (m) | Dip (°) |
|-------------------------|-----------------------|---------|
| 125 | 8 | 3.7 |
| 75 | 4 | 3.2 |
| 75 | 6 | 4.2 |
| 50 | 3 | 3.6 |
| 75 | 3 | 2.4 |
| 50 | 5 | 5.4 |
| 75 | 8 | 6.4 |
| 75 | 6 | 4.2 |
| 250 | 14 | 3.2 |
| 150 | 4 | 1.4 |
| 75 | 4 | 2.8 |
| 125 | 12 | 5.4 |
| 75 | 1 | 0.9 |
| 150 | 8 | 3.2 |
| 200 | 10 | 2.8 |

| | | |
|-----|----|-----|
| 75 | 12 | 9.1 |
| 75 | 5 | 3.6 |
| 75 | 12 | 9.1 |
| 250 | 10 | 2.2 |
| 75 | 13 | 9.6 |
| 125 | 9 | 4.1 |
| 200 | 29 | 8.2 |
| 150 | 9 | 3.6 |
| 75 | 5 | 3.6 |
| 200 | 17 | 4.9 |
| 150 | 8 | 3.0 |
| 200 | 11 | 3.0 |
| 200 | 19 | 5.4 |
| 50 | 2 | 2.8 |

Table A4- 46: Data used to compile average dip of eastward dipping slopes on the top of ooze mounds – CDP 4002.

ILN 2634 – Northward dipping slopes

| Horizontal Distance (m) | Vertical Distance (m) | Dip (°) |
|-------------------------|-----------------------|---------|
| 250 | 40 | 9.0 |
| 250 | 48 | 10.9 |
| 475 | 14 | 1.7 |
| 300 | 28 | 5.2 |
| 250 | 12 | 2.8 |
| 125 | 15 | 7.1 |
| 425 | 31 | 4.2 |
| 350 | 21 | 3.4 |
| 175 | 7 | 2.3 |
| 250 | 29 | 6.7 |
| 900 | 100 | 6.3 |
| 125 | 9 | 3.9 |
| 300 | 29 | 5.6 |
| 175 | 12 | 3.9 |
| 250 | 38 | 8.6 |
| 300 | 33 | 6.2 |
| 125 | 9 | 3.9 |
| 250 | 19 | 4.3 |
| 125 | 3 | 1.6 |
| 550 | 50 | 5.2 |
| 425 | 36 | 4.9 |
| 350 | 40 | 6.5 |
| 125 | 9 | 3.9 |
| 425 | 28 | 3.7 |
| 50 | 12 | 13.5 |
| 300 | 17 | 3.3 |
| 250 | 24 | 5.5 |

Table A4- 47: Data used to compile average dip of northward dipping slopes on the top of ooze mounds – ILN 2634.

ILN 2634 – Southward dipping slopes

| Horizontal Distance (m) | Vertical Distance (m) | Dip (°) |
|-------------------------|-----------------------|---------|
| 250 | 33 | 7.5 |
| 600 | 34 | 3.3 |
| 300 | 14 | 2.6 |
| 250 | 34 | 7.8 |
| 425 | 22 | 3.0 |
| 300 | 12 | 2.3 |
| 425 | 43 | 5.8 |
| 125 | 3 | 1.6 |
| 350 | 5 | 0.8 |
| 475 | 2 | 0.2 |
| 600 | 48 | 4.6 |
| 175 | 41 | 13.3 |
| 125 | 7 | 3.2 |
| 175 | 28 | 8.9 |
| 475 | 43 | 5.2 |
| 250 | 3 | 0.8 |
| 175 | 22 | 7.3 |
| 250 | 19 | 4.3 |
| 175 | 3 | 1.1 |
| 250 | 41 | 9.4 |
| 350 | 45 | 7.3 |
| 650 | 65 | 5.7 |
| 50 | 7 | 7.8 |
| 425 | 31 | 4.2 |
| 50 | 7 | 7.8 |
| 300 | 19 | 3.6 |
| 250 | 38 | 8.6 |

Table A4- 48: Data used to compile average dip of southward dipping slopes on the top of ooze mounds – ILN 2634.

CDP 4942 – Westward dipping slopes

| Horizontal Distance (m) | Vertical Distance (m) | Dip (°) |
|-------------------------|-----------------------|---------|
| 400 | 15 | 2.2 |
| 325 | 17 | 3.0 |
| 125 | 9 | 3.9 |
| 200 | 36 | 10.2 |
| 125 | 3 | 1.6 |
| 125 | 33 | 14.7 |
| 325 | 40 | 6.9 |
| 200 | 15 | 4.4 |
| 200 | 10 | 3.0 |
| 125 | 12 | 5.5 |
| 250 | 29 | 6.7 |
| 200 | 17 | 4.9 |
| 250 | 34 | 7.8 |
| 125 | 17 | 7.8 |
| 200 | 26 | 7.4 |
| 400 | 29 | 4.2 |
| 250 | 19 | 4.3 |

| | | |
|-----|----|------|
| 125 | 41 | 18.3 |
|-----|----|------|

Table A4- 49: Data used to compile average dip of westward dipping slopes on the top of ooze mounds – CDP 4942.

CDP 4942 – Eastward dipping slopes

| Horizontal Distance (m) | Vertical Distance (m) | Dip (°) |
|-------------------------|-----------------------|---------|
| 450 | 15 | 2.0 |
| 200 | 9 | 2.5 |
| 200 | 29 | 8.3 |
| 200 | 19 | 5.4 |
| 75 | 10 | 7.8 |
| 125 | 31 | 13.9 |
| 250 | 43 | 9.8 |
| 450 | 17 | 2.2 |
| | 9 | 6.5 |
| 75 | 26 | 4.5 |
| 325 | 29 | 5.1 |
| 325 | 12 | 5.5 |
| 125 | 17 | 3.9 |
| 250 | 12 | 5.5 |
| 125 | 22 | 5.1 |
| 250 | 26 | 4.5 |
| 325 | 15 | 4.4 |
| 200 | 60 | 5.3 |
| 650 | | |

Table A4- 50: Data used to compile average dip of eastward dipping slopes on the top of ooze mounds – CDP 4942.

ILN 2398 – Northward dipping slopes

| Horizontal Distance (m) | Vertical Distance (m) | Dip (°) |
|-------------------------|-----------------------|---------|
| 325 | 15 | 2.7 |
| 400 | 41 | 5.9 |
| 475 | 34 | 4.1 |
| 400 | 34 | 4.9 |
| 150 | 22 | 8.5 |
| 250 | 12 | 2.8 |
| 250 | 22 | 5.1 |
| 550 | 34 | 3.6 |
| 1200 | 12 | 0.6 |
| 325 | 21 | 3.6 |
| 550 | 26 | 2.7 |
| 250 | 24 | 5.5 |
| 475 | 24 | 2.9 |
| 325 | 29 | 5.1 |
| 250 | 10 | 2.4 |
| 150 | 17 | 6.5 |
| 250 | 5 | 1.2 |
| 400 | 48 | 6.9 |
| 325 | 15 | 2.7 |
| 250 | 12 | 2.8 |
| 250 | 3 | 0.8 |
| 150 | 26 | 9.8 |
| 150 | 5 | 2.0 |

| | | |
|-----|----|-----|
| 75 | 2 | 1.3 |
| 325 | 19 | 3.3 |
| 250 | 10 | 2.4 |
| 475 | 45 | 5.4 |
| 400 | 31 | 4.4 |
| 400 | 36 | 5.2 |
| 150 | 3 | 1.3 |
| 250 | 14 | 3.2 |
| 150 | 22 | 8.5 |
| 150 | 9 | 3.3 |
| 150 | 7 | 2.6 |
| 150 | 12 | 4.6 |
| 325 | 10 | 1.8 |
| 475 | 31 | 3.7 |
| 475 | 38 | 4.6 |
| 250 | 14 | 3.2 |
| 150 | 15 | 5.9 |
| 150 | 9 | 3.3 |

Table A4- 51: Data used to compile average dip of northward dipping slopes on the top of ooze mounds – ILN 2398.

ILN 2398 – Southward dipping slopes

| Horizontal Distance (m) | Vertical Distance (m) | Dip (°) |
|-------------------------|-----------------------|---------|
| 325 | 17 | 3.0 |
| 325 | 29 | 5.1 |
| 250 | 24 | 5.5 |
| 325 | 28 | 4.8 |
| 150 | 28 | 10.4 |
| 150 | 7 | 2.6 |
| 325 | 14 | 2.4 |
| 475 | 28 | 3.3 |
| 75 | 10 | 7.8 |
| 150 | 7 | 2.6 |
| 650 | 40 | 3.5 |
| 650 | 46 | 4.1 |
| 250 | 24 | 5.5 |
| 325 | 9 | 1.5 |
| 75 | 5 | 3.9 |
| 250 | 21 | 4.7 |
| 150 | 10 | 3.9 |
| 250 | 17 | 3.9 |
| 800 | 22 | 1.6 |
| 325 | 5 | 0.9 |
| 325 | 3 | 0.6 |
| 75 | 34 | 24.7 |
| 325 | 31 | 5.4 |
| 150 | 7 | 2.6 |
| 250 | 12 | 2.8 |
| 325 | 7 | 1.2 |
| 875 | 41 | 2.7 |
| 400 | 12 | 1.7 |
| 325 | 28 | 4.8 |
| 150 | 5 | 2.0 |
| 400 | 5 | 0.7 |
| 325 | 2 | 0.3 |
| 725 | 9 | 0.7 |

| | | |
|------|----|-----|
| 150 | 5 | 2.0 |
| 150 | 7 | 2.6 |
| 650 | 36 | 3.2 |
| 800 | 53 | 3.8 |
| 1200 | 33 | 1.6 |
| 150 | 26 | 9.8 |
| 150 | 5 | 2.0 |
| 400 | 22 | 3.2 |

Table A4- 52: Data used to compile average dip of southward dipping slopes on the top of ooze mounds – ILN 2398.

